1

ORNL-4238
UC-20 – Controlled Thermonuclear Processes

THERMONUCLEAR DIVISION

SEMIANNUAL PROGRESS REPORT

FOR PERIOD ENDING OCTOBER 31, 1967

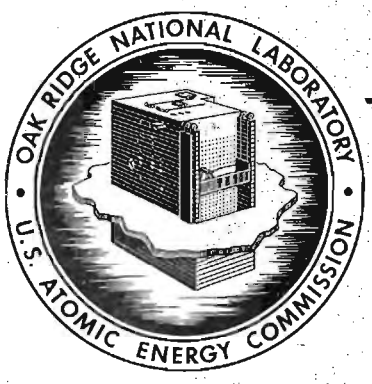

OAK RIDGE NATIONAL LABORATORY
operated by
UNION CARBIDE CORPORATION
for the
U.S. ATOMIC ENERGY COMMISSION

Printed in the United States of America. Available from Clearinghouse for Federal
Scientific and Technical Information, National Bureau of Standards,
U.S. Department of Commerce, Springfield, Virginia 22151
Price: Printed Copy $3.00; Microfiche $0.65

ORNL-4238

Contract No. W-7405-eng-26

THERMONUCLEAR DIVISION
SEMIANNUAL PROGRESS REPORT
for Period Ending October 31, 1967

MAY 1968

OAK RIDGE NATIONAL LABORATORY
Oak Ridge, Tennessee
operated by
UNION CARBIDE CORPORATION
for the
U. S. ATOMIC ENERGY COMMISSION

Reports previously issued in this series are as follows:

ORNL-2693	Period Ending January 30, 1959
ORNL-2802	Period Ending July 31, 1959
ORNL-2926	Period Ending January 31, 1960
ORNL-3011	Period Ending July 31, 1960
ORNL-3104	Period Ending January 31, 1961
ORNL-3239	Period Ending October 31, 1961
ORNL-3315	Period Ending April 30, 1962
ORNL-3392	Period Ending October 31, 1962
ORNL-3472	Period Ending April 30, 1963
ORNL-3564	Period Ending October 31, 1963
ORNL-3652	Period Ending April 30, 1964
ORNL-3760	Period Ending October 31, 1964
ORNL-3836	Period Ending April 30, 1965
ORNL-3908	Period Ending October 31, 1965
ORNL-3989	Period Ending April 30, 1966
ORNL-4063	Period Ending October 31, 1966
ORNL-4150	Period Ending April 30, 1967

Contents

Introduction

A. H. Snell

Progress into the Target Plasma Program appears in separated places in the text that follows. Theoretical "thinking ahead," summarized in Sect. 1.1.2, is mainly concerned with further investigation into loss-cone effects. Considerations couched on a Vlasov-Poisson treatment indicate that density thresholds for microinstabilities can be raised to values approximately corresponding to $\omega_{pi}^2 \geq (N\omega_{ci})^2$, N being the harmonic number. Although the use of a short plasma should suppress convective modes somewhat beyond these limits, some trouble may be encountered at reactor densities by nonconvective modes of high frequency. Refilling the low-energy end of the loss-cone distribution by adding cold ions (to about 10% of the hot ions) promises to reduce low-frequency fluctuations with $k_\perp \neq 0$, and it also contributes cyclotron damping (Sect. 1.1.3). Section 1.1.4 treats the benefits to be derived by spreading the injected hydrogen atoms in energy and in angle, the two kinds of spreading being treated sufficiently generally to reveal the effects of either by itself, or of the two in combination. Directional spread is found to be necessary in order to derive full benefits from energy spread.

In hardware, the Target Plasma Program appears in the INTEREM experiment (Sect. 4) and in the superconductivity work for IMP (Sects. 8.5 and 8.7), and it also has been aided by new cross-section measurements (Sect. 6.2). In INTEREM, since Ioffe bars have not yet been installed, comparisons have been made in mirror geometry between the behavior of an H^0-injection-created plasma with and without the presence of an electron-cyclotron-heated target plasma. The results are encouraging in that when the target plasma is present, neither high- nor low-frequency instabilities are found in the hot-ion plasma to densities of at least 5×10^8 cm^{-3}, which is about 100 times above the DCX-1.5 instability threshold and 11 times above the PHOENIX instability threshold when PHOENIX is operated under otherwise comparable conditions. The hot plasma takes the form of a thin disk; it is well behaved with respect to injected beam current (Fig. 4.3), ambient pressure (Fig. 4.4), and microwave power (Fig. 4.5). Higher densities could presumably be obtained with a larger H^0 beam or more microwave power, and especially at lower pressures – wherein abides the hope of magnetic-well stabilization. A discussion is given in Sect. 4.1.4 of the performance of INTEREM vis-à-vis three kinds of expected instabilities.

In the IMP superconducting work the most direct experiment was a quench test of a small pair of superconducting coils connected in opposition and immersed transversely in an external field of 60 to 80 kG (maximum). Such an arrangement subjects the windings to stresses comparable with (or scalable into) the stresses expected in IMP. Above 15 kG external applied field (or 45 kG maximum combined field), the wound material quenches at short-sample current values. In current density, the performance is just fair; one would hope for better material.

The cross-section work associated with Target Plasmas pertains to charge-transfer cross sections of 15- to 50-keV H^0 and H^+ particles in magnesium vapor. Results as given in Fig. 6.4 include new cross sections and some remeasurements that show departures from previously published values.

In summary, the Target Plasma Program moves ahead on several points. New major steps will come when Ioffe bars are installed in INTEREM and when 5.5-mm microwave resonant electron heating is attempted in ELMO.

Our report also describes continuing work on DCX-1.5 and DCX-2 (Sects. 2 and 3). In the

former, detailed studies of three instability modes (flute, "z-mode," and "θ-mode") have been carried out, with attention to refined theory, and experimentally taking into account variations of plasma potential with radius. For the flute, the growing and the nongrowing stages are separately investigated. The energy spread of the injected beam (77 "mA" of 20-keV H^0) has now been increased to 40%. In DCX-2, a rather complicated set of measurements, qualitatively new in plasma physics, describes by correlation measurements the several wave patterns that are set up by Harris instabilities with the injected beam either off or on, and with and without hydrogen arc dissociation. At risk of oversimplifying Sect. 3, one might say that the general picture is one of normal modes of standing waves fitted into the length of DCX-2, with some reflection from the ends and some power loss into the cold plasma at the ends. With the H^+ plasma suppressed, leaving only the hollow cylindrical plasma generated by the spiraling H_2^+ beam, one has an ideal realization of the theoretical model for the Burt-Harris modes, and indeed the comparison with theory is gratifying, especially when the effects of Landau damping are taken into account (Sect. 3.4).

The experiments on the levitated toroidal quadrupole are beginning to yield results, a principal one being summarized in Fig. 5.38. Here the loss of gun-injected plasma from the system is seen to depend upon the size of the probe inserted to measure it; extrapolation to zero probe size and corrections for gas scattering and the changing magnetic field leave a residual cross-field diffusion rate of 1/30 of the Bohm rate.

Some new kinds of measurements are now being applied to the studies of turbulent heating by beam-plasma interaction. At low currents in the electron beam, klystron-like modes have been recognized, but there is also evidence from bremsstrahlung intensity that heating takes place through the $\omega_{pe} = \omega_{ce}$ resonance. The discussion is given in Sect. 5.1.

The high-pressure helium arc work has reached its principal limited goal; that is, the radial radiation loss to the wall from the central core has been measured as about 50 W per centimeter length of arc at 4000 A. However, as is universal in plasma physics, the situation is not simple. A layer of photoionized gas surrounds the core, and power is lost to the ends. The arc is stable at pressures above 10 torrs, but as Sect. 5.4 further describes, the experiments have been confined to pressures below 50 torrs, which is not high enough to reveal evidence of gas confinement. At higher pressures, the existing arc is not fully ionized to He^{2+}. The current density will have to be increased to get into a regime that might show gas confinement. The density has been confirmed at $\eta_e = 10^{16}$ cm^{-3} by refraction of a laser beam.

* * * * *

The foregoing may be a sufficient summary to convey the flavor of the last six months' activities. This is the last of 16 semiannual reports for which I have contributed the introduction, because the divisional Directorship is about to be transferred to Dr. Postma. The fusion work is, I believe, in healthy shape. Through the efforts of the staff, the Target Plasma Program is well launched, including the superconducting engineering. The theoretical group continues to choose problems of telling pertinence. The toroidal multipole work is coming up fast, the electron cyclotron heating work is almost unique, and the remarkable empirical turbulent heating results will shortly be supported by better physical understanding as the program progresses.

Abstracts

1. PLASMA THEORY AND COMPUTATION

In this report we summarize recent studies of several aspects of resonant loss-cone instabilities: the general properties of the unstable oscillations, particularly in plasmas containing hot electrons; the stabilization effects resulting from addition of low-temperature ions to a hot-ion, hot-electron plasma; the results, with respect to stability criteria, of varying the energy and angle spread of the hot-ion distribution; and the behavior of these same modes at high densities, approaching reactor values. To date these studies have shown that the instabilities can be weakened or in some cases effectively eliminated by the various procedures studied in this report. Complete stabilization may, however, rely on effects not yet understood, such as the finite-length effects mentioned in this report or the effects associated with spatial variation in the confining magnetic field. Since these future studies will probably expand about solutions of the infinite-homogeneous-plasma–uniform-magnetic-field model investigated in the present work, we are continuing these detailed and increasingly realistic calculations while developing new analytical techniques required to understand the effects of spatial variations in plasma density and magnetic field strength.

2. INJECTION AND ACCUMULATION: NEUTRAL INJECTION EXPERIMENTS (DCX-1.5)

Investigations of the properties of plasma formed by injection of a 20-kev H^0 beam in the simple 2:1 mirror geometry (B_0 = 10 to 14 kG) have continued. As before, emphasis was given to the properties of the flute instability and to those of the two microinstabilities. An array of secondary-emission detectors for charge-exchange neutrals was used to study changes of hot-plasma axial distributions due to instabilities. An array of gridded cold-plasma collectors at one end of the plasma yielded similar information concerning radial distributions. The cold-plasma collectors and the lithium beam transmission technique were used to study plasma potential fluctuations.

Flute frequencies as a function of hot-ion density were measured. These results and instability threshold data are compared with theory. Although questions still remain as to the effects of zero-order electric fields, the experimental identification of a recently predicted constant frequency branch (of the flute dispersion relation) is suggested.

Other work with neutral injection included deliberate introduction of beam energy spread by unbalance of the ion source high-voltage supply, and installation of a new beam line.

One final experiment was performed with 600-keV H_2^+ injection. This was an attempt to stabilize the negative mass instability with inductive end walls. The results were negative.

3. INJECTION AND ACCUMULATION: MULTIPLE-PASS EXPERIMENTS (DCX-2)

Ion cyclotron harmonic instabilities have been studied in three different energetic plasma situations: (1) the equilibrium energetic proton plasma during the beam-on time, (2) the decaying energetic proton plasma during the afterglow period following beam turnoff, and (3) the injected H_2^+ beam with no energetic proton plasma present. The dominant instabilities are Harris-type modes, as shown by the measured phase relationship between perpendicular ion motion and axial electron oscillations.

The axial and azimuthal mode patterns of the beam-on plasma instabilities at the first few proton cyclotron harmonics have been measured in detail. The various harmonics have different mode

patterns and are independent on a long time scale, indicating that they are separate instabilities and not just a nonlinear manifestation of one instability. Each mode forms a standing-wave pattern which is either symmetric or antisymmetric about the machine midplane, implying reflections at the end of the energetic plasma region. Outward propagating waves are found in the cold plasma beyond this region that are time correlated with the oscillations in the energetic plasma interior.

The spectrum and correlation properties of the instability rf observed after beam turnoff are quite different from those found during the beam-on time and may reflect an entirely different instability behavior rather than a continuation of the beam-on plasma instability behavior.

The study of the microinstability in the injected ion beam has been extended to include the effects of finite length and electron temperature. Electron Landau damping of this microinstability has been demonstrated, and the instability wavelengths are found to be axial normal modes of the plasma cylinder.

4. ELECTRON-CYCLOTRON HEATING

INTEREM

The concept of a "target plasma," into which a beam of energetic particles is injected and can be trapped, now has assumed a wider role in our thinking of open-ended geometries in the light of the new calculations of instability thresholds in an energetic ion plasma which take into account the presence of a more dense hot-electron component.* The experiments in INTEREM now assume a direct relevance to the theory. Particularly encouraging, for future experiments, is the apparent stable confinement of a hot-ion density of $> 5 \times 10^8$ ions/cm^3 ($\omega_{pi}/\omega_{ci} > 1$) produced by injection of $\sim$55 mA of 20-keV H^0 into an ECH plasma at a pressure (gage) of 3×10^{-6} torr. The linear increase of ion density with beam current, the absence of axial spread of the plasma, and the absence of gyrofrequency fluctuations all point to plasma stability. A comparison with the relevant theories shows that the plasma stability may not be attributed solely to the hot electrons, but rather the short axial extent may serve to limit the possible instability modes. Thus extrapolation to other plasma geometries should not be made without caution.

*See Sect. 1.1, this semiannual report.

5. PLASMA PHYSICS

In the hot-electron plasma a dependence of the bremsstrahlung on the magnetic field strength was found. With a weak electron beam, klystron-like modes were observed. As the beam current is increased and electron heating occurs, the spectrum becomes much more complex. The spectrum resembles white noise, and there is a measurable spread and loss in beam energy at maximum electron temperature.

Studies of neutral light emission from the plasma of Burnout IV and V during operation give electron densities in the range of 10^{12} to 10^{13} cm^{-3}. The e-folding decay time of the neutral light was found to be on the order of 300 μsec.

The neutral gas surrounding the plasma of Burnout V was analyzed and found to contain low-molecular-weight compounds of carbon and deuterium in amounts up to 5%.

The objective of high-pressure arc experiments has continued to be the study of the properties of a fully ionized plasma surrounded by neutral gas. We have now measured the radiation transfer of energy to the walls, which is small, and the total radial energy transfer by all processes. We have measured the axial potential gradient and radial potential profile using a tungsten wire probe swept rapidly through the arc. We have measured the electron density by observing the deflection of a 10.6-μ laser beam passed transversely through the arc plasma.

Earlier determinations of arc profiles in He^+ light indicated that at a gas pressure of 50 torrs or less the 1-cm-radius arc column is almost entirely doubly ionized. New observations give values for total radial energy outflow per unit length, which increases with magnetic field but is rather insensitive to pressure between 4 and 50 torrs. Potential is now found to have a 3-V/cm gradient along the axis at peak currents and to be constant across the 1-cm-radius arc column. Outside it rises rapidly to anode potential. Electron density at 4 torrs is 1.2×10^{16}/cm^3 on axis, is nearly constant within a 1-cm radius, and approaches zero at 2 cm. Increase with pressure up to 20 torrs is

slight. All observations agree in showing the arc column to be stable except at the very lowest pressures. Instabilities seen at the lowest pressures disappear as pressure is increased.

The arc profiles obtained with the spectrometer in monochromatic light and the total radiation profiles obtained more recently with the thermocouple radiometer agree in suggesting that the partially ionized thin shell around the arc column is the primary source of radiation. It thus seems possible now to argue that knowledge of the total radiation in this layer would permit predicting the radiation limitations at the same pressure of a plasma-gas system of any diameter. Although the short-wavelength part of this radiation is not readily accessible for measurement because of strong absorption in the surrounding gas, the part that is transmitted and observed may provide information from which the total can be estimated. Present energy-transfer data are encouraging, but extension to higher gas pressure is still needed to allow evaluation of prospects of gas-bounded plasmas for fusion systems.

Spectroscopic studies of radiations from the high-density helium arc lead to $\overline{T}_e \sim 33{,}000°K$ from N^{2+} spectral lines obtained by using a small impurity of nitrogen. The helium spectrum "thermometer" method of Griem, which uses the relative intensities of He^+ λ 4686 Å to He λ 5876 Å, has been applied with the Abel inversion technique to obtain electron temperatures ranging from 35,000 to 62,000°K. Attempts to confirm the electron densities, previously measured from the Holtzmark broadening of He^+ λ 3203 Å, by using the Vidal line merging theory were inconclusive because of the intense background radiation from other sources.

Time-of-flight measurements are made on ion acoustic waves to determine the dispersion as the frequency increases toward the ion plasma frequency. The wave velocity shows the theoretically predicted decrease. In addition, a second, fast wave is observed, which propagates at frequencies above the ion plasma frequency, in agreement with Sessler's observations. It is suggested that the faster component may be a burst of accelerated ions.

Further studies of ion acoustic wave propagation reveal that we can measure accurately T_i, the collisional atom-ion wave damping, and γ_e, the adiabatic compression coefficient for the plasma electrons.

Study of electron transport in the PIG and the symmetric arc has been continued. An oscillating voltage is seen on a split cylinder surrounding the arc, and this oscillation decreases in frequency and amplitude as a positive bias voltage is applied to the split cylinder.

Electron-cyclotron heating has been accomplished without using a cavity by coupling microwave radiation directly from a dipole antenna to the plasma.

Our levitated multipole experiments are now under way in both a levitated quadrupole and a levitated hexapole. Both electron-cyclotron-resonance-produced plasma and gun-type plasma have been studied. We find a plasma lifetime of about 30 times the Bohm value.

6. ATOMIC AND MOLECULAR CROSS SECTIONS

The series of measurements of highly excited Rydberg states of isotopic hydrogen molecules has been concluded. Excited molecular state populations are smaller than those measured for H^0 and result from autoionization of excited vibrational levels of the molecules. Average Rydberg state lifetimes have been determined to be 3.5×10^{-7} sec for H_2, in agreement with theory, and 3.3×10^{-7} sec for HD lifetimes, which is approximately 10^2 greater than theory.

The charge-transfer cross sections, σ_{01}, σ_{10}, $\sigma_{0\bar{1}}$, and $\sigma_{1\bar{1}}$, for protons and hydrogen atoms in magnesium have been measured in the energy interval 15 to 50 keV. Preliminary results are reported of experiments to obtain energy-dispersed beams of hydrogen atoms using water vapor jets.

Measurements of the partial or the subshell contribution to the total photoabsorption cross section are reported for krypton and xenon in the photon energy range 300 to 2500 eV. Reasonably good agreement is obtained between experiment and theory. The simultaneous emission of two electrons occurs in 20% of the photoabsorption events. Studies have continued of the double-electron ejection from the *KL* shell of neon and argon and the *KM* shell of argon.

7. HIGH-CURRENT ION BEAM PRODUCTION AND INJECTION

The ion-optical studies described in the last report have been continued. It has been found that the limitation of beam quality is due entirely to the ion optics of the extraction region in the situations studied. Efforts to control the shape of the plasma surface have not produced significantly better results, but a new source which is being developed should provide better control of the plasma density gradient.

An unsuccessful test of the 600-keV non-PIG accelerator indicated the need for changes in the casting procedure used to make the epoxy insulators.

8. MAGNETICS AND SUPERCONDUCTIVITY

Because of a planned change of frequency of the microwave heating used in "ELMO," it is necessary to raise the magnetic field strength in the throats of the mirror coils from 21 to 39 kG. The existing mirror coils are helical pancake coils with hollow watercooled conductors. The regular pancake design could not be employed, since the space is very restricted. With increased field strength even coils of the helical pancake design could not be accommodated. There was only the choice either drastically to change the whole facility design or to use a coil type with a still higher current density. It was decided to use the latter solution by employing ribbon coils. Their design and preliminary tests are described, and several specific technological problems are discussed in detail.

The experimental mapping of magnet fields requires devices for placing the probes on exactly defined positions. Such a "positioner" has been designed and built. The positions of the probes are determined in a cylindrical coordinate system. The three field components can be measured simultaneously. The positioner is supposed to operate with vertical, horizontal, or oblique orientation of the axis. The new positioner design is described, and the performance of this device is discussed.

Important design details of magnet coils with water-cooled hollow conductors are the "crossovers." Several crossover designs have been used with more or less success. It seemed to be advisable to study in great detail the cast crossovers, which display different properties from those of previously used machined crossovers. A special form of this new type of crossover appears to be superior except for cases where very high current densities are required.

Our basic work on superconductivity is under joint sponsorship of the Thermonuclear Branch of the USAEC and of the George C. Marshall Space Flight Center, NASA. Experiments were made with bare strips of superconducting Nb–25% Ti and with various types of commercially available stabilized Nb-Ti conductors. The critical currents, the flux flow zones and the takeoff and the recovery currents were studied as functions of the applied magnetic field. The current-voltage characteristics of the flux flow zone were indicative of heat transfer from conductor surface to liquid helium in the form of $\dot{Q} = h^* \tau^{2.5}$. This conclusion from our flux flow measurements is in accordance with direct heat-transfer observations by several authors and our own experimental work on the same subject.

Presently we are working on the superconducting magnet system of IMP (see Sect. 8.7). The testing of the superconducting winding material is, of course, very important. We developed a new test method, the "cusp coil test," which is discussed in detail in this report.

Previously, for our micro Hall probes, we did extensive developmental work on the production of thin films by vacuum evaporation of indium arsenide and indium antimonide. For several of our experiments with superconductors we need thin coatings of copper or of dielectrics, for instance, aluminum oxide. These thin films are preferably produced by rf sputtering instead of by vacuum evaporation. Therefore, we extended our thin film work to rf sputtering, and we built an apparatus for this purpose. Preliminary working results are reported.

1. Plasma Theory and Computation

1.1 LOSS-CONE INSTABILITIES

1.1.1 Introduction

It has been known for many years that the non-Maxwellian velocity-space distributions resulting from mirror confinement of energetic plasma could lead to unstable electrostatic oscillations at frequencies near harmonics of the ion gyrofrequency. Such predictions have usually been based on solutions of the Vlasov and Poisson equations for the fluctuating electric field, $\mathbf{E}_1$:

$$\nabla \cdot \mathbf{E}_1 = -\frac{q^2 N}{m\epsilon_0} \int d\mathbf{v} \int^t dt' \, \mathbf{E}_1 \cdot \frac{\partial f_0}{\partial \mathbf{v}} ,$$

for various steady-state distributions, $f_0(\mathbf{r}, \mathbf{v})$, chosen to model more or less closely a realistic mirror-confined plasma. The results applicable to the infinite homogeneous plasma model may be understood conveniently by studying the class of distribution functions

$$f_0(v_\perp^2, v_{||}^2, T, j) = \frac{1}{\pi^{3/2} \alpha_\perp^2 \alpha_{||} j!} \left(\frac{v_\perp}{\alpha_\perp}\right)^{2j} e^{-\left(v_\perp^2/\alpha_\perp^2\right) - \left(v_{||}^2/\alpha_{||}^2\right)} , \tag{1}$$

where $\alpha_{||}^2 = T\alpha_\perp^2$ and where $j = 0, 1, 2, \ldots$ (the characteristics of these distributions are discussed in detail in Sect. 1.1.4). Plasma configurations of this type will support both the Harris instabilities[1] and loss-cone instabilities[2-4] and illustrate very clearly the underlying physical phenomena.

There have been many observations of large-amplitude fluctuations at gyrofrequency harmonics, although it has only recently become possible to make a sufficiently detailed comparison between theory and experiment to permit an evaluation of the applicability of the theory to laboratory plasmas. Where comparison has been possible, notably in low-density ($\omega_{pi} < \omega_{ci}$) plasmas, the theory has been found to be a useful guide, although some quantitative features are not fully understood, for example, the effects of finite plasma length and spatial variations in the magnetic field. Since the Vlasov-Poisson

---

[1] E. G. Harris, *J. Nucl. Energy* **2C**, 138 (1961).

[2] L. S. Hall, Warren Heckrotte, and Terry Kammash, *Phys. Rev.* **139**, A1117 (1965).

[3] G. E. Guest and R. A. Dory, *Phys. Fluids* **8**, 1853 (1965).

[4] R. F. Post and M. N. Rosenbluth, *Phys. Fluids* **9**, 730 (1966).

theory does appear to have a substantial regime of validity, it seems appropriate to use this theory to estimate the extent to which microinstabilities can be prevented in mirror-confined fusion plasmas.

In what follows we shall consider several aspects of this question, in particular the stabilization effects associated with (1) increasing electron temperature, (2) adding low-temperature (Maxwellian) ions, and (3) spreading the distribution of fast ions in energy and velocity-space angle. We first present in Sect. 1.1.1 a heuristic stability discussion of resonant $|\omega - N\omega_{ci}| \ll (N\omega_{ci})$ loss-cone modes in order to demonstrate that by increasing the electron temperature one can increase the threshold density (for instabilities with frequency near the Nth harmonic of the gyrofrequency) to a value $\omega_{pi\,(\text{threshold})}^2 \gtrsim (N\omega_{ci})^2$. Above this density new modes of oscillation are possible, even in the presence of very hot electrons, although temporal growth rates are found to decrease with increasing electron temperature. Also, these modes tend to have large axial wavelengths and may, perhaps, be suppressed in finite-length laboratory plasmas. In order to explore this possible stabilization effect, we study the wavelengths and growth rates of the nonconvectively unstable resonant modes, finding that axial wavelengths decrease with increasing frequency to values less than the 100 gyroradii critical length set by the convective (high-density) loss-cone modes.

Since these modes are driven by the inverted energy population resulting from the loss cone, one anticipates that some degree of stabilization may be obtained by partially filling the loss cone with low-temperature ions. In Sect. 1.1.3 we show that for well-spread fast ion distributions rather small fractional densities of cold ions have strong beneficial effects, suggesting that a useful optimization of stability with respect to cold ions is possible at cold-to-hot density ratios around 10%. In this regard we consider some illustrative examples showing the main stabilization effects possible through the addition of cold ions.

The increased stability obtained by spreading the trapped ion population in energy and velocity-space angle is explored in Sect. 1.1.4. Here we use as the stability criterion the critical density above which the growth is nonconvective and find that marked improvement is possible at low densities, but that additional measures may be necessary for densities such that $\omega_{pi} > \omega_{ci}$. This important density regime is then considered in Sect. 1.1.5, where some preliminary results are presented which illustrate the present efforts.

1.1.2 Effects of Increased Electron Temperature

The basic features of the resonant loss-cone modes may be seen from a marginal stability analysis of the Harris dispersion relation:[1]

$$1 = \sum_{\text{species}} \frac{\omega_p^2}{k^2} \sum_{n=-\infty}^{\infty} \int dv \, \frac{J_n^2(k_\perp v_\perp/\omega_c)}{k_{||}v_{||} - (\omega - n\omega_c)} \left(k_{||} \frac{\partial f_0}{\partial v_{||}} + \frac{n\omega_c}{v_\perp} \frac{\partial f_0}{\partial v_\perp} \right). \tag{2}$$

We consider the class of distribution functions

$$f_0(v_\perp^2,\, v_{||}^2) = \frac{1}{\pi^{3/2}\alpha_\perp^2\alpha_{||}j!}\left(\frac{v_\perp}{\alpha_\perp}\right)^{2j} \exp\left(-\frac{v_\perp^2}{\alpha_\perp^2} - \frac{v_{||}^2}{\alpha_{||}^2}\right),$$

$j = 0, 1, 2, \ldots$, for the ions, and

$$f_0(v^2) = \frac{1}{\pi^{3/2}\alpha_e^3} \exp\left(-\frac{v^2}{\alpha_e^2}\right)$$

for the electrons.

The ion distributions, chosen to simulate the loss-cone effect, are described in detail in Sect. 1.1.4. For these distributions and for $\omega \ll \omega_{ce}$, the Harris dispersion relation may be written in the form

$$\frac{k^2 v_e^2}{\omega_{pe}^2} \cong Z'\left(\frac{\omega}{k_{||}v_e}\right) - \frac{2T_e}{T_{\perp i}} \sum_{n=-\infty}^{\infty} \left[\frac{n\omega_{ci}}{k_{||}\alpha_{||i}} D_n Z\left(\frac{\omega - n\omega_{ci}}{k_{||}\alpha_{||i}}\right) - \frac{1}{2}\frac{\alpha_{\perp i}^2}{\alpha_{||i}^2} C_n Z'\left(\frac{\omega - n\omega_{ci}}{k_{||}\alpha_{||i}}\right)\right], \qquad (3)$$

where the coefficients $C_n(\lambda)$ and $D_n(\lambda)$ are defined as

$$C_n(\lambda) \equiv \int d\mathbf{v}\, J_n^2\left(\frac{k_\perp v_\perp}{\omega_{ci}}\right) f_0\,(v_{||}^2,\, v_\perp^2)\ ,$$

$$D_n(\lambda) \equiv \frac{-\alpha_{\perp i}^2}{2} \int d\mathbf{v}\, J_n^2\left(\frac{k_\perp v_\perp}{\omega_{ci}}\right) \frac{1}{v_\perp}\frac{\partial}{\partial v_\perp} f_0(v_{||}^2,\, v_\perp^2)\ ,$$

with

$$\lambda \equiv \frac{k_\perp^2 \alpha_{\perp i}^2}{2\omega_{ci}^2}\ ;$$

$Z(\zeta)$ is the plasma dispersion function,[5]

$$Z(\zeta) = \pi^{-1/2} \int_{-\infty}^{\infty} dx\, \exp(-x^2)/(x - \zeta)\ , \qquad \mathrm{Im}\ \zeta > 0\ ,$$

with derivative $Z'(\zeta)$.

The marginal stability analysis is carried out by searching for real solutions, $(\omega, \mathbf{k})$, to Eq. (3). This is done by separating Eq. (3) into its real and imaginary parts (for real ω and $\mathbf{k}$), looking for zeros of the

[5] B. D. Fried and S. D. Conte, *The Plasma Dispersion Function*, Academic Press, New York, 1961.

(density-independent) imaginary part, and then evaluating the corresponding density using the real part of Eq. (3). For real ω and k, the imaginary part of the dispersion relation is given by

$$0 \cong -2i\sqrt{\pi}\left\{\frac{\omega}{k_{||}v_e}\, e^{-(\omega/k_{||}v_e)^2} + \sum_{n=-\infty}^{\infty} \times \left[\frac{T_e}{T_{\perp i}}\frac{n\omega_{ci}}{k_{||}\alpha_{||i}} D_n + \frac{T_e}{T_{||i}}\left(\frac{\omega - n\omega_{ci}}{k_{||}\alpha_{||i}}\right) C_n\right] * e^{-[(\omega - n\omega_{ci})/k_{||}\alpha_{||i}]^2}\right\} . \quad (4)$$

If $|\omega - N\omega_{ci}| \ll N\omega_{ci}$, we may approximate the infinite series by the single resonance $n = N$. In addition, if

$$\left|\frac{\omega - N\omega_{ci}}{N\omega_{ci}}\right| \ll \frac{T_{||i}}{T_{\perp i}} ,$$

we may retain only the "loss-cone" D_N term. Under these conditions, the imaginary part of the dispersion relation vanishes if

$$\left(\frac{\omega - N\omega_{ci}}{k_{||}\alpha_{||i}}\right)^2 \cong \left(\frac{\omega}{k_{||}v_e}\right)^2 + \ln\left(\frac{T_e}{T_{\perp i}}\frac{v_e}{\alpha_{||i}}|D_N|\right) \quad (5)$$

for $D_N < 0$.

Equation (5) furnishes a natural basis for distinguishing two quite distinct regimes of plasma behavior:

low electron temperature: $\left(\frac{T_e}{T_{\perp i}}\frac{v_e}{\alpha_{||i}}|D_N|\right) < 1$,

high electron temperature: $\left(\frac{T_e}{T_{\perp i}}\frac{v_e}{\alpha_{||i}}|D_N|\right) > 1$.

Low-Electron-Temperature Regime. – Consider first the low-electron-temperature regime. Since

$$\left(\frac{\omega - N\omega_{ci}}{k_{||}\alpha_{||i}}\right)^2 \cong \left(\frac{\omega}{k_{||}v_e}\right)^2 - \ln\left[\left(\frac{T_e}{T_{\perp i}}\frac{v_e}{\alpha_{||i}}|D_N|\right)^{-1}\right] ,$$

then

$$\left(\frac{\omega - N\omega_{ci}}{k_{||}\alpha_{||i}}\right)^2 \to 0$$

as

$$\left(\frac{\omega}{k_{\parallel} v_e}\right)^2 \rightarrow \ln \left(\frac{T_{\perp i} \alpha_{\parallel i}}{T_e v_e |D_N|}\right) .$$

In this limit, that is, for

$$\frac{\omega}{k_{\parallel} v_e} \approx \frac{N\omega_{ci}}{k_{\parallel} v_e} \approx \sqrt{\ln \frac{T_{\perp i} \alpha_{\parallel i}}{T_e v_e |D_N|}} ,$$

the real part of the dispersion relation is dominated by the electron term; hence,

$$\frac{k^2 v_e^2}{\omega_{pe}^2} \approx \text{Re } Z' \left(\frac{\omega}{k_{\parallel} v_e}\right) \approx \frac{k_{\parallel}^2 v_e^2}{\omega^2} .$$

These modes satisfy the well-known threshold density criterion

$$\frac{\omega_{pe}^2}{N^2 \omega_{ci}^2} \approx 1 + \frac{k_{\perp}^2}{k_{\parallel}^2} \approx 1 + 8 \frac{M}{m} \frac{T_e}{T_{\perp i}} \ln \left(\frac{T_{\perp i} \alpha_{\parallel i}}{T_e v_e |D_N|}\right) ,$$

showing that, by raising the electron temperature, threshold densities can be increased to a rough limit

$$\frac{\omega_{pi}^2}{N^2 \omega_{ci}^2} \sim 1 .$$

It is worth noting that the marginal stability boundary may be a less realistic stability criterion for finite plasmas than the convective-absolute boundary discussed in Sect. 1.1.4, whose dependence on electron temperature is less striking.

High-Electron-Temperature Regime. – To illustrate the properties of the high-electron-temperature regime, we consider the case

$$\frac{T_e}{T_{\perp i}} \frac{v_e}{\alpha_{\parallel i}} |D_N| = 1 .$$

Equation (5) then requires

$$\left(\frac{\omega - N\omega_{ci}}{k_{\parallel} \alpha_{\parallel i}}\right)^2 = \left(\frac{\omega}{k_{\parallel} v_e}\right)^2 ,$$

or

$$(\omega - N\omega_c) = \pm \omega (\alpha_{\parallel i} / v_e) .$$

When these values are substituted into the real part of the dispersion relation we find

$$\frac{k^2 v_e^2}{\omega_{pe}^2} = -2 \quad \text{if } \omega - n\omega_{ci} = +\omega\left(\frac{\alpha_{\|i}}{v_e}\right)$$

or

$$\frac{k^2 v_e^2}{\omega_{pe}^2} = 2\left[1 + Z_r'\left(\frac{\omega}{k_\| v_e}\right)\right] \quad \text{if } \omega - n\omega_{ci} = -\omega\left(\frac{\alpha_{\|i}}{v_e}\right) \quad .$$

The second branch permits marginally stable oscillations if $\omega/(k_\| v_e) > 0.55$, that is, if axial wavelengths exceed

$$\left(\frac{\lambda_\|}{\rho_i}\right)_{\text{critical}} \approx \frac{1.1\pi}{N}\left(\frac{M}{m}\frac{T_e}{T_{\perp i}}\right)^{1/2} . \tag{6}$$

Notice that the waves carry negative energy[6] if $0.55 < \omega/(k_\| v_e) < 1.5$, since the sign of the energy density is determined from

$$\bar{U} \sim \frac{\partial \kappa}{\partial \omega} \sim -Z_r''\left(\frac{\omega}{k_\| v_e}\right) .$$

Threshold densities are given roughly by

$$\left(\frac{\omega_{pi}^2}{N^2\omega_{ci}^2}\right)_{\text{threshold}} \sim 2.5\,\frac{T_e}{T_{\perp i}} ,$$

where $T_e/T_{\perp i}$ is restricted to values around unity by the condition

$$\frac{T_e}{T_{\perp i}}\frac{v_e}{\alpha_{\|i}}|D_N| = 1 ,$$

imposed on this illustrative case.

Thus, although threshold densities can be increased to $\omega_{pi}^2(\text{threshold}) \sim (N\omega_{ci})^2$ by increasing the electron temperature, complete stabilization at fusion densities is not predicted from the infinite homogeneous plasma model on which this theory is based. We note from Eq. (6), however, that the modes which may occur at high densities and with hot electrons have relatively long axial wavelengths and hence may not be possible in finite-length laboratory plasmas. To explore finite-length stabilization, it is necessary to distinguish between convective and nonconvective growth in order to estimate the critical

[6] L. D. Landau and E. M. Lifshitz, *Electrodynamics of Continuous Media*, Addison-Wesley, Reading, Mass., 1960.

plasma length for stability. For nonconvective growth this length may be as small as one-half wavelength; for convective growth it could be considerably longer, depending on spatial growth rates and reflection processes at the plasma extremities.

We have applied the Bers-Briggs[7] criteria for nonconvective instabilities as described in Sect. 1.1.5. The results are that the resonant loss-cone modes are nonconvectively unstable, with growth characteristics illustrated in Figs. 1.1–1.3. In Fig. 1.1 we show the dependence of temporal growth rates on electron temperatures for the first two gyrofrequency harmonics and four different densities: $\omega_{pi}^2/\omega_{ci}^2 =$ 2.25, 12.25, 25, and 50. Figure 1.2 shows the axial wavelength variations for the same circumstances, and Fig. 1.3 shows the dependence of growth rate and wavelength on density for one particular electron temperature and mode.

The most prominent features of these figures are (1) the rapid decrease of growth rate with increasing electron temperatures; (2) the relatively long axial wavelengths, even at high electron temperature; and (3) the increase in growth rate and decrease in axial wavelength with increasing density. These characteristics suggest the necessity of finding additional stabilization techniques effective at high density and high harmonics.

[7] R. T. Briggs, *Electron-Stream Interaction with Plasmas*, MIT Press, Cambridge, Mass., 1964.

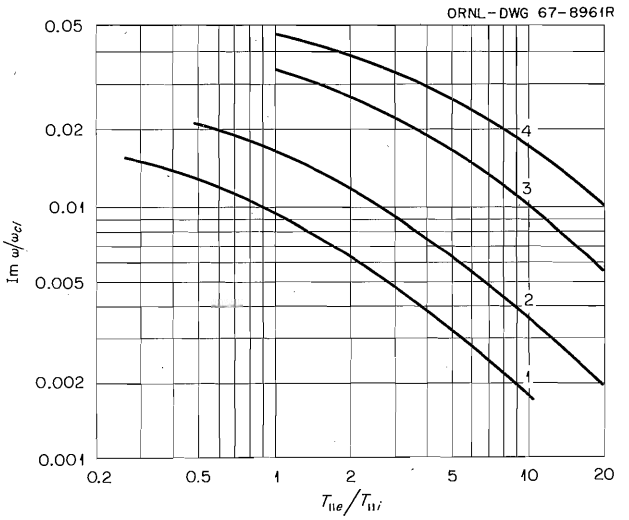

Fig. 1.1. The Dependence of Growth Rate on Electron Temperature. (1) $\omega_{pi}^2/\omega_{ci}^2 = 2.25$, $\omega \approx \omega_{ci}$, $\lambda = k_\perp^2 \rho_i^2/2 = 5$; (2) $\omega_{pi}^2/\omega_{ci}^2 = 12.25$, $\omega \approx 2\omega_{ci}$, $\lambda = 15.5$; (3) $\omega_{pi}^2/\omega_{ci}^2 = 25$, $\omega \approx 2\omega_{ci}$, $\lambda = 15.5$; (4) $\omega_{pi}^2/\omega_{ci}^2 = 50$, $\omega \approx 2\omega_{ci}$, $\lambda = 15.5$.

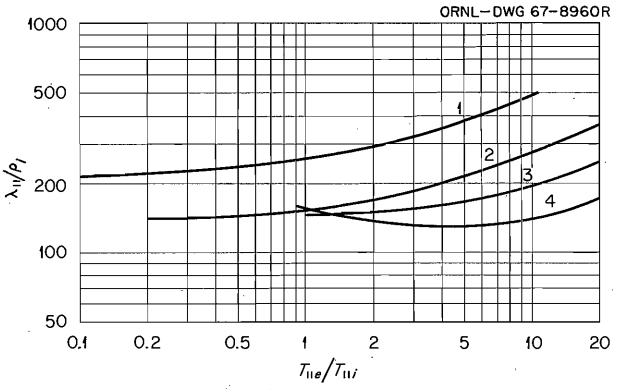

Fig. 1.2. The Dependence of Axial Wavelength on Electron Temperature for the Same Parameters as in Fig. 1.1.

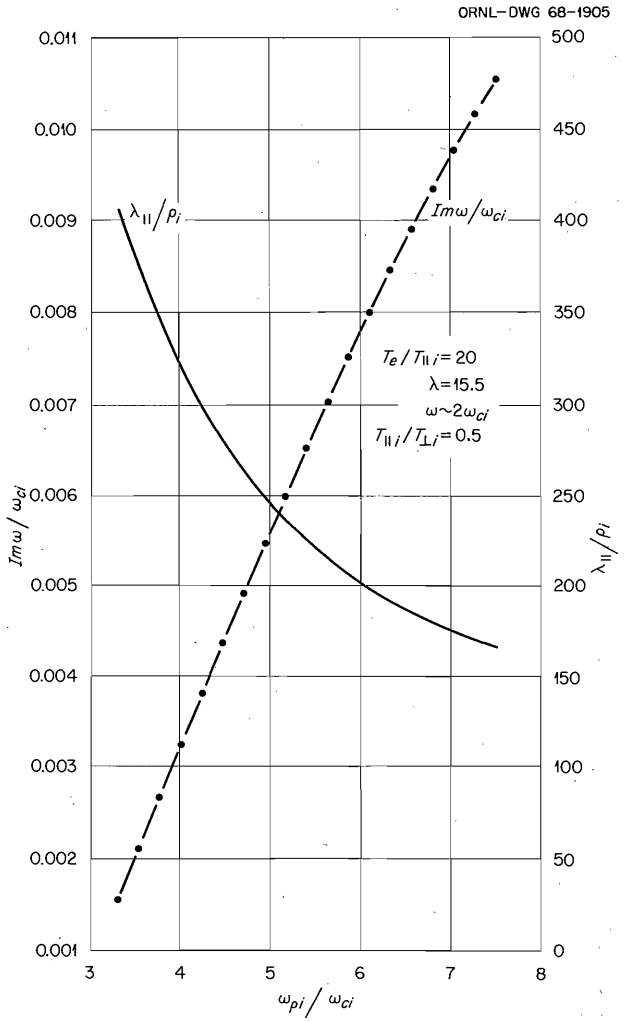

Fig. 1.3. The Dependence of Growth Rate and Axial Wavelength on Density for $\omega \approx 2\omega_{ci}$, $\lambda = 15.5$, and $T_e/T_{11i} = 20$.

1.1.3 Effect of Cold Ions on Loss-Cone Instabilities

We have studied the possibility of stabilizing the loss-cone modes described above by adding low-temperature Maxwellian ions to the hot-ion–electron plasma. Our initial effort has been directed primarily at understanding the behavior of marginal stability boundaries as the relative cold-ion density, N_C/N_H, is increased. This is a natural extension of the earlier analysis of flutelike ($k_{||} = 0$) high-frequency modes in multicomponent plasmas[8] to include waves propagating partially along the magnetic field, $k_{||} \neq 0$. This extension does, however, raise the question of convective or nonconvective growth of the unstable modes, but as yet only preliminary results are available in that regard.

The cold ions give rise to two important effects:

1. They make a large positive contribution to the dielectric response of the plasma to fluctuations with $k_\perp \neq 0$ and $\omega \lesssim \omega_{ci}$. This can cut off wave propagation for such fluctuations.
2. The cold ions can lead to strong cyclotron damping if $|\omega - \omega_{ci}| < k_{||} v_{ci}$, where v_{ci} is the cold-ion thermal speed, assumed isotropic.

The cold-ion (perpendicular) dielectric constant is approximately

$$\epsilon_\perp \text{ (cold ion)} \approx 1 - \frac{\omega_{pi}^2}{\omega_{ci}^2} \frac{k_\perp^2}{k^2} \left[\frac{\omega^2}{\omega^2 - \omega_{ci}^2} - \frac{1}{2} \frac{\omega}{k_{||} v_c} \operatorname{Im} Z\left(\frac{\omega - \omega_{ci}}{k_{||} v_c} \right) \right] ,$$

so that the complete dispersion relation becomes

$$\frac{k^2 v_e^2}{\omega_{pe}^2} \cong Z'\left(\frac{\omega}{k_{||} v_e} \right) \qquad \text{electron term}$$

$$- \frac{N_H}{N_T} \sum_{n=-\infty}^{\infty} \frac{2T_e}{T_{\perp i}} D_n \frac{n\omega_{ci}}{k_{||} \alpha_{||i}} Z\left(\frac{\omega - n\omega_{ci}}{k_{||} \alpha_{||i}} \right) \qquad \text{hot-ion ``loss-cone''}$$

$$+ \frac{N_H}{N_T} \sum_{n=-\infty}^{\infty} \frac{T_e}{T_{||i}} C_n Z'\left(\frac{\omega - n\omega_{ci}}{k_{||} \alpha_{||i}} \right) \qquad \text{hot-ion ``anisotropy''}$$

$$+ \frac{N_C}{N_T} \frac{T_e}{T_{\perp i}} \lambda \left[\frac{2\omega^2}{\omega^2 - \omega_{ci}^2} - \frac{\omega}{k_{||} v_c} \operatorname{Im} Z\left(\frac{\omega - \omega_{ci}}{k_{||} v_c} \right) \right] . \qquad \text{cold ion}$$

In searching for marginally stable solutions, we look for zeros of the imaginary part of the dispersion relation for real values of ω and k, that is,

---

[8] W. M. Farr and R. E. Budwine, *Thermonuclear Div. Semiann. Progr. Rept. Apr. 30, 1967*, ORNL-4150, p. 19.

$$0 = e^{-[(\omega)/(k_{||} v_e)]^2}$$

$$+ \frac{N_H}{N_T} \frac{T_e}{T_{\perp i}} \left[\frac{n\omega_{ci}}{\omega} \frac{v_e}{\alpha_{||}} D_n + \frac{T_{\perp i}}{T_{||i}} \left(\frac{\omega - n\omega_{ci}}{\omega} \right) \frac{v_e}{\alpha_{||}} C_n \right] e^{-[(\omega - n\omega_{ci})/k\alpha]^2}$$

$$+ \frac{N_C}{N_T} \frac{T_e}{T_{\perp i}} \frac{\lambda}{2} \frac{v_e}{v_c} e^{-[(\omega - \omega_{ci})/k_{||} v_c]^2} .$$

This equation shows the relative importance of cold-ion cyclotron damping for frequencies near the fundamental cold-ion gyrofrequency. This damping is significant, in the case of loss-cone modes, if

$$\frac{N_C}{N_H} \gtrsim \frac{2v_c}{\alpha_{||}} \frac{D_n}{\lambda} \sim 10^{-2} .$$

For larger fractional cold-ion densities, growing "loss-cone" modes will be possible only if

$$(k_{||} v_c)^2 < (\omega - \omega_{ci})^2$$

and

$$(\omega - n\omega_{ci})^2 \lesssim (k_{||} \alpha_{||})^2 ,$$

together with the usual requirement that D_n be negative. Notice that because of the cold-ion cyclotron damping, the former band of unstable frequencies is split into two distinct bands:

$$\omega - \omega_{ci} > k_{||} v_c$$

and

$$\omega - \omega_{ci} < -k_{||} v_c .$$

In general the real part of the dispersion relation will be rather complicated. However, if $T_e \gtrsim T_{\perp i} \approx T_{||i}$, it is possible for the cold-ion term to dominate, giving

$$\frac{k^2 v_e^2}{\omega_{pe}^2} \sim \lambda \frac{N_C}{N_T} \frac{T_e}{T_{\perp i}} \frac{\omega_{ci}}{\omega - \omega_{ci}}$$

if $N_C/N_H \gtrsim 2D_n/\lambda$. The lower-frequency branch, $\omega - \omega_{ci} < -k_{||} v_c$, may then be cut off by the cold-ion term, while the upper-frequency branch, $\omega - \omega_{ci} > k_{||} v_c$, occurs only at relatively low density:

$$\frac{\omega_{pe}^2}{k^2 v_e^2} \approx \frac{1}{\lambda} \frac{N_T}{N_C} \frac{T_{\perp i}}{T_e} \frac{\omega - \omega_{ci}}{\omega_{ci}} < \frac{1}{\lambda} \frac{N_T}{N_C} \frac{T_{\perp i}}{T_e} \frac{k_{||} \alpha_{||}}{\omega_{ci}} .$$

Notice that highly anisotropic plasmas ($T_{\parallel i} \ll T_{\perp i}$) are much less sensitive to the cold-ion contributions. The cold-ion density is significant only if

$$\frac{N_C}{N_H} \gtrsim \frac{T_{\perp i}}{T_{\parallel i}} \frac{C_n}{\lambda} .$$

Since in the case of the loss-cone modes the fractional cold-ion density is near the stability boundary for flutelike modes (see, for example, Fig. 1.9 of ref. 8), it may be possible to find an optimum cold-ion density which is large enough to help stabilize the $k_{\parallel} \neq 0$ loss-cone modes but too small to support the $k_{\parallel} = 0$ modes.

To illustrate the stability properties of plasmas containing cold ions, hot ions, and electrons, we present the results of studies of two particular plasma configurations, chosen to model the PR-5 experiments of Ioffe *et al.*[9] and the DCX-2 "central-peak" plasma.[10] The parameters which enter the theory are summarized in Table 1.1. The stability boundaries for increasing cold-ion densities are shown in Figs. 1.4 and 1.5 (PR-5) and Fig. 1.6 (DCX-2). Consider first the PR-5 behavior.

Table 1.1. Experimental Parameters for the PR-5 and DCX-2 Plasmas

Experiment	$T_e/T_{\perp i}$	$T_e/T_{\parallel i}$	$T_{\text{cold}}/T_{\parallel i}$	$T_{\parallel i}/T_{\perp i}$
PR-5	10^{-2}	10^{-1}	10^{-1}	10^{-1}
	4×10^{-2}	4×10^{-1}	10^{-1}	10^{-1}
DCX-2	6×10^{-5}	6×10^{-2}	10^{-1}	10^{-3}

With no cold ions present the plasma supports the usual loss-cone mode, with $\omega - \omega_{ci} \sim -\omega_{ci}\alpha_{\parallel}/v_e$ (here we restrict our attention to modes near the first harmonic). Threshold densities for this mode are given by

$$\frac{\omega_{pe}^2}{\omega_{ci}^2} \sim 900 \text{ or } \frac{\omega_{pi}^2(H)}{\omega_{ci}^2} \sim \frac{1}{2}\left(\frac{N_H}{N_T}\right) .$$

Since the observed hot-ion density is such that $\omega_{pi}^2(H)/\omega_{ci}^2 \sim 10$, one may anticipate that in the absence of cold ions the plasma will be unstable.

With 2% cold ions present a second unstable oscillation appears in the marginal stability analysis, distinguished by a positive shift in frequency, that is, to frequencies *above* the gyrofrequency. As the relative density of cold ions is increased, this mode remains prominent, whereas the two-species loss-cone mode disappears (as a result of the positive dielectric constant of the cold ions in the frequency

[9] H. T. Baiborodov *et al.*, Institute of Atomic Energy Report No. 1331.

[10] *Thermonuclear Div. Semiann. Progr. Rept. Oct. 31, 1966*, ORNL-4063, p. 12.

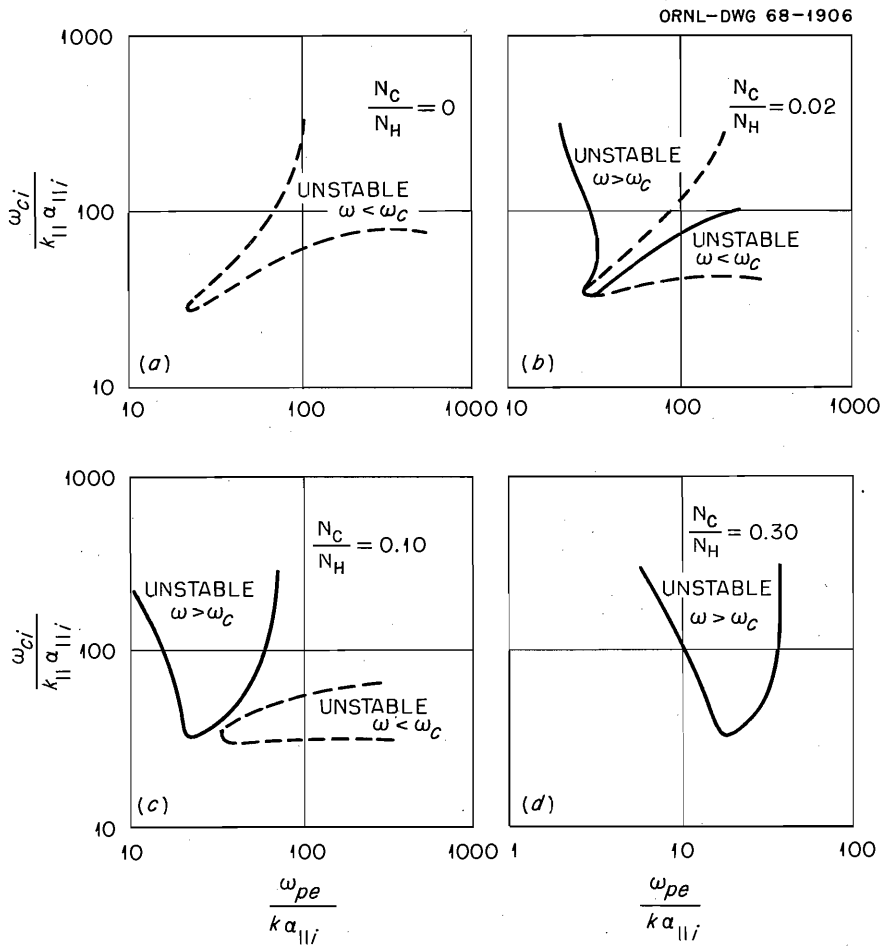

Fig. 1.4. Marginal Stability Boundaries for Case 1 of Table 1.1. (*a*) $N_{cold}/N_{hot} = 0$, (*b*) $N_{cold}/N_{hot} = 0.02$, (*c*) $N_{cold}/N_{hot} = 0.10$, (*d*) $N_{cold}/N_{hot} = 0.30$.

range just below gyrofrequency). Thus, with 10% cold ions present, only the higher-frequency branch can propagate.

This mode, which is the "double-humped" instability of Hall *et al.*,[11] can occur only at relatively low densities in plasmas of finite length. Thus, with as little as 10% cold ions present, the plasma is effectively stable at the observed density. Notice, however, that preferentially rapid decay of the cold-ion density leads to an unstable configuration at that same (hot-ion) density. This appears to be a plausible explanation of the afterglow instabilities observed by Ioffe in the PR-5 experiments. Figure 1.5 shows the same behavior at a slightly greater electron temperature.

The situation is quite different in DCX-2, since the Harris modes are affected by cold ions only for relatively large cold-ion densities. Figure 1.6 shows this insensitivity in the marginal stability boundaries. However, preliminary results of the convective/nonconvective analysis of these modes show a

[11] L. S. Hall, Warren Heckrotte, and Terry Kammash, *op. cit.*

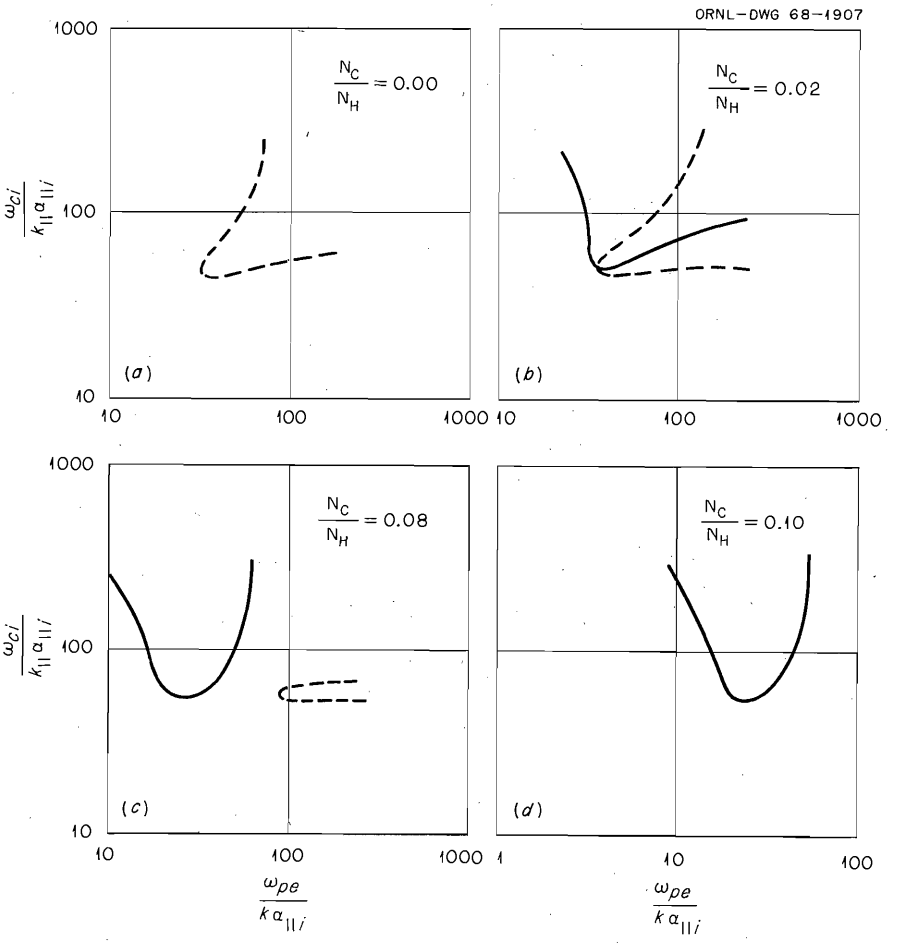

Fig. 1.5. Marginal Stability Boundaries for Case 2 of Table 1.1. (*a*) $N_{cold}/N_{hot} = 0$, (*b*) $N_{cold}/N_{hot} = 0.02$, (*c*) $N_{cold}/N_{hot} = 0.08$, (*d*) $N_{cold}/N_{hot} = 0.10$.

transition from nonconvective (at low cold-ion densities) to convective (at high cold-ion densities), which may modify the effective stability criterion to a considerable extent. That analysis is still in progress.

1.1.4 Effects of Spreading the Distribution in Energy and Velocity-Space Angle

Mirror-confined plasmas are necessarily anisotropic and peaked in energy. In the preceding sections we discussed the instabilities associated with these intrinsic departures from thermal equilibrium. In many present-day experiments, however, the plasma is created in such a way as to exaggerate to a greater or lesser extent these two nonequilibrium properties, for example, through injection of a nearly monoenergetic beam of fast particles, trapped so that $\langle E_{\perp} \rangle >> \langle E_{\parallel} \rangle$. In order to relate observed instabilities to the present theory it is necessary to study as realistic a model as is analytically tractable. Moreover, by studying the stability properties over a range of anisotropies and energy spreads, one may be able to determine the most effective possible experimental procedures for improving stability.

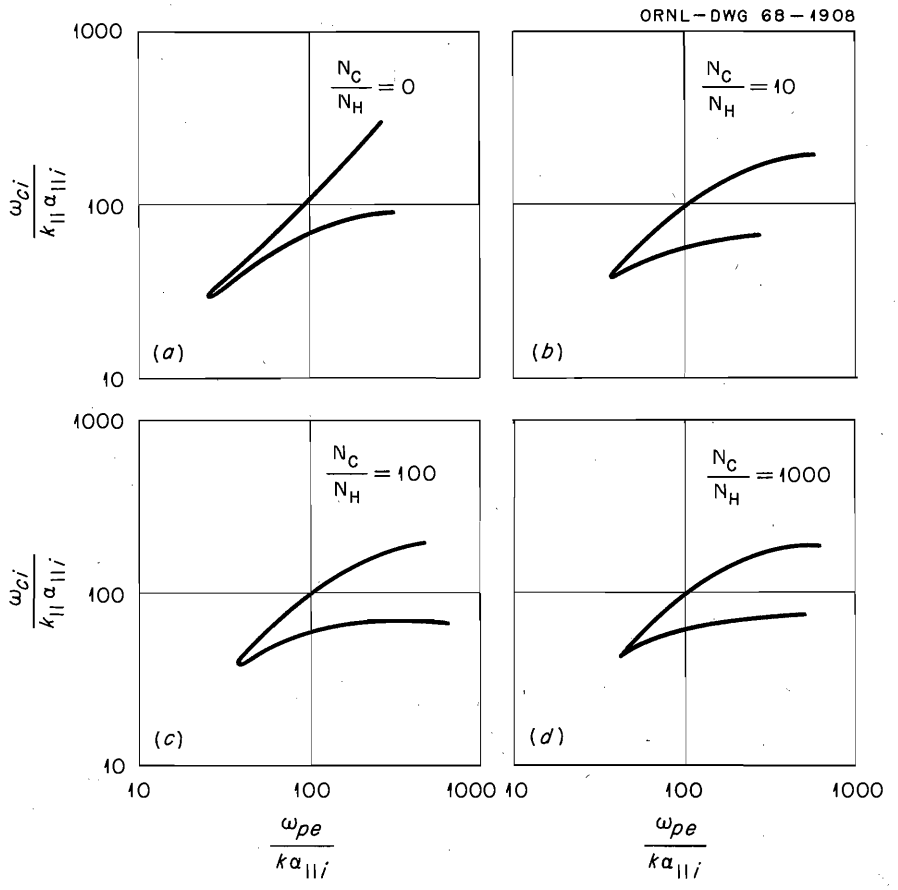

Fig. 1.6. Marginal Stability Boundaries for Case 3 of Table 1.1. (*a*) $N_{cold}/N_{hot} = 0$, (*b*) $N_{cold}/N_{hot} = 10$, (*c*) $N_{cold}/N_{hot} = 100$, (*d*) $N_{cold}/N_{hot} = 1000$.

The class of distributions mentioned in Sect. 1.1.1,

$$f_0(v_\perp^2, v_\parallel^2) = \frac{1}{\pi^{3/2}\alpha_\perp^2\alpha_\parallel j!}\left(\frac{v_\perp}{\alpha_\perp}\right)^{2j}\exp\left(-\frac{v_\perp^2}{\alpha_\perp^2}-\frac{v_\parallel^2}{\alpha_\parallel^2}\right),$$

characterized by the two parameters j and T ($\equiv \alpha_\parallel^2/\alpha_\perp^2$), furnishes a convenient way of studying the effect on the loss-cone and Harris instabilities of variations in the degree of anisotropy and peaking in energy. These distributions have the property that, if they are all normalized to a given peak energy, the width of the distribution in perpendicular energy decreases as $j^{-1/2}$, tending toward a delta function as $j \to \infty$. This normalization is accomplished, for example, by requiring that

$$\alpha_\perp^2 = v_\perp^2(\text{peak})/j, \quad j \neq 0 .$$

In fact,

$$\frac{\delta E_\perp}{\langle E_\perp \rangle} \simeq \frac{2}{\sqrt{j}} ,$$

so that the spread in perpendicular energy is governed only by the parameter j.

A convenient description of the degree of anisotropy is in terms of the ratio

$$\frac{\langle E_{\parallel} \rangle}{\langle E_{\perp} \rangle} \simeq \frac{\alpha_{\parallel}^2}{j\alpha_{\perp}^2} \equiv \frac{T}{j}.$$

Alternatively, the angular spread is roughly proportional to $(T/j)^{1/2}$. Notice that if we wish to determine the effects of energy spread alone, that is, with anisotropy held constant, we must vary T and j together, holding the ratio T/j constant, whereas, if we wish to study the effect of variations in anisotropy (at constant energy spread), we need vary T only.

In order to illustrate these two types of variations, that is, (1) changes in anisotropy at fixed energy spread and (2) changes in energy spread at fixed anisotropy, we show contours of the distribution function for several choices of the parameters T and j. We have normalized the functions so that $f_0(\max) = 1$ at $v_{\perp}^2 = 1$. Figure 1.7 shows f_0 contours for $j = 1$ and $T \doteq 0.02$, 0.1, and 0.5, demonstrating that T governs the angular spread or, equivalently, the spread in energy parallel to the magnetic field. The effect of variations of this type in f_0 has been discussed previously by Beasley and Cordey.[12] Variations in energy spread at fixed anisotropy are illustrated by Fig. 1.8, for which the ratio $T/j = 0.02$ but for which j and T are (1, 0.02), (5, 0.10), and (10, 0.20).

We exhibit the influence of these two types of variations on plasma stability through their effects on the boundary (in a suitable parameter space) between absolutely unstable and convectively unstable configurations, shown in Figs. 1.9 and 1.10. For densities above the boundary value, the plasma supports absolute instabilities for the harmonic shown. These curves have been obtained by minimizing this critical density with respect to perpendicular wavelengths and thus may not be applicable to plasmas of very small radius, where boundary conditions could restrict the maximum radial wavelength to smaller values than those corresponding to these curves. Apart from such questions, however, we may use these results to compare stability properties of plasmas of different energy spread and equal anisotropy or equal energy spread and different anisotropy.

Figure 1.9 shows the trend toward greater stability resulting from increasing only the angular spread, holding the energy spread constant at the two values shown. Such a variation could be accomplished, for example, by injecting at various angles with respect to the magnetic axis in neutral injection devices such as Pheonix and Alice.

The effects of varying only the energy spread are illustrated in Fig. 1.10, in which the same convective-absolute boundary has been plotted as a function of j for three fixed ratios of T/j. One sees that energy spread has an appreciable stabilizing effect provided the angular spread is relatively large. For highly anisotropic plasmas, however, increasing the energy spread may permit absolute instabilities at lower densities.

---

[12] C. O. Beasley and J. G. Cordey, "Convective and Absolute Ion Cyclotron Instabilities in Homogeneous Plasmas," to be published in *Nuclear Fusion*.

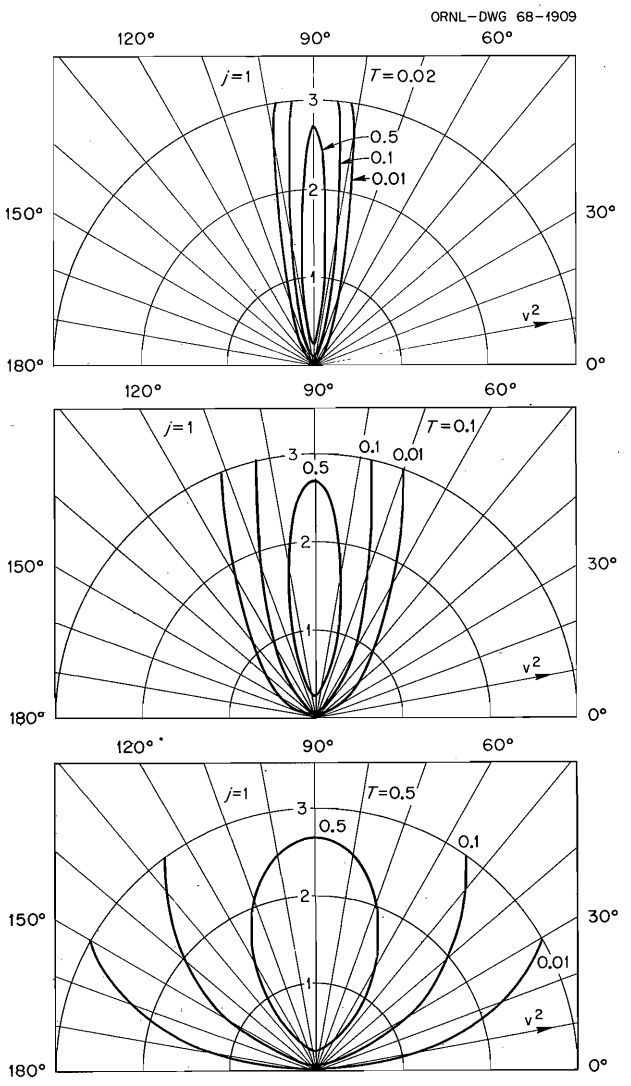

Fig. 1.7. Contours of Constant Values of the Unperturbed Distribution Function, $f_0(E, \theta) \doteq$ 0.01, 0.1, 0.5, for Fixed Energy Spread but Variable Angular Spread, $T/j \doteq$ 0.02, 0.1, 0.5.

1.1.5 Absolute Loss-Cone Modes at High Densities and Electron Temperatures

We are continuing numerical investigation of absolute loss-cone instabilities at high densities ($1 \leqq \omega_{pi}/\omega_{ci} < 30$) and electron temperatures ($1 \leqq T_{\|e}/T_{\|i} \leqq 16$) by considering one ion species only and taking the perpendicular distribution function corresponding to $j = 1$ and $T_{\|i}/T_{\perp i} = 0.5$ throughout.

We look for absolute modes at the first five harmonics of ω_{ci}. Around each harmonic number, N, the perpendicular wavelength is chosen to maximize the growth rate. Table 1.2 shows the values of λ used.

An absolute instability may occur if there exist values of complex $k_{\|}$ and ω such that

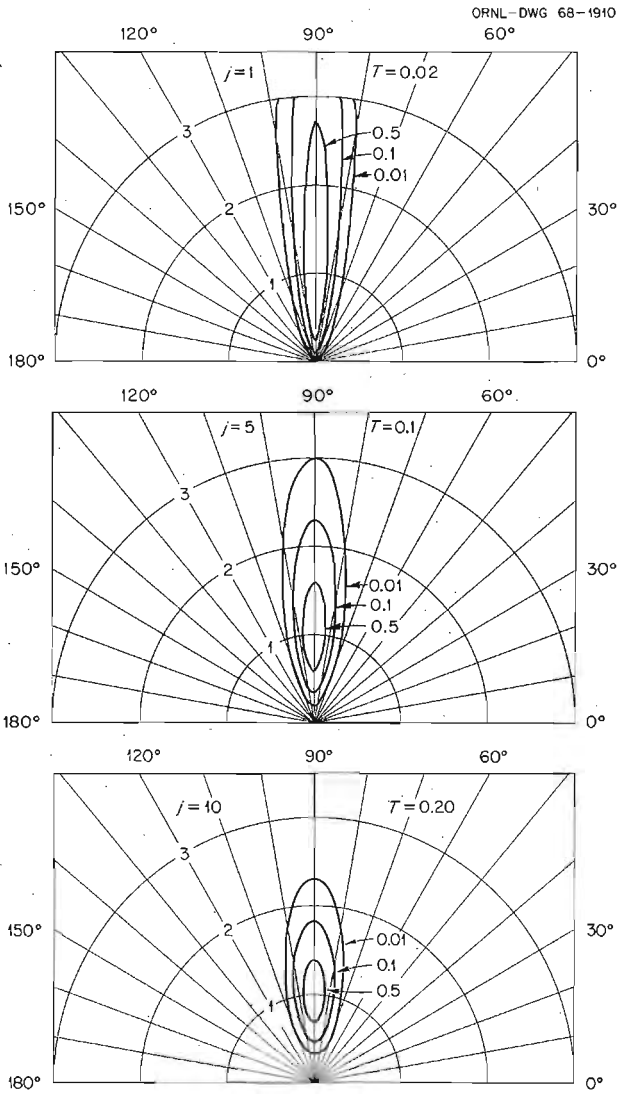

Fig. 1.8. Contours of Constant Values of the Unperturbed Distribution Function, $f_0(E, \theta) \doteq 0.01, 0.1, 0.5$, for Fixed Angular Spread ($T/j = 0.02$) but Variable Energy Spread, $j \doteq 1, 5, 10$.

Table 1.2. Values of λ for Maximum Growth Rate

N	1	2	3	4	5
λ	4.5	15.5	24	37	53

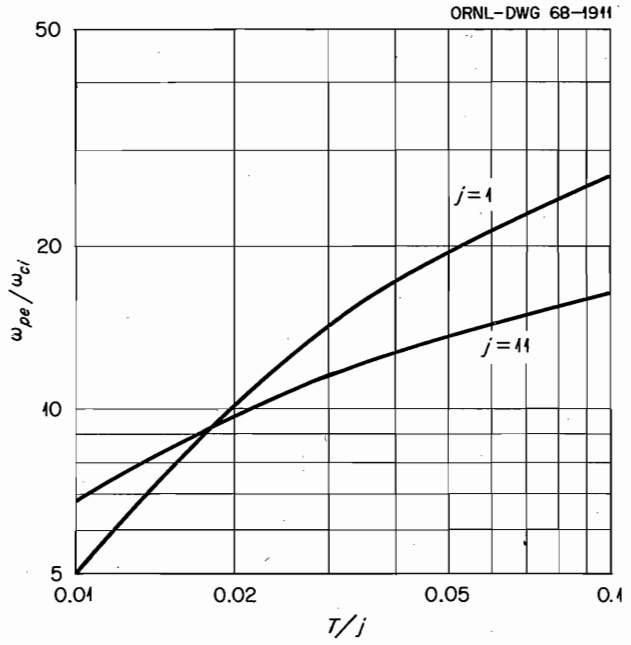

Fig. 1.9. The Dependence of the Transition Density (Above Which the Instability Passes from Convective to Nonconvective) on Angular Spread (T/j) for Two Values of Energy Spread.

$$D(k_{||}, \omega, p) = 0 ,$$
$$\frac{\partial D}{\partial k_{||}} (k_{||}, \omega, p) = 0 , \tag{7}$$

where p stands for all other parameters.[13,14] These two equations determine a saddle point (S.P.) of the function $\omega(k_{||}, p)$ defined through

$$D[k_{||}, \omega(k_{||}, p), p] \equiv 0$$

and yield one pair of solutions for $k_{||}$ and ω for given p.

Equation (7) implies a double root of $\omega(k_{||}, p)$. To find out if this root represents an absolute instability, one has to trace back the two contours

$$\omega_i^{(\alpha)} (k_{||}, \omega_r = \omega_r^{\text{S.P.}}, p), \quad \alpha = 1,2 ,$$

---

[13]R. T. Briggs, *op. cit.*

[14]L. S. Hall and W. Heckrotte, "Instabilities: Convective vs Absolute," to be published in the *Physical Review;* this work contains an up-to-date list of references.

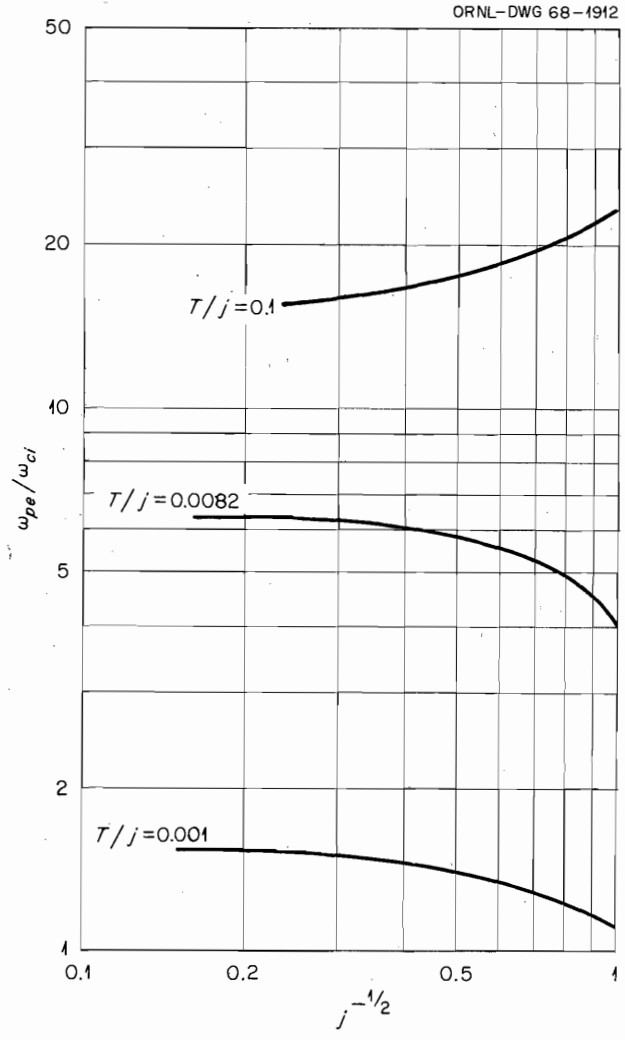

Fig. 1.10. The Dependence of the Transition Density on Energy Spread ($\sim j^{-1/2}$) for Three Values of Angular Spread: $T/j \doteq 0.001, 0.0082, 0.1$.

in the $k_{||}$ plane, which merge at the S.P. to yield the double root, until ω_i reaches its Bromwich value, σ_0. If these "end points" lie in different half-planes, the double root is of the "pinching" type and the instability is absolute. Thus, what one needs is a mapping of $\omega_r(k_{||}, p)$ and $\omega_i(k_{||}, p)$. To find the saddle points we scan the ridges and troughs of

$$\omega_i = \omega_i(k_{||r}, k_{||i}, p) \tag{8}$$

and study the level curves of this function and of $\omega_r(k_{||}, p)$. To decide on the "pinching" question, we look at the contours of fixed

$$\omega_r(k_{||r}, k_{||i}, p) = \omega_r^{\mathrm{S.P.}} \tag{9}$$

in the $k_{||}$ plane and the location of the points where $\omega_i \gtrsim \sigma_0$ for these contours.

We note in passing that Eq. (9) also coincides with the "ridge" of the function (8). If, and only if, this ridge turns out to run parallel to the $k_{||i}$ axis, then the maximum of (8) as a function of $k_{||r}$ (for fixed $k_{||i}$) coincides with the top of the ridge defined by (9). Often, however, the ridge is curved and/or skewed. This is important for the determination of the maximum possible growth rate for real $k_{||}$, σ_0. If the ridge is skewed, the plot $\omega_i(k_{||r},\ k_{||i} = 0)$ shows a maximum which overestimates σ_0 (e.g., by 30% for the case $\omega_{pi}^2/\omega_{ci}^2 = 1000$, $\omega \approx 2\omega_{ci}$, $T_e/T_{||i} = 5$.

In Fig. 1.11 we show level curves of the function

$$\omega_i = \omega_i(k_{||},\ p) \tag{10}$$

for $\omega_{pi}^2/\omega_{ci}^2 = 1000$, $T_e/T_{||i} = 10$ for frequencies around the second harmonic.

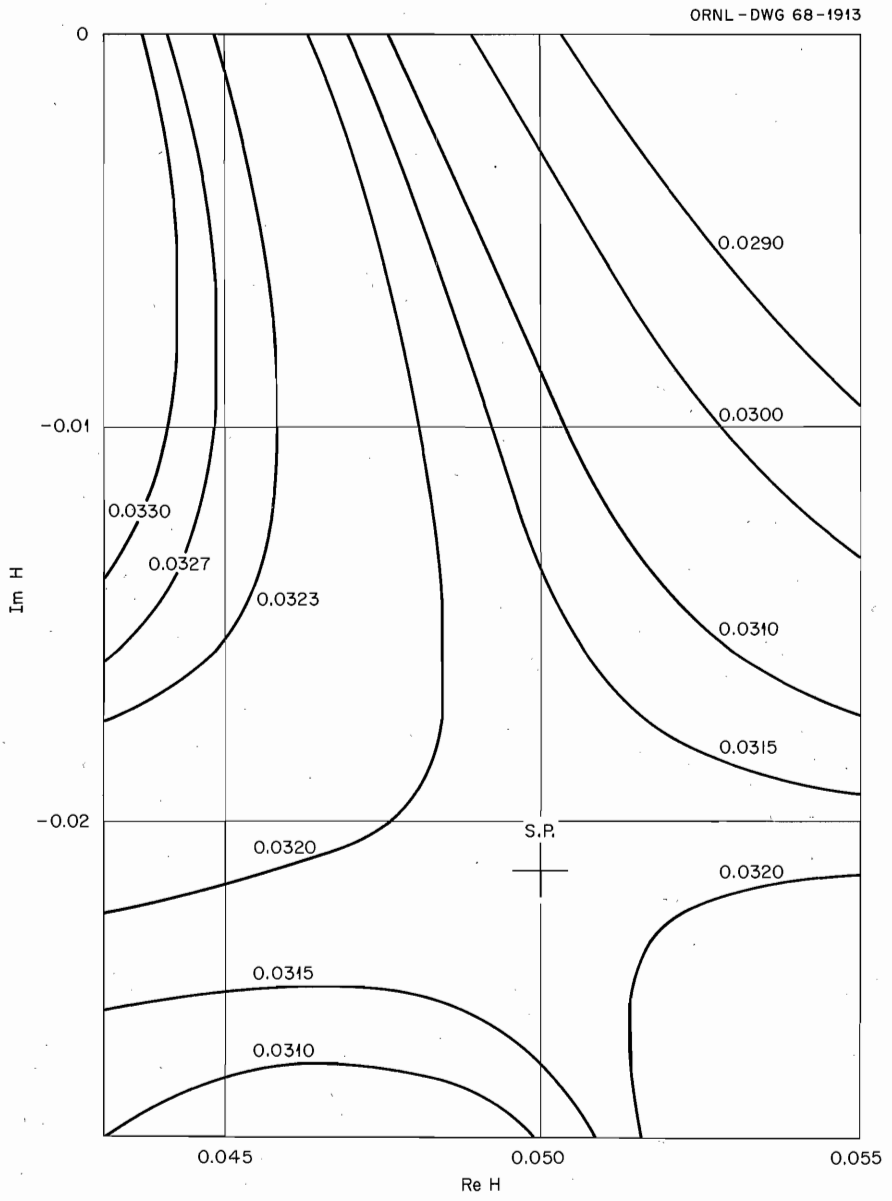

Fig. 1.11. Contours of Constant Values of Im w in the Complex h Plane for $\omega_{pi}^2/\omega_{ci}^2 = 1000$, $\omega \approx 2\omega_{ci}$, $\lambda = 15.5$, and $T_e/T_{||i} = 10$.

The saddle point lies in the lower half $k_{||}$ plane; the ridge is skewed by $\sim 45°$. Rather close to the S.P. one sees a branch point ($d\omega/dk_{||} \to \infty$) of the function (10), demonstrating that $\omega(k_{||}, p)$ has more than one sheet, although the function

$$D = D(k_{||}, \omega)$$

is analytic in both $k_{||}$ and ω. These branch points seem to be characteristic of high values of θ.

One is mainly interested in the growth rates and parallel wavelengths at the S.P. as a function of density [characterized by $\epsilon \equiv (\omega_{pi}/\omega_{ci})^2$] and electron temperature ($\theta = T_{||e}/T_{||i}$) around harmonics of the ion gyrofrequency. The scaling used is

$$w \equiv \frac{\omega}{\omega_{ci}}, \qquad h \equiv \frac{k_{||}\alpha_{||i}}{\omega_{ci}},$$

both w and h being complex.

Figure 1.12 shows the dependence of the saddle-point parameters, w and h, on electron temperature for the second, third, and fourth harmonics and $\epsilon = 1000$. Note the exponential decrease of growth rate with electron temperature and the occurrence of a minimum unstable wavelength, typically of the order of 100 gyroradii.

Figure 1.13 shows the variation of growth rate and parallel wavelength over a rather large range of densities, for fixed values of the remaining parameters. Note the saturation of growth rates.

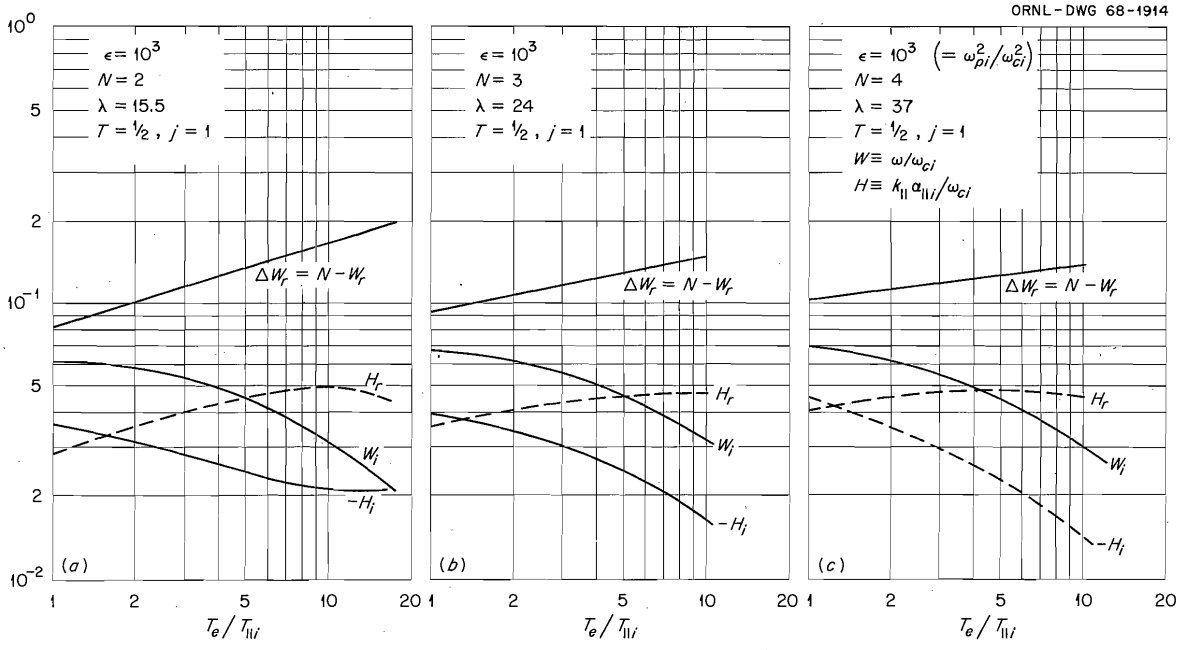

Fig. 1.12. The Dependence of Saddle-Point Characteristics on Electron Temperature for $\omega_{pi}^2/\omega_{ci}^2 = 1000$. (a) $\omega \approx 2\omega_{ci}$, $\lambda = 15.5$; (b) $\omega \approx 3\omega_{ci}$, $\lambda = 24$; (c) $\omega \approx 4\omega_{ci}$, $\lambda = 37$.

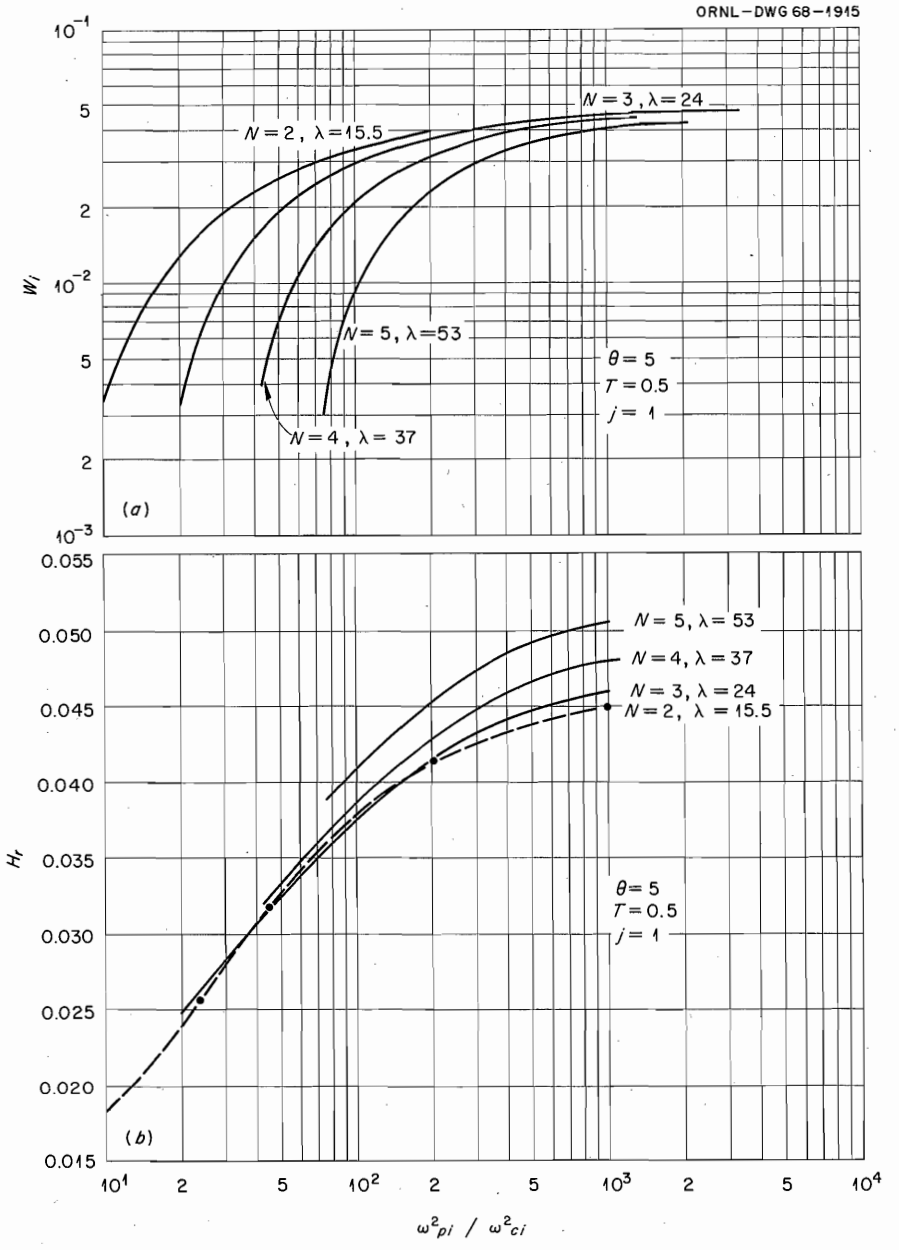

Fig. 1.13. The Dependence of Growth Rate (1.13*a*) and Axial Wavelength (1.13*b*) on Density for $N = 2, 3, 4,$ and 5 and $T_e/T_{\|i} = 5$.

Our present efforts are directed toward obtaining sufficiently complete information on the most dangerous resonant modes possible in plasmas of fusion densities to be able to study possible stabilization techniques such as addition of cold ions and use of nonuniform magnetic fields.

1.2. OSCILLATIONS AND INSTABILITIES IN A FINITE PLASMA

C. C. Cheng[15] E. G. Harris[16]

This is a preliminary account of some work in progress.

We consider a finite plasma confined by electric and magnetic fields that may be derived from the vector and scalar potentials $\mathbf{A}_0(\mathbf{x})$ and $V_0(\mathbf{x})$. Included in these fields are the self-consistent fields produced by the current and charge densities in the plasma. The Hamiltonian for a particle of species s in these fields is

$$H_{0s} = \frac{1}{2m_s} |\mathbf{p} - \frac{e_s}{c} \mathbf{A}_0(\mathbf{x})|^2 + V_0(\mathbf{x}) .$$

It is convenient to treat this problem quantum mechanically. We assume that the solution of the time-independent Schroedinger equation

$$H_{0s} \chi_{sn}(\mathbf{x}) = \epsilon_{sn} \chi_{sn}(\mathbf{x}) \tag{1}$$

is known.

In the second quantization formalism we write

$$\psi_s(\mathbf{x}) = \sum_n C_{sn} \chi_{sn}(\mathbf{x}) \tag{2}$$

and

$$H_0 = \sum_s \int d^3x \, \psi_s^+(\mathbf{x}) H_{0s} \psi_s(\mathbf{x}) = \sum_s \sum_n \epsilon_{sn} C_{sn}^+ C_{sn} , \tag{3}$$

where C_{sn}^+ and C_{sn} are, respectively, the creation and annihilation operators for a particle of species s in the nth state. We shall assume that both electrons and ions are Fermions, so that these operators obey the usual anticommutation relations.

Now, we consider the system perturbed by an electrostatic potential $\phi(\mathbf{x})$. (For simplicity we shall limit our present considerations to electrostatic waves.) The Hamiltonian of the perturbation is

$$H_1 = \sum_s e_s \int d^3x \, \psi_s^+(\mathbf{x}) \phi(\mathbf{x}) \psi_s(\mathbf{x}) = \sum_s e_s \langle n|\phi|m\rangle_s C_{sn}^+ C_{sn} , \tag{4}$$

and the complete Hamiltonian is $H = H_0 + H_1$. We define the "distribution function" $F(n, m; t)$ by

$$F_s(n, m; t) = \left\langle C_{sn}^+(t) C_{sm}(t) \right\rangle = \sum_\alpha P_\alpha \left\langle \alpha | C_{sn}^+(t) C_{sm}(t) | \alpha \right\rangle , \tag{5}$$

where P_α is the probability that the system is in the state $|\alpha\rangle$. The angle brackets denote both a quantum mechanical and a statistical average. From the Heisenberg equations of motion

---

[15] University of Tennessee.

[16] Consultant from the University of Tennessee.

$$-\frac{\hbar}{i}\frac{\partial}{\partial t} C^{+}_{sn} C_{sm} = C^{+}_{sn} C_{sm} H - H C^{+}_{sn} C_{sm} \tag{6}$$

one can find

$$-\frac{\hbar}{i}\frac{\partial}{\partial t} F_s(n, m; t) = (\epsilon_{sm} - \epsilon_{sn}) F(n, m; t) - e_s \sum_k \left[\left\langle m|\phi|k \right\rangle F_s(n, k; t) - \left\langle k|\phi|n \right\rangle F_s(k, m; t) \right] . \tag{7}$$

This is the quantum mechanical analog of the Vlasov equation. We linearize Eq. (7) by writing

$$F_s(n, m, t) = F_{s0}(n)\, \delta_{nm} + F_{s1}(n, m; t) \tag{8}$$

and by treating F_{s1} and ϕ as small quantities whose product may be neglected. Also we assume that

$$F_{s1}(n, m; t) = F_{s1}(n, m; \omega)\, e^{-i\omega t} . \tag{9}$$

Equation (7) gives

$$F_{s1}(n, m; \omega) = -e_s \frac{F_{s0}(n) - F_{s0}(m)}{\hbar\omega - (\epsilon_m - \epsilon_n)} \left\langle m|\phi|n \right\rangle . \tag{10}$$

Next, we calculate the charge density in the plasma:

$$\rho(\mathbf{x}, t) = \sum_s e_s \psi^{+}(\mathbf{x}, t)\, \psi(\mathbf{x}, t) = \sum_s \sum_n \sum_m e_s C^{+}_{sn}(t) C_{sm}(t) \chi^{*}_{sn}(\mathbf{x}) \chi_{sm}(\mathbf{x}) . \tag{11}$$

The average charge density is

$$\left\langle \rho(\mathbf{x}, t) \right\rangle = \sum_s \sum_n \sum_m e_s F_s(n, m; t)\, \chi^{*}_{sn}(\mathbf{x}) \chi_{sm}(\mathbf{x}) . \tag{12}$$

The part of $\langle \rho \rangle$ due to F_{s0} contributes to the unperturbed potential V_0. It is the part due to F_{s1} which must be substituted into Poisson's equation for ϕ. Thus

$$\nabla^2 \phi(\mathbf{x}) = -4\pi \sum_s \sum_n \sum_m e_s F_{s1}(n, m; \omega) \chi^{*}_n \chi_m = \sum_s 4\pi e_s^2 \sum_n \sum_m \frac{F_{s0}(n) - F_{s0}(m)}{\hbar\omega - (\epsilon_n - \epsilon_m)} \left\langle m|\phi|n \right\rangle_s \chi^{*}_{sn} \chi_{sm} . \tag{13}$$

This is an integrodifferential equation for ϕ. It must be solved with appropriate boundary conditions. It is homogeneous in ϕ. Solutions will only exist when ω takes on certain values. Equation (13) plays the role of the dispersion relation for an infinite plasma.

The principal advantage of the quantum mechanical formulation is that it permits us to derive Eq. (13) without being specific about the nature of the system being discussed. To proceed further one must choose a sufficiently simple system, so that Eq. (1) can be solved. As an illustration, we shall discuss an infinite homogeneous plasma with $\mathbf{B}_0 = \nabla \times \mathbf{A}_0 = 0$. Then $n \to k$ and

$$\chi_{s\mathbf{k}}(\mathbf{x}) = \frac{1}{\sqrt{V}} e^{i\mathbf{k}\cdot\mathbf{x}} , \tag{14}$$

$$\epsilon_{s\mathbf{k}} = \frac{\hbar^2 k^2}{2m_s} , \tag{15}$$

where V is the volume of the box in which the system is quantized. Equation (13) becomes

$$\nabla^2 \phi(\mathbf{x}) = \sum_s 4\pi e_s^2 \sum_{\mathbf{h}_1} \sum_{\mathbf{h}_2} \frac{F_{s0}(\mathbf{h}_1) - F_{s0}(\mathbf{h}_2)}{\hbar w - (\epsilon_{s\mathbf{k}_2} - \epsilon_{s\mathbf{k}_1})} \times \left\langle \mathbf{k}_2 | \phi | \mathbf{k}_1 \right\rangle e^{i(\mathbf{h}_2 - \mathbf{h}_1)\cdot\mathbf{x}} . \tag{16}$$

If we assume a solution of the form

$$\phi(\mathbf{x}) = \phi_{\mathbf{q}} e^{i\mathbf{q}\cdot\mathbf{x}} , \tag{17}$$

then we find that

$$\left\langle \mathbf{k}_2 | \phi | \mathbf{k}_1 \right\rangle = \delta_{\mathbf{q},\mathbf{k}_2 - \mathbf{k}_1} , \tag{18}$$

$$\left[1 - \sum_s \frac{4\pi e_s^2}{\hbar q^2} \sum_{\mathbf{k}_1} \frac{F_{s0}(\mathbf{h}_1) - F_{s0}(\mathbf{k}_1 + \mathbf{q})}{\omega - \hbar(\mathbf{q}\cdot\mathbf{k}_1 + q^2/2m_s)} \right] \phi_{\mathbf{q}} = 0 . \tag{19}$$

The factor which multiples $\phi_{\mathbf{q}}$ is just $\epsilon(\mathbf{q}, w)$, the plasma dielectric constant. Setting it equal to zero gives the dispersion relation for plasma oscillations. We can put $\epsilon(\mathbf{q}, w)$ in a more familiar form by going to the classical limit by the prescription

$$\hbar \to 0 ,$$

$$\hbar\mathbf{k}_1 = m_s\mathbf{v} ,$$

$$\sum_{\mathbf{k}_1} \to \int d^3v ;$$

then

$$\epsilon(\mathbf{q}, w) = 1 - \sum_s \frac{4\pi e_s^2}{m_s q^2} \int d^3v \frac{\mathbf{q}\cdot\partial F_{s0}(\mathbf{v})/\partial\mathbf{v}}{(w - \mathbf{q}\cdot\mathbf{v})} , \tag{20}$$

which is the usual result.

It is not much more difficult to find the dispersion relation for an infinite homogeneous plasma in a uniform magnetic field. We shall not present that derivation here; the usual result is obtained.

The problems of most interest are those in which the plasma is finite. One problem which is tractable but nontrivial is shown in Fig. 1.14. The plasma is contained between perfectly reflecting walls at $z = 0$

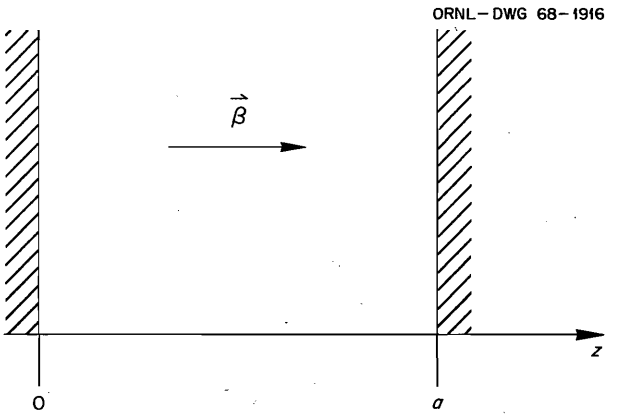

Fig. 1.14. Model of a Finite Plasma Contained Between Two Perfectly Reflecting Walls. There is a uniform magnetic field in the z direction.

and $z = a$. These are intended to crudely approximate magnetic mirrors. There is a uniform magnetic field in the z direction. This model has been investigated previously by Cotsaftis[17] and Arsenin.[18] We have recently derived the dispersion relation for this system and are presently investigating its consequences.

1.3 ENERGY EXCHANGE OF A TEST PARTICLE WITH A PLASMA

G. Joyce[19] D. J. Sigmar K. C. Hines[20]

The following is an abstract of an article that has been submitted for publication.

The change of energy of a test particle moving through a plasma is of interest experimentally and theoretically. Most calculations have been made by averaging over binary collisions or by treating the plasma as a dielectric and calculating the polarization energy loss. We have obtained an energy exchange expression from the Balescu-Lenard equation which reduces to these calculations in certain approximations, and which illuminates the validity of these approaches.

As an application, we have considered a Maxwellian electron plasma with a positive ion background and electrons for test particles. Numerical calculations were done for three densities, 10^{10}, 10^{13}, and 10^{16} cm^{-3}, and three temperatures, 4×10^{8}, 4×10^{7}, and 4×10^{4}°K respectively. It is possible to find an almost universal energy-loss vs test-particle-speed curve, which is shown in Fig. 1.15. v_0 is test particle speed, scaled by v_e, the thermal speed of the plasma electrons. η is defined through

$$-\frac{\partial F_{\text{test}}}{\partial t} = \eta\left(\frac{v_0}{v_e}\right) \frac{2n_e e^4}{\sqrt{\theta_e m_e}} \sqrt{8\pi} \left[\ln S\left(\frac{v_0}{v_e}\right) - \frac{1}{2}\right] .$$

[17] M. Cotsaftis, *Nucl. Fusion* **7**, 3 (1967).

[18] V. V. Arsenin, *Soviet Phys. – Tech. Phys.* **12**, 442 (1967).

[19] Permanent address: University of Iowa, Iowa City.

[20] Permanent address: University of Melbourne, Australia.

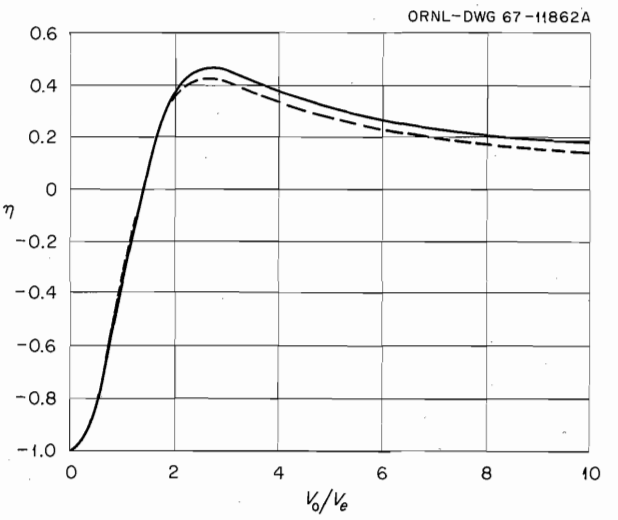

Fig. 1.15. Numerical Evaluation of the Normalized Energy Loss η of an Electron Test Particle as a Function of Incident Velocity for (1) $n = 10^{16}$ cm^{-3}, $T = 4 \times 10^{4}$°K (——); (2) $n = 10^{13}$ cm^{-3}, $T = 4 \times 10^{7}$°K (– – –); (3) $n = 10^{10}$ cm^{-3}, $T = 4 \times 10^{8}$°K (– – –).

θ_e is the electron temperature; $S = S^0 [1 + \frac{1}{2} (v_0/v_e)^2]$ is a velocity-dependent cutoff scaled by the Debye length over the distance of closest approach. For the case $n = 10^{16}$, $T = 4 \times 10^4$, $S^0 \approx 330$.

Our systematic theory is compared with calculations made in the high-velocity and the binary-collision limit.

2. Injection and Accumulation: Neutral Injection Experiments (DCX-1.5)

R. J. Colchin
J. L. Dunlap
R. S. Edwards
L. A. Massengill
H. Postma
R. G. Reinhardt
W. J. Schill
E. R. Wells

2.1 INTRODUCTION

Detailed studies of the plasma formed in this facility by injection of 20-keV H° were continued. As before, emphasis was given to the properties of the low-frequency instability (the flute) and to those of the two microinstabilities (the θ and Z modes).

New data were obtained by using:

1. an axial array of secondary-emission detectors to sample charge-exchange loss from the plasma,
2. the Li^+ beam transmission technique to determine plasma potential,
3. gridded probes at the ends of the plasma to analyze cold-plasma losses along field lines.

The experimental techniques are described in Sect. 2.2. Most of the data and their implications are discussed in Sect. 2.3, which deals with density profile determinations, and in Sect. 2.4, which treats the various instability modes.

A new technique for introducing energy spread into the injected H° beam is detailed in Sect. 2.5. Also a new neutral-beam line was installed. Described in Sect. 2.6, it has permitted injection of peak H° beams of 77 mA.

The option of 600-keV H_2^+ injection (the DCX-1 mode) was lost during this report period, when a portion of the 600-keV injector system was transferred to the Electronuclear Division. Before this injector was dismantled, experiments were performed to investigate stabilization of the negative mass instability by inductive end walls. Stabilization was not achieved; the details are given in Sect. 2.7.

2.2 EXPERIMENTAL TECHNIQUES

This section is concerned primarily with descriptions of the experimental techniques. Most of the data are presented and discussed in Sects. 2.3 and 2.4.

2.2.1 Charge-Exchange Measurements with Secondary-Emission Detectors

We continue to employ secondary-emission detectors (SED) mounted outside the periphery of the plasma to detect energetic charge-exchange neutrals lost from the plasma. The hot-ion density and axial profile are obtained from measurements with these detectors. They are calibrated by runs at high ambient neutral density. Under these conditions, trapping is by gas ionization and loss is by charge exchange. The cross sections (σ_{01} and σ_{10}) for the bleed gas (helium) are accurately known, so the density calculations are straightforward. The calibration procedure is repeated at intervals to ensure that the secondary-emission coefficient, and hence the calibration factor, does not change significantly during a series of runs. The reported density values are believed to be accurate to within a factor of 2.

A variety of detector configurations have been employed. In each, the energetic neutrals impinge upon a copper surface, which is screened to prevent response to fluctuating potentials in the plasma region. A collection of five detectors arranged symmetrically about the median plane was used to determine the axial profile of charge-exchange flux under conditions for which an individual instability mode was dominant.

Most of the SED data presented in this report were obtained by using a single detector with a Z extent of $\frac{3}{4}$ in. centered on the median plane. This particular detector was calibrated by the procedure described above, with the assumption that the detector is sensitive to 50% of the flux lost to the subtended azimuth. The latter consideration resulted from the profiles obtained with the five-unit array.

2.2.2 Potential Measurements with Lithium Ion Beam

We have attempted to study the positive space potential of the plasma by determining the acceleration potential required to transmit a lithium ion beam across the plasma. The basic technique[1] has been described before and has been used to advantage by several investigators. It is particularly useful in the investigation of low-frequency phenomena. In this particular application the collector was mounted on one of a pair of movable end walls (Fig. 2.1). This end wall was slotted ($\frac{1}{2}$ in. wide $\times$ $4\frac{1}{2}$ in. long) along a radius vector, and the collector plate was secured behind the slot. A grounded screen was again used to prevent electrostatic pickup. The opposite end wall was similarly slotted, and the two slots were aligned in azimuth. The ion gun was positioned behind this second end wall. It was provided with a screw-drive mechanism which allowed precise positioning along the radius vector and maintained the beam ($\frac{3}{8}$ in. in diameter) centered within the slot. Thus the arrangement permitted potential probing at different plasma radii (to $r \approx 4$ in.). The end walls were movable to allow control of the flute instability as detailed in the previous report.[2] Their locations were symmetric with respect to the median plane.

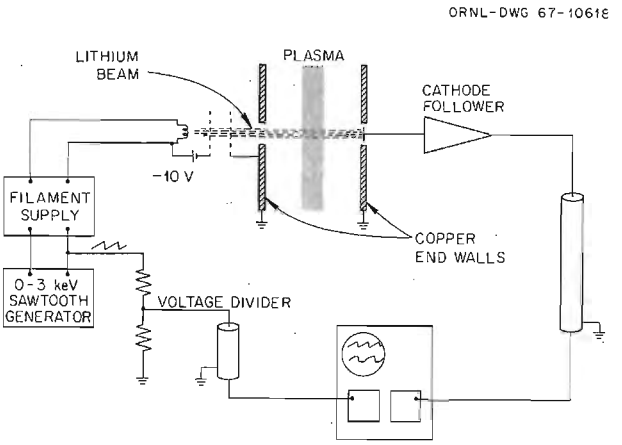

Fig. 2.1. Lithium Beam Potential Probe.

2.2.3 Cold-Plasma Measurements with Gridded Probes

In these experiments an end wall was arranged to incorporate an array of plane gridded probes. The array extended along a radius vector. Each probe incorporated three screens between the plasma and the collector. The one closest to the plasma was grounded to the end wall, the intermediate one was attached to a variable-potential high-voltage supply and acted as the analyzing grid, and the third was biased (-22.5 V with respect to the collector) for secondary-emission suppression. Internal connections allowed the use of common high-voltage and bias supplies. Each collector fed a fast ($\sim$0.1- to 0.2-μsec rise time) current to the voltage amplifier which in turn was connected for oscilloscope display.

One array consisted of four probes, with each collector $\frac{3}{4}$ in. in diameter and with collector centers spaced at $1\frac{1}{4}$-in. intervals. Figure 2.2 presents representative data obtained from this array with analyzer biases of 0, +100, and +500 V. A short interval of steady-state response is shown at the beginning of the traces; then injection is stopped and the plasma allowed to decay. Halfway along each sweep the beam is cut back on. The plasma builds up, passing through Z and θ instability modes, and finally into the flute instability.

[1] G. R. Haste and C. F. Barnett, *J. Appl. Phys.* 33, 1397 (1962).

[2] *Thermonuclear Div. Semiann. Progr. Rept. Apr. 30, 1967*, ORNL-4150, p. 41.

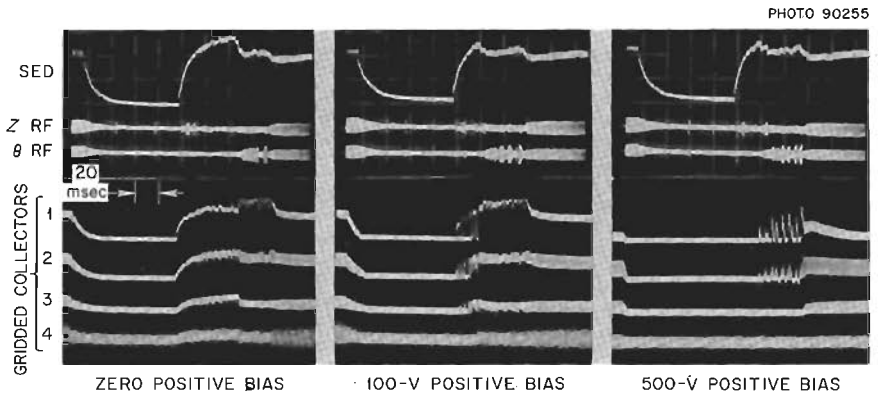

Fig. 2.2. Responses of Charge-Exchange Neutral Detector (SED), Magnetic Probes, and Cold-Plasma Collectors During Plasma Decay and During Buildup Through Z, θ, and Flute Instabilities. The suppressor grid of the cold-plasma collector was operated with −22.5 V bias. In steady state, $n_+ \approx 3 \times 10^7$ cm^{-3}.

A second array consisted of 11 individual probes, with each collector $\frac{3}{8}$ in. in diameter and with collector centers spaced at $\frac{1}{2}$-in. intervals. This one allowed a detailed study of cold-plasma variations with radius.

2.3 DENSITY PROFILES

To obtain an axial plasma profile, five secondary-emission detectors (described in Sect. 2.2.1) were positioned along the Z axis. Data from these detectors are shown in Fig. 2.3 for various levels of the flute instability. The result of strong instability is primarily a decrease in the neutral particle flux from the central peak, increasing the FWHM (full width at half maximum) from near 1 in. to nearly 1.5 in.

Because these flux profiles are quite narrow, their identification with the plasma profile is reasonably accurate. The plasma is evidently highly anisotropic ($T_{\parallel i}/T_{\perp i} \cong 0.005$). The neutral beam is collimated to a diameter of 1.5 in. at the entrance to the plasma region. Assuming that little axial spreading may be ascribed to the relatively weak Z mode, the top trace of Fig. 2.3 closely approximates the unperturbed beam and plasma density profiles.

Radial plasma profiles were measured by the array of 11 gridded probes described in Sect. 2.2.3. One of the grids was biased highly negatively so that no electrons could reach the collector. It is assumed that the ions collected were cold, arising from a background gas atom (or molecule) which had lost an electron through charge exchange with a fast trapped proton. Then

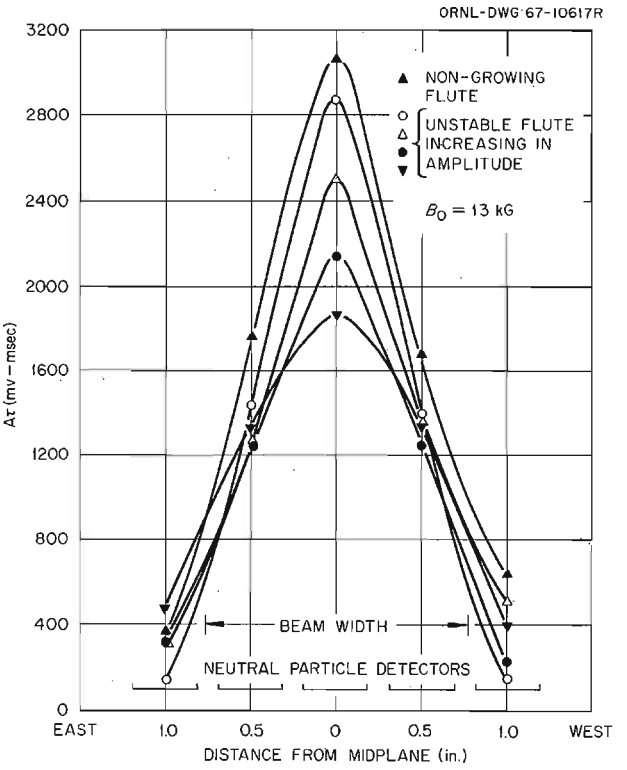

Fig. 2.3. Axial Hot-Plasma Profiles from Five Charge-Exchange Loss Detectors for Various Levels of the Flute Instability. ΔT is proportional to fast-ion density. Z-mode activity accompanied the nongrowing flute.

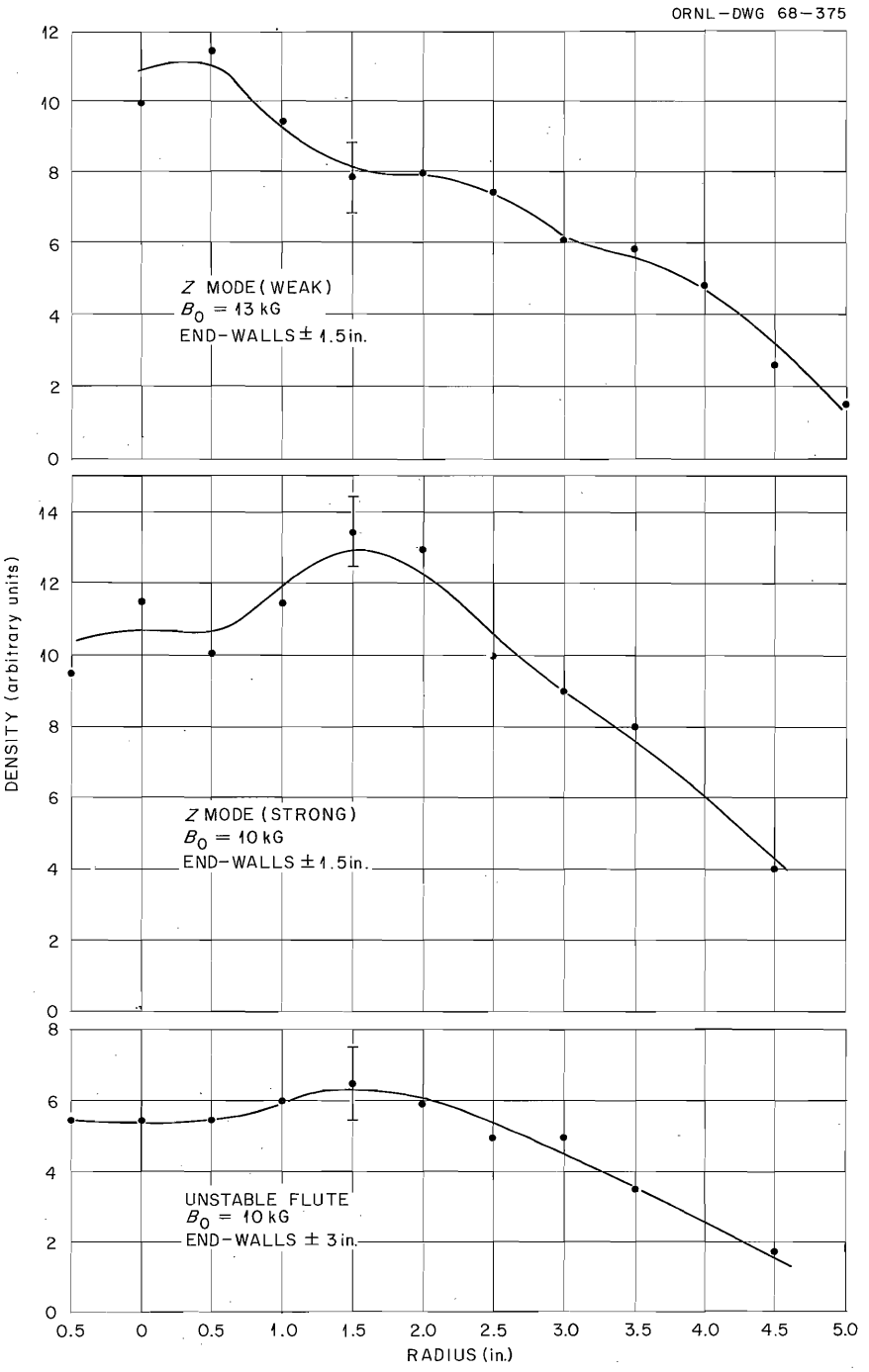

Fig. 2.4. Radial Hot-Plasma Profiles from Ion Saturation Current to Gridded Cold-Plasma Collectors. Data are shown for three instability conditions. For the upper curve, gas and Lorentz trapping contributed approximately equally. Lorentz trapping dominated for the two lower curves. Error bars represent uncertainties in extracting data from oscillograms. Hot-ion densities recorded by median plane SED were 1 to 3 $\times$ 10^7 cm^{-3}.

to the extent that the radial distribution of cold ions is unaffected by instabilities, the resulting ion saturation currents to the probe array vary with radius as does the trapped hot-ion density. Figure 2.4 illustrates typical radial density profiles determined in this fashion under weak Z mode, strong Z mode, and fluting conditions.

To find the radial density profiles expected on the basis of single-particle motion, an orbit-following code was used. Particles were assumed to be ionized at 1-cm intervals along an injection line confined to the median plane. The orbit of each ion was followed for 600 nsec. A grid of concentric, 1-cm-wide rings was set up, and at each orbital integration step (every tenth nanosecond) a counter for the annular zone containing the particle was incremented. The number of counts recorded in each zone divided by its area determined the gas ionization density. The counts resulting from each particle were multiplied by an appropriate weighting factor to find the corresponding Lorentz density. Injection lines at $y = 0$, ± 0.25, and ± 0.5 in. were included. Each line was weighted according to the relative flux of beam particles, as determined from the upper curve of Fig. 2.3. The results of these calculations are displayed in Fig. 2.5. Comparison of Figs. 2.4 and 2.5 indicates that both strong Z and flute instabilities flatten the central peak calculated on the basis of single-particle motion.

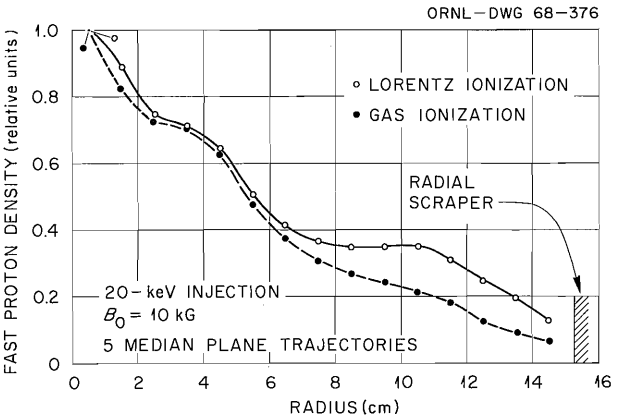

Fig. 2.5. Radial Density Profiles from Computer Calculations of Single-Particle Orbits. The results do not depend critically upon the value of B_0.

2.4 INSTABILITY STUDIES

This section details results arising from application of the experimental techniques outlined previously. Data from other sources are also included, as are comparisons with theory.

2.4.1 *Z* Mode

Measurements of the Z mode were made using lithium beam and gridded probe techniques. Data from both sources show that Z rf bursts, plasma potential fluctuations, and axial electron expulsion are correlated.

Associated with each Z rf burst is a simultaneous pulse of electrons in the axial direction. These electrons appear most frequently and with largest amplitude near the axis, and presumably define the region of greatest rf activity. Often, electron pulses occur at the axis which are correlated with losses to detectors centered 1.25 and 2.5 in. off axis. A particularly strong burst may be detected on collectors out to 3.75 in.

Attempts were made to measure the "steady-state" plasma potential between Z rf bursts. The interpretation of these potentials is complicated by the presence of the stable flute mode.[2] "Steady-state" potentials depend somewhat on plasma conditions, but have not been observed above 200 V. They are relatively constant with radius out to 2 in., falling off slowly at larger radii. The ambipolar potential expected for stable plasma should be below 25 V according to a calculation using the Fowler-Rankin code.[3]

Along with a Z rf pulse there are associated plasma potential fluctuations. Coincident with an electron burst, the potential sharply increases due to the deficiency of electrons in the plasma. It then quickly decreases as the electrons are replaced. This sequence is illustrated in Fig. 2.2. On plasma buildup (top trace) the first signals seen on the Z rf probe (second trace) are those of the Z mode. Simultaneous signals to the gridded probes were caused by cold ions, since the -22.5 V used to suppress secondary emission also rejected all electrons from the plasma, except during bursts. The middle set of pictures shows that cold ions were able to overcome a 100-V repelling bias only during an

[3] T. K. Fowler and M. Rankin, *J. Nucl. Energy: Pt. C* 4, 311 (1962).

electron burst. No cold ions were able to overcome the 500-V repulsive bias present during the last picture. Figure 2.6 shows the cutoff voltage of these cold-ion bursts as a function of radius, and hence the limits of positive potential fluctuations with Z-mode instability.

With θ and unstable flute modes suppressed, the Z mode is observed at the highest densities so far attained. It is present throughout the Lorentz trapping regime with a threshold lying in the gas trapping region. In an attempt to measure this threshold, potential spikes were recorded at densities down to 2 to 3 $\times$ 10^6 particles cm^{-3} on the most sensitive monitor, the gridded probes. This is near $\omega_{pe}/\omega_{ci} = 1$.

Because this instability involves motion of electrons along magnetic-field lines, it has been speculated that the Z mode is a Harris instability. Calculations using DCX-1.5 parameters indicate that the $m = 1$ Harris instability should have a threshold near $\omega_{pe}/\omega_{ci} \approx 1.5$ and a longitudinal wavelength of approximately 10 gyroradii. This wavelength is about five times the actual length of the hot-ion plasma.

2.4.2 Flute Instability

We have measured, as a function of hot-ion density, the frequencies of the fluting modes, both the stable and the unstable oscillations. In displaying these data, it is convenient to normalize to the ion drift frequency. Such normalization is a necessity for comparison with theoretical predictions. Although the drift frequency varies considerably with radius for fixed B_0 (Fig. 2.7), experimentally we note that the unstable oscillation is characterized by a single (fundamental) frequency component. This observation suggests that the drift frequency at one particular radius dominates. A logical choice is that radius at which the density is a maximum with ∇B and ∇n in the same direction. Figure 2.4 indicates that this condition occurs at a radius of about 2 in. Figure 2.7 shows a drift frequency of 40.8 kHz at this radius, and this value has been chosen for normalization of the frequency data which follow.

Figure 2.8 traces the behavior of the normalized flute frequencies as a function of density. As the plasma density is increased from zero, stable flute oscillations appear. Our observations of these confirmed those reported earlier.[4] The mean frequency

[4] *Thermonuclear Div. Semiann. Progr. Rept. Apr. 30, 1967*, ORNL-4150, sect. 2.2.3, pp. 41–43.

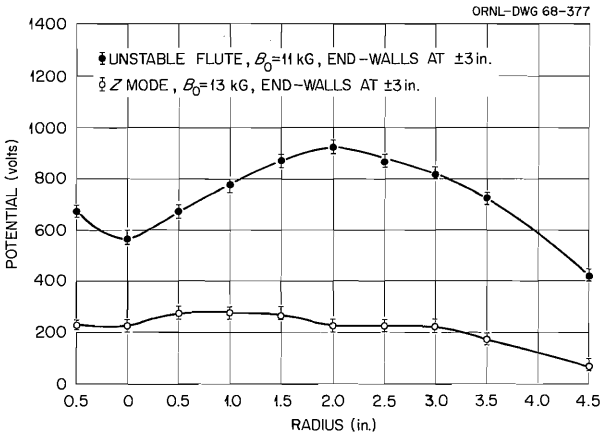

Fig. 2.6. Plasma Potential as a Function of Radius for Z and Unstable Flute Modes. The data are from gridded probe measurements with positive analyzing bias. Potential values are equal to the bias voltages required to repel cold ions during the instability. From the median plane SED, $n_+ = 1$ to 2 $\times$ 10^7 cm^{-3}.

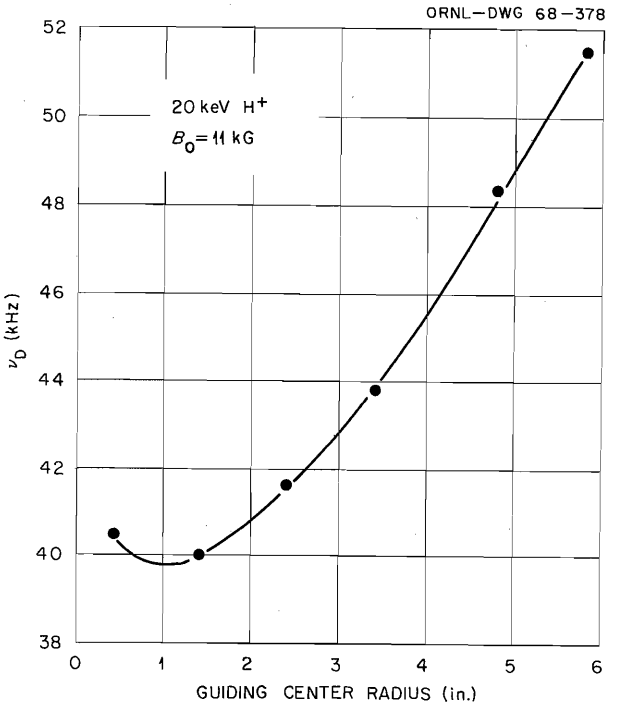

Fig. 2.7. Calculated Ion Drift Frequency as a Function of Guiding Center Radius. Data points are from orbit following computer computations.

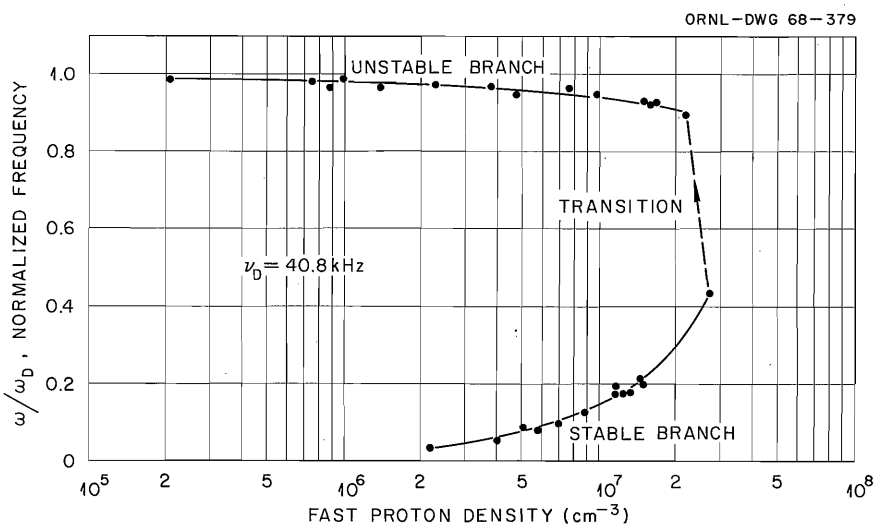

Fig. 2.8. Normalized Flute Frequencies as a Function of Density. All data points are for injection of 20-keV H^0 and have been normalized to $B_0 = 11$ kG. Densities are from median plane SED.

of the lowest frequency band ($m = 1$) was determined by autocorrelation techniques in steady-state operation under conditions for which this band dominated. These signals have a short correlation time, one or two periods of the lowest frequency signal. Since these stable oscillations appear along with the Z instability, the short correlation time perhaps reflects the influence of that mode. The frequency of the stable oscillation increases as the density increases. At the instability point a jump in frequency to near the ion drift frequency occurs, along with a decrease in density. Correlation times for these unstable oscillations are much larger; the flute completely dominates the plasma and the flute frequency is constant for fixed density. As the density decays after injection stops, the frequency increases slightly (by 10% for two orders of magnitude change in density).

We are still concerned with the possible effects of $E \times B$ shifts on the frequency data of Fig. 2.8. Thus far we have not succeeded in measuring values of the zero-order E_r field that are required to estimate these effects. The situation is complicated by the presence of both rotating and static (nonrotating) potential components. Further complications arise because of axial and radial variations of both components. In the face of these complexities, we need to extract enough information about the potential distribution to define at least a maximum value of static E_r in the vicinity of the flute. As will be seen in later comparisons with theory, the value during the unstable flute is of particular interest.

One measure of potential arises from gridded probe data with positive analyzing bias like those of Fig. 2.2. Increasing bias gradually reduces the collected slow-ion current to zero, and the bias required for cutoff should approximate the peak potential along the flux tube intercepting the collector. Figure 2.6 shows potential values as a function of radius secured in this manner while operating with the unstable flute in steady state. The data suggest peak radial fields at the supposed flute location ($r \approx 2$ in.) of $+100 \geqq E_r \geqq -100$ V/cm. Although interesting, the value does not represent limits on the desired *static* E_r required for knowledge of the $E \times B$ frequency correction; rather it represents limits for the total E_r field that arises from the combination of the two potential components. From these measurements, the only evidence of their relative amplitudes arises from the observation that no electrons are generated with energy greater than about 20 eV. Thus the static potential is positive, as expected, and at least about equivalent in amplitude to the oscillating component.

The lithium beam technique could in principle provide the required separation of potential components. However, the $E \times B$ shift of the beam

itself prevented this measurement with the collector described in Sect. 2.2.2. A different collector which may prove successful is under construction.

We now wish to consider the observed frequency data (Fig. 2.8) in relation to two theoretical calculations, that of Guest and Beasley[5] and that of Varma.[6] Guest and Beasley included the effects of conducting walls separated from the ends of the hot plasma by cold plasma. The calculation employed slab geometry, and the dispersion relation is

$$\frac{\omega_c}{\omega_p^2} + \frac{\omega_D}{\omega(\omega + m\omega_D)} + \frac{\omega_c}{\omega_p^2} \frac{2R_p}{mL \tanh (mL_c/R_p)} = 0 .$$

In this equation $R_p^{-1} = -(1/n)\ (dn/dr)$, L_c = distance from the hot plasma to an end wall, L = length of the hot plasma, m = mode number, and ω_D = gradient B drift velocity divided by R_p. This relation is quadratic in ω. The first two terms give the usual flute dispersion relation (no end walls), and the third term represents the effect of the end walls.

Varma has included the conservation of the magnetic moment through first order. His dispersion relation, as derived by us for slab geometry, is

$$\frac{\omega_c}{\omega_p^2} + \frac{\omega_D}{\omega(\omega + m\omega_D)} \left(1 - 2\frac{R_p}{R_c}\right) - \frac{\omega_D}{(\omega + m\omega_D)^2} \frac{R_p}{R_c} = 0 ,$$

where $R_c^{-1} = -(1/B)\ (dB/dr)$. Again the first two terms represent the usual quadratic flute equation. With the third term included the resulting dispersion relation is a cubic. Three roots are now possible, one of which will remain real.

Figure 2.9 is a plot of the real parts of the Guest-Beasley and Varma dispersion relations for DCX-1.5 parameters. The Varma relation exhibits the lower instability threshold, characteristic of formulations which do not contain the end-wall correction. In addition to producing the third branch of nearly constant frequency, Varma's relation also distorts the usual parabolic curve. As a result, it predicts instability at a frequency lower than $\omega/\omega_D = 0.5$.

Detailed comparisons of Fig. 2.9 with the experimental frequency observations (Fig. 2.8) show that the observed density threshold for instability is closer to that of Guest-Beasley, while the observed ω/ω_D at threshold and the behavior of the frequency upon decay are closer to predictions of Varma's relation.

The threshold density from Varma's relation would be raised somewhat by inclusion of the end-wall correction, the general validity of which has been demonstrated[5] by earlier work. The interesting question is then whether the experimental observations confirm the characteristic results of

[5] *Thermonuclear Div. Semiann. Progr. Rept. Apr. 30, 1967*, ORNL-4150, sect. 2.3.4, pp. 43–46.

[6] R. K. Varma, *Nucl. Fusion* **7**, 57 (1967).

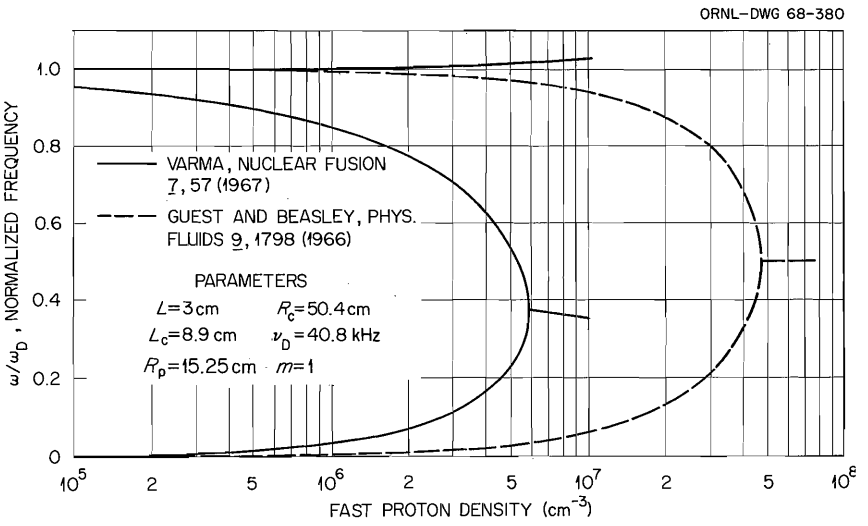

Fig. 2.9. Real Frequency Solutions of the Guest-Beasley and the Varma Flute Dispersion Relations.

Varma's magnetic-moment treatment: distortion of the usual parabolic frequency curve and the existence of a third frequency branch near ω_D. We have just cited evidence tending to confirm these results, the observation of critical $\omega/\omega_D < 0.5$ (suggestive of the distortion) and the behavior of ω during decay from unstable densities (suggestive of a nearly constant frequency branch near ω_D). This evidence cannot be considered definitive as yet. Our choice of ω_D seems accurate enough, since the decaying branch extrapolates to $\omega/\omega_D = 1$ at zero density. However, as discussed earlier in this section, the measurements of ω at higher densities may be influenced by zero-order electric fields, and the magnitude of this effect has not been determined.

If the observed high-frequency branch does indeed represent a third root to the true dispersion relation, it would seem reasonable to ascribe the frequency jump at instability threshold (Fig. 2.8) to nonlinear effects shifting the frequency up to this uppermost frequency branch. If, however, the dispersion relation is quadratic, so that only the parabolic curve exists below threshold, the jump might be ascribed to an $E \times B$ shift. Then the observed behavior of the frequency curve upon plasma decay presumably continues to reflect a changing $E \times B$ shift. There are two observations which argue against behavior dominated by $E \times B$ shift and therefore which favor the existence of a third root. One observation is that the frequency changes during decay are small, whereas the potential, and presumably the electric field, changes are large. The second is that the curve of frequency vs decaying density is reproducible with differing combinations of pressures and input beam currents, that is, reproducible under conditions which intuitively should result in different $E \times B$ shifts.

2.4.3 θ Mode

Characteristic features of the θ-mode microinstability were described in the previous report.[7] These included frequency distribution of the rf $\dot{B}$ signals, changes of proton energy spectrum during the instability, and control either by operation at high B_0 ($\approx$12 kG) or by deliberate introduction of proton energy spread. During the present report period, other features of the mode have emerged from studies using the lithium beam potential probe and also the gridded cold-plasma collectors.

The mode is in its most virulent form with $B_0 \approx 10$ kG. The rf bursts are of large but fluctuating amplitude. Under these conditions, we observe large positive potentials (to several hundred volts) in coincidence with the bursts. Within $r < 1.5$ to 2.0 in. the potentials scale with the amplitude of the fluctuating rf level. Just the opposite effect is observed at larger radii. During bursts, electrons are ejected with energies to about 50 eV. If the injected neutral beam is shut off in the midst of a large rf burst, the rf envelope decays smoothly with a time constant much longer than that for density decay (1 sec compared with tens of milliseconds).

As previously noted, the θ mode is a strong function of magnetic field. With $B_0 = 11$ kG, it is much weaker than with 10 kG. The rf bursts are of much lower amplitude, and they occur at more frequent intervals with greater regularity. Gridded probes show positive potential fluctuations to several hundred volts on axis, and potentials decrease with increasing radius. A peculiar effect observable with this field strength is that upon onset of the instability, cold-ion current increases within $r < 1$ in. and decreases thereafter (as compared with levels with the Z-mode present). This effect is evident in Fig. 2.2 on the first collector, under zero bias. One explanation is that ions have been rearranged toward the axis; this could account for the potential behavior as described in the last paragraph. An alternative explanation is that the central density was being suppressed by the Z mode.

2.5 BEAM ENERGY SPREADING

We previously reported[8] beam energy spreading that was achieved by placing a transformer secondary in series with the high-voltage supply to the ion source and controlling the primary voltage. The inductive transients introduced by this transformer upon beam turnoff proved troublesome, and for this reason we have worked on an alternative arrangement.

[7] *Thermonuclear Div. Semiann. Progr. Rept. Apr. 30, 1967*, ORNL-4150, sect. 2.2, pp. 37–38.

[8] *Thermonuclear Div. Semiann. Progr. Rept. Apr. 30, 1967*, ORNL-4150, p. 46.

As normally connected, the three-phase input to the high-voltage supply is controlled by three transformers with a common motor drive. One of these was disconnected and replaced by a separately controlled Variac. This arrangement allows operation with balanced three-phase input (for minimum dc voltage ripple), or with varying degrees of unbalanced input. Furthermore, the inductive transients of the earlier scheme are avoided.

With the new technique, we can produce plasmas with about 40% energy spread (FWHM) in the hot-ion distribution.

2.6 NEUTRAL-BEAM DEVELOPMENT

Extensive changes were made in the neutral-beam injection line during the early portion of this report period. A diagram of the initial configuration was given in an earlier report.[9] Figure 2.10 shows the present configuration. Specific changes were:

1. The distance between the ion source and the magnesium conversion cell was reduced.
2. The magnesium cell was mounted in the center of a pumping chamber.
3. A swivel connection was provided at the junction of the lens coil assembly and the cell chamber to allow more flexibility in beam alignment.
4. The earlier lens coil, which proved adequate to focus H_2^+ beams up to 33 keV, was replaced by one powerful enough to focus well beyond 50 keV (the limit of the present high-voltage supply).
5. The source mounting arrangement was altered to incorporate a water-cooled plate in good thermal contact with the snout. Local outgassing and the resulting high-voltage breakdown at this point are much reduced.
6. Diffusion pump baffles were changed from water to refrigeration cooling.
7. Apertures were relocated and in some instances resized. The magnesium-cell aperture is now $1\frac{3}{16}$ in. in diameter rather than $\frac{7}{8}$ in. This change is partially to compensate for reduction of aperture size by gradual accumulation of magnesium deposits. The final limiting aperture is still located at the entrance to the main vacuum tank and is still $1\frac{1}{2}$ in. in diameter. The liner apertures are $2\frac{3}{8}$ in. in diameter to prevent clipping of the beam.
8. The wooden support platform was replaced by one of stainless steel.

The new arrangement permits 100 to 150 hr of operation before cleaning and recharging of the magnesium cell is required. It has allowed a maximum injected 20-keV H° beam of 77 mA (equivalent). Typical operating currents of 20 to 30 mA are easily obtained. There has been no emphasis on operation at higher currents, because these

[9] *Thermonuclear Div. Semiann. Progr. Rept. Oct. 31, 1966*, ORNL-4063, Fig. 1.1, p. 2.

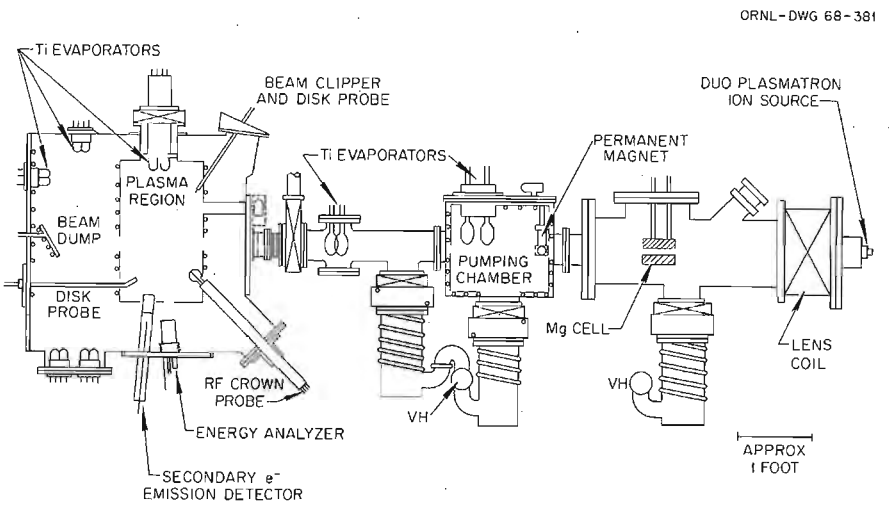

Fig. 2.10. Schematic Diagram of DCX-1.5.

lower the charge-exchange lifetime of the hot ions. This effect should be reduced soon upon installation of a burial line, which is nearly completed.

2.7 NEGATIVE MASS STABILIZATION EXPERIMENT

Before dismantling the DCX-1 600-keV H_2^+ injection system, an unsuccessful attempt was made to stabilize the negative mass instability through the action of inductive end walls. This idea was first introduced by Neil and Briggs.[10] New calculations were carried through in order to take more clearly into account the detailed instability mechanism and geometry of the DCX-1.

These new calculations started with Liouville's equation for the negative mass instability as derived by Fowler.[11] The electric field energy was generalized to include the perturbed electric field's action on inductive end walls, and the interaction of fields in the walls back on the beam. Each wall was circular and divided into 24 pie-shaped segments. Each segment, in turn, was joined to the next by an inductor. A wall was situated at each end of the plasma, and one segment of each wall was grounded.

The stability criterion obtained was that

$$L' > \frac{1}{m^2\omega_c^2}\left(\frac{A_m}{3\epsilon_0 R} - \frac{1}{c'}\right),$$

where L' = inductance per unit angle of an end wall, c' = capacitance per unit angle between an end wall and the beam, R = mean radius of the beam, m = mode number, ϵ_0 = dielectric constant, and A_m is a geometrical constant depending on m. With end walls at ±5 in. from the midplane, the calculated inductance necessary for stabilization of an $m = 1$ mode was 7 μH in each inductor.

End walls as described above were constructed, and high-Q inductors were wound with taps at 5 and 10 μH. Insertion of ferrite cores approximately doubled these values. All coils were self-resonant above 25 MHz.

The above equation predicts stabilization of the negative mass instability at all densities. Initial experiments proved this not to be the case. Attempts were then made to find if the inductive nature of these end walls was raising the instability threshold. No effect was observed; grounded and inductive end walls gave identical thresholds.

These negative results may be blamed on several causes. First, the calculation may have been overly optimistic. Some calculational uncertainty arises in obtaining a value for c'. The inductors used may have been too small, although they were three times larger than the predicted necessary size. Second, the calculation omitted several factors which may have been of physical importance. Chief among these were the effects of capacitance between end walls and the ac resistance of the inductors. Third, each inductor contained 2 m of wire, enough that a pulse from each passage of the instability could not propagate entirely through an inductor before another pulse arrived. The net effect may have been a disadvantageous phase mixing of signals.

2.8 ACKNOWLEDGMENTS

Carl Parker and Eric Ferguson were responsible for calculation of the density plots in Sect. 2.3. Part of that work used a Lorentz trapping code supplied by A. C. Riviere of the Culham Laboratory. They also computed the proton drift frequency and the numerical solution to Varma's equation discussed in Sect. 2.4.2. Glenn Haste used the Fowler-Rankin code to find the ambipolar potential quoted in Sect. 2.4.1. Mozelle Rankin evaluated geometrical constants for the negative mass stability criterion, and C. O. Beasley furnished the Harris mode calculations of Sect. 2.4.1.

---

[10] V. K. Neil and R. J. Briggs, *Plasma Phys.* 9(5), 631 (1967).

[11] T. K. Fowler, *Calculation of the Negative Mass Instability for DCX-1*, ORNL-CF-61-7-1 (July 3, 1961).

3. Injection and Accumulation: Multiple-Pass Experiments (DCX-2)

P. R. Bell[1] J. C. Ezell J. F. Lyon
J. F. Clarke J. E. Francis E. C. Moore
J. S. Culver C. F. Harrison[2] R. F. Stratton
S. M. DeCamp G. G. Kelley J. P. Wood

3.1 INTRODUCTION

The emphasis this report period has been on the study of microinstabilities occurring in different plasmas in the DCX-2. These instabilities occur at frequencies near harmonics of the ion cyclotron frequency and, for the most part, appear to be Harris-like modes,[3] that is, instabilities caused by coupling between perpendicular cyclotron motion of energetic ions and axial plasma oscillations of cold electrons, driven by the anisotropy of the ion velocity distribution function. Three different plasma situations have been studied during this period: (1) the energetic proton plasmas obtained by hydrogen arc dissociation and by hydrogen gas dissociation in the presence of the injected H_2^+ beam, that is, the steady-state behavior during the beam-on time; (2) the energetic proton plasma obtained by hydrogen arc dissociation in the absence of the injected beam, that is, during the afterglow period following beam turnoff; and (3) the injected ion beam and its accompanying ionization-produced cold plasma in the absence of the energetic proton plasma, that is, with the normally dominant energetic proton plasma suppressed by the insertion of obstacles.

3.2 BEAM-ON PLASMA INSTABILITY MODES

3.2.1 Hydrogen Arc Dissociation – The RF Spectrum

Some instability mode identifications have been made for the energetic proton plasmas produced by dissociation of the injected H_2^+ beam on a hydrogen gas background and on a hydrogen arc. With hydrogen arc dissociation the energetic proton pitch angle distribution is characterized by a dominant central peak at small pitch angles and smaller side lobes at larger pitch angles determined by the injected beam axial velocity distribution. The properties of these two separate energetic proton groups have been discussed in detail in previous reports.[4–6] For these beam-on rf studies the total energetic proton density was $\sim 10^9$ ions/cm^3, the injected beam was generally about 25 mA of 540-kV H_2^+, and the background pressure was $\sim 1.5 \times 10^{-6}$ torr.

Magnetic-loop rf probes (similar to that shown in Fig. 3.1) were the main diagnostic tool used in the beam-on instability study, since radial electric probes detect only net charge fluctuations in the plasma, while the more selective magnetic probes

[1] On leave, NASA Manned Spacecraft Center, Houston, Tex.

[2] Analytical Chemistry Division.

[3] E. G. Harris, *J. Nucl. Energy: Pt. C* **2**, 138 (1961).

[4] *Thermonuclear Div. Semiann. Progr. Rept. Apr. 30, 1966*, ORNL-3989, p. 15.

[5] *Ibid., Apr. 30, 1965*, ORNL-3836, p. 27.

[6] *Ibid., Oct. 31, 1964*, ORNL-3760, p. 17.

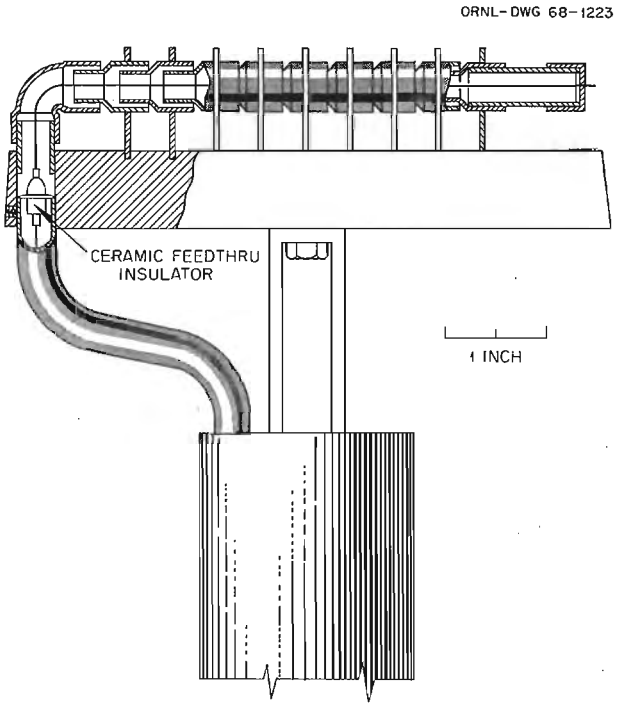

Fig. 3.1. Magnetic-Loop RF Probe Characteristics. Probe cross section. Center conductor is held away from the discontinuous shielding around center conductor by ceramic beads (not shown), and the return is through the shield and plate via the ground connection at right-hand end.

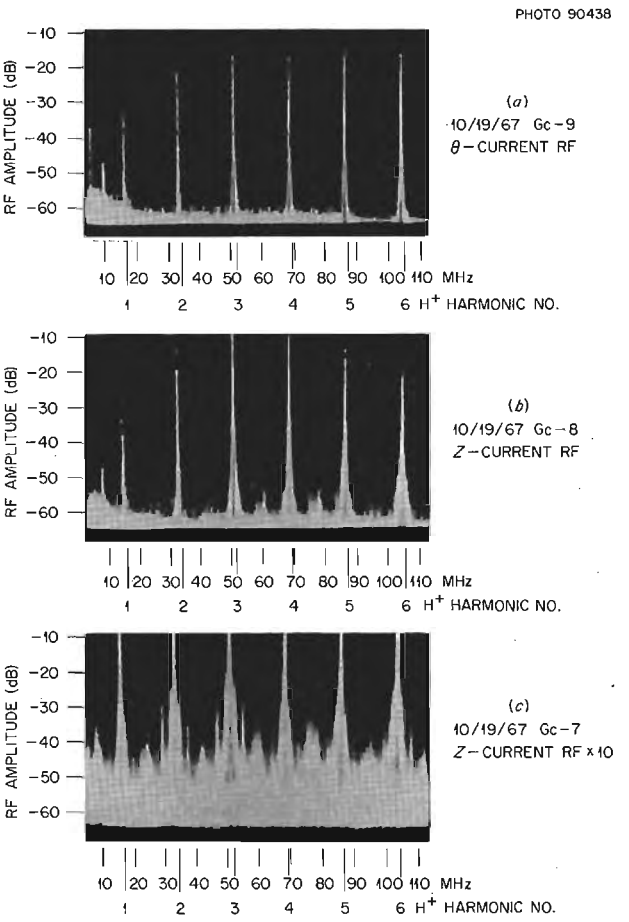

Fig. 3.2. Beam-On RF Spectra with Hydrogen Arc Dissociation. (*a*) θ-current rf signals, (*b*) Z-current rf signals, and (*c*) Z-current rf signals with 20-dB gain. The first six proton cyclotron harmonics are numbered. The small peaks halfway between the proton lines in *b* and *c* are the odd harmonics of the H_2^+ ion cyclotron frequency from the beam instability described in Sect. 3.4. The peaks below 10 MHz are spurious (spectrometer birdies).

are shielded from electric fields and can be oriented to detect signals produced by axial plasma currents (z currents) or azimuthal plasma currents (θ currents), of importance in the identification of the instability mode. The rf spectra obtained during the beam-on time with magnetic-loop rf probes at the machine midplane are shown in Fig. 3.2. Figure 3.2*a* shows the lower frequency part of the θ-current rf spectrum, while Fig. 3.2*b* shows the corresponding part of the z-current rf spectrum. The z-current and θ-current rf signals are of comparable magnitudes, and their spectra contain strong lines at many harmonics of the proton cyclotron frequency. These lines are rather narrow ($\sim$150 kHz), implying long growth and decay times for the instability compared with the ion cyclotron period, and show no Doppler splitting, indicating that $k_z V_z$ is zero. This suggests that the main instability is in the central peak proton group rather than in the much weaker side lobe group, since the central peak protons have no mean axial velocity ($V_z = 0$), while the side lobe protons have a large mean axial velocity. The other alternative (that $k_z = 0$) is not compatible with the observed axial mode patterns to be described, nor with the predicted stability of the Harris mode for $k_z = 0$.

Figure 3.2*c* shows the z-current rf spectrum of Fig. 3.2*b* with a factor of 10 gain increase. Sharp peaks symmetrically positioned about the proton cyclotron harmonic lines are now visible, indicating a weaker instability in the side lobe proton group.

These lines are proton lines, since no corresponding lines are seen in the H_2^+ ion cyclotron harmonics also present in this spectrum.

The correlation properties of the z-current and θ-current rf signals and the electron current signal to a biased gridded probe located axially beyond the energetic plasma boundary are of interest for instability mode identification. These signals have been studied, and beam-on instability mode patterns have been established for the first three proton cyclotron harmonics, using a row of seven magnetic probes extending the length of the energetic plasma region (234 cm), a ring of six probes at the machine midplane, and a ring of four probes 69 cm from the midplane.

3.2.2 Proton Fundamental Mode Pattern

The correlation properties of the instability rf at the proton fundamental were studied with hydrogen arc dissociation using a 2- to 20-MHz bandpass filter to isolate the sharp proton fundamental at 17.4 MHz. Some of the results obtained are shown in Fig. 3.3. Figures 3.3*a* and *b* show that the z-current rf signals are time correlated and in phase on opposite sides of the midplane, while the θ-current rf signals are 180° out of phase across the midplane. Figure 3.3c shows that the z-current rf and the θ-current rf at the same location are time correlated with each other and hence represent the same instability. The z-current rf and the current to a gridded probe located axially beyond the energetic plasma boundary and biased to collect electrons are time correlated as shown in Fig. 3.3*d*. The gridded probe signals are electron current signals rather than electric rf picked up on the gridded probe, since a negative bias eliminates these signals. Figure 3.3e shows that θ-current rf signals observed on probes located 69 cm from the midplane but separated azimuthally by 180° are also well correlated and 180° out of phase. This good azimuthal correlation on opposite sides of the machine (probes 91 cm apart) shows that both probes are seeing the same disturbance and not uncorrelated effects local to each probe.

These results are summarized in the axial mode pattern of the dominant instability at the proton

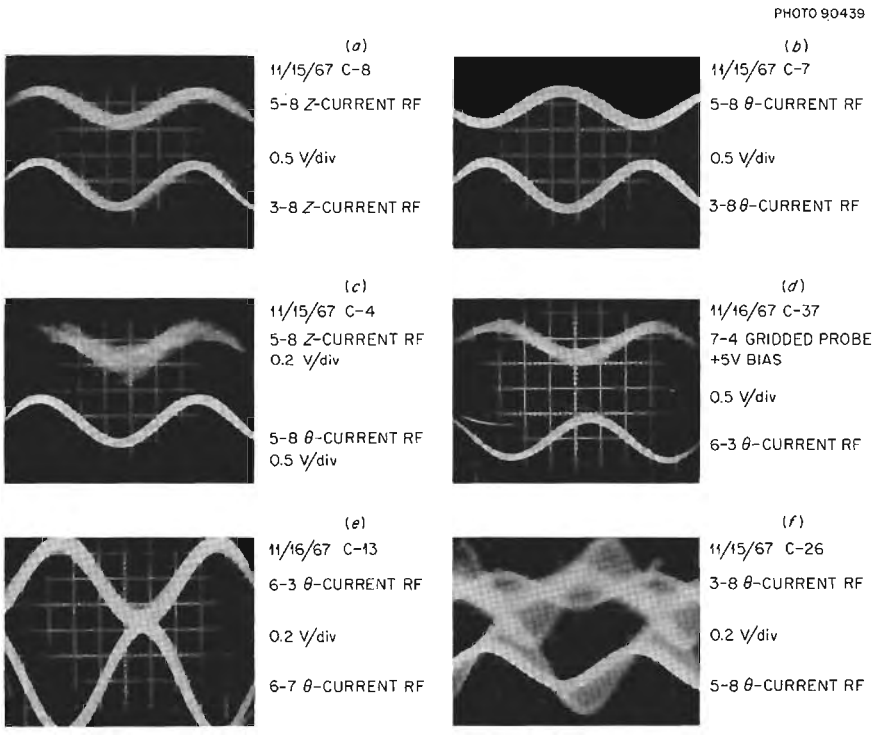

Fig. 3.3. Correlation Properties of the Instability RF at the Proton Cyclotron Fundamental Obtained with Hydrogen Arc Dissociation. The time scale for all pictures is 0.01 μsec/division. Figure 2.1 in ORNL-3472 is a key to port locations; 3-8 means ring 3 position 8, etc. Ring 4 is in the midplane.

fundamental shown in Figs. 3.4*a* and *b*. In these plots of instability amplitude and phase vs axial distance from the midplane, the beam injector is located at −107 cm, and the axial boundaries of the dominant central peak plasma and the weaker side lobe plasma are located at about ±69 and ±117 cm respectively. The θ-current rf signals are most likely from ion clump rotation, while the z-current rf signals are undoubtedly from axially moving electrons. Figure 3.4*a* shows the variation of the z-current and θ-current phase along the machine, referenced to the z-current signal at +69 cm. Positive phase indicates that the signal leads the reference z-current signal at +69 cm, and negative phase indicates that it lags the reference signal. Figure 3.4*b* shows the variation along the machine of the z-current and θ-current signal amplitude. The z-current rf along the machine is well correlated with the reference z-current rf at +69 cm except at the midplane, where the correlated component of the z-current rf is smaller and shows a phase difference of $\sim\pi/2$. The θ-current rf is also well correlated along the machine except near the midplane, where the signal component correlated with the large-amplitude θ-current trigger signal at +69 cm goes through a null and shows a phase shift similar to that found in the z-current rf.

The θ-current rf is approximately out of phase (as defined above) with the z-current rf in the injector end of the plasma and in phase in the other half of the plasma, except for large phase differences observed on the end probes, beyond the axial boundary of the central peak plasma. The relative phase of the current signals thus corresponds to electrons moving along flux lines away from a deficiency of energetic ions (out-of-phase currents) in one half of the machine toward an excess of energetic ions (in-phase currents) in the other half. Inside the energetic proton

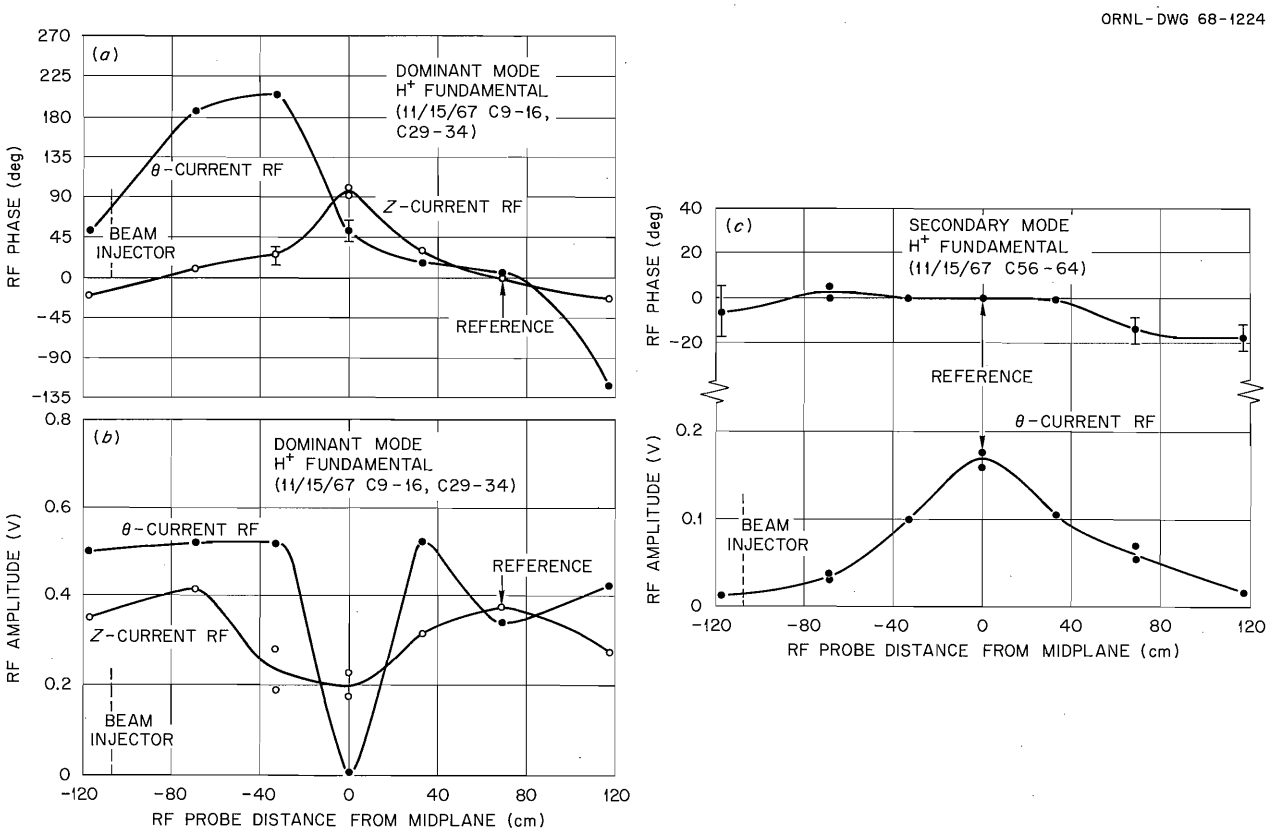

Fig. 3.4. Hydrogen Arc Dissociation. Mode pattern of the instability signals at the proton cyclotron fundamental showing the variation along the machine of (*a*) the relative phase, (*b*) the amplitude of the Z-current rf and the θ-current rf of the dominant instability mode, and (c) the relative phase and amplitude of the θ-current rf signals of the secondary instability mode.

plasma (between −69 cm and +69 cm) the relative phase of the z-current and θ-current rf signals (either in phase or 180° out of phase) indicates the presence of standing waves and hence reflections at the end of the energetic plasma region. The phase shift on the end probes suggests that waves are traveling out of the energetic plasma region and into the cold plasma bounding the energetic proton plasma on both ends. Instability rf signals are seen on magnetic probes 48, 69, and 208 cm beyond the central peak plasma boundary at ±69 cm that are time correlated with the instability rf signals in the energetic plasma interior. The outermost probe above is outside the main 3.3-to-1 mirror.

The z-current and θ-current rf signals are well correlated with each other and well correlated azimuthally around the machine, again indicating that the instability probably involves the plasma as a whole, rather than consisting of small disturbances azimuthally localized near the probes. The existence of a time correlation between z-current rf and θ-current rf, together with the relative phase between these signals having the expected values, and their correlation with axial electron currents indicate that this is a Harris instability.

The anomalous behavior near the midplane of the dominant instability at the proton fundamental may be due to the presence of a secondary mode at the proton fundamental. Evidence for this additional mode is seen in Fig. 3.3*f*. This figure shows θ-current rf signals on opposite sides of the midplane, similar to those in Fig. 3.3*b*, but taken at a lower triggering level of the bottom signal. In addition to the large-amplitude out-of-phase signals in the upper trace, corresponding to that seen in Fig. 3.3*b*, there is a smaller in-phase component. Since this component of the θ-current rf is in phase on opposite sides of the midplane, it does not go through a null, whereas the larger-amplitude component does. Thus the secondary, smaller-amplitude instability can be studied by correlating the different rf signals against it at the midplane, where it dominates over the main instability mode. The results of such a study are given in Fig. 3.4c, which shows the variation along the machine of the phase and amplitude of the secondary instability at the proton fundamental. These θ-current rf signals are approximately in phase along the machine, with the maximum amplitude signals at the midplane about a third that of the main instability mode amplitude. The θ-current signal amplitude slowly decreases, and the correlation becomes poorer with increasing distance from the midplane. These θ-current signals are uncorrelated with z-current signals along the machine, uncorrelated with θ-current signals around the machine (except for some correlation on probes displaced azimuthally by 45°), and uncorrelated with electron current signals to a gridded probe located axially beyond the energetic plasma boundary. The lack of correlation around the machine indicates that this disturbance is localized in azimuth, unlike the dominant instability at the proton fundamental. The lack of observed correlation with z-current rf or electron currents is surprising, since axial electron currents are expected to be associated with any ion clump rotation because of the finite length of the plasma.

3.2.3 Second- and Third-Harmonic Mode Patterns

The correlation properties of the instability rf at the second harmonic of the proton cyclotron frequency were studied with hydrogen arc dissociation using a 25- to 45-MHz band-pass filter to isolate the sharp second harmonic line at 34.7 MHz. Some of the results obtained are shown in Fig. 3.5. Figures 3.5*a* and *b* show that the θ-current rf signals at the second harmonic are in phase on opposite sides of the midplane, while the z-current rf signals are 180° out of phase across the midplane, the reverse of that found at the proton fundamental. Figure 3.5c shows that the z-current rf and the θ-current rf are not as well correlated as the corresponding signals at the proton fundamental. Figure 3.5*d* shows that the z-current rf and the electron current to a gridded probe located axially beyond the energetic plasma boundary are time correlated. As in the case of the main instability at the proton fundamental, a negative bias eliminates these signals, so that they are really instability-driven electron currents. Figure 3.5e shows that θ-current rf signals on probes at the midplane but azimuthally on opposite sides of the machine are only weakly correlated.

The axial mode pattern of the dominant instability at the second harmonic is summarized in Fig. 3.6. Figure 3.6*a* shows the variation of the z-current and θ-current phase along the machine, referenced

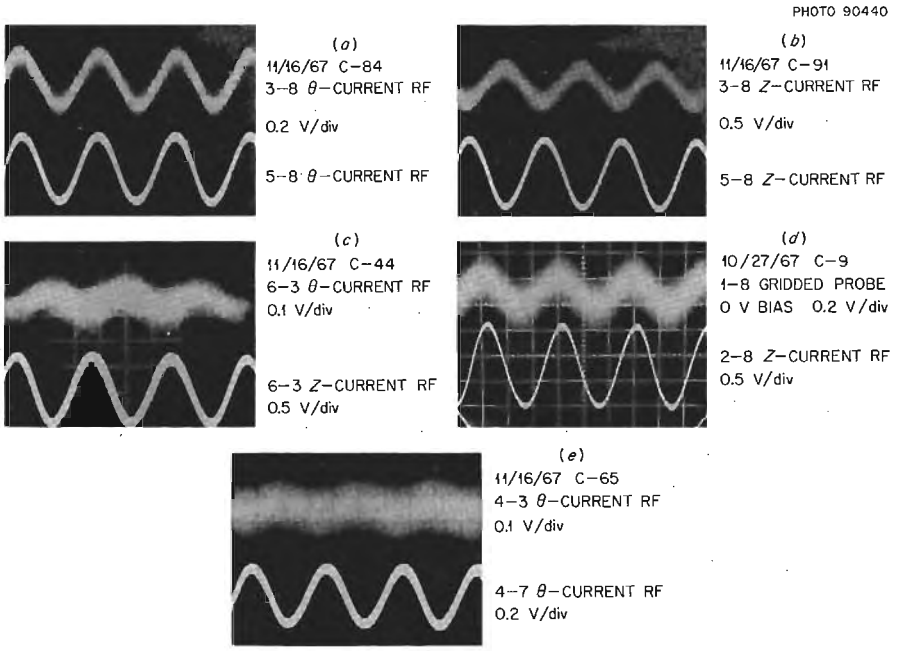

Fig. 3.5. Correlation Properties of the Instability RF at the Proton Second Harmonic Obtained with Hydrogen Arc Dissociation. The time scale for all pictures is 0.01 μsec/division.

to the z-current signal at +33 cm, while Fig. 3.6*b* shows the axial variation of the amplitude of the z-current and θ-current rf. The θ-current rf is approximately in phase along the length of the machine and is well correlated with a reference θ-current signal at +33 cm. The correlation becomes poorer for the end probes (at ±117 cm from the midplane, beyond the axial boundary of the central peak plasma), although the signals are still in phase with the other θ-current rf signals. The z-current rf signals also show a worsening of correlation on the end probes as well as a phase shift from that found in the central peak plasma region. The z-current and θ-current rf signals at the second harmonic are not as well correlated with each other as are the signals at the proton fundamental, but the relative phase of these signals is such that electron current flows along flux lines toward regions of energetic ion excess. Again the approximate in-phase or 180° out-of-phase relationship between the z-current and θ-current rf signals in the central peak plasma region indicates standing waves (and hence reflections at the energetic plasma boundary), while the phase shifts beyond −69 and +33 cm suggest waves traveling out of the energetic plasma region. Indeed, these waves are observed in the cold plasma both inside and outside the main 3.3-to-1 mirror.

The z-current and θ-current rf signals are not as well correlated azimuthally around the machine as are the signals at the proton fundamental; so the main second-harmonic instability probably consists of relatively localized disturbances rather than an instability involving the whole plasma. However, the presence of correlation between z-current rf and θ-current rf signals, together with the expected phase relation between these signals, and their correlation with axial electron currents indicate that these disturbances are also Harris instabilities.

The axial symmetry of the z-current and θ-current rf signals at the second harmonic is just the reverse of that found for the main instability at the proton fundamental. Since these axial mode patterns are quite different, the second-harmonic instability must be a separate instability and not just a nonlinear result of the fundamental.

As in the case of the instability at the proton fundamental, there is a weaker, secondary instability at the second harmonic. When this secondary instability is most prominent, the dip in the θ-

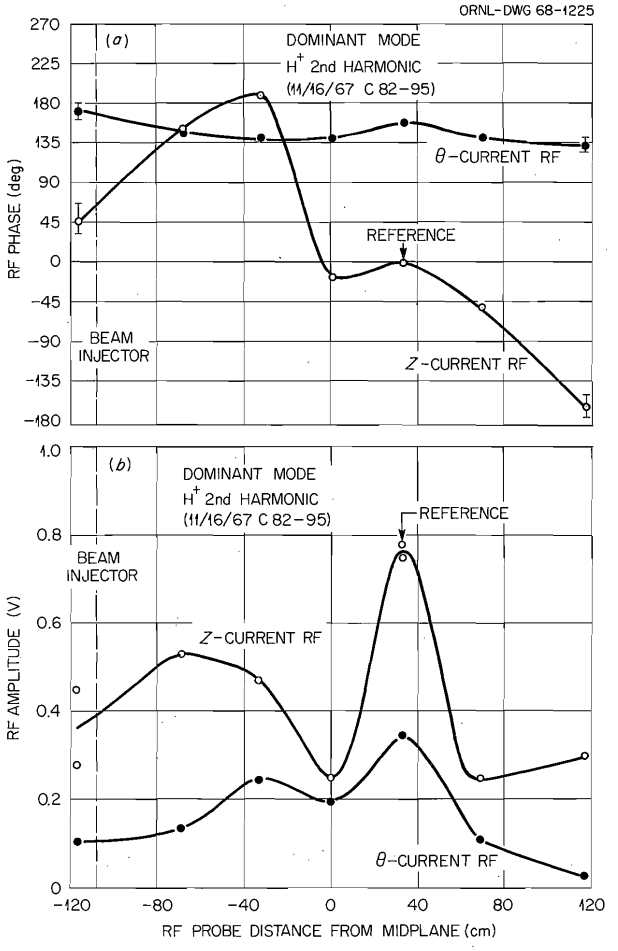

Fig. 3.6. Hydrogen Arc Dissociation. Mode pattern of the instability signals at the proton second harmonic showing the variation along the machine of (*a*) the relative phase and (*b*) the amplitude of the Z-current rf and the θ-current rf of the dominant instability mode.

current rf amplitude and the magnitude of the correlated z-current signal at the midplane are smaller; so that the θ-current rf is peaked at the center, and the correlated component of the z-current rf goes through a null at the midplane. As with the secondary instability at the proton fundamental, this instability was studied by correlating the different rf signals against it at the midplane, where it dominates over the main instability mode at the second harmonic. This mode seems to be localized in the injector end of the plasma. The z-current and θ-current rf signals increase in amplitude and the correlation improves toward the beam injector. The phase of the correlated z-current and θ-current rf signals does not change significantly across the midplane. The z-current and θ-current signals of the secondary mode are better correlated than those of the primary instability at the second harmonic, and appear to be approximately 180° out of phase with each other. The relative phase of the z-current and θ-current rf signals is again indicative of a Harris mode, though localized near the injector. The correlation properties of this secondary mode azimuthally around the machine are unknown; so it is not known whether this mode is localized or extends over the cross section of the plasma.

The correlation properties of the instability rf at the third harmonic of the proton cyclotron frequency have also been studied, although in not as much detail as the instabilities at the fundamental and second harmonic, by examining unfiltered signals from the magnetic-loop probes. An incomplete axial mode pattern for the main instability at the third harmonic is shown in Fig. 3.7. The amplitude and relative phase of the instability rf are plotted vs distance from the machine midplane. The θ-current rf is symmetric (in phase) about the midplane, while the z-current rf is antisymmetric (out of phase), similar to the axial mode pattern found

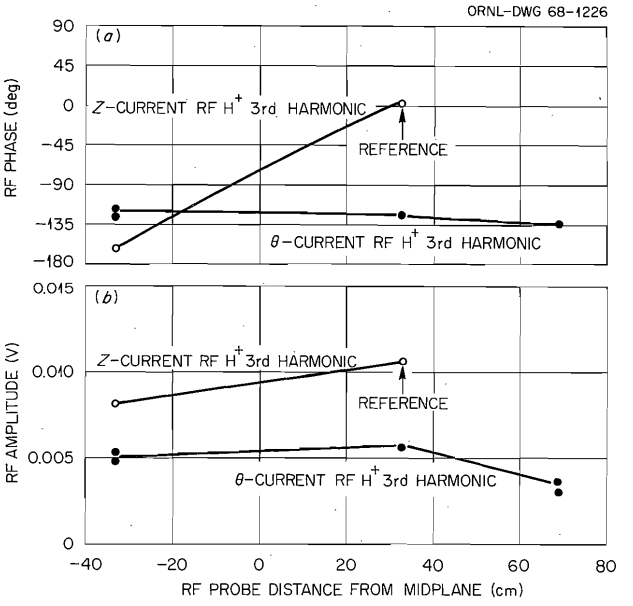

Fig. 3.7. Hydrogen Arc Dissociation. Incomplete mode pattern of the instability signals at the proton third harmonic showing the variation along the machine of (*a*) the relative phase and (*b*) the amplitude of the Z-current rf and the θ-current rf.

for the main second-harmonic instability. The z-current and θ-current rf signals are well correlated axially along the machine, well correlated with each other, and well correlated azimuthally around the machine. The correlation and relative phase of the z-current and θ-current rf signals suggest that this is a Harris instability of sizable extent, similar to the instability at the proton fundamental but having the opposite axial mode pattern. The question of whether a secondary mode also exists at the third harmonic has not yet been investigated. Instability modes above the third harmonic have not been studied; so nothing can be said of their mode structure or of their relationship to instabilities at the lower cyclotron harmonics.

3.2.4 Relationship Between Different Harmonic Modes

The instability modes at the first three harmonics of the proton cyclotron frequency have been described in some detail. Figure 3.8 gives some indication of the relationship that exists between modes at different harmonics of the proton cyclotron frequency. Figure 3.8*a* shows that some correlation exists between the filtered components at the proton fundamental and second harmonic of a z-current rf signal. Using unfiltered signals and an intermediate triggering level of the bottom trace, the type of trace shown in Fig. 3.8*b* is obtained. The fixed phase relationship between the fundamental and third harmonic signals indicates coupling between these modes. Using unfiltered signals and triggering only on the largest amplitude signals gives only the proton fundamental with no third harmonic present. The mode pattern obtained agrees with the dominant instability mode pattern found at the proton fundamental, using filtered signals. Figures 3.8*a* and *b* and other correlation pictures show that rf signals at different harmonics are at least sometimes correlated, although probably not for most of the beam-on time. However, no thorough study of the relationship of the different modes at the different proton cyclotron harmonics has as yet been undertaken.

The time relationship of different modes at the same harmonic is shown in Fig. 3.9. These

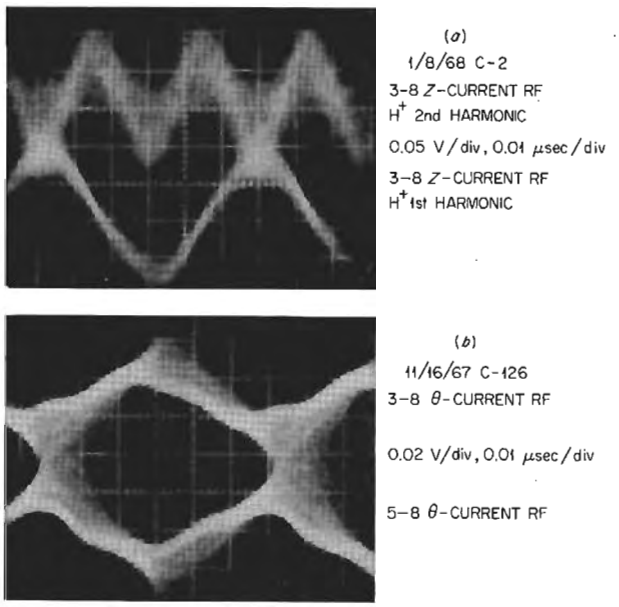

Fig. 3.8. Hydrogen Arc Dissociation. (*a*) Correlation between the proton fundamental and second harmonic components of a Z-current rf signal at ring 3, position 8, and (*b*) correlation between unfiltered θ-current signals on opposite sides of the machine midplane ($Z = \pm 33$ cm).

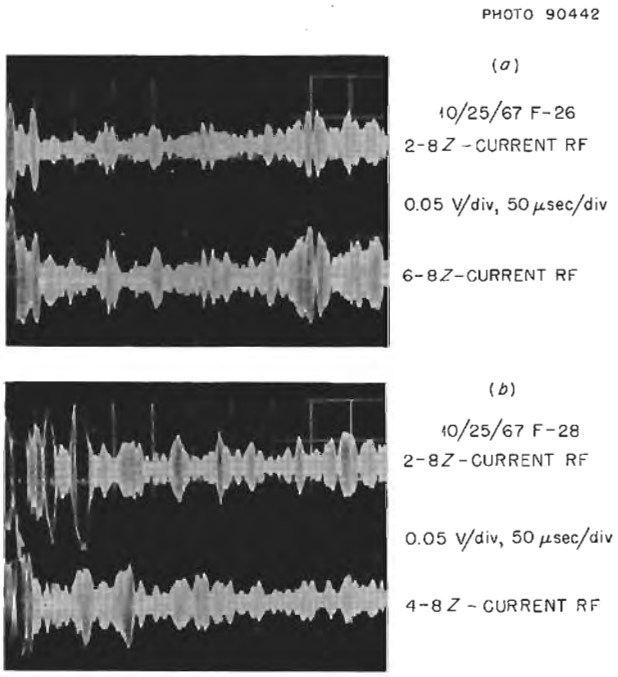

Fig. 3.9. Hydrogen Arc Dissociation. Long-time correlation between second harmonic Z-current rf signals of (*a*) the dominant instability mode on opposite sides of the machine midplane ($Z = \pm 69$ cm) and (*b*) the dominant instability mode at $Z = -69$ cm (top trace) vs the secondary instability mode at $Z = 0$.

pictures show second-harmonic filtered z-current rf signals on a long time scale, 5000 times longer than the other pictures. Many rf bursts of varying duration are seen with no appreciable gaps in the rf emission. Figure 3.9*a* shows second-harmonic z-current signals on probes 69 cm on opposite sides of the midplane. The same bursts are seen in both traces, reflecting the good correlation between these signals found on a short time scale. Figure 3.9*b* shows one of these signals compared against its counterpart at the machine midplane. The top trace, taken 69 cm from the midplane, shows the main instability mode at the second harmonic, while the lower trace, taken at the midplane, shows the secondary mode which dominates only at the midplane. It can be seen that these two modes can occur at the same time but are more or less independent, reflecting the lack of correlation seen on a short time scale.

3.2.5 Gas Dissociation Mode Patterns

The beam-on instability modes described thus far were obtained with energetic plasmas produced by hydrogen arc dissociation of the injected beam. Instability mode studies were also conducted using plasmas produced by hydrogen gas dissociation, although in not as much detail, and a more complicated correlation behavior was found. With hydrogen gas dissociation, there is a transition pressure[7] ($\sim 3 \times 10^{-6}$ torr) below which the proton pitch angle distribution is characterized by a dominant central peak and weak side lobes, as is always found with arc dissociation. Above the transition pressure the central peak vanishes, and the side lobes increase in density. The pitch angle distribution remains in this side-lobe dominant regime as the pressure is further increased. Although the total trapped density and background pressure do not change significantly during the transition from a dominant central peak plasma to a dominant side-lobe plasma, the rf spectrum does reflect this change. Below the transition pressure the rf spectrum is characterized by a strong proton fundamental and weaker higher harmonics. Above the transition pressure the proton fundamental is weak or absent, and the even proton harmonics dominate the spectrum. This behavior can be seen in Fig. 3.10, which shows the θ-current correlation between two probes at the midplane that are separated azimuthally by 45°. Figures 3.10*a*, *b*, and c show the azimuthal correlation below, at, and above the transition pressure respectively. Both the proton fundamental and the second harmonic are present in Fig. 3.10*b* but not at the same time, since the two harmonics do not add. As the pressure falls during the beam-on time (plasma pumping) the transition occurs; so both modes appear during the relatively long exposure time, a significant fraction of a beam-on pulse.

[7] *Thermonuclear Div. Semiann. Progr. Rept. Apr. 30, 1966*, ORNL-3989, p. 19.

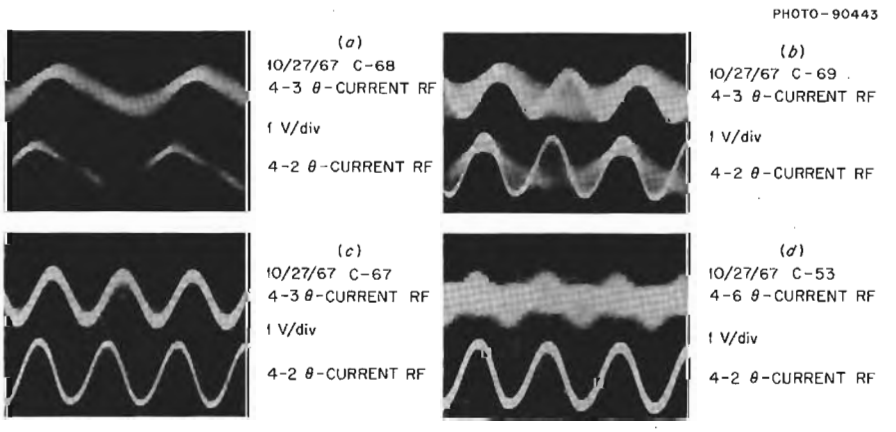

Fig. 3.10. Correlation Obtained with Hydrogen Gas Dissociation Between Unfiltered θ-Current RF Signals on Probes at the Midplane Separated Azimuthally by 45° (*a*) Below, (*b*) At, and (c) Above the Pressure at Which the Central Peak Disappears. (*d*) 180° Change in Correlation Between Two θ-Current rf Signals Separated Azimuthally by 180° Resulting from a Pressure Change. The time scale for all pictures is 0.01 μsec/division.

The azimuthal mode pattern of the instabilities at the proton fundamental (below the transition pressure) and second harmonic (above the transition pressure) has been established from azimuthal correlation pictures similar to those of Fig. 3.10, and the results are shown in Fig. 3.11*a*. The phase of the instability varies approximately linearly with azimuthal angle of probe separation, with a slope $l = 1$ for the proton fundamental and a slope $l = 2$ for the second harmonic, corresponding to the phase front $\omega t - l\theta$ = constant. This indicates that these instabilities are large disturbances approximately centered in the plasma. With arc dissociation the azimuthal mode pattern is more complicated. For comparison, the proton fundamental *z*-current azimuthal mode pattern obtained with arc dissociation and with an energetic proton plasma having a factor of 10 higher density is also shown in this figure. This mode pattern probably results from several instability cells being phase correlated and occurring at the same time.

In most other respects the instability mode patterns obtained with hydrogen gas dissociation are more complicated than those obtained with hydrogen arc dissociation. The azimuthal mode patterns shown in Fig. 3.11*a* were obtained in the central peak regime far below the transition pressure and in the side-lobe regime just above the transition pressure. At other pressures the phase change is no longer proportional to the angular separation of the probes. In addition, the phase varies during the beam-on time as the pressure changes during a beam pulse. This type of behavior can be seen in Fig. 3.10*d*, which shows the correlation between two θ-current signals on

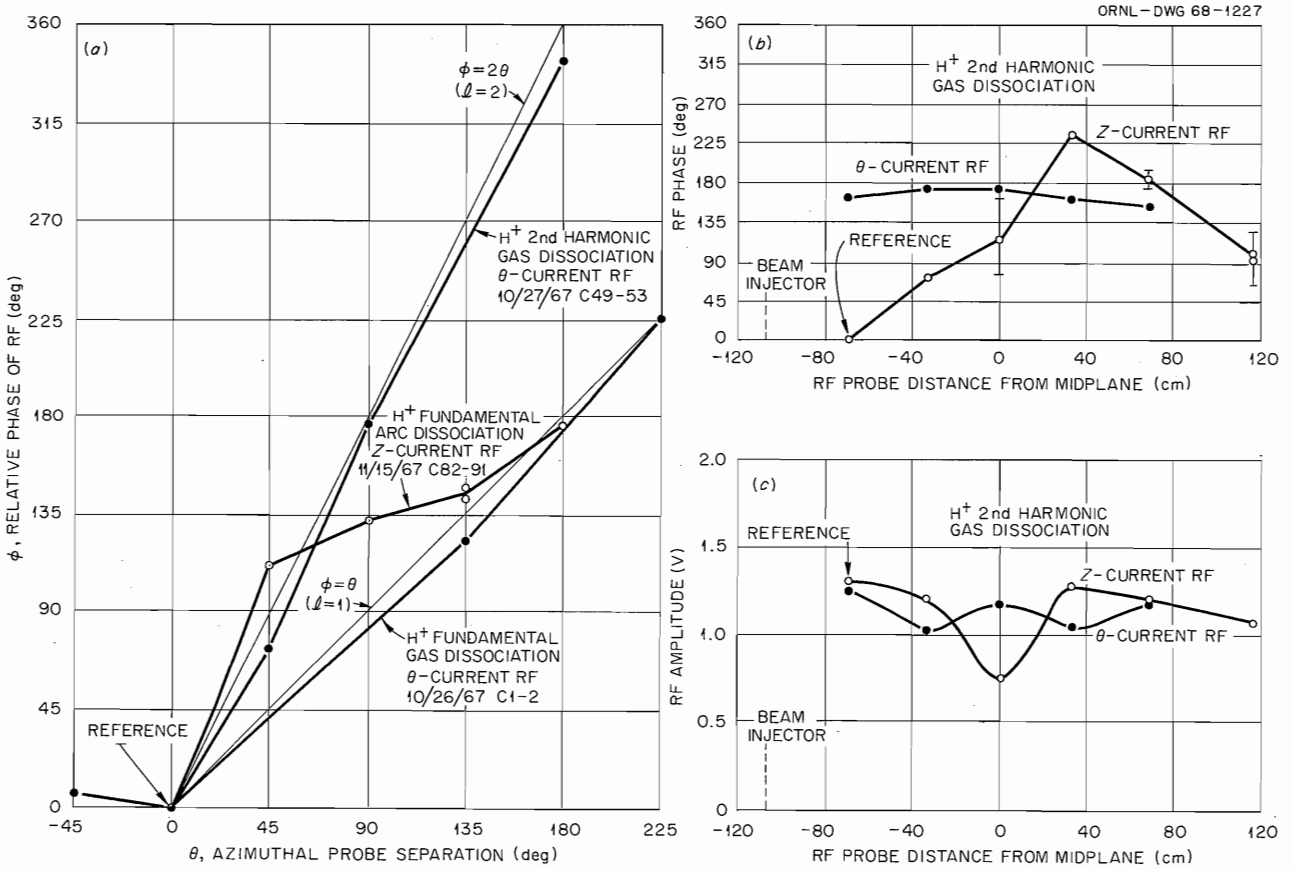

Fig. 3.11. (*a*) Azimuthal Mode Patterns at the Proton Fundamental and Second Harmonic Obtained with Gas Dissociation. (*b* and *c*) Axial Mode Pattern of the Instability Signals at the Second Harmonic Obtained with Gas Dissociation Showing the Variation Along the Machine of (*b*) the Relative Phase and (*c*) the Amplitude of the *z*-Current RF and the θ-Current RF.

opposite sides of the machine (180° apart in azimuth) near the beginning of the beam-on pulse. As the pressure changes from its beam-off value of 4.5×10^{-6} torr toward its equilibrium beam-on value of 3.5×10^{-6} torr, the correlation changes from 180° out of phase to exactly in phase, a significant change in the azimuthal mode pattern.

The axial mode pattern for the instability at the second harmonic with gas dissociation is shown in Figs. 3.11*b* and c. The axial variation of the instability phase along the machine in Fig. 3.11*b* and its amplitude in Fig. 3.11c are referenced to the *z*-current signal at −69 cm. The θ-current rf signals are very well correlated along the machine and are approximately in phase with the reference θ-current signal at −69 cm. This phase relationship between two axially displaced θ-current signals does not seem to change as the pressure changes during the beam-on time. The *z*-current rf signals are not as well correlated along the machine as the θ-current rf signals, as is indicated by the error brackets on the *z*-current phase which show the amount of relative phase shift during the beam-on time. This shift in phase is largest at the midplane, where the correlated component of the *z*-current rf has a minimum, and at the last probe position, near the axial boundary of the side-lobe dominant plasma. There is good correlation between the *z*-current and θ-current rf signals, and these signals are in phase at +69 cm and 180° out of phase at −69 cm, as might be expected for a Harris mode. The ±90° phase difference at other axial positions is not understood. Correlation measurements with the electron current signals to a gridded probe have not been made. The second-harmonic mode is not a small localized disturbance and probably involves the bulk of the plasma, but an exact mode identification has not yet been made.

Very little is known about the instability at the proton fundamental other than that it also is not a localized disturbance near the probes. Its *z*-current and θ-current rf signals are correlated and in phase at the midplane, but their axial mode pattern has not been established. When this instability is strongest (in the central peak dominant regime just below the transition pressure), a much weaker second harmonic is also present. The top trace in Fig. 3.12 shows the proton fundamental component, and the bottom trace shows the second harmonic component of a *z*-current rf signal observed beyond the axial boundary of the energetic proton plasma.

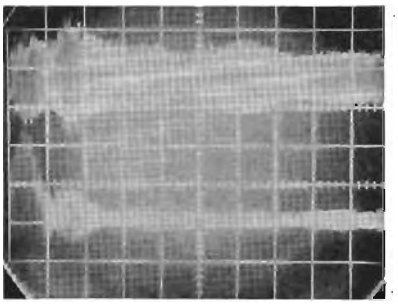

Fig. 3.12. Long-Time Correlation Between the Proton Fundamental (Top Trace) and Second Harmonic Components of a *Z*-Current RF Signal Obtained with Gas Dissociation.

This figure demonstrates the independence of these harmonics on a long time scale (0.2 msec full scale).

In summary, the axial and azimuthal mode patterns of the instabilities at the first few harmonics of the proton cyclotron frequency have been established during the beam-on time with energetic proton plasmas produced by hydrogen gas dissociation and hydrogen arc dissociation of the injected beam. The presence of correlation between *z*-current and θ-current rf signals, together with the expected phase relationship between these signals, and their correlation with axial electron currents indicate that most of these instabilities are Harris-like modes. Some of these instabilities seem to consist of uncorrelated, localized disturbances, while others probably consist of a single centralized disturbance. The axial mode patterns of these instabilities are not the same at the different harmonics, in general being either symmetric or antisymmetric about the machine midplane. These modes appear to be standing waves inside the plasma region, implying reflections at the energetic plasma boundary, and traveling waves outside in the cold-plasma end regions. While the different harmonic modes may sometimes be correlated on a short time scale, they are generally not correlated on a long time scale. This independence and the occurrence of different axial mode patterns show that the higher harmonics are not just nonlinear, large-amplitude results of the instability at the proton fundamental but are really separate instabilities.

3.3 BEAM-OFF PLASMA INSTABILITY STUDIES WITH HYDROGEN ARC DISSOCIATION

Some work has also been done during this report period on the instabilities occurring in the energetic proton plasma during the afterglow period following beam turnoff. Previous experiments had shown that the highly anisotropic, energetic central peak plasma formed as the result of a strong micro-instability is itself unstable[8] with hydrogen arc dissociation in the absence of the H_2^+ beam that maintains it, but is stable[9] at the lower energetic plasma densities obtained with gas dissociation. At the highest densities ($\sim 5 \times 10^9$ ions/cm^3) obtained with hydrogen arc dissociation, there was generally a period of fairly continuous rf emission (bursts) lasting up to 0.1 sec after beam turnoff, followed by short-duration, widely separated rf bursts that persisted up to 2 sec after beam turnoff. These later rf bursts were correlated with axial expulsion of ions with energies up to a few hundred electron volts and a small increase in the radial charge-exchange loss of energetic protons due to energy spreading.

During this report period an operating regime has been found in which the phenomena described above still occur. There are, however, some important differences in the new regime. The rf bursts had previously been found to consist primarily of the proton fundamental with progressively smaller amounts of the higher harmonics present. The new regime gave the beam-on and beam-off rf spectra obtained at the machine midplane with magnetic probes in both the θ-current and z-current orientations that are compared in Fig. 3.13. Here only the even harmonics of the proton cyclotron frequency are evident after beam turnoff (except for a small third-harmonic peak in the θ-current rf signal), in contrast to the presence of all the harmonics during the beam-on time. The peaks at the fourth and sixth proton harmonics seen in the beam-off rf spectrum may not be real instability signals. If disturbances at the fourth and sixth harmonics were really unstable, then disturbances at the third and fifth harmonics should also be unstable, but no instability signals are seen at these frequencies. The signals at the

[8] *Thermonuclear Div. Semiann. Progr. Rept. Oct. 31, 1966*, ORNL-4063, p. 12.

[9] P. R. Bell *et al.*, *Phys. Rev. Letters* **16**, 1152 (1966); *Thermonuclear Div. Semiann. Progr. Rept. Apr. 30, 1966*, ORNL-3989, p. 15.

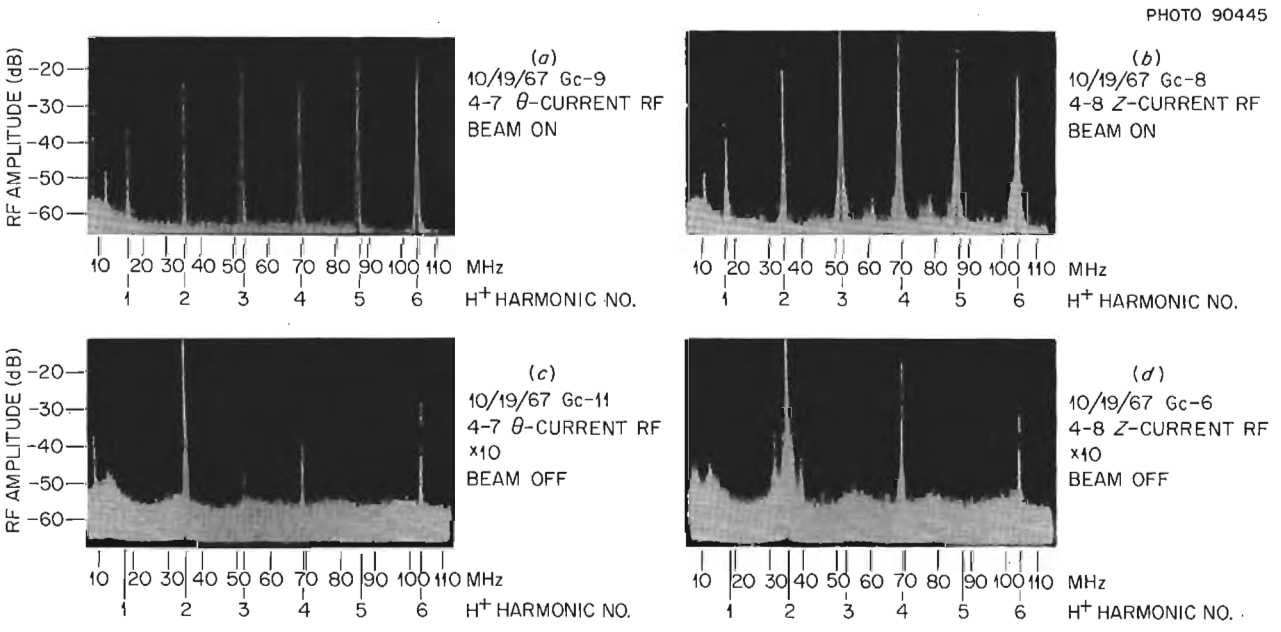

Fig. 3.13. RF Spectra Obtained at the Machine Midplane with Hydrogen Arc Dissociation. (*a*) Beam-on θ-current rf signal, (*b*) beam-on z-current rf signal, (*c*) beam-off θ-current rf signal, (*d*) beam-off z-current rf signal. The first six proton cyclotron harmonics are numbered.

second, fourth, and sixth proton harmonics are correlated with the bursts occurring after beam turnoff, whereas the very much weaker first, third, and fifth proton harmonic signals are not correlated with these bursts. The absence or weak occurrence of the proton fundamental is surprising if the beam-off instability is a Harris instability like the beam-on instability, since the electrons are not hot enough even during the beam-on time to completely damp the proton fundamental. The presence of a strong second harmonic and no proton fundamental suggests the possibility of a flutelike ion-ion mode.[10] It is interesting that the beam-off θ-current rf signals in Fig. 3.13c (most likely from ion clump rotation) do not show the Doppler shifted peaks produced by the streaming side-lobe plasma that are present in the z-current rf (from axial electron currents) during both the beam-on time (Fig. 3.2c) and the beam-off time (Fig. 3.13*d*).

The beam-on rf spectra and the beam-off rf burst spectra seen in Fig. 3.13 differ considerably. Examples of other aspects of the beam-off rf behavior that are also quite different from that observed during the beam-on time are shown in Fig. 3.14. Figure 3.14*a* shows the axial correlation between two θ-current rf signals, at the machine midplane and 33 cm from the midplane. The bright beam-on signals are in phase, while the faint beam-off signals are larger in amplitude and 180° out of phase. A similar increase in amplitude can be seen in Fig. 3.14*b*, which shows z-current and θ-current rf signals at the proton fundamental obtained with gas dissociation but with most of the energetic proton plasma suppressed by the insertion of obstacles. The sudden increase in the z-current rf signal at the time of beam turnoff again indicates a significant change in the instability behavior after removal of the injected beam. It may be that the more-or-less continuous rf period following beam turnoff is not just a continuation of the beam-on plasma instability behavior, but instead reflects an entirely different instability behavior. Generally, there is a quiet period immediately following beam turnoff, before the almost continuous period of rf bursts occurs, which supports this assertion. Axial and azimuthal mode patterns for these instability signals have yet to be established.

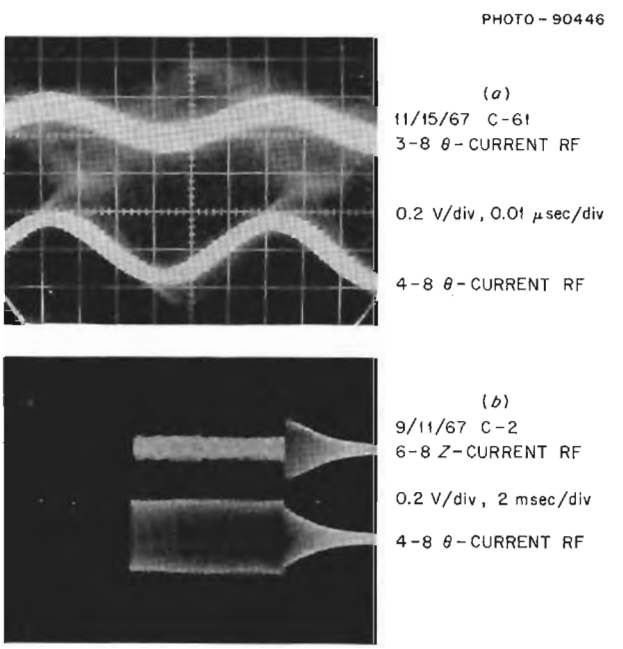

Fig. 3.14. Change in RF Behavior at Beam Turnoff. (*a*) Correlation at the proton fundamental between two θ-current rf signals separated axially by 33 cm during the beam-on time (bright traces) and the beam-off time (faint traces). (*b*) z-current and θ-current rf signals at the proton fundamental on a long time scale near beam turnoff. Only a weak gas-dissociation-produced energetic proton plasma was present.

3.4 ION BEAM MICROINSTABILITY STUDIES

The injected ion beam is unstable as evidenced by the many harmonics of the H_2^+ ion cyclotron frequency that can be seen in the rf spectrum during the beam-on time (see, for example, Fig. 3.2). However, this instability has little effect on the H_2^+ ions, since the beam ions follow single-particle orbits[11] with no noticeable spreading of the beam in space, energy, or pitch angle, except perhaps at low pressure.[12] This instability is nevertheless interesting, since the plasma geometry is controllable and closely fits an existing instability model, that of Burt and

[10] *Thermonuclear Div. Semiann. Progr. Rept. Apr. 30, 1967*, ORNL-4150, p. 19.

[11] *Thermonuclear Div. Semiann. Progr. Rept. Oct. 31, 1966*, ORNL-4063, p. 11.

[12] *Ibid., Apr. 30, 1966*, ORNL-3989, p. 21.

Harris.[13] An additional motivation for studying this instability is that its behavior is representative of the more general class of Harris-type instabilities found to occur in high-energy injection machines. The general features of the ion beam microinstability were discussed in the previous report.[14] We have since studied the effects of finite length and electron temperature on this microinstability and have definitely identified the mode as a Harris-type instability.

The beam geometry is still as shown in Fig. 3.15. To isolate the microinstabilities associated with the injected beam, the down-going beam was stopped on a water-cooled beam target 224 cm from the injector in order to eliminate the counterstreaming returning beam. The small H_3^+ component of the beam and the energetic proton plasma formed by background gas dissociation of the H_2^+ beam were absorbed by obstacles, as shown in Fig. 3.15, leaving a hollow cylindrical shell of H_2^+ ions 26 cm in diameter, 1 cm thick, and 224 cm long.

Burt and Harris analyzed an infinitely long, uniform, hollow beam of energetic ions one Larmor diameter across in a uniform magnetic field with inner and outer beam radii r_1 and r_2. The beam ions are assumed to be neutralized by a cold-electron background and subjected to a perturbation of the form $F(k_r r) \exp [i(\omega t - l\theta -$

[13] P. Burt and E. G. Harris, *Phys. Fluids* 4, 1412 (1961).

[14] *Thermonuclear Div. Semiann. Progr. Rept. Apr. 30, 1967*, ORNL-4150, p. 48.

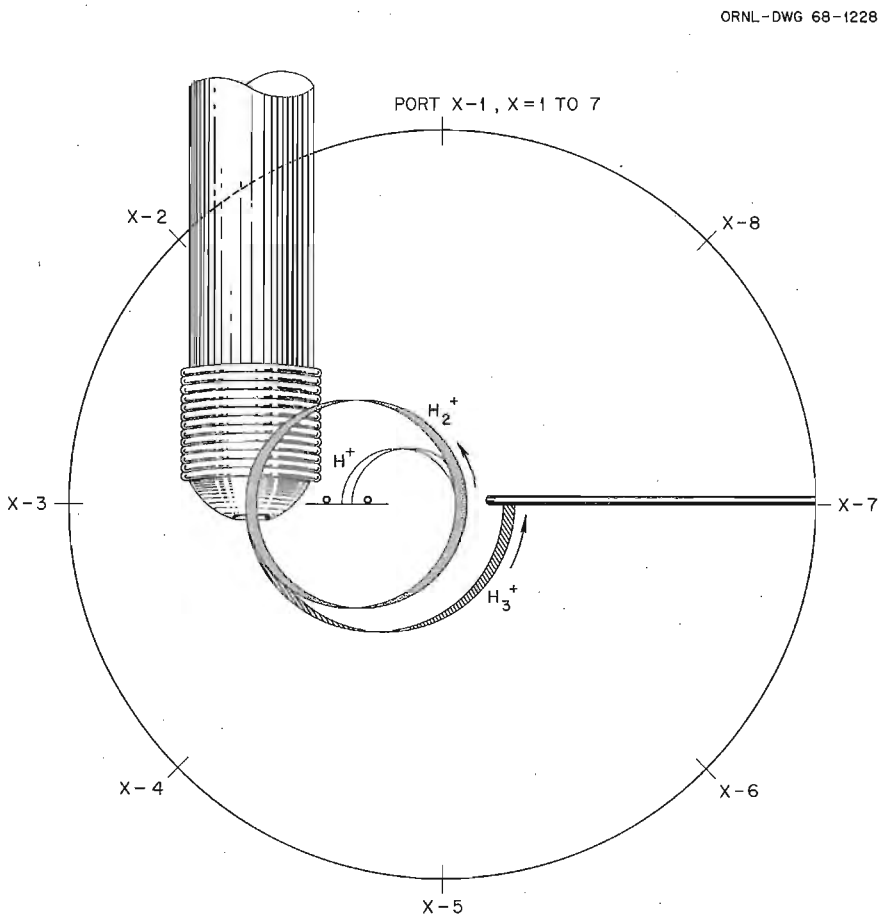

Fig. 3.15. Schematic Cross Section of DCX-2 Showing the Beam Injector and the Beam Targets Used to Intercept the H_3^+ Component of the Injected Beam and the Dissociation Protons from the H_2^+ Beam. The numbering of ring ports is also given.

$k_z z)]$, where l is the azimuthal mode number. The form factor $F(k_r r)$ and the radial wave vector k_r are determined by matching boundary conditions at r_1 and r_2. The nonuniform density of the actual beam has a relatively small effect on the instability predictions in the long-wavelength limit,[15] since the beam thickness is small compared with the radius of the beam cylinder. The axial wave vector k_z is undetermined for an infinitely long plasma, but in practice is set by the length of the plasma.

With a beam perturbation of the form given above, the dispersion relation as given by Harris[16] is

$$\frac{1}{\omega_{pe}^2} = \left(\frac{k_z}{k}\right)^2 \left[\left(\frac{m}{M}\right) \int \frac{f_i(v_z)\, dv_z}{(\omega - l\omega_{ci} - k_z v_z)^2} + \int \frac{f_e(v_z)\, dv_z}{(\omega - k_z v_z)^2}\right] + \left(\frac{k_r}{k}\right)^2 \left[\left(\frac{m}{M}\right) \times \int \frac{f_i(v_z)\, dv_z}{(\omega - l\omega_{ci} - k_z v_z)^2 - \omega_{ci}^2} + \int \frac{f_e(v_z)\, dv_z}{(\omega - k_z v_z)^2 - \omega_{ce}^2}\right], \quad (1)$$

where ω_{pe} is the electron plasma frequency, ω_{ci} and ω_{ce} are the ion and electron cyclotron frequencies, m is the electron mass, M is the ion mass, and k is the total wave vector. For electron densities above the instability threshold, $\omega_{pe} \sim l\omega_{ci}$, unstable oscillations are expected for frequencies near $\omega = l\omega_{ci} + k_z V_z$ caused by unstable coupling between clumping of the ion beam and axial cold-electron plasma oscillations.

Previous study[14] of this ion beam microinstability revealed some of these expected properties. Oscillations at many harmonics of the H_2^+ ion cyclotron frequency were observed. The ionization-produced cold-electron density threshold for occurrence of the first two harmonics, $l = 1$ and 2, agreed with the condition $\omega_{pe} \gtrsim l\omega_{ci}$. The rf signals were also correlated axially along the machine and azimuthally around the machine and showed the expected azimuthal mode pattern. The azimuthal correlation showed that the different rf probes were seeing the same disturbance and not effects local to the probe. On the basis of these measurements the instability was identified as a Harris-type mode.

Much stronger evidence is now available to support this identification. The previous rf measurements were made with an array of radial electric rf probes that detected only charge fluctuations in the plasma. Since the physical basis of a Harris-type instability is an unstable coupling between rotating ion clumps and axial electron current oscillations, the more selective magnetic-loop rf probes have been used during this report period. Figure 3.16 shows part of the rf spectrum obtained with an electric probe, a θ-current magnetic probe, and a z-current magnetic probe. Strong signals are shown for the first four harmonics of the H_2^+ ion cyclotron frequency.[17] The three rf signals are of comparable magnitudes and should be time correlated with each other and with the electron current out of the plasma region if these signals actually represent a Harris instability.

Figure 3.17*a* shows that there is time correlation between θ-current and z-current rf signals at the second H_2^+ harmonic on probes separated axially by 185 cm, nearly the full length of the beam-plasma system. The electric rf signals are also time correlated with these signals. Figure 3.17*b* shows time correlation between an electric rf signal at the machine midplane and the signal on a gridded probe that is located 15 cm axially beyond the beam target and is biased to accept electrons. The spectrum of the gridded probe signals when no bias is applied is shown in Fig. 3.17c. The first and second H_2^+ harmonics are present with no bias. A bias of −50 V stops the second harmonic and a bias of −100 V stops the fundamental. Thus the gridded probe signals are electron currents rather than electric rf signals picked up on the gridded probe. The time correlation between z-current rf, θ-current rf, and

[15] Private communication from Glenn Haste.

[16] E. G. Harris, *The Effect of Finite Ion and Electron Temperatures on the Ion Cyclotron Resonant Instability*, CLM-R32, Culham, 1963.

[17] Note that the harmonics referred to in this section are the harmonics of the H_2^+ ion cyclotron frequency and not of the proton cyclotron frequency referred to in sects. 3.2 and 3.3.

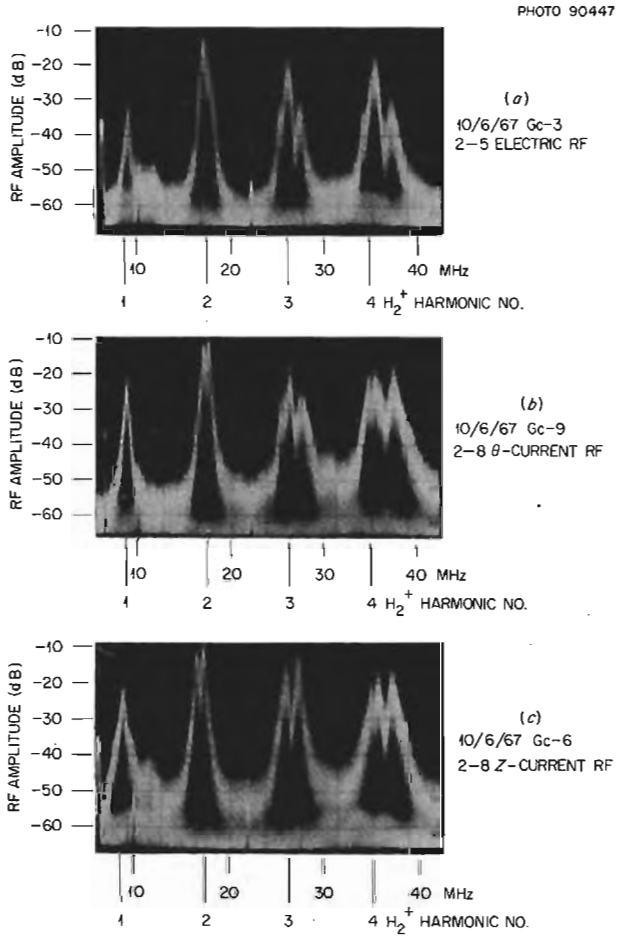

Fig. 3.16. Ion Beam RF Spectra from (*a*) Electric RF Signals, (*b*) θ-Current RF Signals, and (c) Z-Current RF Signals. The first four harmonics of the H_2^+ ion cyclotron frequency are indicated. These molecular peaks can be seen between the stronger proton peaks in Figs. 3.2(*b*) and (c). The sharp peaks at 10 and 22 MHz are frequency markers.

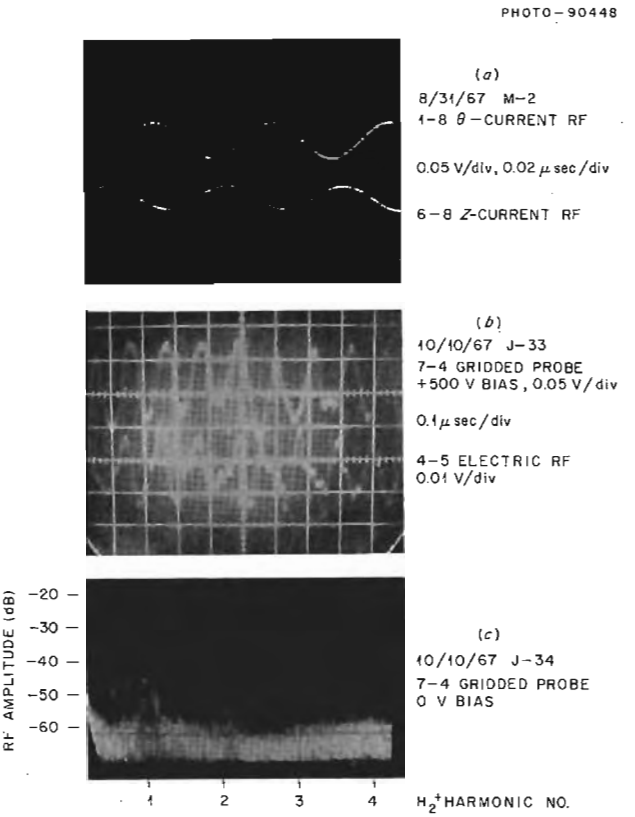

Fig. 3.17. (*a*) Correlation Between Z-Current and θ-Current RF Signals at the H_2^+ Second Harmonic. (*b*) Correlation Between Unfiltered Signals from an Electric RF Probe and a Gridded Probe Biased at +500 V to Accept Electrons and Repel Ions. (c) Spectrum of the Gridded Probe Signals for 0 V Bias.

axial electron current, and the instability thresholds and azimuthal mode structure found previously definitely identify the ion beam instability as a Harris-type mode.

In the previous report[18] the change in the electric rf spectrum along the machine length was interpreted as showing the existence of two unstable waves near each cyclotron harmonic, one a convective instability and the other an absolute instability. These spectra were similar to that in Fig. 3.16*a*. The upper frequency sideband at each cyclotron harmonic increased in strength with distance along the beam, whereas the lower frequency sideband remained relatively constant in amplitude along the beam length. The upper sideband was interpreted as an unstable wave propagating parallel to the axial beam velocity and growing with distance along the beam, that is, a convective instability, while the lower sideband was interpreted as an absolute instability propagating antiparallel to the axial beam velocity. It has since been found that there is generally not one, but several parallel and antiparallel waves near each cyclotron harmonic, and the issue of convective and absolute growth of these instabilities is in doubt. The electric rf signals led to the conclusion of convective and absolute

[18] *Thermonuclear Div. Semiann. Progr. Rept. Apr. 30, 1967*, ORNL-4150, p. 52.

waves, and this was also predicted in some later calculations by Glenn Haste on the Burt-Harris instability. However, the new array of magnetic-loop rf probes does not show this behavior, and the z-current and θ-current rf signals contradict this interpretation. More study is needed to clarify this point.

The existence of more than two waves at a cyclotron harmonic is shown in Fig. 3.18. This figure shows in greater detail a single harmonic peak of the rf spectrum, in this case the second H_2^+ ion cyclotron harmonic. Since we expect frequencies near $l\omega_{ci} + k_z V_z$, where V_z is the axial component of the ion beam velocity, the upper and lower frequency bands are interpreted as corresponding to positive and negative values of the Doppler frequency shift $k_z V_z$. Since the beam goes only one way, V_z has only a positive sign. Thus the upper and lower frequency bands correspond to positive and negative values of k_z, that is, unstable waves propagating parallel and antiparallel to the axial beam velocity. The existence of beats in the rf signals and the beat propagation velocity measurements along and around the machine discussed in the previous report support this picture.

Using the measured value[19] for V_z, we obtain wavelengths from the frequencies of the peaks in the rf spectrum that are in rough agreement with other wavelength measurements. This method has been used for the wavelength determinations for the different modes at each cyclotron harmonic. It has the advantage of being able to separate different modes at the same harmonic, whereas the other measurements give a weighted average over all the modes at a harmonic. There are some difficulties with this measurement, however. The two higher frequency peaks in Fig. 3.18 are clearly separate, while the larger of the lower frequency peaks may be either a single peak or two unresolved peaks that fall near each other. There is also about a 50-kHz measurement uncertainty in the location of these peaks.

[19] *Ibid.*, p. 50.

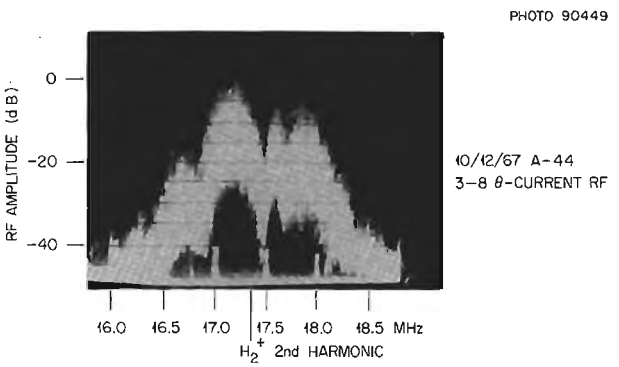

Fig. 3.18. Structure of One of the H_2^+ Ion Cyclotron Lines (Second Harmonic, θ-Current Signal).

Using this method to determine the axial instability wavelengths, the effect of finite length and electron temperature on these wavelengths was studied. The parameters varied in this study were electron density, electron temperature, and magnetic field. The electron density and temperature were changed by changing the background gas pressure. The total beam energy was changed along with the magnetic-field strength so as to keep the injected beam orbit diameter and trajectory constant.

Figure 3.19 shows the structure of the first four H_2^+ cyclotron harmonics taken with a high background pressure of N_2 (high ω_{pe} and low T_e) at half the normal magnetic-field value. As can be seen, the number of different wavelength modes increases with increasing harmonic number l. This can be explained by electron Landau damping of the shorter wavelength (higher k_z) modes. Since the unstable wave phase velocity $v_p = \omega/k_z = l\omega_{ci}/k_z$, the range of undamped k_z increases as l increases. The demonstration of Landau damping of the ion beam Harris instability can be made more quantitative by plotting the measured frequency shifts Δf of the instability peaks against the harmonic number l, as is done in Figs. 3.20 and 3.21. With $\Delta\omega = k_z V_z$, the measured frequency shift $\Delta f = V_z/\lambda_z$, since $\omega = 2\pi f$ and $k_z = 2\pi/\lambda_z$, where λ_z is the axial instability wavelength. In order to compare $1/\lambda_z$ for the half- and full-field cases, the results have been plotted as V_B/λ_z rather than as V_z/λ_z, where $V_B = V_z$ at full field. Since V_z at half field is half that at full field in order to keep the injection geometry unchanged, the vertical axis in Figs. 3.20 and 3.21 represents Δf for the full-field cases and $2\Delta f$ for the half-field cases. The Landau damping criterion is usually given as $v_T/v_p \gtrsim 3$, where $v_T = (kT_e/m)^{1/2}$ is the axial electron thermal velocity. With $v_p = \omega/k_z$ and $\omega \sim l\omega_{ci}$, the Landau damping criterion reduces to

$$\frac{V_B}{\lambda_z} \lesssim \frac{3V_B}{2\pi} m^{1/2} \frac{l\omega_{ci}}{(kT_e)^{1/2}}$$

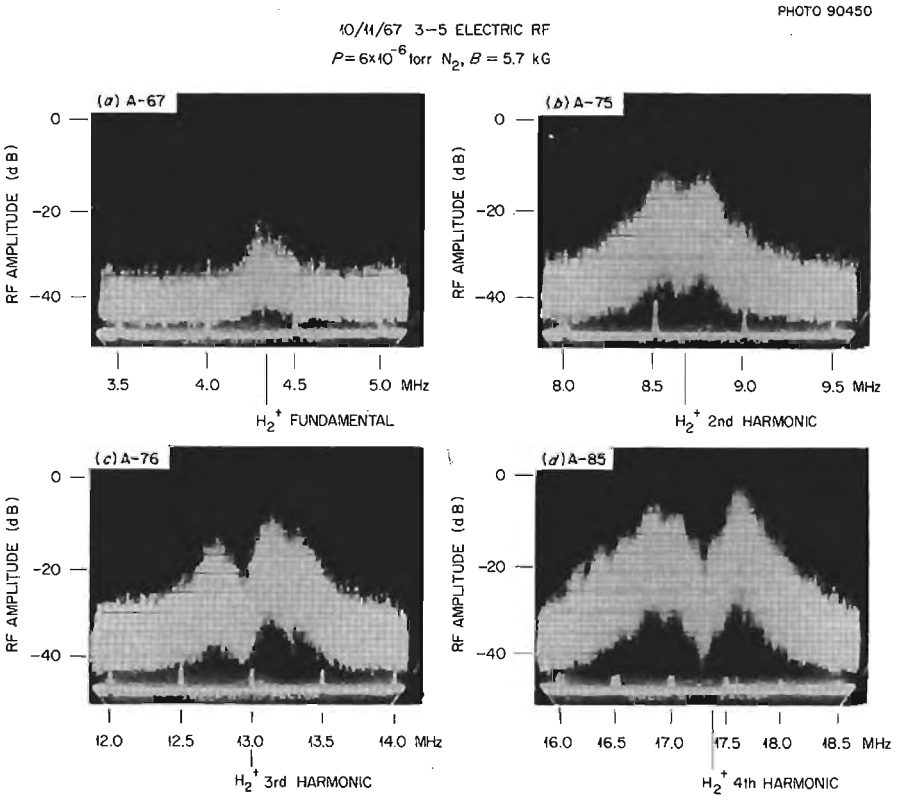

Fig. 3.19. Structure of the First Four H_2^+ Ion Cyclotron Harmonics Observed on an Electric RF Probe at High Pressure and Half Field. The H_2^+ harmonics are indicated.

for a wave to be undamped. Thus undamped longer wavelength modes can exist below the Landau damping lines in Figs. 3.20 and 3.21, while the shorter wavelength modes above this line should be damped.

Figure 3.20 shows the effect of decreasing the electron temperature from 25 eV to 8 eV at the normal full-field setting by raising the background pressure. All modes found for T_e = 25 eV (the circles) fall below the 25-eV Landau damping line. When T_e is decreased to 8 eV, new, shorter wavelength modes (the squares) appear at the molecular fundamental that are not seen at higher electron temperature. Figure 3.21 shows the effect of decreasing the magnetic field to half the normal value at low T_e. Both the half-field modes (the circles) and the additional modes that appear at full field (the squares) lie below their respective Landau damping lines. The fact that shorter-wavelength modes seen at higher harmonic numbers do not appear at the lower harmonics if they fall above the Landau damping line is strong evidence for the Landau damping explanation. Even stronger evidence is the fact that short-wavelength modes that appear at the full-field value do not appear at half field, where they fall above the Landau damping line. The half-field case should be more unstable than the full-field situation, since ω_{ci} is lower and hence ω_{pe}/ω_{ci} is higher for the same value of ω_{pe}; yet there are additional shorter-wavelength modes at full field. Occasionally, modes are seen above the calculated Landau damping line, but these modes are weaker than the modes below this line. The strongest modes are those lying just below the Landau damping line.

The points in Figs. 3.20 and 3.21 show some tendency to cluster about certain values of V_B/λ_z. If the values of V_B/λ_z are averaged over the harmonic number l, a set of nonoverlapping groups of V_B/λ_z values is obtained. If the order of these groups is labeled by an integer m and the

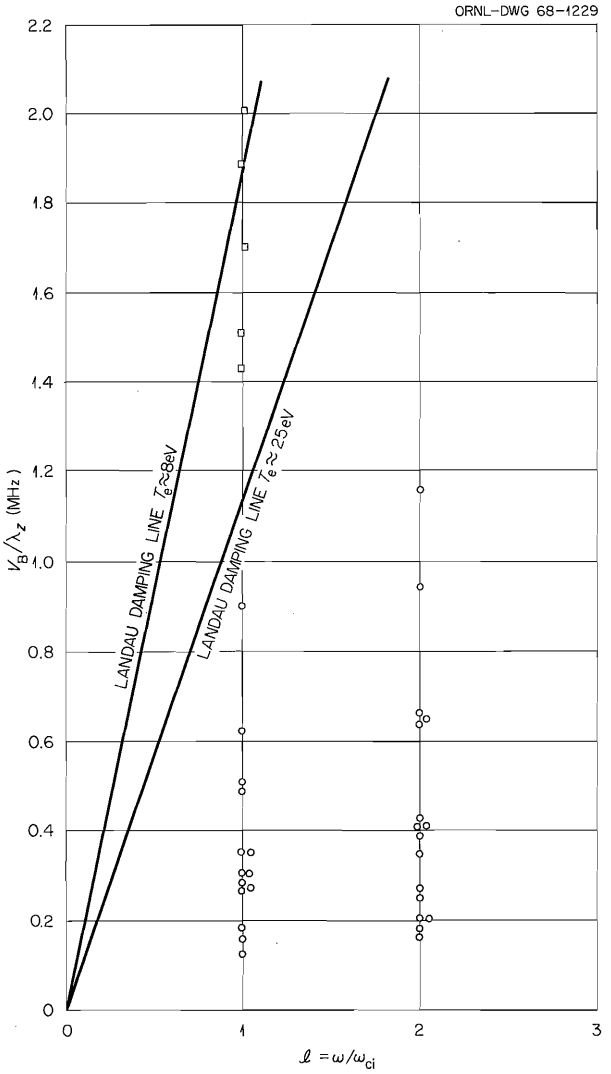

Fig. 3.20. Effect of Decreasing Electron Temperature on the Instability Wavelengths. The circles indicate the modes found for $T_e = 25$ eV, and the squares indicate the additional modes that are found for $T_e = 8$ eV.

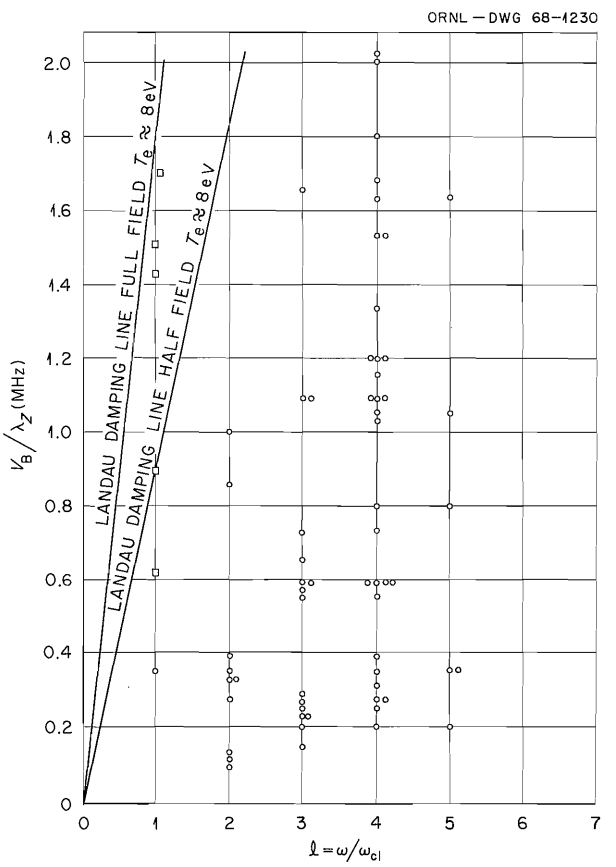

Fig. 3.21. Effect of Decreasing Magnetic Field on the Instability Wavelengths. The circles indicate the modes found for half field, and the squares indicate the additional modes found at full field.

results plotted against m, a plot similar to that of Fig. 3.22 results. The data plotted in this figure were obtained at full field and high T_e from z-current rf spectra. The linear relationship between V_B/λ_z and m indicates that λ_z may be set equal to $2L/m$ or equivalently that the effective plasma length L is an integral multiple of half wavelengths. The value obtained for L is 220 cm, which agrees, perhaps fortuitously, with the 224-cm length of the beam. In this case the instability wavelengths appear to be axial normal modes of the beam cylinder, where m is the mode number. The same procedure for data taken at half field yields overlapping groups of V_B/λ_z values, perhaps due in part to the larger percentage uncertainty in frequency at the lower field value, and no value for L can be obtained.

As mentioned earlier in this section, the ion beam–cold plasma geometry closely fits the instability model of Burt and Harris. In their original calculation[20] they found that the shortest wavelengths had the fastest growth rates; so they took the short-wavelength limit of the dispersion relation [Eq. (1)]. The longest instability wavelength

[20] P. Burt and E. G. Harris, *Phys. Fluids* 4, 1412 (1961).

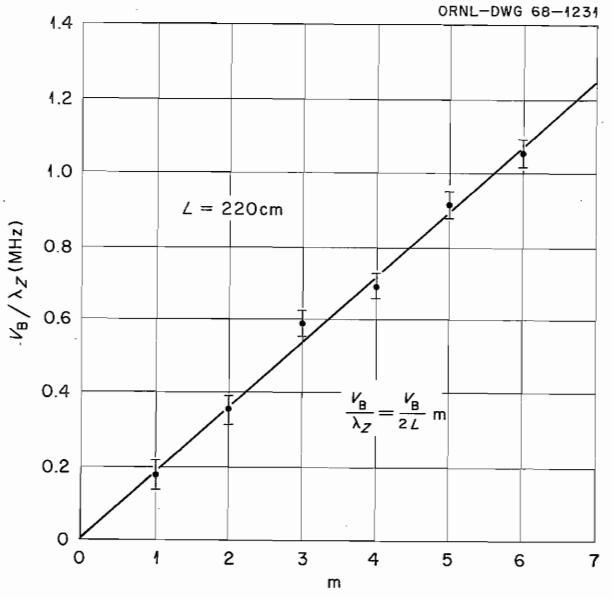

Fig. 3.22. Average V_B/λ_z vs Mode Number.

permitted by the beam parameters in the short-wavelength limit is $\lambda_z \sim 10$ cm, obtained by setting $k_r \cong 3$ cm^{-1} (beam thickness equal to half a radial wavelength). Shorter axial wavelengths are obtained if k_r is larger (more half wavelengths across the beam). The measured values for λ_z are an order of magnitude larger than these predictions, since the faster growing short-wavelength modes predicted by Burt and Harris fall in the electron Landau damping region. The largest amplitude peaks (and presumably the fastest growth rates) do occur just below the electron Landau damping region, as would be expected if the instability growth rate increased with decreasing wavelength. Glenn Haste of our laboratory has examined the Burt-Harris instability in the long-wavelength limit ($k_z V_z \ll \omega_{ci}$ as is found experimentally) for the H_2^+ fundamental. He finds[21] that the fastest growing instabilities in this limit have $\lambda_z \sim 75$ to 100 cm for the DCX-2 ion beam parameters, which is in good agreement with the measured instability wavelengths. The corresponding value for k_r is ~ 0.5 to 0.45, which indicates only a small potential variation across the beam thickness.

In summary, the microinstability in the injected ion beam has definitely been identified as a Harris mode. However, magnetic rf probe data indicate that the interpretation of the presence of convective and absolute waves from the axial variation of the rf spectrum obtained with electric probes may be incorrect. Several different wavelength modes are associated with each H_2^+ cyclotron harmonic, and these modes appear to be axial normal modes of the plasma cylinder. The short wavelengths predicted to be the most unstable by Burt and Harris are not observed because of electron Landau damping of this microinstability. The longer-wavelength modes predicted by Glenn Haste are seen, and obey the Landau damping criterion as the magnetic field and electron temperature are changed.

[21] Unpublished thesis calculations.

4. Electron-Cyclotron Heating

4.1 HIGH-DENSITY TARGET PLASMA EXPERIMENTS

M. C. Becker[1] A. C. England[2]
C. W. Blue N. H. Lazar
R. A. Dandl[1] O. D. Matlock
H. O. Eason M. W. McGuffin

4.1.1 Introduction

One of the main hopes for attainment of high ion densities in open-ended systems has been and still is high-energy ion injection and trapping. This concept resulted, at ORNL, in the construction of the DCX-1 and DCX-2 devices. In both of these experiments strong microinstabilities at gyrofrequency are found which either lead to direct particle losses, as in DCX-1,[3] or, at the very least, lead to unpredictable gross changes in the plasma characteristics, as in DCX-2.[4] Similar behavior is seen in the other high-energy ion injection devices throughout the world (see, e.g., the experiments in Alice,[5] Phoenix,[6] and OGRA I and II[7]).

In evaluating these instabilities, G. Guest pointed out that the presence of an added density of warm electrons would tend to suppress ion-electron gyrofrequency modes as a result of Landau dumping. In reviewing the possible effects of such an additional plasma, a catalog of the pertinent instabilities has been constructed (Table 4.1). A detailed examination of the instabilities has led to the following observations:

1. The addition of the cold ions, by adding a second component to the ion distribution function, can lead to additional instability modes. However, for sufficiently large n_{Cold}/n_{Hot} the expected wavelengths are small, and the resulting effect on the confined ions is, therefore, also expected to be small.

2. With the addition of hot electrons, one is forced to modify one's simple conceptions of mode-mode coupling. For low densities and relatively cold electrons, the simple model of coupling of ion gyrofrequency and electron plasma oscillations seems to be valid, and warming the electrons slightly will tend toward stability as a result of Landau damping. However, for $\omega_{pi} > \omega_{ci}$ and $T_{e\parallel}/T_{i\parallel} > (m_e/M_i)^{1/3}$, the influence of the electrons is more complicated and the physical mechanisms not yet completely understood. From numerical calculations, however, generally speaking, as the temperature is raised the most significant change is on the growth rate, which decreases with increasing temperature. The results of analysis to date indicate that for temperatures of at least several tens of kilovolts, the growth rates are $\sim 10^{-2}$ to $10^{-3}\ \omega_{ci}$ – sufficiently slow to expect other effects, for example, field curvature, to influence stability.[8]

However, a clear bonus is obtained with the use of this added plasma since the trapping efficiency for injected neutrals can, in principle, be enhanced by orders of magnitude over Lorentz trapping by taking advantage of the charge-exchange process

[1]Instrumentation and Controls Division.

[2]On leave, Institut für Plasmaphysik.

[3]J. L. Dunlap *et al.*, *Phys. Fluids* **9**, 199 (1966).

[4]P. R. Bell *et al.*, *Plasma Physics and Controlled Nuclear Fusion Research*, Culham, vol. II, 77 (1965).

[5]C. C. Damm, *International Meeting on Open-Ended Geometry*, Gatlinburg, Tenn. (1967).

[6]D. R. Sweetman, *International Meeting on Open-Ended Geometry*, Gatlinburg, Tenn. (1967).

[7]L. I. Artemenkov *et al.*, *Plasma Physics and Controlled Nuclear Fusion Research*, Culham, vol. II, 45 (1965).

[8]A much more extensive discussion of these instabilities may be found in sect. 1.1. Most of the observations were pointed out to us by G. Guest, R. A. Dory, W. M. Farr, and others in the Theory Group.

Table 4.1. Classification of Significant Gyrofrequency Instabilities in Open-Ended Systems

	No Added Cold Ions ($n_C/n_H = 0$) $T_e \cong 0$	$n_C/n_H > 1$
Ion-electron	1. $k_{\|\|}$ = finite;[a,b] convective near threshold ($\omega_{pe} \sim l\omega_{ci}$), absolute at higher densities	1. Stable for $\omega_{pi} < \omega_{ci}$ if $l\omega_{ci}/k_{\|\|} \gtrsim 3v_e$
	2. For $\omega_{pi} \gg \omega_{ci}$, convectively unstable at $\omega = \omega_{pi}$[c]	2. Instability predicted for $\omega_{pi} > \omega_{ci}$ with slow growth rate ($\omega_I \sim 10^{-2} - 10^{-3}\ \omega_{ci}$) and long wavelength; $k_{\|\|} \approx 1/100\ \rho_i$ for model loss-cone ion distributions. In general, growth rates decrease as $\sim T_e^{-1/2}$ (Sect. 1.1)
Ion modes	Drift-cyclotron instability: threshold near $\omega_{pi} \sim (R/\rho)^{3/2}\omega_{ci}$[c]	1. "Double-distribution" instability with $k_{\|\|} = 0$.[d] Predicted to yield instabilities at $l\omega_{ci}$ ($l \geqq 2$). Maximum growth near $l = \omega_{pi(\text{total})}/\omega_{ci} \approx 1$; thus very short wavelengths at large n_C/n_H
		2. Double distribution with $k_{\|\|} \neq 0$. Difficult to generalize because of complicated dependence on n_C/n_H, T_{ic}/T_{ih}, T_e/T_i, and L[e]

[a]G. E. Guest and R. A. Dory, *Phys. Fluids* **8**, 1853 (1965).

[b]C. O. Beasley and J. G. Cordey, Culham report CLM-P140 (1967).

[c]R. F. Post and M. N. Rosenbluth, *Phys. Fluids* **9**, 730 (1966).

[d]W. M. Farr and R. E. Budwine, *Thermonuclear Div. Semiann. Progr. Rept. Apr. 30, 1967*, ORNL-4150; L. D. Pearlstein, M. N. Rosenbluth, and D. B. Chang, *Phys. Fluids* **9**, 953 (1966).

[e]L. S. Hall, W. Heckrotte, and T. Kamash, *Phys. Rev.* **139**, A1117 (1965).

between cold ions in the added plasma and the injected energetic neutrals. For example, at 20 keV, the cross section for charge exchange is 3×10^{-16} cm^2/atom[9] and, thus, for an added (or target) plasma density of 10^{12} particles/cm^3, the trapping efficiency for a path length of two larmor radii in a field of 2.5 kG (20 cm) is 6×10^{-3}, more than an order of magnitude higher than most present Lorentz injection systems.

4.1.2 ECH Plasmas in INTEREM Facility

Experiments designed to examine the role of the target plasma were initiated some years ago, even before the presently sophisticated theoretical investigation of instabilities could be completed. The experiments were carried out in the INTEREM device (Fig. 4.1). The magnetic field configuration has undergone three modifications, and a fourth configuration is presently being installed:

I. The field coils were initially arranged in a simple mirror configuration with 3:1 mirror ratio.

II. The mirror coils were then changed so that a 2:1 mirror ratio was obtained, and, in addition, a pair of outboard coils were added which stretched the field to 3 m and provided additional mirror confining regions on either side of the main mirror trap.

III. The cavity was shortened and the external coils deenergized.

[9]*Atomic and Molecular Collision Cross Sections of Interest in Controlled Thermonuclear Research*, ORNL-3113 (Rev).

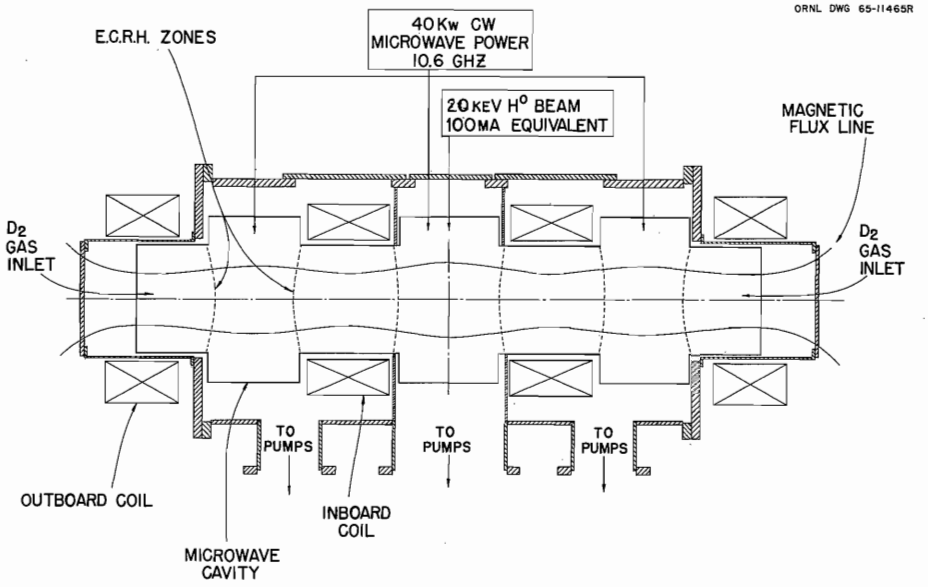

Fig. 4.1. Schematic Layout of Three-Region INTEREM Geometry.

IV. A system of quadrupole coils are being added to provide a magnetic well.

The target plasma has been produced by application of microwave power of up to 40 kW at a frequency of 10.6 GHz in configurations I and II. The results of some of these experiments have been described earlier.[10] The electron plasma density is in the range 4 to 7×10^{11} particles/cm^3, with a temperature of the predominant electron group of ~120 keV. A cold electron group with approximately equal density is present and appears to effect stabilization of the otherwise inherently flute-unstable plasma. The ambient pressure was $\sim 10^{-5}$ torr. The measured observed diamagnetic field change due to the presence of the plasma in configuration I was $\Delta B = 500$ G over a plasma radius of 25 cm and a length of 30 cm, corresponding to $\beta = 0.4$. Because of gradual tube deterioration, most recently the available power for configurations II and III has been reduced to ~25 kW and the resultant β, at least in II, has been less, ~0.1 ($\Delta B \sim 150$ G).

[10] W. B. Ard *et al.*, *Plasma Physics and Controlled Nuclear Fusion Research*, Culham, vol. II, 153 (1965).

4.1.3 Energetic Ion Plasma Studies

At the time of the Culham meeting, an ion beam of ~10 mA had been injected into configurations I and II, and a stable ion plasma was observed.[10] It is informative to review the particle equilibrium equations to note the critical parameters. The dominant trapping process is charge exchange of the injected neutral atoms with the target plasma ions, but ionization by electrons and neutral atoms also contributes. Experiments with gas ionization, at low accumulated density, will yield accumulated ion densities, $n_+^{(0)}$, of

$$n_+^{(0)} = \frac{I_0 n_0 \sigma_{01} 2R}{\pi R^2 L} \left(\frac{1}{n_0 \sigma_{10} v_+} \right) . \qquad (1)$$

When the same beam is injected into a target plasma,

$$n_+^{(T)} = \frac{I_0 \{ n_e [\sigma_{10} + (\langle \sigma v \rangle_{01}^{(e)} / v_+)] + n_0' \sigma_{01} \} 2R}{\pi R^2 L} \times \frac{1}{n_0' \sigma_{10} v_+} . \qquad (2)$$

The charge-exchanging cross sections, σ_{01} and σ_{10}, of hydrogen atoms with protons can be found in a

compilation of atomic cross sections such as ORNL-3113:[9] $\sigma_{01} = 7.5 \times 10^{-17}$ cm^2, $\sigma_{10} = 3 \times 10^{-16}$ cm^2; $\langle \sigma v \rangle_{01}^{(e)}$ is the ionization rate of neutral hydrogen atoms by hot electrons in the target plasma, with a value of $\sim 1.5 \times 10^{-8}$ cm^3/sec, almost independent of electron energy.

It may be noted that $n_+^{(0)}$ is independent of n_0, the neutral pressure (Eq. 1). The quantity n_0' in Eq. (2) is the neutral density averaged over the ion plasma radius, R, inside the target plasma. This density is reduced below the ambient neutral pressure, n_0, by ionization by the electrons in the target plasma and is given by

$$n_0' = n_0 e^{-n_e(\langle \sigma v \rangle_I^e / v_0)t}, \qquad (3)$$

where v_0 is the neutral particle velocity and where t is the target plasma thickness; n_0' may be experimentally determined from the decay time of the energetic ion plasma with target plasma trapping.

The ion density is determined from an absolute measurement of charge-exchange current and an independent determination of τ_{cx}. In these measurements, silicon barrier detectors cooled to liquid-nitrogen temperatures are used as proportional counters to determine the charge-exchange flux from the plasma. Assuming the ion energy is unmodified from the injected energy (20 keV) the detector gain is found to be $\sim$3000.[11] Generally, both $I_{cx}\tau$ and I_{cx} are measured, the former by electronically integrating the latter over time.

Since 1966, a new high-current beam system has been installed. The ion source designed by Kelley, Morgan, and Davis[12] for INTEREM consists of a modification of the Sukhumi[13] design of a duoplasmatron geometry which favors a large H_2^+ yield. A magnesium vapor cell is used to convert the H_2^+ 40-keV beam to 20-keV H^0 atoms. Beams of $\sim$100 mA of 20-keV H^0 are now conventionally available through the final $\sim 1\frac{3}{4}$-in. aperture, $\sim$54 in. from the lens coil.

To establish the plasma length, a collimated detector has been translated horizontally (parallel to the field axis) and the current measured as a function of position. A typical scan is shown in Fig. 4.2. The full width at half maximum of 0.55 cm is remarkably narrow but appears to reflect the beam distribution. Also shown in Fig. 4.2 is the scan with gas trapping; no significant width change is observable when the target plasma is present. The angular distribution of particles in the midplane has also been measured independently, and the results also show very little difference from gas trapping to target plasma trapping. An estimate of the Coulomb scattering rate of trapped protons with target plasma ions suggests up to 50% spread over the incident beam width can be expected. In any case, no large angular divergence changes which must be ascribed to the presence of instabilities have been found.

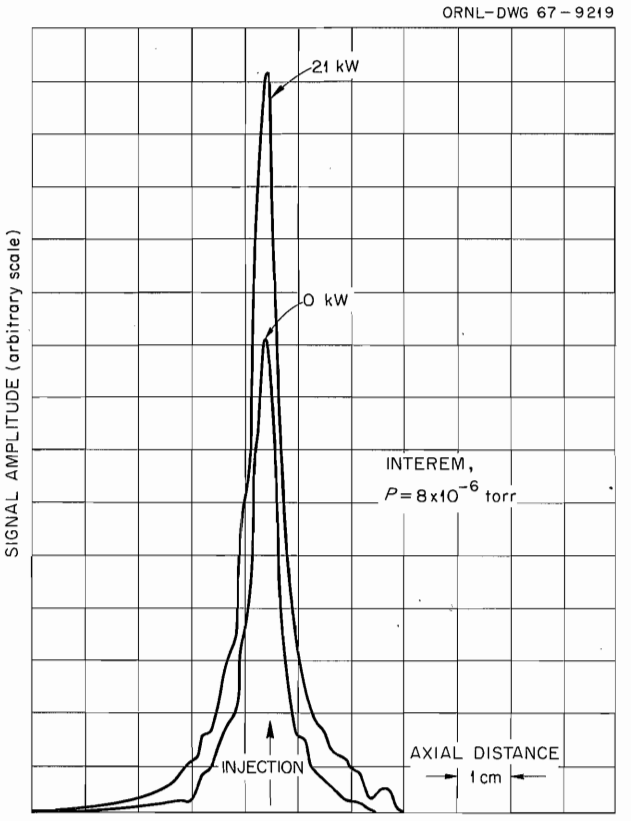

Fig. 4.2. Axial Scan of Charge-Exchange Neutral Current Emitted from INTEREM Plasma with 0 kW and 21 kW Applied Microwave Field.

The accumulated energetic ion density has been measured as a function of beam current (Fig. 4.3), ambient pressure (Fig. 4.4), and applied microwave power (Fig. 4.5 at 4×10^{-6} torr). The maximum

[11] C. F. Barnett and J. A. Ray, *Thermonuclear Div. Semiann. Progr. Rept. Apr. 30, 1965,* ORNL-3836, 70.

[12] G. G. Kelley *et al., Thermonuclear Div. Semiann. Progr. Rept. Apr. 30, 1967,* ORNL-4150, 114.

[13] O. F. Poroshin and J. S. Coutant, report No. 600, Physico-Tech. Inst. U.S.S.R. (translated by Culham Translations Office, July 1964).

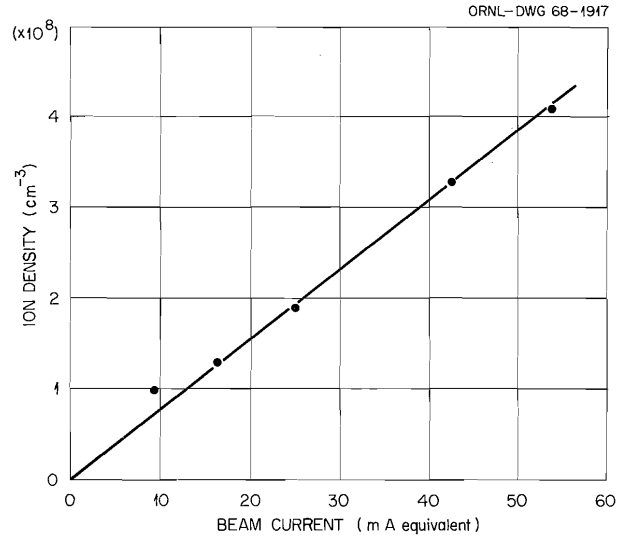

Fig. 4.3. Energetic Ion Density Accumulated in INTEREM as a Function of Injected Neutral Beam Current. Pressure = 3×10^{-6} torr, applied power = 23 kW.

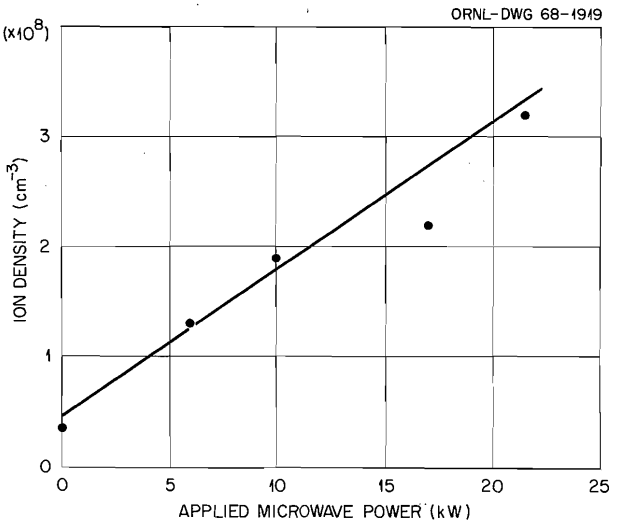

Fig. 4.5. Energetic Ion Density Accumulated in INTEREM as a Function of Applied Microwave Power. Pressure was 6×10^{-6} torr, beam current was 54 mA.

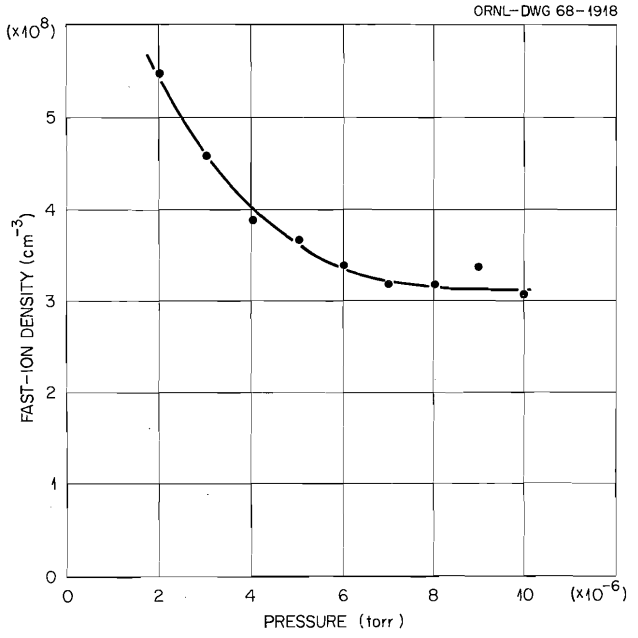

Fig. 4.4. Energetic Ion Density Accumulated in INTEREM as a Function of Ambient Pressure. The beam current was 55 mA, the applied power was 23 kW.

density, 5×10^8 ions/cm^3, corresponds to $\omega_{pi} \cong 1.1\omega_{ci}$ for the magnetic field on axis in the midplane. The linear dependence of density with beam current, the absence of axial spread, and the absence of any indication of ion-cyclotron rf fields all indicate stability of the trapped ions. Earlier measurements of the energy distribution at the lower beam currents ($n_+^{(T)} \approx 10^7$ ions/cm^3) showed the energy spread was within the detector resolution, also reflecting the absence of gyrofrequency instability. There is, similarly, no evidence of lower-frequency fluctuations which might be associated with interchange instability.

The behavior of trapped ion density as a function of power used to generate the target plasma is of additional interest, since it reflects the target plasma density as a function of power. From Eqs. (2) and (1),

$$\frac{n_+^{(T)}}{n_+^{(0)}} = \frac{n_e}{n_0'} \frac{[\sigma_{10} + (\langle \sigma v \rangle_I^e / v_+)]}{\sigma_{01}} + 1$$

$$= \frac{(I_{cx}\tau)_{meas}^{(T)}}{(I_{cx}\tau)_{meas}^{(0)}} . \qquad (4)$$

Also,

$$n_0' = \frac{1}{\tau_{meas}^{(T)} \sigma_{10} v} . \qquad (5)$$

Thus from the measured data, n_e as a function of applied power can be deduced (Fig. 4.6). We also indicate n_e as a function of pressure at the highest power presently available (22 kW) (Fig. 4.7). These results are entirely consistent with the increasing trapped ion density observed as a function of power and decreasing pressure.

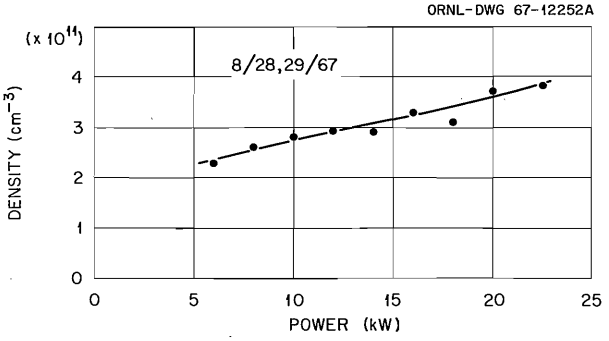

Fig. 4.6. Effective Trapping Density in Microwave Plasma in INTEREM as a Function of Power for Three-Region Geometry.

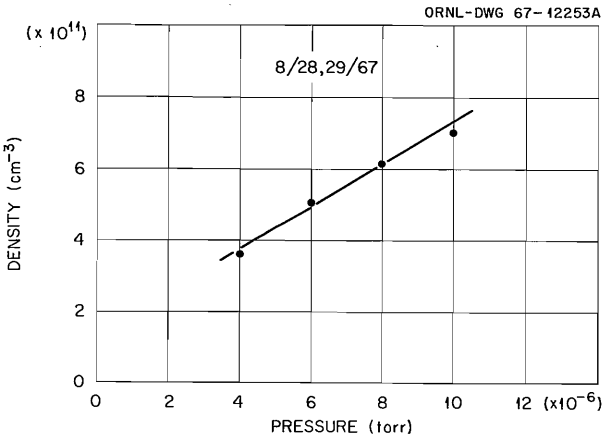

Fig. 4.7. Effective Trapping Density as a Function of Pressure in Three-Region INTEREM Geometry. Applied microwave power was 22 kW.

4.1.4 Discussion of Instabilities

In view of the observed stability of the trapped energetic ion plasma it is informative to examine the possible instability regimes to determine if any predicted thresholds have been crossed. The low-frequency stability is not surprising in view of the presence of the dense cold plasma.[14] Nevertheless, it is of interest to remember the expected instability threshold density if the target plasma were absent. Using the crude model described by Kuo *et al.*,[15] in the absence of the target plasma, the threshold density for flute instability in a field assumed to have the form $B = B_0/(1 + B_1 r^2)$ is given by

$$n_+ = \frac{5.8T(1 + B_1 r_0^2)^2 - 1}{32\pi e^2 r_0^2}, \qquad (6)$$

where r_0 is the assumed plasma radius. For the 2:1 central mirror field in INTEREM, Eq. (6) indicates a threshold density of 7×10^6 cm^{-3}. It has been shown that, for the conditions in the Phoenix experiment, this estimate is about a factor of 5 too low. The corrected density is still a factor of 10 lower than the density observed in INTEREM.

Three specific gyrofrequency instability modes have been examined to evaluate if the target plasma can play a role in raising stability boundaries. These are: (1) the conventional ion-electron anisotropy-driven mode;[16] (2) the flutelike ion-ion double-distribution mode;[17] and (3) the double-distribution, finite $k_{||}$ mode described by Hall, Heckrotte, and Kamash.[18] The ion-electron instability mode described by Guest and Dory can be applied directly to the INTEREM plasma. The anisotropy may be estimated from the field curvature and plasma axial extent, and, in the midplane, $T_{||i}/T_{\perp i} = 3 \times 10^{-4}$. Several groups of electrons are present, but if the electron temperature is assumed to be low ($T_{||e}/T_{||i} = 0.05$), the cold ions are ignored, and the radial wavelength is chosen for maximum growth, then (assuming axial wavelengths of twice the hot ion plasma length) the plasma is predicted to be stable. The critical

---

[14] G. E. Guest and C. O. Beasley, Jr., *Phys. Fluids* **9**, 1798 (1966).

[15] L. G. Kuo *et al.*, *Phys. Fluids* **7**, 988 (1964).

[16] G. E. Guest and R. A. Dory, *Phys. Fluids* **8**, 1853 (1965).

[17] W. M. Farr and R. E. Budwine, *Thermonuclear Div. Semiann. Progr. Rept. Apr. 30, 1967*, ORNL-4150; L. D. Pearlstein, M. N. Rosenbluth, and D. B. Chang, *Phys. Fluids* **9**, 953 (1966).

[18] L. S. Hall, W. Heckrotte, and T. Kamash, *Phys. Rev.* **139**, A1117 (1965).

parameter is the short axial length. The recent estimates by Guest (see Sect. 1.1 of this report), which would indicate that for longer plasma lengths the threshold density for instability would be raised by the presence of the hot electrons, have not yet been unambiguously substantiated by the INTEREM results.

The second mode of special concern, the flutelike double-distribution instability, was investigated by Pearlstein *et al.*[17] for $k_\perp \rho \ll 1$ and, in greater detail, by Budwine and Farr[17] for various assumed velocity distributions. Using Budwine and Farr's results for delta function distributions, one finds the boundaries for instability as a function of total plasma density, $(\omega_{pi}/\omega_{ci})^2_{\text{total}}$, as shown in Fig. 4.8, where the resonances are predicted at thresholds given by $(\omega_{pi}/\omega_{ci})^2 = (l^2 - 1)$. In INTEREM, $(\omega_{pi}/\omega_{ci})_{\text{total}} \approx 37.5$. It should be remarked that if one assumes the resonances will not produce observable effects, the INTEREM plasma would be expected to be stable against the nonresonant form of this instability as given in the limit by Pearlstein *et al.*[17]

A third mode of some concern, since it has been reported as responsible for anomalous losses from a hot electron plasma, is the one discussed by Hall, Heckrotte, and Kamash[18] for a "double-humped" distribution. To attempt to apply their model to the INTEREM case involves some stretching of the model, since they neglected the presence of electrons and since the theory is given in a form applicable to densities where $\omega_{pi} < \omega_{ci}$. Nevertheless, if one uses their expressions directly as applicable to INTEREM, one finds instability for a parameter

$$S = \frac{2\pi\rho_L}{L}\left(\frac{\omega_{ci}}{\omega_{pi}}\right)^2\left(\frac{n_H + n_C}{n_C}\right)\left(\frac{T_{\parallel C}}{T_{\perp H}}\right)^{1/2} < 0.4 \ .$$

In INTEREM at $\omega_{pi} = \omega_{ci}$, this parameter is 2.2 with the plasma length taken as 1 cm. However, at lower densities where $(\omega_{pi}/\omega_{ci})^2 < 0.1$ ($n_{\text{Hot}} <$

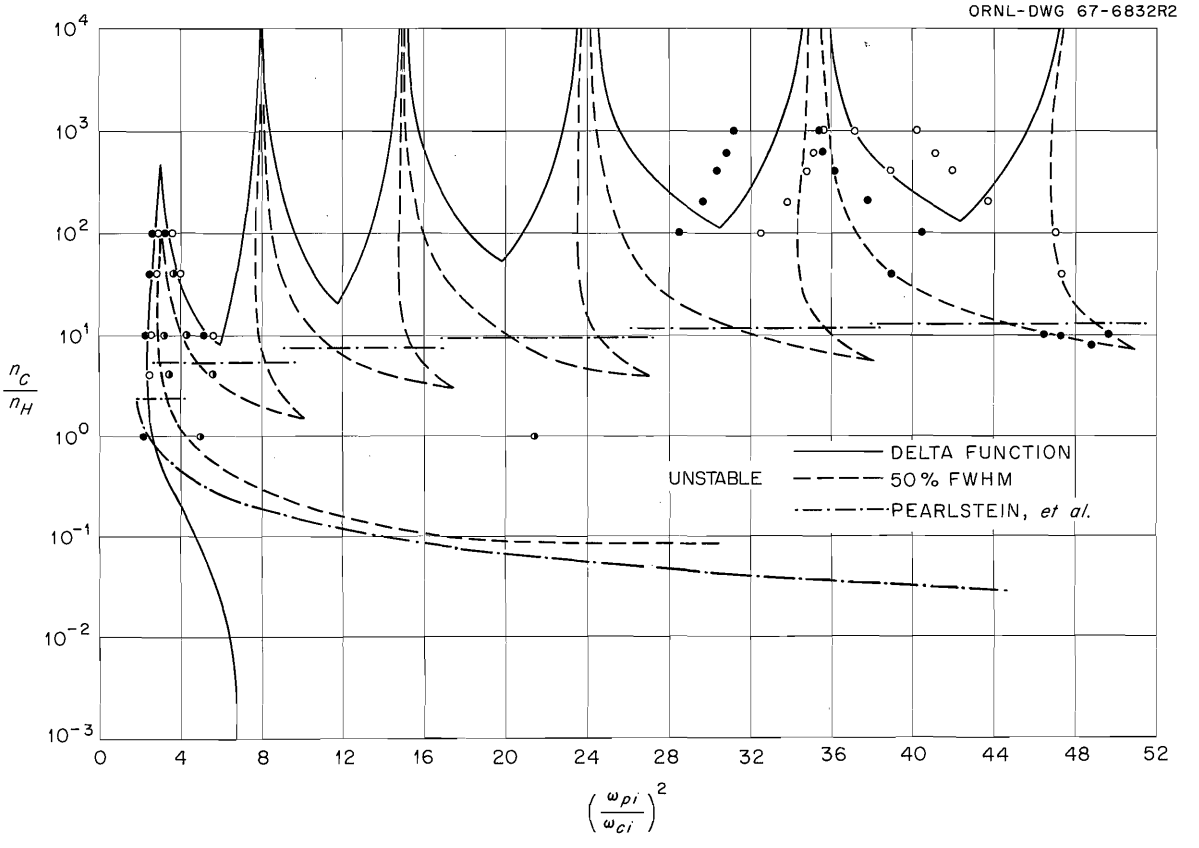

Fig. 4.8. The Stability Boundaries for High-Frequency Flutelike Ion-Ion Instabilities[17] Plotted as a Function of the Parameters Total Plasma Density $(\omega_{pi}/\omega_{ci})^2$ and Ratio of Cold to Hot Plasma Density (n_C/n_H).

5×10^7 ions/cm^3) this mode should have been present, but no evidence for it was seen.

Thus, one may reasonably hope for continued freedom from the effects of the "double distribution" of ions. The influence of the hot electrons on the ion-electron modes or $k_{\parallel} \neq 0$ double-distribution modes at high densities, however, has not yet been put to a satisfactory test.

5. Plasma Physics

5.1 BEAM-PLASMA INTERACTIONS; THE HOT-ELECTRON PLASMA

R. V. Neidigh D. J. Rose

5.1.1 Introduction

Electron heating by beam-plasma interaction has been observed in several experiments conducted at ORNL[1] and elsewhere.[2,3] In this report period we have repeated some earlier ORNL experiments in order to increase our understanding of the heating mechanism. This is the progress report.

5.1.2 Field Dependence of Bremsstrahlung

According to theories generally accepted, the electron heating takes place via "thermalization" of waves that were generated in a region where the plasma frequency ω_{pe} equals the electron cyclotron frequency ω_{ce}. According to ref. 3, the wave generation region should be the mirror on the cathode side of the hot-electron device, and the thermalization region should be the field gradient just inside the mirror.

Whether these ideas are true in detail or not, if the heating occurs via the resonance between ω_{pe} and ω_{ce}, then there might be a predictable dependence of the bremsstrahlung on the magnetic field strength, as follows. If the system geometry and field shape are kept the same, we would have (since $\omega_{pe} \propto n_e^{1/2}$, $\omega_{ce} \propto B$) $n_e \propto B^2$ at any fixed point in the system. The total bremsstrahlung from the hot (Maxwellian) electrons will be $S \propto Z^2 n_e (n_i + n_0) T_e^{1/2}$, very closely. Here, n_i is the ion density, and n_0 is the neutral gas density.

In the electron heating experiment, the gas is strongly ionized ($n_e = n_i$), $n_e \approx 10^{11}$ cm^{-3}, and we would expect $n_0/n_e \approx 1$ by simple calculation of density from pressure readings. However, it is easy to calculate that the neutral gas density inside the hot-electron plasma is substantially reduced because the atoms are heated to 1–3 eV by "elastic" collisions with the hot-electron gas, without actually being ionized. Spectroscopic data confirm this view. Thus in the plasma core, we expect $n_0 \ll n_e$ and $S/T_e^{1/2} \propto B^4$.

Figure 5.1 shows the measured $S/T_e^{1/2}$ in arbitrary units, plotted vs magnetic field, for two experiments in helium gas, and constant mirror ratio about 2.5. Detector sensitivity was changed in the two experiments.

In the past we found that electron heating could not be accomplished above a midplane field strength of about 3000 G. These data may show that, indeed, we could have found increased heating at greater field strengths had we maintained the same mirror ratio and provided for increased electron density in the heating zones.

5.1.3 The RF Spectrum

The spectrum in the observed region 0 to 10 GHz is so complicated that its leading features must be carefully isolated. Our experiments and those of ref. 3 show that conditions for electron heating (electron beam injected axially into a mirror, with a *de jure* or *de facto* electric reflector in the system) are similar to conditions for operating a reflex klystron. With a weak electron beam and only enough gas to neutralize space charge, we see klystron-like modes appearing, typically at 45 MHz, ≅100 MHz, and higher specific frequencies. These can be experimentally associated with electromagnetic modes of the empty system. Figure 5.2

[1] I. Alexeff *et al.*, *Phys. Rev.* **136**, A689 (1964).

[2] L. D. Smullin and W. D. Getty, *Phys. Rev. Letters* **9**, 3 (1962).

[3] M. Seidl and P. Sunka, *High-Frequency Instabilities in Beam-Generated Plasmas*, IPPCZ-81 Research Report, May 1967.

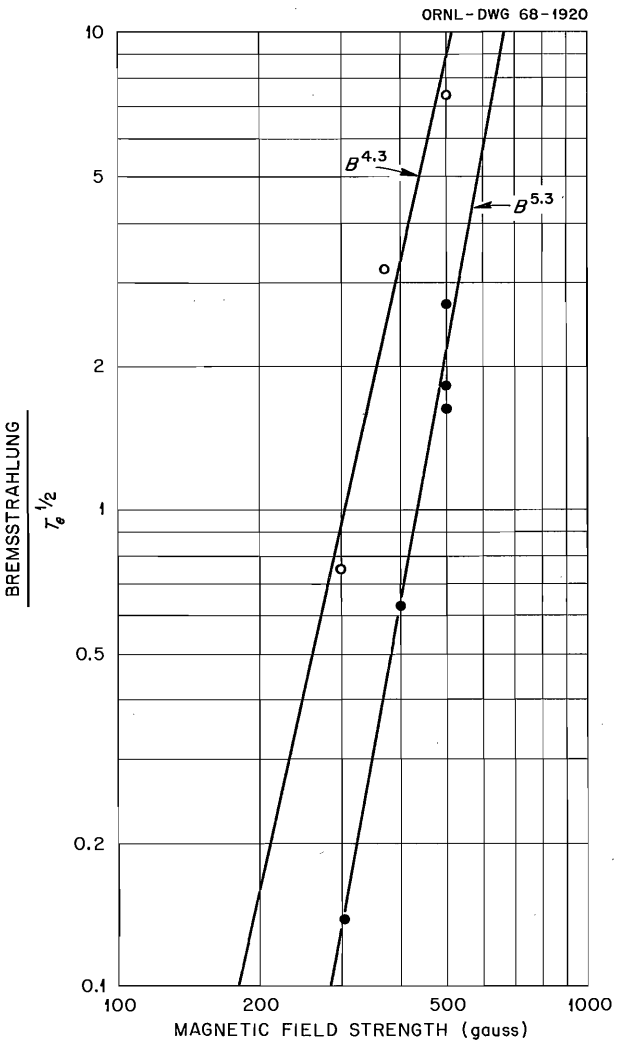

Fig. 5.1. Bremsstrahlung/(Electron Temperature)$^{1/2}$ vs Magnetic Field Strength. The significance of the data is the approximate B^4 dependence of bremsstrahlung/$T_e^{1/2}$, which can only be true if the plasma is highly ionized. The two curves were made with different gas feed rates and pumping speeds.

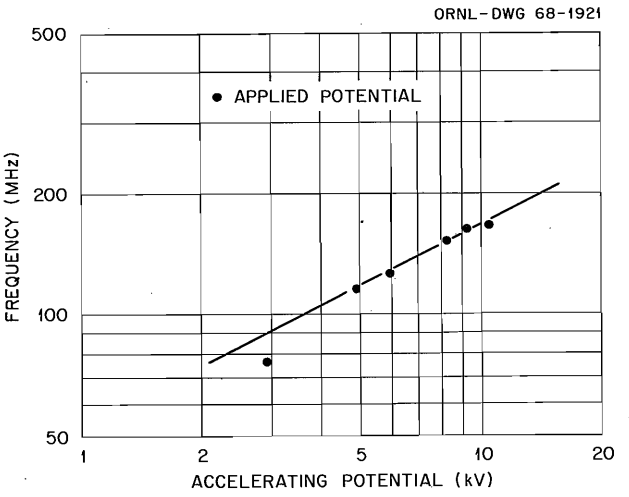

Fig. 5.2. Radiation Frequency vs Accelerating Potential. The transit time of the bunched electron beam is clearly a linear function of the square root of the accelerating potential.

shows one such mode and its frequency variation with electron accelerating potential. The variation indicates that the device operates on electron transit time. Under these conditions there is no electron heating.

When electrons are heated, at higher electron current and gas flow, the spectrum becomes much more complex. Figure 5.3 shows this fact; when T_e exceeds 10 keV, the pattern resembles white noise over the entire spectral range shown.

5.1.4 Beam Energy Spread

The disagreement between the Smullin[4] and Stix[5] theory for heating electrons in the beam-plasma experiments might be resolved if indeed we could measure experimentally the correlation length for turbulent electrostatic fluctuations. Calculations by Montgomery[6] on the final state of the two-stream instability of the "bump on the tail" variety indicate that we might indirectly determine the correlation length from the energy spread in the beam for this case:

$$\text{correlation length} \sim \frac{\text{beam velocity}}{\omega_{pe}} \frac{\text{beam energy}}{\text{energy spread}}.$$

We are addressing ourselves to this problem. We have found qualitatively that without plasma the beam does not spread in energy even though reflected at the opposite end of the magnetic axis. With bunching of the beam, but without electron heating, an apparent energy spread was detectable by measuring the potential of the insulated reflector.

---

[4] L. D. Smullin, *Phys. Fluids* 8, 1412 (1965).

[5] T. H. Stix, *Phys. Fluids* 7, 1960 (1964).

[6] Private communication.

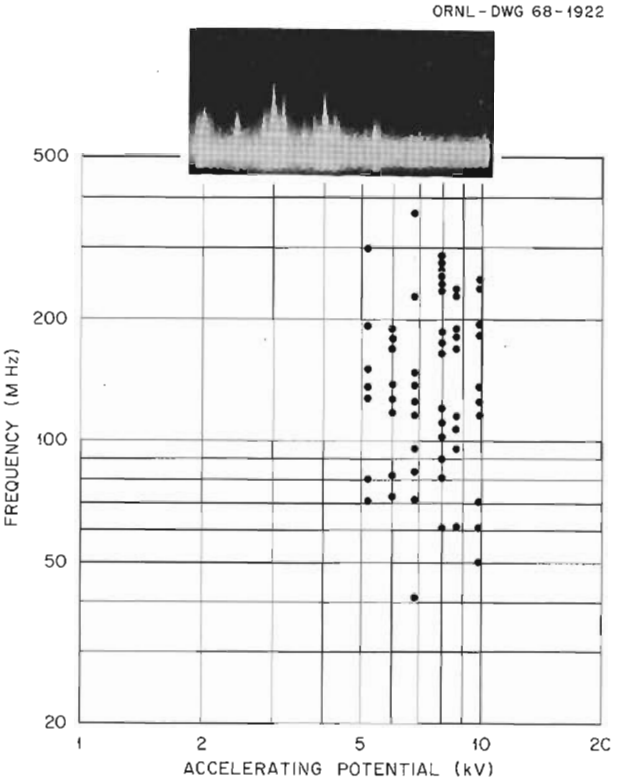

Fig. 5.3. Radiation Spectrum Accompanying Weak Interaction with the Plasma. Compare with Fig. 5.2. The inset is the spectrum at 5.9 kV. Its range is 0 to 300 MHz. Discrete frequencies degenerate to white noise when strong beam-plasma interaction exists and $T_e > 10$ keV, and this T_e generally occurs when the accelerating potential applied to the electron beam exceeds a few kilovolts.

A fall in potential of the reflecting electrode at the onset of heating is a characteristic of the heating mode. A measure of the energy spread was made by allowing a small portion of the beam to pass through a hole in the reflecting electrode, after which it is measured on a catcher. Figure 5.4 shows how the catcher potential varies as the main beam current is changed, in three modes of operation. When there is no beam-plasma interaction, the catcher (and the reflector) acquire the accelerating potential, irrespective of beam current. When beam-plasma interaction is present, the catcher potential drops rather slowly as beam current is increased, indicating now a spread of energy (and velocity) in the beam. This spread of energy in the beam corresponds in this case to a T_e(beam) of about 300 eV, which is much less than the T_e(plasma).

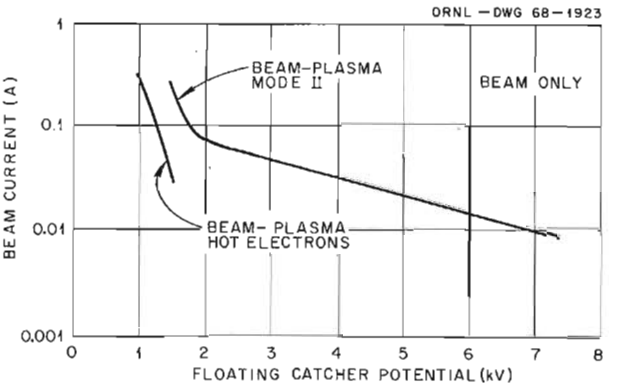

Fig. 5.4. Energy Distribution in the Beam. The curves depict a portion of the high-energy side of the beam. They were obtained by varying the cathode temperature and show the effect on the beam for two modes of interaction with the plasma.

5.2 STUDIES OF NEUTRAL LIGHT EMISSION FROM THE BURNOUT PLASMAS

R. Hefferlin[7] W. D. Jones
R. V. Neidigh S. R. Sowder[8]

5.2.1 Introduction

This report summarizes some studies which have been made of the excitation light emitted from the Burnout IV and Burnout V plasma devices. In Burnout IV, the radial variation of intensity of both molecular and atomic excitation light was measured. In Burnout V, the decay time, upon crowbarring of the electron-beam power supply, of both molecular and atomic excitation light was measured. An interpretation of the Burnout IV data gives an electron density in the range of 10^{12} to 10^{13} cm^{-3}. The e-folding decay time of the neutral light from Burnout V was found to be on the order of 300 μsec.

5.2.2 Burnout IV Experiments

Figure 5.5 is a scale drawing showing the basic features of the plasma device. The configuration is a $1\frac{1}{2}$ to 1 mirror with an 8-kG central field.

[7]Consultant, Southern Missionary College.

[8]Summer Participant, Southern Missionary College.

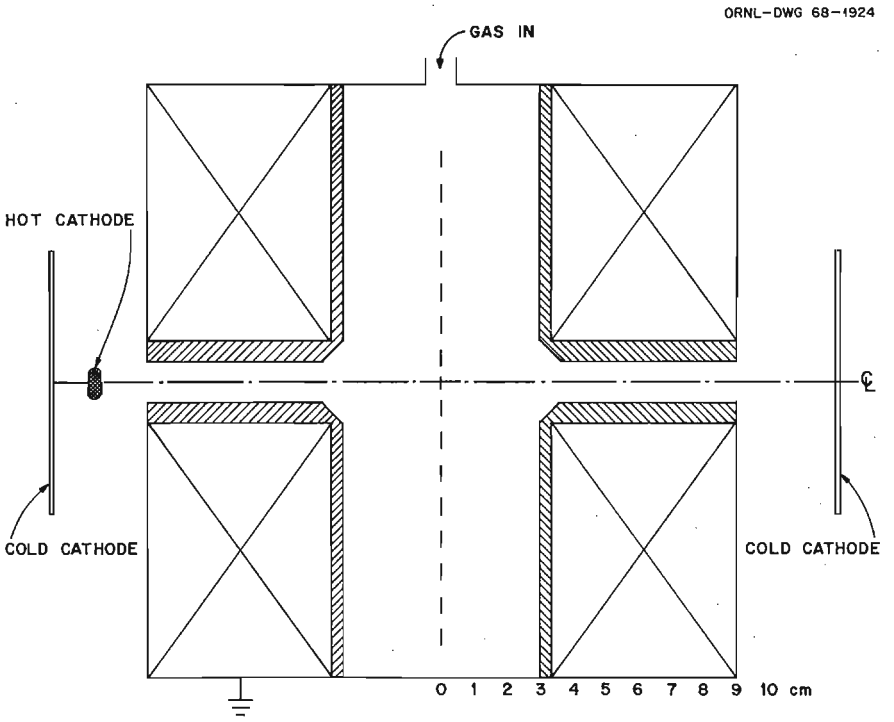

Fig. 5.5. Scale Drawing Showing the Basic Features of Burnout IV.

The entire central section of the machine is grounded and acts like a hollow anode. Deuterium gas is fed peripherally into this center section at the midplane. An on-axis reflex electron beam interacts with the gas to form a plasma and then interacts with the plasma to heat it. Present evidence seems to indicate that a fairly dense, highly ionized, hot, turbulent plasma exists in the device.[9]

From plasma recombination losses on the cavity wall and from the peripheral gas feed, it is expected – and experiment verifies – that the plasma is surrounded by a blanket of molecular gas. If the plasma is as hot and dense as we have reason to believe, then a fairly rapid attenuation of the neutral molecules is expected as they try to penetrate into the plasma. Since the intensity of excited light emitted from the plasma is a direct function of the excited neutral density, one, a priori, expects a corresponding rise and fall in intensity of neutral light as we look further and further into the plasma.

From both dissociative excitation and dissociative ionization processes, a large fraction of the original neutral molecules is converted into fast so-called Franck-Condon neutral atoms. Again, as for the molecules, one expects these neutral particles to be attenuated by the plasma. Due to their much faster velocity, however, their characteristic attenuation length is expected to be much larger than that for the molecules. Thus, a priori, what we expected to see, as we looked at the radial variation of intensity of excited molecular and atomic light, was a strong dependence of the molecular light on radius but a relatively weak dependence of the atomic light on radius.

Figure 5.6 shows how the light intensity data were obtained. This figure shows a cross-sectional view of the plasma and the light-measuring apparatus. By means of the movable lens-filter-photomultiplier assembly and the vacuum window exposing the middle section of the plasma at the midplane, a radial scan of the relative intensity of any spectral line or region could be obtained easily. Abel inversions of the raw data were necessary, however, in order to obtain a true dependence of the light intensity on radius.

[9] I. Alexeff, W. D. Jones, and R. V. Neidigh, *Phys. Rev. Letters* 18, 1109 (1967).

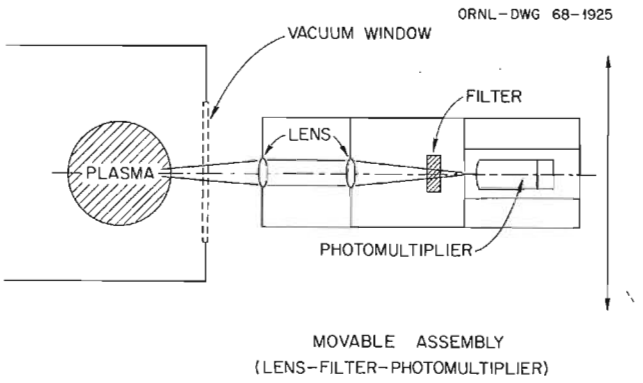

Fig. 5.6. Cross-Sectional View of the Plasma Column and of the Light-Intensity-Measuring Apparatus for Burnout IV.

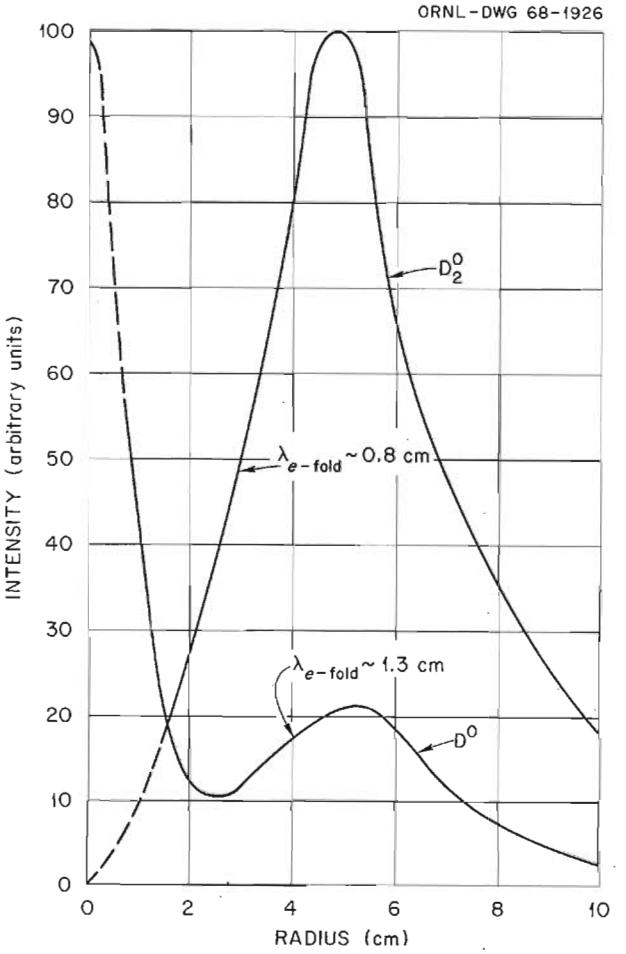

Fig. 5.7. Radial Dependence of Molecular and Atomic Excitation Light Intensity in Burnout IV. The intensity of the molecular light was some 100 times as large as the atomic light. The band pass of the filtering systems used in the respective measurements was 5700–6300 Å for molecular light and 6563 ± 3 Å for the Balmer α light.

Figure 5.7 shows Abel-inverted data for both molecular and atomic light. On the vertical axis is plotted relative intensity and on the horizontal axis the distance from the axis of the machine. The vertical scale is not the same for the two sets of data, the observed molecular light being some 100 times more intense than the atomic light. It is noted that, except at the very center of the machine, the radial dependence of the light intensity for the molecular and atomic light is qualitatively very similar. As we proceed from the outside inward, the light goes through a maximum, as might be expected if the gas encounters a relatively abrupt dense wall of electrons. Both visual observation and probe measurements have given us reason to expect that this might be the case. Inside the maxima there is a region of 3 or 4 cm over which the light intensity decreases in a fairly exponential manner. The molecular light seems to decay toward zero intensity at the machine axis, as if the attenuation of molecules is complete at the center of the plasma. On the other hand, the intensity of atomic light increases rapidly near the center. Thus far we have been able to interpret this only to mean that the attenuation of atoms is not complete at the center of the plasma and that the electron density increases rapidly at the center. The latter speculation seems quite reasonable, since this is just the region we would expect to be occupied by the unreacted reflex electron beam.

The observation we found initially surprising was that the quantitative dependence on radius of the two light intensities in the two exponential regions is also the same, the atomic light e-folding distance being less than twice that for the molecular light. Examination of the rate coefficients for the various plasma processes available for neutral particle attenuation reveals that ionizing collisions with electrons constitute the dominant process leading to attenuation of molecules. For atoms, there are two competing processes whose rate coefficients are approximately equal – ionization by electron collisions and resonant charge exchange with plasma ions. The sum of these two coefficients for atoms is equal approximately to

the ionization rate coefficient for molecules. The velocity of the Franck-Condon atoms, however, is approximately 30 times that of the room-temperature molecules. Thus the attenuation length for Franck-Condon atoms should be approximately 30 times that for molecules.

If we somewhat arbitrarily choose an electron density of 10^{13} cm^{-3}, use an average ionization rate coefficient for molecules equal to 5×10^{-8} cm^3/sec, and a molecular speed of 1.2×10^5 cm/sec, we find an e-folding attenuation length of 2.4 mm. The observed e-folding distance for the excited molecular light intensity is about 8 mm. If we make the assumption that the electron density is varying slowly compared with the indicated rather rapid rate of variation of neutral molecular density, comparison of experiment and this first-approximation theory yields an electron density of 3×10^{12} cm^{-3}. If the electron density increases radially inward, then this value represents an upper limit on electron density, under the assumptions. As will be pointed out below, however, the basic assumption of a radial outer shell as the only source of molecules for penetration into the plasma is incorrect, so that the above electron density value may be more nearly a lower limit rather than an upper limit.

Using the above value of electron density, the thermal speed of a 6-eV Franck-Condon neutral, and an average total-loss-rate coefficient of 5×10^{-8} cm^3/sec gives a theoretical attenuation length of about 17 cm. This is more than an order of magnitude larger than the 1.3-cm attenuation length observed for the atomic excitation light. Even if we use an electron density of 10^{13} cm^{-3}, the disagreement is still a factor of 5. If we take a closer look at the shape of the plasma, we see that over most of its volume it is a rather flat disk and that the nearest distance from the central planar region of the disk to the nearest wall is a maximum of 3 cm. Thus the dominant loss process for Franck-Condon neutrals from the plasma is not a plasma process but rather is simply atoms escaping at their thermal speed. Wall sheaths make the effective escape length from the plasma even shorter than the 3-cm distance to the wall. Once at the wall, the fast atom either is reflected back into the plasma or else recombines with another atom to form a molecule, whereupon the process repeats. Thus we see that the penetration of neutral atoms into the plasma is governed primarily by diffusion processes rather than by plasma processes. A rough calculation of the diffusion length gives about 2 cm. While this puts theory and experiment in better agreement, unfortunately we learn less about the properties of the plasma.

Both from normal plasma recombination processes at the wall and from some recombination of the rapidly escaping Franck-Condon neutrals, we see that the initial model of an outer cylindrical shell source of neutral molecules is not complete. The recombination gives rise to a strong source of molecules at the side walls of the cavity. Thus we have not only an outer shell of molecules but a radial source as well. This additional source counteracts, to some extent, the radial attenuation by ionization, leading to an experimental light-intensity attenuation length which is larger than the one calculated using only the shell source. On this basis, since the calculated density varies inversely with attenuation length, the above value of 3×10^{12} cm^{-3} represents a lower limit on the electron density.

5.2.3 Burnout V Experiments

Using basically the same technique shown in Fig. 5.6, we have made some preliminary studies of the time rate of decay of neutral light coming from the plasma, upon turnoff. Turnoff of the plasma was effected by crowbarring the electron-beam power supply, using a knife switch. The present data suggest similar decay rates for molecular and atomic light. The decay seems to be approximately exponential, with an e-folding time of about 300 μsec. An interpretation of this decay time as being that of the plasma is somewhat premature at this point. The plasma could be decaying quite rapidly, for example, while neutral light could be being generated for a long time by a small trapped group of hot electrons. A double-diamagnetic-loop experiment is in preparation to attempt to measure directly the decay time of the stored energy in the plasma.

The upper trace in Fig. 5.8 shows the voltage appearing across a voltmeter in parallel with the electron-beam power supply, after crowbarring of the supply. The lower trace shows a typical light intensity decay curve for excited molecular light. Both traces have a weak slope caused by the oscilloscope's being located in a weak external magnetic field. Faster sweep speeds show that the power-supply voltage drops immediately to zero,

PHOTO 90773

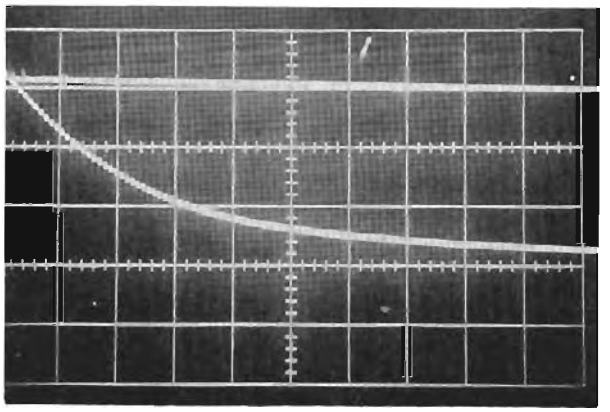

Fig. 5.8. Plasma Turnoff Experiment in Burnout V. The signal on the upper trace is proportional to the voltage across the electron-beam power supply after crowbarring. The lower trace shows the decay of the molecular excitation light emitted from the plasma. Sweep speed = 100 μsec per large division.

PHOTO 90774

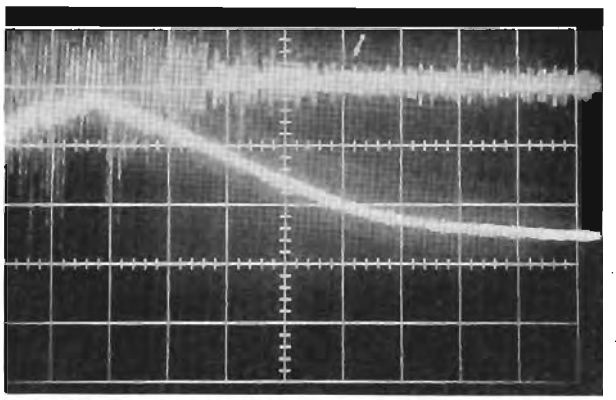

Fig. 5.9. Modulation of Intensity of Neutral Excitation Light from the Plasma by Sporadic RF Bursts. The top trace shows typical low-frequency activity during steady-state operation. The bottom trace shows the corresponding relative intensity variation of the emitted Balmer α light. Sweep speed = 100 μsec per large division.

but then has a damped 1-MHz oscillation with a decay time of 3 to 5 μsec.

An additional interesting observation was made, that the neutral light intensity is strongly modulated by sporadic bursts of low-frequency (few-megahertz range) rf. Figure 5.9 shows such data during steady-state operation. The upper trace shows the relative rf activity, while the lower trace shows the Balmer α light emitted from the plasma. In this case the scope was triggered by the rf burst. Whether the modulation is due to direct excitation by the rf, to accelerated electron heating or cooling, etc., is not presently known.

5.3 BURNOUT V GAS ANALYSIS

D. M. Richardson[10] R. V. Neidigh

The neutral gas from a midplane port of the Burnout V liner was analyzed using a Veeco model GA-3 residual gas analyzer. The principal finding was that gas sampled during the operation of the device in the bakeout period and after D-D reaction protons were observed contained low-molecular-weight compounds of carbon and deuterium in amounts up to 5%. The light-hydrogen impurity increased from about 1 ½ to as much as 3% during operation. In these experiments the machine was run with a single hot graphite cathode and with graphite liners in the mirror orifices. The main objective of the experiment, that is, to see if D-D reaction-proton production was dependent on reduction of impurities in the plasma, was not realized. It appears that the sampling rate is too slow (10 min/scan), errors introduced by the analyzer are too great (factor of 5 change in sensitivity over the mass range), and the analyzer's remoteness from the plasma makes it unprofitable to continue the experiment. Information gleaned from the limited experiment is presented.

The sampling probe was metal gasketed and electrically heated and was 3.75 m long with an estimated speed for air of 2 liters/sec. The spectrometer and ion gage were also metal gasketed and electrically heated and were mounted at equivalent positions of the auxiliary pumping system. The estimated speed at the ion gage was 210 liters/sec for air.

Under favorable conditions of rf noise the analyzer required 10 min to scan the range m/e 2 to 90. In order for the mass spectra to be interpretable, it

[10] Reactor Chemistry Division.

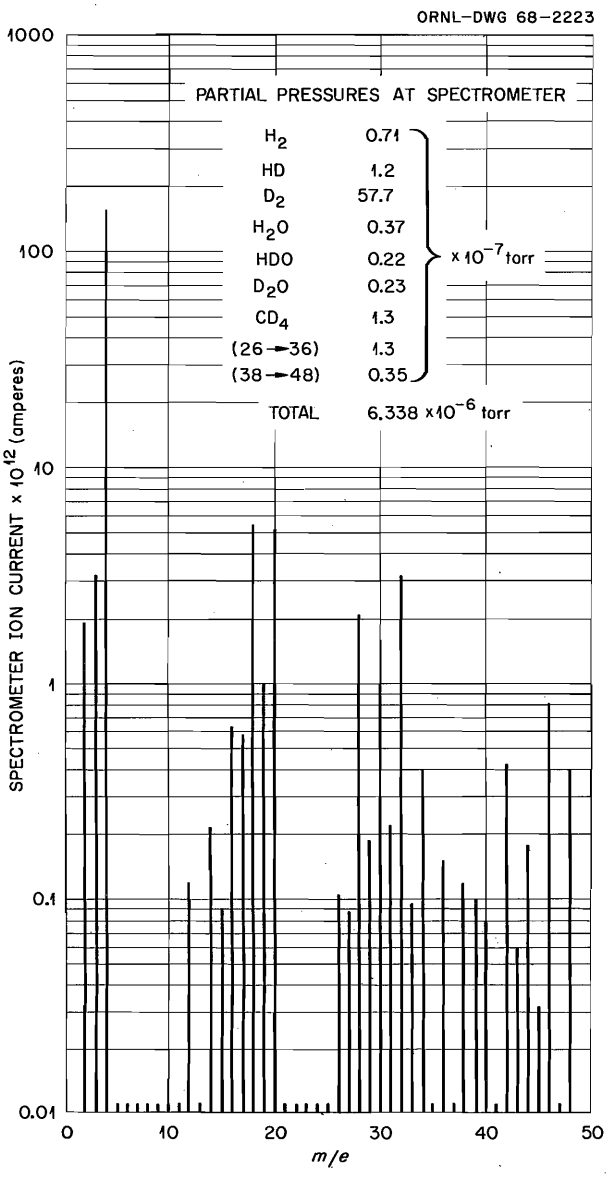

Fig. 5.10. Mass Spectrum at Gas Analyzer During Burnout V Operation.

was necessary that the total pressure as well as other parameters of the Burnout V operation remain steady throughout the scan. Changes in the arc produced changes in gas composition as well as in the rate of arc pumping from the liner.

Mass spectra obtained during Mode II operation are graphed in Fig. 5.10. The spectra are corrected for residual gas background at the spectrometer and normalized in accordance with the transmission characteristics of the GA-3.[11] After comparison of these peak heights with standard patterns,[12] a reasonable identification of gas species was possible, and the fraction of the total spectrometer ion current due to each species was calculated. Since the energies of the ionizing electrons of the ion gage and the spectrometer were nominally identical, it was assumed that the fraction of total ion current due to each species was the same in the ion gage. These fractions of ion gage current were multiplied by appropriate gage factors to obtain the "true" partial pressures at the spectrometer, and are tabulated on Fig. 5.10.

The partial pressures of neutral gas at the inlet to the probe, at normal temperature, were calculated for each gas species according to the estimated speeds of the system. The results are shown in Table 5.1.

Table 5.1. Estimated Pressures at Burnout V Liner During Operation

Species	Pressure (torrs)	Percent of Total
	$\times 10^{-4}$	
H_2	0.075	1.12
HD	0.126	1.88
D_2	6.121	91.13
H_2O	0.039	0.58
HDO	0.023	0.34
D_2O	0.025	0.37
CD_4	0.136	2.02
(*m/e* 26 → 36)[a]	0.135	2.01
(*m/e* 38 → 48)[b]	0.037	0.55
Total	6.717	

[a]Spectra indicate C_2D_2, C_2D_4, and C_2D_6.
[b]Spectra indicate C_3D_x.

[11] *Thermonuclear Div. Semiann. Progr. Rept. Oct. 31, 1966*, ORNL-4063, pp. 128–29.

[12] *Mass Spectral Data Sheets*, American Petroleum Institute, Research Project 44.

5.4 HIGH-PRESSURE ARC

V. J. Meece
R. G. Reinhardt
C. E. Nielsen[13]
W. L. Stirling

5.4.1 Introduction

The objective of high-pressure arc experiments has continued to be the study of the properties of a fully ionized plasma surrounded by neutral gas. The possible thermonuclear importance of the plasma-gas system was discussed, and our procedure for producing it with a pulsed high-current arc in a magnetic field was described in our last report.[14] In the present report, we present new data on arc power balance and radial energy transfer, on the radial potential profile and axial potential gradient, and on the electron density in the arc, and we comment on the significance of this new information.

5.4.2 Observations of the Arc

Total radiation to the walls has been measured with a new radiometer designed to minimize the effects of convection from gas pressure change. Total power output from the arc and its distribution have been measured with a water-cooled enclosure. The gradient in the arc column and also the radial potential profile have been observed by using the rotating probe assembly mentioned in our previous report, and the electron density profile in the arc column has been observed by measurement of the deflection of a beam of 10.6-μ laser light.

Radiometer. – It seemed probable that the convective heating difficulties experienced in using the earlier radiometer were traceable to the fact that there was a large volume beyond the thermocouple into which the gas that might flow through the collimating apertures could be compressed as the pressure in the arc chamber varied with the pulsing of the arc. Accordingly, the new radiometer was designed with the thermocouple placed in the end of the volume of gas with no space beyond for gas flow to occur. We hoped by this means to minimize the amount of transfer of hot gas through the collimating apertures and perhaps to achieve a reading that would be solely a response to the radiation received by the thermocouple with no contribution from the hot gas. Whether or not this objective was completely achieved, the result was a very great reduction in the readings of the thermocouple when exposed to the arc.

The thermocouple with collimating apertures was calibrated by exposure to a frosted light bulb radiating diffusely approximately 1 W/cm^2, and under these conditions it gave 5 μV deflection. This is about the same radiation sensitivity as exhibited by the earlier "radiometers" that gave much larger and erratic readings when exposed to the arc. The new radiometer is only marginally sensitive enough to give usable readings upon exposure to the arc, the maximum deflection being about half the calibration reading, so that we expect observations made with it to show some scatter. Results obtained by scanning across the arc over a vertical distance of 2 in. are plotted in Fig. 5.11. The closest collimating aperture was 3 in. from the arc axis, and the cone of radiation accepted by the collimator includes an area of 1 cm diameter at the arc. Readings at each position were taken by alternately displacing and aligning movable apertures in the collimator that functioned to absorb or admit radiation without changing appreciably the gas flow path to the thermocouple.

We see in Fig. 5.11 that the position of the arc is well defined at all three pressures for which a radiation profile was observed. The definition, which is perhaps surprisingly sharp in view of

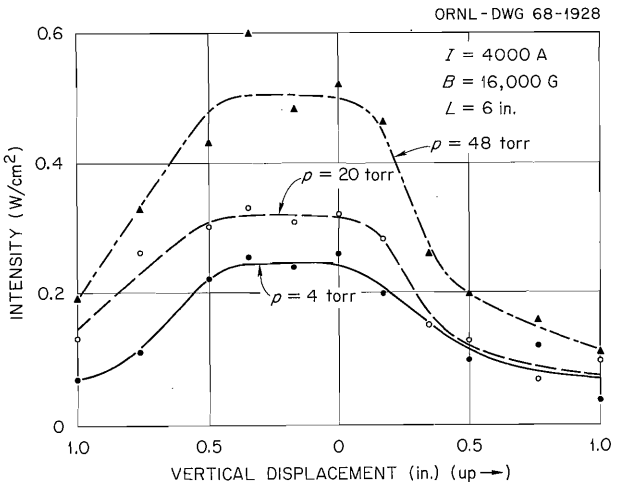

Fig. 5.11. Total Radiation Profiles of the Arc.

[13] Consultant from The Ohio State University.

[14] *Thermonuclear Div. Semiann. Progr. Rept. Apr. 30, 1967*, ORNL-4150, pp. 81–90.

the angular spread allowed by the collimator, suggests that at last we have a genuine radiation observation. On this supposition, we infer from these profiles that (1) the radiation detected mostly originates within a 1.5-cm-radius cylinder and (2) it is not strongly absorbed by the gas, since intensity increases with pressure (in contrast to the observed behavior of the radiation that produces photoconductivity at the same distance), and it is therefore of wavelength >510 Å. All of the spectrum of He^0 and all of the lines from transitions to excited states of He^+ are in this range. The radiation increase with gas pressure is less than proportional. If we may assume both that the radiation source is in thermal equilibrium at all three pressures and that no great temperature change occurs we may conclude that total outward radiation transfer of energy varies likewise less than proportionally with gas pressure.

Energy transfer to the walls represented by the radiation detected is readily estimated. At 20 torrs, $\frac{1}{3}$ W/cm^2 from a cylinder of 9-cm circumference is 3 W/linear cm. The diffuse background level may be $\frac{1}{10}$ W/cm^2 from a 50-cm-circumference cylinder, which is 5 W/linear cm. Even when multiplied by 20 to convert average to instantaneous power transport, these constitute negligible contributions to the total power transport discussed in the next section. This radiation is therefore of interest only for what it can indicate about the shorter-wavelength radiation not transmitted to the walls.

Power Balance. – The observation that only a small fraction of the power input to the arc could be accounted for by radiation transfer directly to the walls left open the question of how the energy is in fact transferred away from the arc. In order to obtain further information about this, we constructed a water-cooled enclosure arranged with several rings along the length of the arc so that the distribution of the power received by the walls could be determined. Water was circulated by separate paths through each of the separate sections of this enclosure, and the power received by each section was determined from readings of flowmeters and thermometers mounted in the water lines. The construction of this enclosure is shown in Fig. 5.12. Power received by all the different rings was observed, but we believe that the power received by the second most nearly central ring is probably the best indication of the radial power transfer from the arc, and accordingly the following figures are plotted showing the power received by the second ring. These figures represent the variation of the power with magnetic field, with gas pressure, with arc length, and with arc current. To simplify comparisons we have in general chosen $B = 16$ kG, $p = 10$ torrs, $l = 8$ in., and $I_A = 4000$ A as a "base point," and (with the exception of Fig. 5.15, which is shifted to $I_A = 5000$ A because of limitations of data available) each heavy curve shows the variation of average power to the second ring as one parameter is varied from this base point. Figure 5.13 shows that the power increases

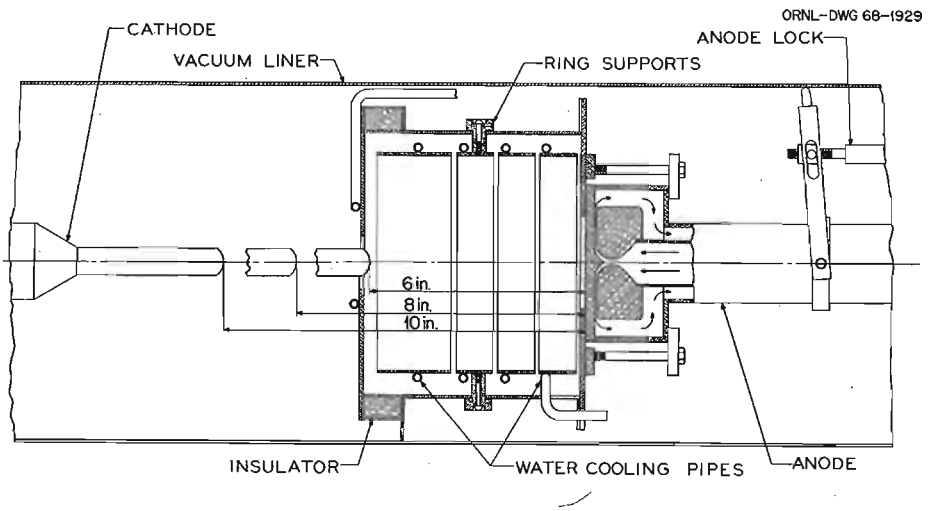

Fig. 5.12. Water-Cooled Enclosure Around Arc – Vertical Section Through Axis. End near cathode and all four rings electrically insulated; outer supporting cylinder at same potential as anode and vacuum liner. Shows also structure of water-cooled anode and positions of cathode for three different lengths of arc.

with magnetic field. The cause for this increase is not known, but we have observed earlier an increase of the total potential difference across the arc with increasing magnetic field. In Fig. 5.14 we see that the dependence of the power received by the center ring upon pressure is relatively slight. The variation with length indicated in Fig. 5.15 is likewise slight except for the 6-in. arc. We interpret this large increase, as the length is decreased to 6 in., as a consequence of direct radiation from the incandescent tungsten cathode. The 8- and 10-in. arcs are produced by withdrawing the tungsten cathode to positions from which very little of the direct radiation can reach the second ring. Power increases with arc current, as shown in Fig. 5.16, more rapidly than linearly. This fact is accounted for at least in part by the increase of the current pulse length that occurs when current peak amplitude is increased. Variation of the pulse length with amplitude is shown in the photographs of Fig. 5.17, in which the top traces represent the total arc potential difference and the bottom traces the arc current. The duration of the current pulse is at most about one 120th of a second, while the duration of the potential pulse is longer than one 120th of a second. We have compared the power input during the arc pulse with the total power accounted for by the various rings of the water-cooled enclosure, the end plates of the water-cooled enclosure, and the anode and cathode. The results in one case are summarized in Table 5.2.

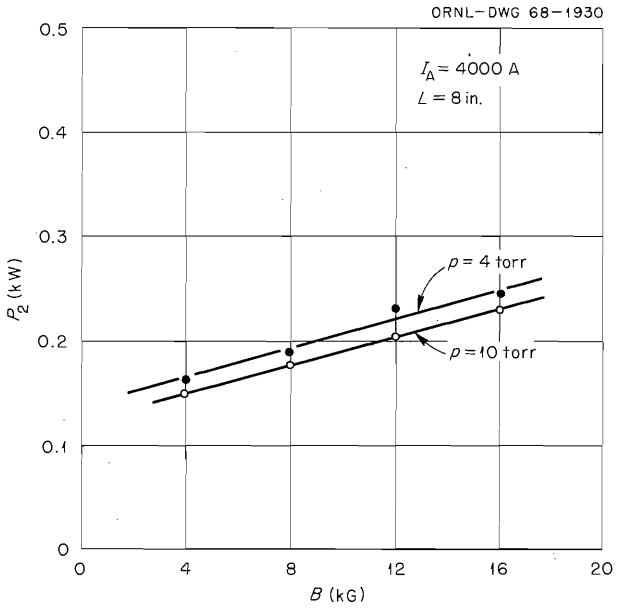

Fig. 5.13. Variation of Radial Power Transport with Magnetic Field. The average power received by the second ring is plotted as the ordinate.

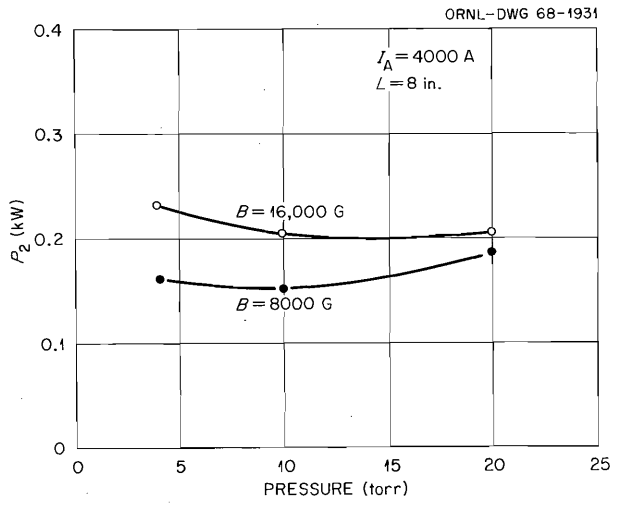

Fig. 5.14. Variation of Radial Power Transport with Pressure.

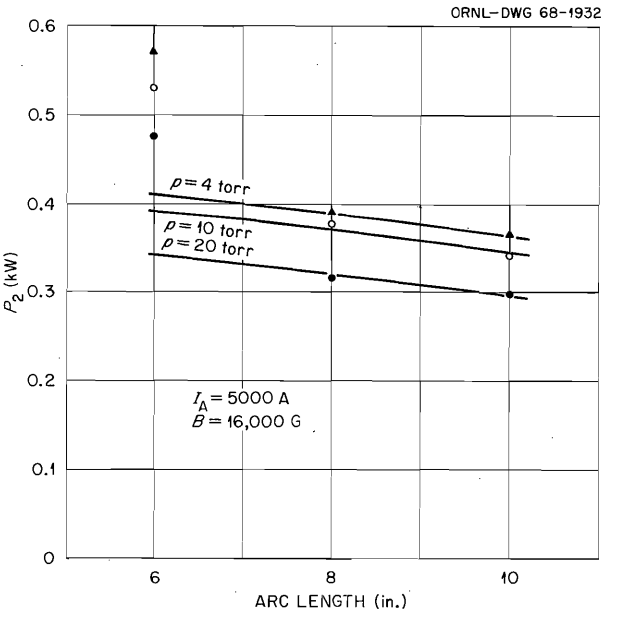

Fig. 5.15. Variation of Radial Power Transport with Arc Length.

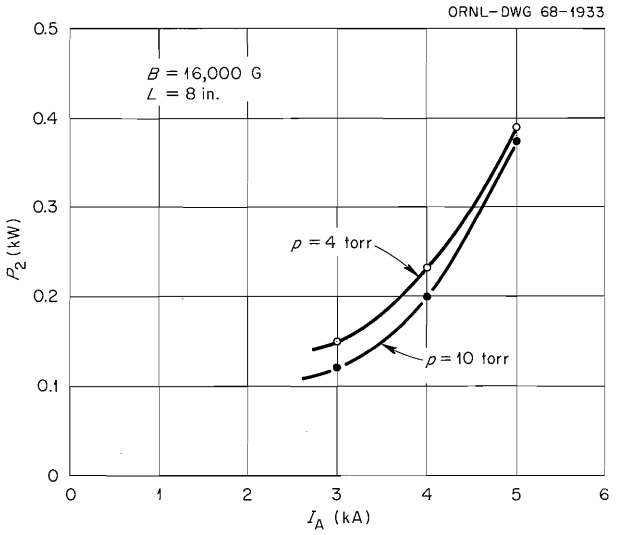

Fig. 5.16. Variation of Radial Power Transport with Arc Current.

Table 5.2. Power Balance in Helium Arc

A.	Electrical input (average power)[a]	9.75 kW
B.	Received by water flowing through electrodes and enclosure:	
	1. Cathode	1.42 kW
	2. Cathode plate	1.41
	3. Ring No. 1 (nearest cathode)	0.57
	4. Ring No. 2	0.30
	5. Ring No. 3	0.27
	6. Ring No. 4	0.24
	7. Anode and end plate	3.12
		7.33 kW
C.	Unaccounted for:	2.42 kW
	1. Estimated radiation from cathode outside of enclosure	1 kW
	2. Additional losses attributable to blast of hot gas through holes in cathode plate from pressure increase at each arc pulse, and to air cooling of uninsulated water lines	

[a]Input integrated over one pulse, 975 J; 10 pulses/sec.

Rotating Probe Assembly. – As mentioned in our last report, we designed rotating probes to measure the axial potential gradient in the arc column. These probes have now been operated successfully and have given not only the desired information about potential gradient in the arc column but also valuable information about the radial potential variations across the arc and in the region around the arc. The arrangement of the rotating probes is shown schematically in Fig. 5.18. The probes are $\frac{1}{16}$-in.-diam tungsten wires mounted on hollow tubes which are rotated at 3200 rpm. The support tubes are cooled by high-pressure air through the concentric air tubes shown in the figure. The probe supports are coupled to 1800-rpm synchronous motors so as to turn 3200 rpm. Rotating at this rate they are not synchronous with the arc pulses, so that the probe wires traverse the arc only every third arc pulse. This design has the advantage of allowing more time for the probe wires to cool between traverses of the arc pulse, and it turns out that a $\frac{1}{16}$-in. tungsten wire under these conditions is not damaged by the arc. The cooling is a combination of thermal conductivity along the tungsten wire, convection cooling by the motion of the wire through the gas in the arc vessel, and radiation. The conduction along the wire is important, as indicated by the fact that when we used tantalum wires of lower thermal conductivity the ends were melted by the arc. The positions of both probes are adjustable longitudinally to allow sampling of potential at various positions along the arc column, and the phasing of the probes is adjustable by turning the motor supports, which are mounted to allow angular adjustment. The direction of rotation of one of the motor shafts is reversible, so that it is possible for the two probe wires to traverse the arc in the same direction or in opposite directions. A typical radial potential profile obtained with a single probe is shown in Fig. 5.19. In addition to the probe trace, this oscillogram contains also the total potential difference across the arc and the arc current. In this oscillogram the probe is rotating while the arc current is changing, so that the probe trace, of course, does not give an instantaneous representation of the potential profile, but rather a representation of the potential profile modified by the concurrent variation of arc current and arc potential as shown in the other traces. It is remarkable that at early and late times in the arc pulse the probe potential is more positive than anything else

PHOTO 90775

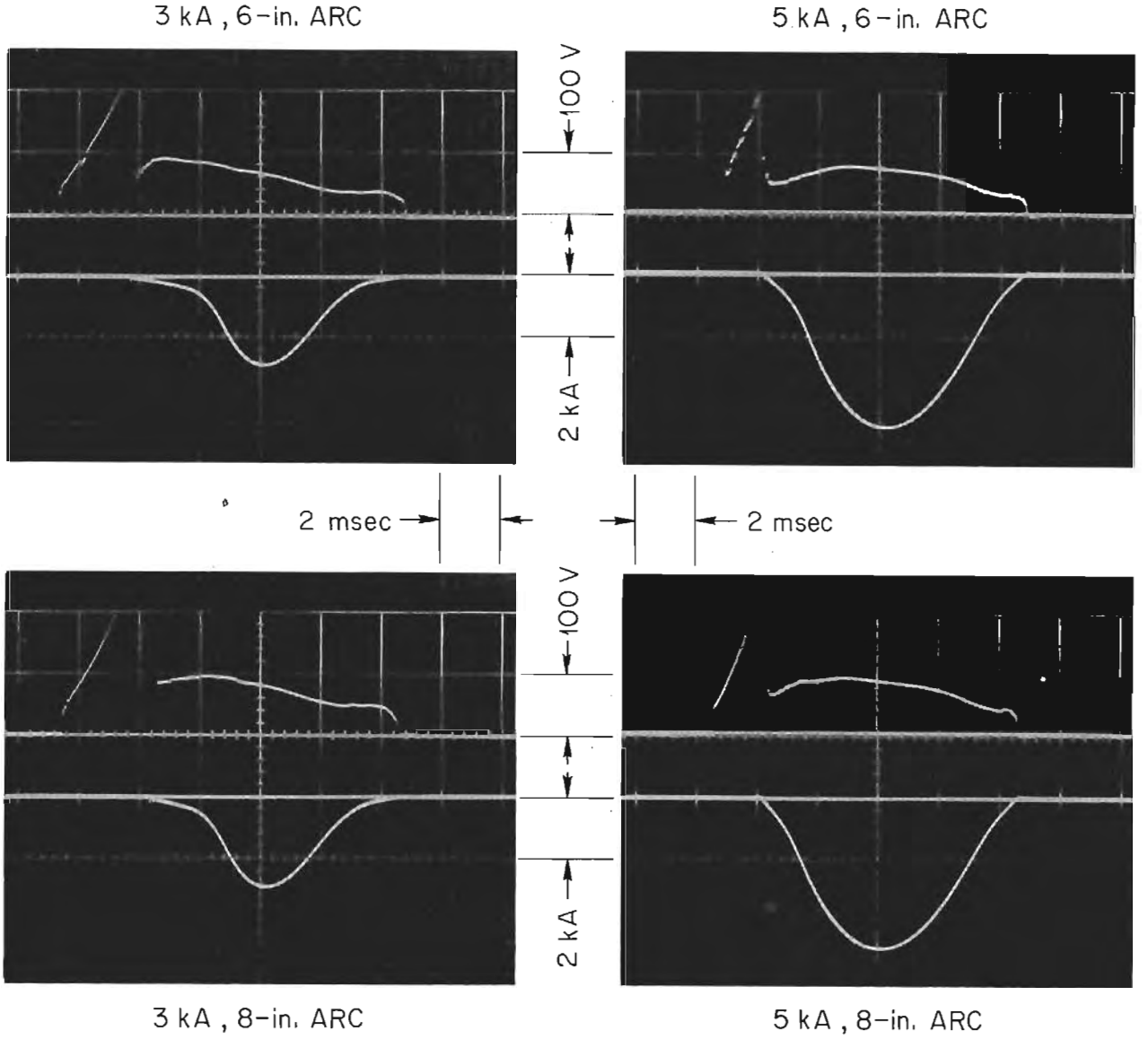

Fig. 5.17. Oscilloscope Traces of Arc Current and Potential Difference. Sample photographs illustrate the dependence of the current and potential pulse shapes upon arc length and peak current. $B = 16$ kG, $p = 10$ torrs.

in the arc chamber. At this time the probe wire is far away from the arc column. We presume that this accumulation of positive charges at the early and late times must indicate energetic ions. These are produced perhaps by instabilities at early times, since it is evident from the potential difference trace that instabilities tend to be present during the building up of the arc current. The ion energy at later times may not be greater than the expected thermal energy of the ions at the arc temperature. In Fig. 5.20, we see the traces from two probes traversing the arc in opposite directions at a distance of $\frac{3}{4}$ in. apart along the arc axis. The probes simultaneously pass close to the axis of the arc, and the disturbance that each probe produces upon the signal of the other is evident. From this result, it seems clear that the best information about axial potential gradient will be obtained not from the simultaneous traversal of the arc by two probes, since each disturbs the

ORNL-DWG 68-1934

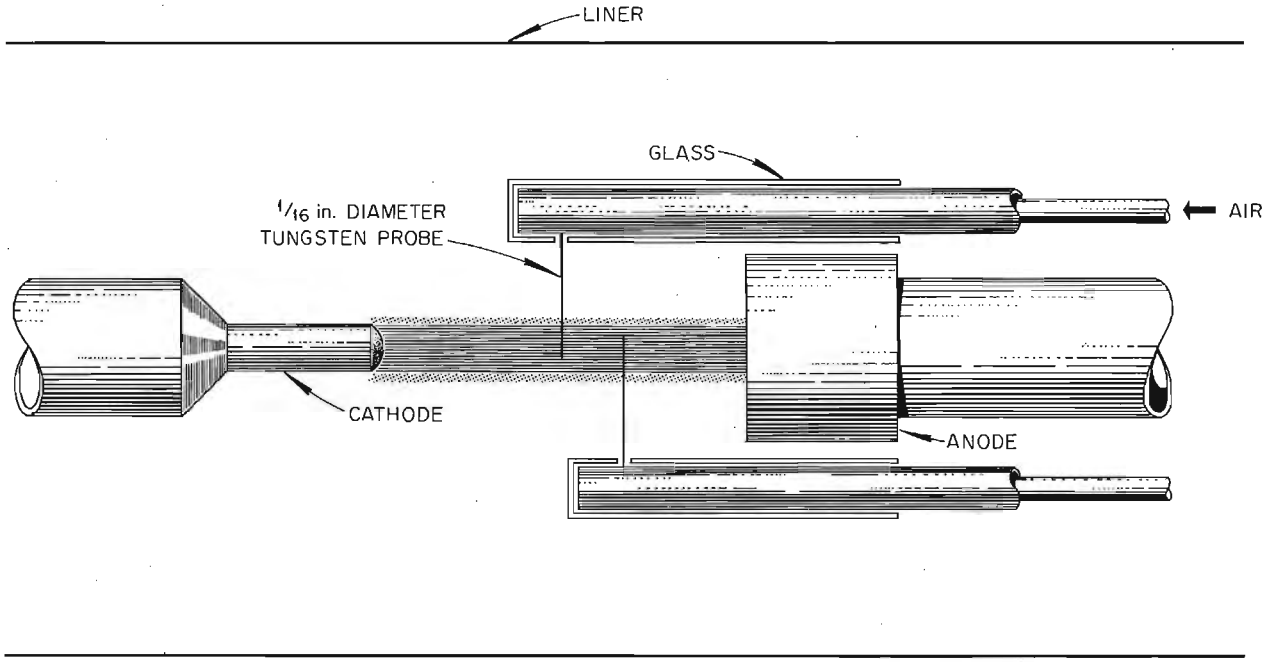

Fig. 5.18. Rotating Probe Arrangement. This is schematic only and does not show such details as probe shaft support bearings, but relative dimensions are approximately correct.

PHOTO 90776

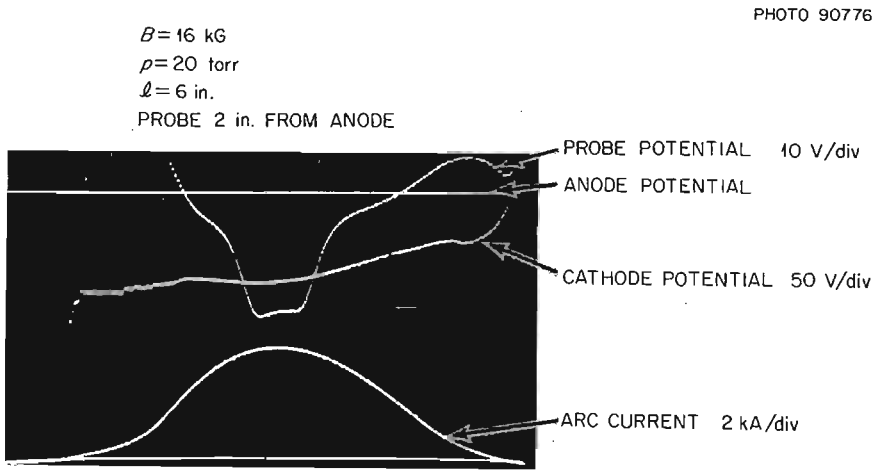

Fig. 5.19. Radial Potential Profile Obtained from Rotating Probe. Probe 2 in. from anode; operating conditions as shown on figure. Probe and cathode potentials measured relative to anode.

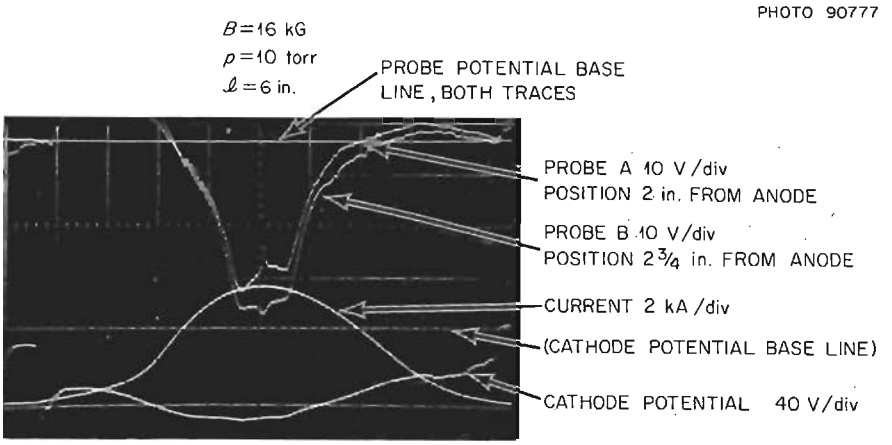

Fig. 5.20. Probe Disturbance of Plasma Indicated by Two Probes. The probes crossed the axis simultaneously, moving in opposite directions with an axial separation of $\frac{3}{4}$ in. Potential difference between them is increased as they pass.

plasma observed by the other, but by observations with a single probe at successively displaced axial positions. Although the single probe will likewise disturb the arc plasma, it may be hoped that the disturbance produced and the relationship of the probe potential to the undisturbed plasma potential will in fact be relatively independent of axial position, so that reasonably good information about axial potential gradient can be derived from the observations of the traces as the probe is displaced axially. Figure 5.21 is a plot of the potentials indicated by a probe traversing the arc during peak arc current at various axial positions. The potential decrease below anode potential is the ordinate and the distance from the anode is the abscissa on this graph. Since the potential is approximately constant as the probe traverses the arc column, these points represent the estimated average probe potential during the probe traversal of the arc. These data were obtained with a stable arc. We have long observed that a fairly small amount of contamination of helium gas by room air as a result of a leak causes the arc to be erratic in behavior and unstable as observed by the magnetic probe. Figure 5.22 is included to show the violent disturbance of the arc potential profile that occurs when there is a substantial leak of room air into the system.

In all of the preceding probe potential traces, the potential observed was developed across a 100-Ω resistor to ground. Resistors between 25 ohms and some thousands of ohms were tried, and the observed probe potential was relatively independent of the load resistor, indicating a very high conductance between the probe and the arc. There was also a high conductance between the probe

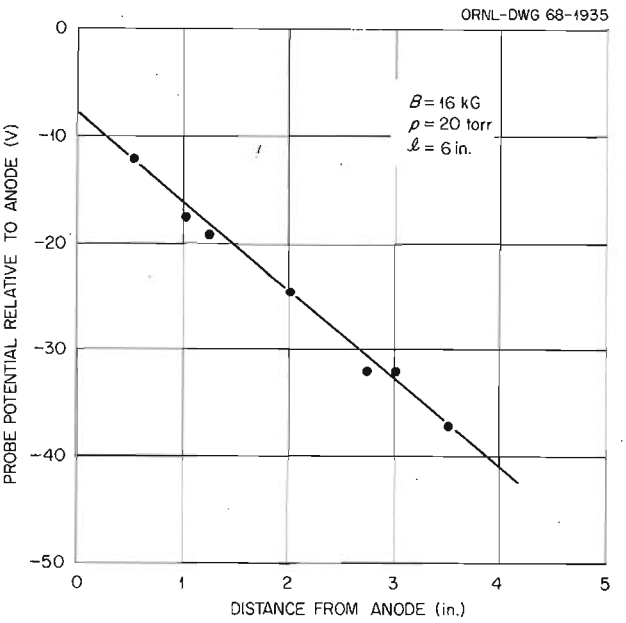

Fig. 5.21. Variation of Probe Potential with Axial Position. Most of the data were taken at 20 torrs pressure as indicated, but results at 10 torrs are indistinguishable.

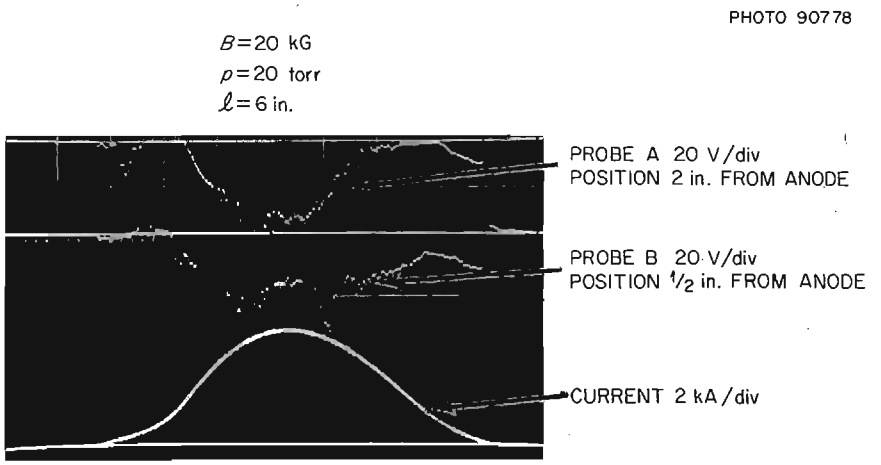

Fig. 5.22. Probe Potential Traces in Contaminated Arc.

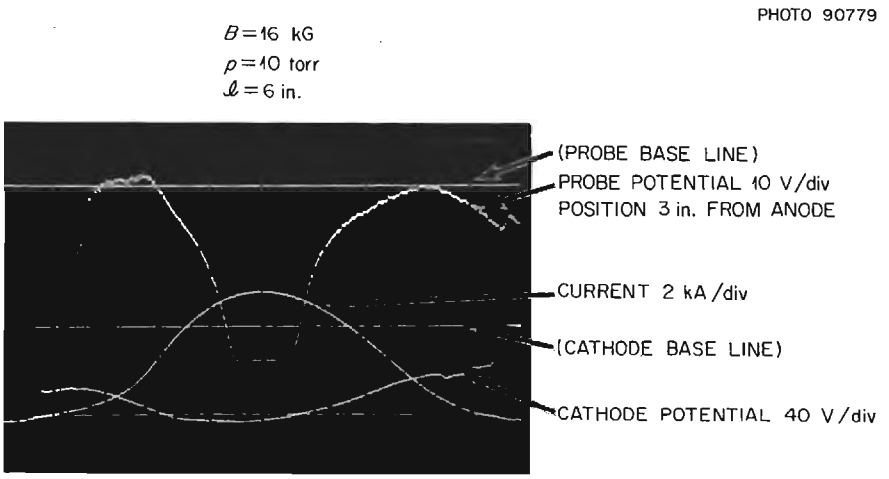

Fig. 5.23. Radial Potential Profile with Stepped Bias on Probe. The four different values of bias applied consecutively to the load resistor are indicated by the traces just visible on the left side of the photograph.

and the region around the arc, since neither the position of the nearly constant potential while the probe traverses the arc nor the shape of the curves in the region near the arc as the probe enters and leaves was modified greatly by a change of the load resistor. In order to obtain, if possible, more information about the nature of this conductivity, we undertook some experiments in which the probe bias was stepped by finite steps, usually about 2 V. An arc potential profile obtained with such a stepped bias is shown in Fig. 5.23. The horizontal segments corresponding to a potential exactly equal to the bias potential for the intermediate values of bias are characteristic of this type of observation. In Fig. 5.24 a similar observation with an enlarged scale is shown. It is clear that the implication of these stepped bias observations is that the conductivity between the probe and its surroundings is relatively small when the bias is close to some potential characteristic of the environment, but that as soon as the bias deviates by some 2 to 4 V from this characteristic potential,

PHOTO 90780

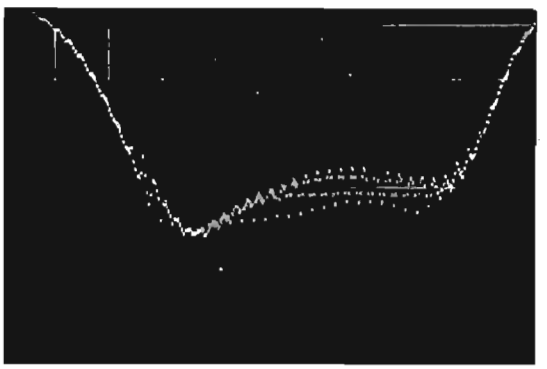

Fig. 5.24. Effect of Stepped Bias, Enlarged Scale.

the conductivity becomes exceedingly large and no additional deviation of the bias will cause the probe potential to vary appreciably. This result is exactly the opposite of what one is accustomed to finding in probe observations of plasmas, which normally are characterized by a conductivity approaching zero as saturation current is reached. In the present observation, there is no indication of a saturation current, but rather the conductivity approaches infinity as the bias deviates appreciably from the floating potential value. Similar results are obtained when the probe is outside of the arc, so that this curious probe characteristic is not simply a function of the relation between the probe and the arc column, but is perhaps to be accounted for by the effect of radiation upon the probe either in producing photoelectric emission or in providing the probe with an adequate source of plasma wherever it may be located. Oscillograms of the probe potential made with the probe traversing the arc at various times show that the potential gradient in the arc column is less when the probe traverses before or after peak current. Roughly the decrease is from the 3 V/cm of Fig. 5.21 to approximately 2 V/cm when the arc current is turning on and turning off.

The fact that direct probing of the arc column yields a larger value of axial potential gradient than we had inferred from the variation of potential drop observed with arc length variation is perhaps partly to be accounted for by variation of the plasma temperature with arc length. We have not obtained adequate data on this matter, but we have repeated the observation of the variation of the total potential drop with arc length, and we continue to find that the variation of total potential is less than it would be if the variation of length simply changed the arc column potential drop proportionally, the resistivity remaining invariant and the end potential drop remaining the same.

The potential indicated by the probe always approaches close to anode potential at a distance of a few centimeters radially from the arc axis. This means that the radial potential gradient is small close to the anode and increases as the probe is moved toward the cathode. The fact that the probe approaches anode potential outside of the arc column implies that the resistance of the probe-plasma system outside of the arc must not be greater than a few ohms, since the probe approaches anode potential even connected to ground with a resistance of some tens of ohms. We suppose that the high conductivity of this region around the arc, which we have verified independently by measuring the conductivity between two electrodes which may be located at various distances from the arc column, results from photoionization of the gas by ultraviolet photons produced within the arc column itself.

Electron Density. – We have determined the radial distribution of electron density by measuring the deflection of a beam of 10.6-μ radiation from a 1-W laser. In addition to the laser, the apparatus used was a telescope consisting of a convex

mirror and a 3-in.-diam concave mirror, by means of which the laser beam was focused to a point slightly beyond the position of the arc column, and a differential thermocouple by which the deflection of the laser beam as it traversed the arc column could be measured. The arc entered and left the arc chamber through Irtran windows, and the differential thermocouple was mounted on a screw thread equipped with a micrometer head so that the thermocouple could be moved across the position of the laser beam focus. For optimum sharpness of definition of the laser beam within the arc the focus should of course be located at the arc, but for optimum sensitivity of the differential thermocouple the focus should be located at the detector. The most satisfactory focus position appeared to be somewhere midway between the two, so that the beam cross section at the arc was 2 or 3 mm and the image at the thermocouple was of about the same magnitude. The differential thermocouple consisted of two copper-constantan junctions of No. 36 wire, each equipped with a rectangular brass receiver of shim stock blackened for maximum absorption of radiation. A rotating disk chopper synchronized with the arc was located at the exit of the laser. The phase of the chopper was adjustable so that the laser beam could be passed through the arc chamber when the arc current was maximum or during the interval of time when the arc was not present. The deflection of the laser beam by the arc column was obtained from the difference of the positions of the differential thermocouple for in-phase and out-of-phase setting of the laser beam chopper. Output of the thermocouple was measured with a Hewlett-Packard 419A microvoltmeter. The laser beam elevation was varied so as to scan across the arc by means of a mirror rotated with a micrometer. The data sequence used in measuring deflection of the laser beam for a particular elevation setting is shown in Fig. 5.25. In this figure the ordinate is the deflection of the microvoltmeter in microvolts and the abscissa is the reading of the micrometer screw. Since this screw had 20 threads to the inch, the distances are given in twentieths of an inch per unit. Three sets of points are shown. The points represented by crosses were taken first, with the phasing adjusted so that the laser traversed the arc chamber when the arc was not present. Then the points represented by circles were taken, with the phase adjusted so that the beam traversed the chamber when the arc was at maximum intensity. Finally, in order to check that no drift had occurred in the position of the laser beam during this interval of time, the points represented by squares were taken. In this case, the average displacement of the laser beam produced by the arc was found to be 0.512 turn of the micrometer screw, which corresponds, in view of the 21-in. distance from the arc to the thermocouple, to a deflection of about 1 mrad. We believe that the reproducibility of the points, as indicated by the agreement of the squares and the crosses, suggests that the actual deflection is known within a few percent of the value obtained. A set of points obtained in this fashion is plotted in Fig. 5.26. The beam deflection, now in inches, is the ordinate, and the position of the beam relative to the arc axis, given in terms of the beam elevation micrometer readings, is the abscissa. On this same scale the cathode diameter of $\frac{3}{4}$ in. is also indicated. The two sets of points are from data taken several hours apart, and their agreement is an indication both of the stability of the system, the arc, and the laser beam and of the accuracy of measurement obtained. The beam deflection traversing the arc depends upon the integral along the path of the beam of the refractive index gradient, which is directly proportional to the density gradient. The refractive index is, of course, slightly less than unity, so the beam is deviated away from the axis of the arc. On Fig. 5.26, two curves are shown, one being the electron density

ORNL-DWG 68-1936

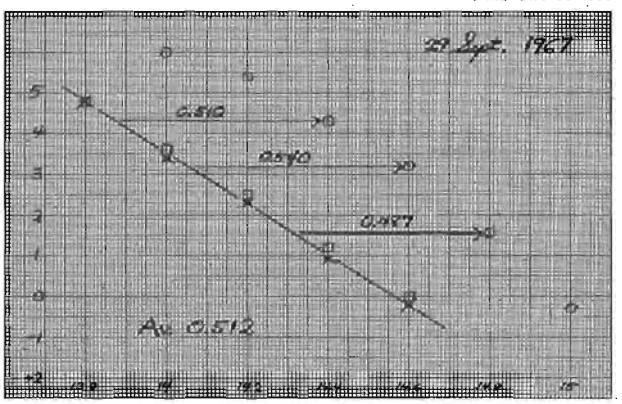

Fig. 5.25. Work Sheet Showing Data Sequence for Measuring Laser Beam Deflection.

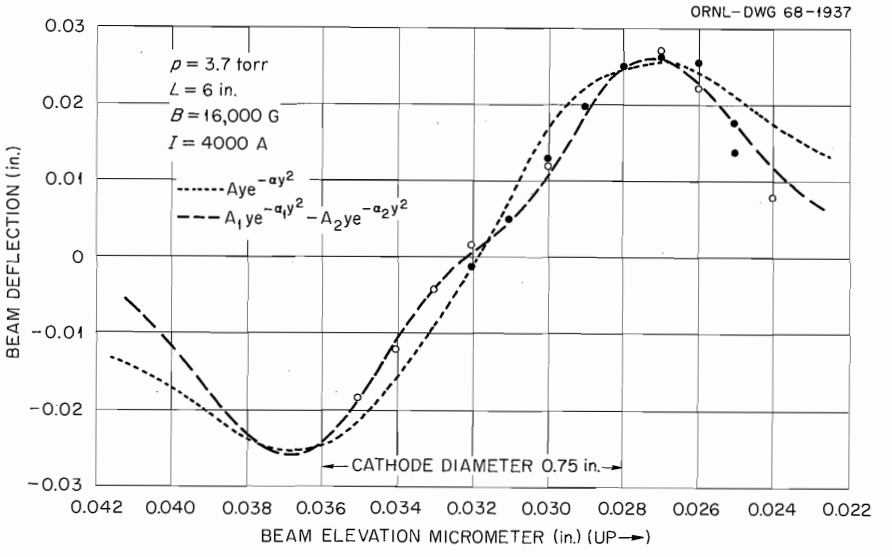

Fig. 5.26. Laser Beam Deflection as a Function of Path Through the Arc. Conditions as indicated.

gradient integrated along the optical path derived from a Gaussian radial distribution of electron density and the other being the similar integral of density gradient derived from a difference of two Gaussians. It will be seen that the difference of two Gaussians gives a relatively good fit to the points, although no effort has been made to optimize the parameters of these two Gaussians; and consequently the radial dependence of electron density can be obtained directly analytically. The result is plotted in Fig. 5.27. We see that the central density is 1.2×10^{16} at 4 torrs pressure, and the width of the distribution is such that there is substantial electron density out to a distance beyond the diameter of the cathode. The magnitude of this central density is in fair agreement with the result obtained earlier by spectroscopic means,[14] but the variation with radius plotted in Fig. 5.27 is entirely different. It is, however, in agreement with results obtained at Munich by an entirely different method, namely the observation of Faraday rotation of a light beam passing lengthwise through the arc column. We have made less complete measurements at higher pressures up to 20 torrs, and the indication is that over this pressure range the electron density varies only slightly. It may be recalled that our earlier optical measurements indicated electron densities of the order of 4×10^{16} at 100 torrs pressure. We do not have measurements with the laser at pressures this high.

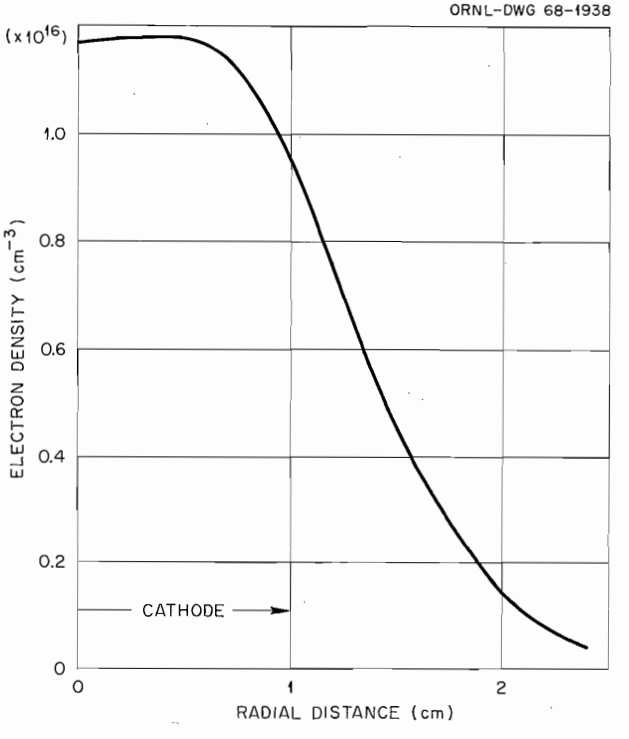

Fig. 5.27. Radial Distribution of Electron Density. This is a plot of the radial distribution function

$$n(r) = 2.69 \times 10^{16} \exp(-0.730r^2) - 1.52 \times 10^{16} \exp(-1.460r^2),$$

from which the line-density gradient represented by the dashed curve of Fig. 5.26 is derived.

5.4.3 Summary and Discussion

The general picture that now emerges from our observations is that of an arc-current-produced plasma surrounded by a layer of partially ionized plasma produced by photoionization. The current-carrying core has a positive resistance characteristic, a maximum potential gradient of about 3 V/cm, a uniform potential across the diameter, and a density of electrons of around $10^{16}/cm^3$ for gas pressures in the range around 10 torrs. Electron density is substantially constant across the diameter of this core, and outside it falls close to zero in a distance about equal to the core radius. The region of measurable photoionization extends considerably farther than this, however. The gas temperature decreases to wall temperature at the walls of the arc vessel 12 cm away, and at the walls only a small fraction of the total energy received is received in the form of radiation. Apparently most of the radiation at the walls is of fairly long wavelength, although there are enough energetic photons there at the lowest pressure to produce measurable photoconductivity of the gas even at that distance.

In all of our recent work the main emphasis has been on operation at low pressures, in general substantially less than 50 torrs. It had become increasingly clear some time ago, as was indicated by the arc profile in the light of ionized helium, that as the pressure is increased above this value the temperature must be decreasing to a point such that we cannot assume full double ionization of the helium in the core. Consequently, useful information about the fully ionized plasma-gas system at higher pressures will be obtainable only by use of higher current densities. It follows that in our recent work we have obtained no new information about the properties of a system with a high enough gas pressure so that the pressure of the gas is the primary contribution to the confinement of the plasma.

We have now established, by three different means of observation, that with sufficient gas pressure the plasma in the arc column is stable. We have evidence for stability from the observations with the magnetic pickup loop, from the observations with the electrostatic probe swept through the arc column, and finally from the observations with the laser beam. The laser beam indicates stability only with respect to such instabilities as would result in substantial fluctuations in electron density that would cause fluctuations of the deflection of the laser beam. Since the sharpness of the laser beam focus appeared to be exactly the same with the arc in the path of the laser beam as with the arc not in the path of the laser beam, we must conclude that to the accuracy of the observations, which we may suppose to be a few percent of the deflections observed, the arc plasma at 4 to 20 torrs gas pressure was not subject to density fluctuations. It should be added, relative to pickup loop and probe data, that we have not simply observed the absence of signals and thus assume stability, but we have observed at the lower gas pressures the presence of instabilities that produced low-frequency signals in the kilocycle range. In the best series of observations exploring this point, we found that as we raised the pressure (in this series of observations we varied both pressure and magnetic field), those signals which were present at the lower pressures disappeared with increase of pressure and were completely absent at pressures of 10 torrs. Having demonstrated that our observing equipment is capable of registering instabilities when present, we feel justified in concluding that under the operating conditions we have been using, the arc is in fact completely stable.

The energy-transfer properties of the system appear to be more difficult to determine than are the stability properties. Although, as described earlier in this report, we now have obtained values for the total radiation reaching the walls, we can still not place a limit on the effect of radiation in transferring energy out of the plasma. As viewed from the walls, there does not appear to be a strong radiation source of the plasma diameter. This fact evidently is a consequence of radiation absorption and emission in the intervening gas. Our first impression after obtaining this result was that a detailed understanding of the situation would be required before any conclusions could be drawn from the experiment regarding larger-size systems. If the transition region were thick, then its character and properties would not be independent of plasma dimensions, and there would be no simple magnitude of energy transfer per unit area characteristic of the plasma-gas boundary.

Fortunately, recent analysis indicates that the scaling problem is probably not so intractable as the thickness of the radiative region initially sug-

gested. First, a general thermodynamic argument shows that the lower limit set by radiation upon energy outflow is set by the value of the net radiation transfer at the cylindrical shell through which the net transfer is a maximum. (It follows of course that if total radiation to the walls is less than net outflow through some cylinder of smaller radius, then radiation at the walls does not provide the desired limit.) Second, consideration of the data provides evidence for the belief that the radiation-transfer maximum is probably fairly sharp and located at a radius between 1 and 2 cm. This location and supposition of thinness rest mainly upon the arc profile in He^+ 4686 Å light and the electron-density profile. The region inside 1 cm is too hot to contain much He^+ or to radiate much from recombination of He^{2+}. The region outside 2 cm contains so much neutral gas that most of the energy radiated from the plasma by collisional recombination of He^{2+} and He^+ or by excitation of He^+ will be strongly absorbed, and the radiation flux outward will therefore decrease more than it is augmented by radiation from neutral He. If then the significant transition region is in fact thin, we may after all use values of radiation per unit area from this transition region of the arc system to predict energy outflow from any size system at the same pressure. Present data do, however, not provide a firm value for this transition region radiation. We know only that it must be less than total measured energy outflow. Since the observed total varies so slightly with pressure, even up to pressures greater than plotted in Fig. 5.14, we believe it plausible to suppose that the radiation is a small fraction of this and contributes less than a few hundred watts per square centimeter of transition region area at pressures up to 50 torrs.

In brief, we have observed that gas stabilizes the arc plasma, we infer that the radiation limit upon energy outflow is set by a thin enough layer to permit extrapolation to larger systems, and we have energy-transfer data that are at present encouraging but still require extension to higher gas pressure before an estimate can be made regarding the suitability of gas-bounded plasmas for fusion purposes.

5.5 FURTHER SPECTROSCOPIC STUDIES OF THE HIGH-DENSITY HELIUM ARC

J. R. McNally, Jr. D. A. Griffin
V. J. Meece

Further spectroscopic studies have been made of the high-density magnetically constrained helium arc.[15] The arc consists of a high-current pulse of about 8 msec duration with the pulse repeating 10 times per second. Currents up to 5000 A have been discharged in helium background gas at pressures of a few torrs of helium. The electrode separation is usually about 15 cm, and the constraining magnetic field is 20,000 G. The cathode is a thoriated tungsten rod (2 cm diam), and the anode is a water-cooled copper target (10 cm diam). Time sampling was performed by using a sector disk synchronized with the peak of the He^+ λ 4686 Å line intensity ($\sim$1 msec out of the 8-msec-long pulse).

The electron excitation temperature in the high-density pulsed helium arc was evaluated by introducing a small feed of nitrogen gas ($\sim$0.5 cc N_2 per second) to give a nitrogen contribution of about 0.2% of the helium. Concentrations above a few percent quenched the He^+ spectra rather severely. Spectral line intensities were measured for N^+ and N^{2+} spectra using a JACO 82,000 spectrometer and corrected for spectrometer efficiency, and the logarithm of the normalized intensities, that is, $\log_{10} I\lambda^3/fg$, was plotted as a function of the excitation energy of the upper electronic state involved in the spectral transition (see Fig. 5.28). The oscillator strengths, f, were taken from Griem.[16] The slope of the line is a measure of the electron excitation temperature. Spectra of doubly ionized nitrogen gave $\overline{T}_e \sim$ 33,000°K; N^+ gave only $\overline{T}_e \sim$ 16,000°K, but this may be due to sampling the outer regions of the arc more preferentially. The spectra of N^{3+}

[15] *Thermonuclear Div. Semiann. Progr. Rept. Apr. 30, 1967*, ORNL-4150, sects. 5.3 and 5.4.

[16] H. R. Griem, *Plasma Spectroscopy*, McGraw-Hill, New York, 1964.

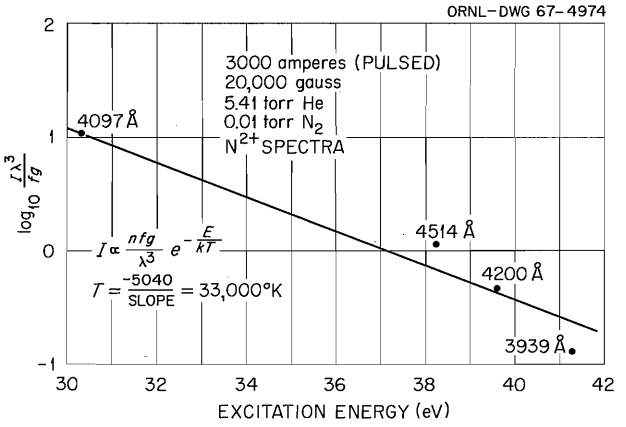

Fig. 5.28. Electron Temperature Determination for Pulsed Helium Arc Using an Impurity of Nitrogen Gas. Plotted are the logarithms of the normalized intensities for several N^{2+} lines vs the excitation energy of the upper state of the transitions; g = statistical weight of upper level = $2J + 1$, f = oscillator strength of upper level, λ = wavelength of transition, I = intensity corrected for spectrometer efficiency.

were too weak to use in this study; however, its low intensity is consistent with the observed electron temperature. The nitrogen intensities were too low to permit the use of Abel inversion techniques to get the profile of the electron temperature vs radius. It is likely that the observed T_e of 33,000°K as measured by doubly ionized nitrogen is more representative of the average electron temperature in the arc core than is that of N^+. Some cooling of the arc by the nitrogen impurity is also to be expected.

Three other methods based on helium lines and helium continua gave *average* electron temperatures ranging from about 40,000 to 54,000°K. However, the continuum methods involve extrapolations of the theoretical curves of Griem,[16] together with a certain amount of uncertainty associated with the correct origin of the continuum.

The use of the helium lines λ 4686 Å (He^+) and λ 5876 Å (He) and the intensity relations of Griem[16] gave an *average* electron temperature of about 46,000°K (not corrected for emission coefficients). Abel inversion of data on these two lines, using the method of Bockasten[17] and a CDC-1604 computer, gave the radial temperature profile shown in Fig. 5.29 for a 5000-A arc at 5 torrs helium background pressure. The electron temperature from this helium spectral "thermometer" method is somewhat higher near the axis than the average excitation temperature of 33,000°K measured by using N^{2+} lines observed from a 3000-A pulsed arc; however, it is still significantly lower than the figure of 400,000°K reported by the Munich group for similar pulsed helium arcs.[18] The higher magnetic field, restricted arc radius, and lower ambient gas pressures for the Munich experiments probably contribute to their higher electron temperatures.

Vidal[19,20] has recently extended the line-merging method of Inglis and Teller[21] to permit rapid analysis of electron densities in thin, homogeneous plasmas at an electron density of

[17]K. Bockasten, *J. Opt. Soc. Am.* **51**, 943 (1961).

[18]See, for example, P. Grassman, thesis, Technische Hochschule Munich (1966).

[19]C. R. Vidal, *J. Quant. Spectry. Radiative Transfer* **6**, 461 (1966).

[20]*Ibid.*, p. 575.

[21]D. R. Inglis and E. Teller, *Monthly Notices Roy. Astron. Soc.* **98**, 694 (1938); *Astrophys. J.* **90**, 429 (1939).

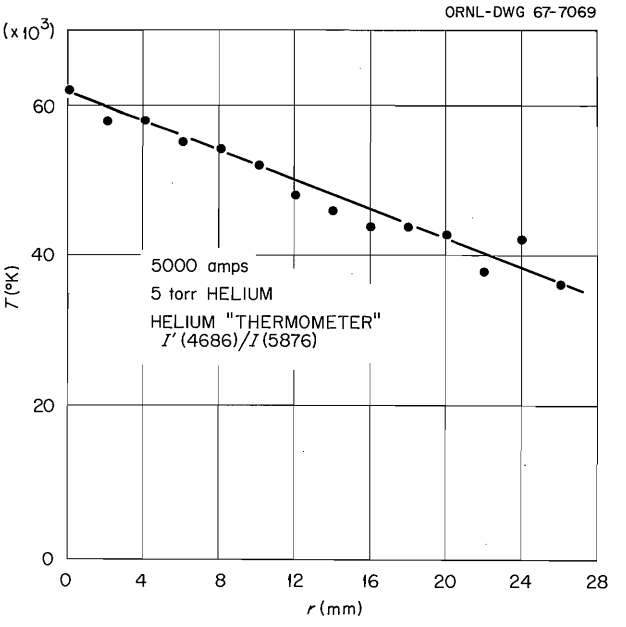

Fig. 5.29. Electron Temperature Radial Dependence Obtained from Abel Inversion of Intensities of λ 4686 Å (He^+) and λ 5876 Å (He) Using the Method of Griem.[16]

3.4×10^{14} e/cm^3 using the $1s2p\ ^3P^o - 1snd\ ^3D$, $1sns\ ^3S$ series. We have attempted to use this method for the much higher density pulsed helium arc (which gives electron densities of about 10^{16} e/cm^3), without success. The spectral background between lines (as well as the line shape itself) does not vary in a way expected for line merging, being somewhat more intense than a merging series of broadening lines. We tentatively attribute this intense background to the recombination continuum expected for the $He^{2+} + e$ recombination into the $n = 4$ and $n = 5$ states of He^+ (and partly to that of $He^+ + e$ into the $1s2p\ ^1P^o$ state of He). These filled states in He^+ subsequently contribute to the strong $4 \rightarrow 3$ transition (λ4686 Å) and $5 \rightarrow 3$ transition (λ 3203 Å). The intensity of the recombination continua would be expected to vary roughly as the square of the electron density, whereas the Vidal line merging method depends on the two-thirds power. Electron densities obtained by the Vidal method were up to $\overline{n_e} = 6 \times 10^{16}$ e/cm^3, but the high spectrum background biases the data upwards. No acceptable electron densities came out of the Vidal method for any arc currents or ambient gas pressures, so we are forced to rely on those obtained previously[15] from the Holtzmark broadening of He^+ lines (n_e up to 2×10^{16} e/cm^3 at the axis for 10 torrs of helium). The Inglis-Teller method,[21] which does not depend on the intensity level of the background, suggested *average* densities of less than 10^{16} e/cm^3, in rough agreement with the Holtzmark broadening results.

5.6 DISPERSION OF ION ACOUSTIC WAVES[22]

I. Alexeff K. Lonngren[23]
W. D. Jones D. Montgomery[24]

5.6.1 Introduction

In previous experiments on externally generated ion acoustic waves, we were unable to propagate the waves at frequencies near the ion plasma frequency.[25] A similar observation was reported by Tanaca *et al.*,[26] who observed a slowdown and subsequent termination of propagation for spontaneously excited ion acoustic waves. The theoretical justification for this cutoff is that as the frequency of the wave is increased toward the ion plasma frequency, the velocity of the ion acoustic wave slows down toward the ion thermal velocity, where ion Landau damping rapidly causes the wave to disappear.[27]

A set of experiments that apparently contradicts the above interpretation has recently been presented by Sessler,[28,29] who has seen signals propagated above the ion plasma frequency that increase in velocity as the frequency is increased.

5.6.2 Experiments and Results

Recently, we have performed two experiments that tend to clarify the relation between the observations of Sessler and the theory. In the first experiment, we transmit pulsed wave trains between two electrodes in the fashion described in ref. 25. However, in place of flat plates for transmitting and receiving electrodes, we use thin wires oriented at 90° to the path of propagation of the wave. In this fashion, we cause the electric field of the electrodes to be cut off by a geometrical convergence factor that goes as the inverse radius of the distance from the wire. This added geometrical convergence factor results in smaller plasma sheaths around the transmitting and receiving electrodes, and improves the coupling between the plasma and the electrodes at higher frequencies. To improve the detection sensitivity, we use a positively biased electron-collecting probe as a receiver[30] and a Princeton

[22]K. Lonngren *et al.*, *Phys. Letters* **25A**, 629 (1967).

[23]Summer Participant, University of Iowa.

[24]Consultant and Summer Participant, University of Iowa.

[25]W. D. Jones and I. Alexeff, *Proceedings VII International Conference on Phenomena in Ionized Gases* (ed. by B. Perovic and D. Tosic), vol. 2, p. 330, Gradevinska Knjiga, Beograd, 1966; I. Alexeff and W. D. Jones, *Phys. Rev. Letters* **15**, 286 (1965).

[26]H. Tanaca, M. Koganei, and A. Hirose, *Phys. Rev. Letters* **16**, 1079 (1966).

[27]B. D. Fried and R. W. Gould, *Phys. Fluids* **4**, 139 (1961); L. Spitzer, *Physics of Fully Ionized Gases*, Interscience, New York, 1963.

[28]G. M. Sessler, *Proceedings VII International Conference on Phenomena in Ionized Gases* (ed. by B. Perovic and D. Tosic), vol. 2, p. 322, Gradevinska Knjiga, Beograde, 1966.

[29]G. M. Sessler, *Phys. Letters* **16**, 277 (1965); *Phys. Rev.* **17**, 243 (1966); *Phys. Letters* **22**, 363 (1966).

[30]I. Alexeff and W. D. Jones, *Appl. Phys. Letters* **9**, 77 (1966).

Applied Research waveform eductor as a coherent detector.

Figure 5.30 shows the type of data we see with the improved, more sensitive apparatus. The bottom trace shows the sine-wave burst applied to the transmitter electrode. The upper trace shows the received signal, consisting of three separate parts. The first part, labeled *A*, is a directly coupled electrostatic signal, lasting only for the duration of the driving signal. The other two signals, labeled *B* and *C*, provide a possible explanation of the anomalous results reported by Sessler. As the frequency of the transmitter signal is increased toward the ion plasma frequency, the received signal splits into a faster and a slower, weaker component. The slower component, labeled *C*, is apparently the ion acoustic wave, and fits the theoretical dispersion relation. The faster component, labeled *B*, is observed to propagate above the ion plasma frequency, and

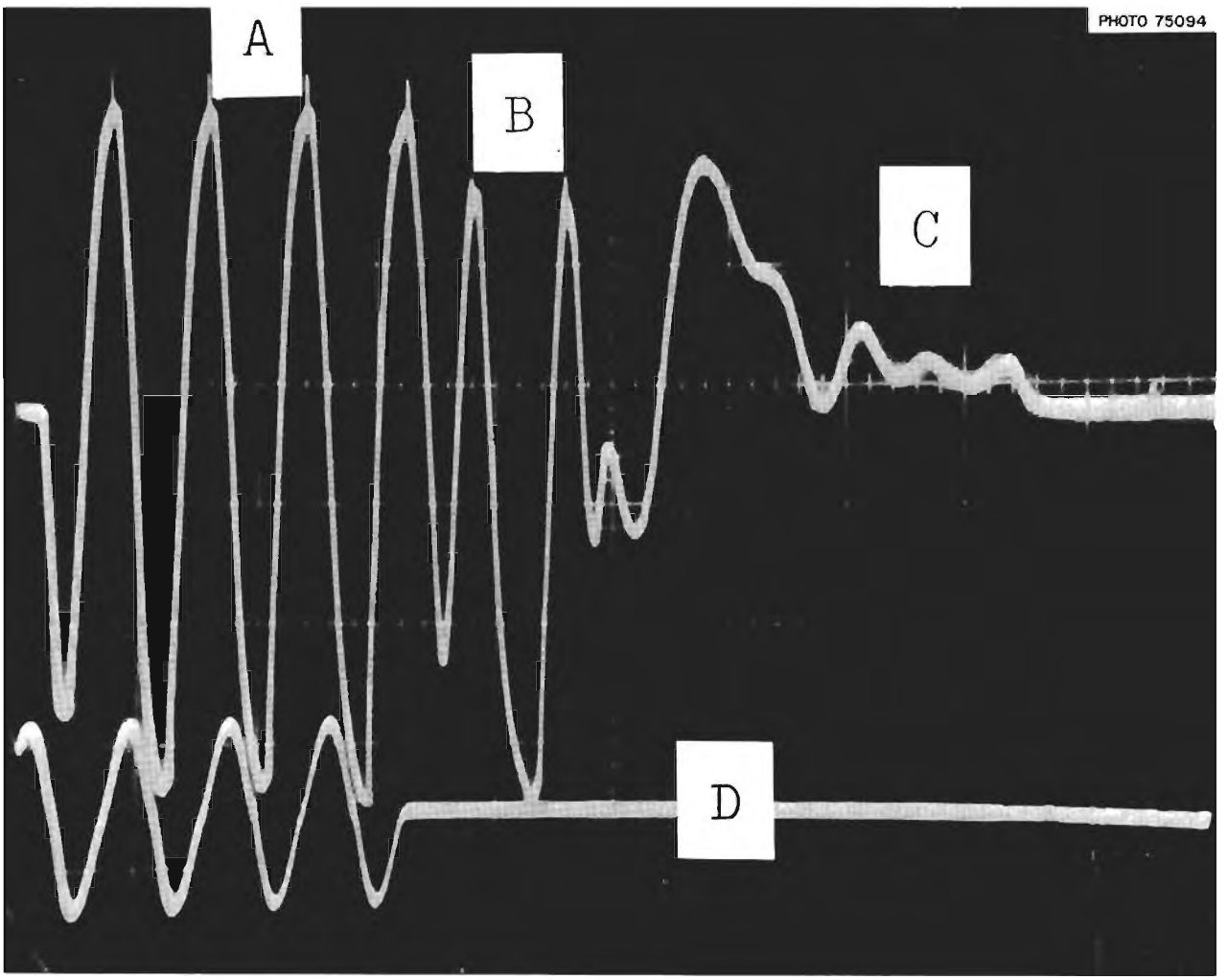

Fig. 5.30. Observation of Transmitted and Received Signals. (*A*) Directly coupled signal, (*B*) "fast" signal, (*C*) ion acoustic wave signal, and (*D*) driving signal. The gas is xenon. The time scale is 20 μsec/cm. The probe spacing is 2 cm, but the wave travels a shorter distance of 1.7 cm because of sheath effects. The ion plasma frequency is 122 kc. The wave frequency is 60 kc. The observed slowdown is computed from the velocity of individual waves in the packet as observed at successive probe spacings. The velocity of the packet itself is difficult to work with because of strong dispersive effects.

does increase slightly in velocity as the frequency is further increased. From these data, we suspect that the faster component is that studied by Sessler. Note that in Sessler's published pictures of his receiver signal, a slower, weaker component appears to be visible.[28]

Figure 5.31 shows a plot of the experimentally observed velocities of the fast and slow components, as a function of frequency. The upper set of points gives the measured velocity of the faster component. As discussed below, we feel that this signal is due to bursts of accelerated ions. The lower set of points gives the velocity of the slower component, which we believe to be the ion acoustic waves. At the highest frequency at which the ion waves could be observed, approximately 0.7 of the ion plasma frequency, the velocity was 35% less than the usual (low-frequency) ion acoustic wave value.

Two theoretical curves have been superimposed on the graph. The lower solid curve gives the theoretical dispersion of ion acoustic waves, as predicted by macroscopic theory.[31] The upper solid curve is based on the dispersion theory of Fried and Gould,[27] their theory being extended to cover the plasma conditions appropriate to these experiments. The upper curve is normalized to the data point through which it passes, thus giving a theoretical low-frequency (nondispersed) velocity. (This nondispersed velocity is in good agreement with that expected on the basis of the plasma electron temperature.) This velocity was then used to draw the theoretical dispersion curve predicted by the macroscopic theory. A priori, the macroscopic theory seems to fit the observations better than the more comprehensive theory of Fried and Gould. We feel, however, that this may not be true. In the first place, the main source of disagreement is the two data points at the higher frequencies. It is at these points where Landau damping becomes severe, and accurate measurements are difficult to make. In the second place, if we have overestimated ω_{pi} by as much as 25%, which could easily happen, the agreement between the Fried and Gould theory and experiment becomes much better.

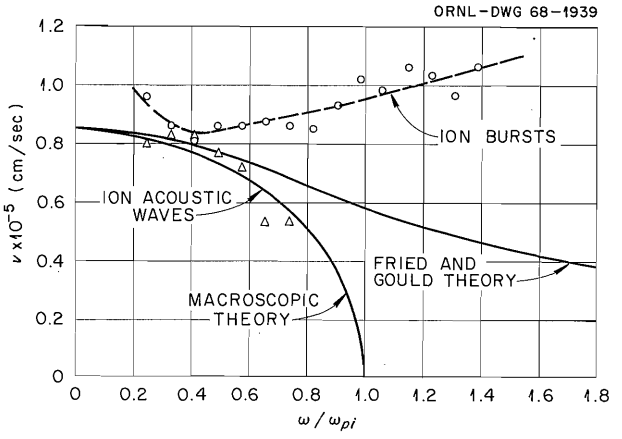

Fig. 5.31. Experimental Velocity as a Function of Frequency. The upper set of points is thought to be produced by groups of ions accelerated by the voltage sine-wave bursts applied to the transmitting electrode. The lower set of points, showing the expected decrease in velocity as $\omega \rightarrow \omega_{pi}$, is thought to be due to ion acoustic waves, also generated at the transmitting electrode by the applied time-varying potential. The two solid curves show the theoretically expected dispersion for ion acoustic waves for two different plasma models. The plasma used was xenon.

To study the properties of the faster signal further, we used a pair of grids for both the transmitting and the receiving electrode systems. This arrangement is similar to that of Sessler, but may have important differences from the two-wire system. However, we again receive both a fast and a slow signal.

We conjecture that the fast signal may be a burst of ions accelerated by the grids. We find, for example, that the velocity of the faster signal varies as the square root of the transmitter voltage. When we use a single transmitter pulse, and a plasma formed of a mixture of neon and xenon, we obtain two received pulses that correspond to the different times of flight of the two masses. In short, we have a time-of-flight spectrometer. For ion wave propagation, one expects, and we have observed in past experiments,[32] only one wave, propagating with a velocity which lies between the ion acoustic speeds of the two components.

---

[31] L. Spitzer, *Physics of Fully Ionized Gases*, 2d ed., sect. 3.2, Interscience, New York, 1962.

[32] I. Alexeff, W. D. Jones, and D. Montgomery, *Bull. Am. Phys. Soc.* **12**, 770 (1967).

5.7 ANOTHER LOOK AT OLD DATA: VARIATION OF ION ACOUSTIC WAVE PROPERTIES WITH ELECTRON TEMPERATURE

I. Alexeff W. D. Jones

5.7.1 Introduction

In an earlier report[33] we described the effects on ion acoustic waves of varying the electron temperature. In that report we discussed, primarily, the dependence of the ion acoustic wave velocity and of ion-wave Landau damping on electron temperature; however, a crude effort was made, also, to extract a value for the plasma ion temperature from the velocity-variation data. An uninterpreted observation was a relatively small temperature-dependent damping persisting at electron temperatures above which Landau damping was expected to occur. In the present report we describe a more accurate way to determine T_i from the old data and present an explanation for the slight damping of the wave at high electron temperatures. Also, the old data provide an independent experimental value for γ_e, the electron compression coefficient. The new value for ion temperature is 0.05 eV, as compared with the value of 0.03 eV suggested in the earlier report. The damping at high electron temperatures can be explained as gas damping. An experimental $\gamma_e = 0.86 \pm 0.03$ is found, as compared with the $\gamma_e = 1$ predicted theoretically.

5.7.2 Determination of Ion Temperature

The velocity of propagation of an ion acoustic wave in the nondispersive region is given by

$$v = (kT_e + 3kT_i)^{1/2}\, m_i^{-1/2} ,$$

where k is Boltzmann's constant, T_e and T_i are electron and ion temperatures, respectively, and m_i is the ionic mass.[33,34] In the earlier report, T_i was determined by treating T_i as an adjustable parameter in the preceding equation to obtain a visual line of best fit on a log-log plot of v_{exp} vs T_e. In the present determination we make a linear plot of v_{exp}^2 vs T_e, noting that this should yield a straight line whose intercept on the v_{exp}^2 axis depends only on T_i (and m_i, which is known). Figure 5.32 shows such a plot of the old data. Using least-squares line fitting, the equation of the line of best fit is found to be

$$v_{exp}^2 = (0.626T_e + 0.115) \times 10^{10}\ (\text{cm/sec})^2 ,$$

with a standard deviation of 0.0641×10^{10} $(\text{cm/sec})^2$. The heavy line superimposed on the graph is the line of best fit. From the intercept of the line of best fit and a calculation of the standard deviation of the intercept, an ion temperature value of 0.0523 ± 0.0114 eV is found. Thus the ions are about twice room temperature. We feel that this represents a fairly accurate technique for determining ion temperature for this type of plasma.

5.7.3 Gas Damping vs T_e

Figure 5.33 shows the original damping data contained in the earlier report.[33] Also shown is

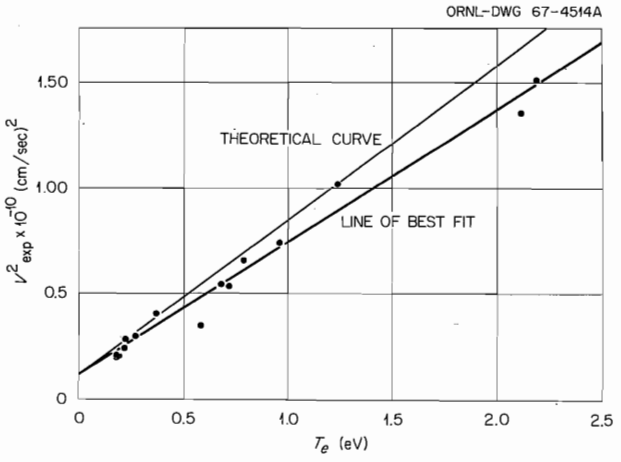

Fig. 5.32. Determination of Plasma Ion Temperature by Measuring the Ion Acoustic Wave Velocity Dependence on Electron Temperature. The heavy line is a calculated least-squares line of best fit; the intercept on the vertical axis gives $T_i = 0.0523 \pm 0.0114$ eV; the slope gives $\gamma_e = 0.86 \pm 0.03$. The theoretical curve uses the experimental intercept and assumes $\gamma_e = 1$. The gas used was xenon.

[33] I. Alexeff and W. D. Jones, *Thermonuclear Div. Semiann. Progr. Rept. Oct. 31, 1966*, ORNL-4063, sect. 5.3, p. 52.

[34] I. Alexeff, W. D. Jones, and D. Montgomery, "Effects of Electron Temperature Variation on Ion Acoustic Waves" (accepted for publication in *Physics of Fluids*).

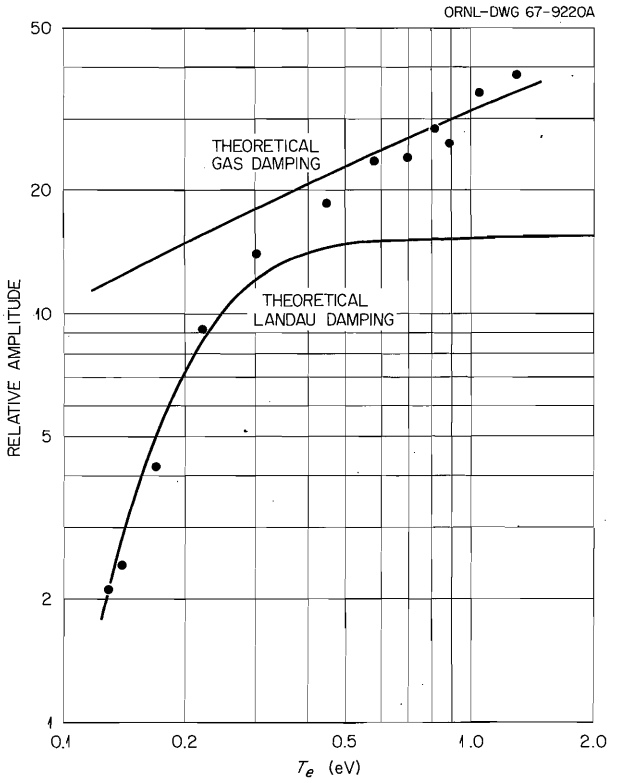

Fig. 5.33. The Experimentally Observed Variation in Amplitude of Ion Acoustic Waves as a Function of Electron Temperature. At high electron temperatures the relatively weak damping is gas damping, whereas at low electron temperatures the much stronger damping is Landau damping.

the theoretical Landau damping curve, showing that Landau damping cannot account for the relatively weak damping occurring at the higher electron temperatures. The upper theoretical curve, showing the expected gas damping rate for changing electron temperature, is the new feature. Comparison of this curve with the experimental points suggests that the damping observed above the Landau damping threshold temperature is due simply to ion-neutral collisions.[35,36] The measured values of 1 millitorr and 0.05 eV for neutral gas pressure and ion temperature, respectively, were used in the theoretical calculation of gas damping rate.

[35]Y. Hatta and N. Sato, *Proceedings V International Conference on Phenomena in Ionized Gases* (ed. by H. Maecke), vol. 1, p. 478, North-Holland Publishing Co., Amsterdam, 1962.

5.7.4 Experimental Value for γ_e

Although the dispersion theory, when applied under the conditions of the present experiment, predicts a velocity given by

$$v = (kT_e + 3kT_i)^{1/2} m_i^{-1/2} ,$$

the more general expression is[33,34]

$$v = (\gamma_e kT_e + \gamma_i kT_i)^{1/2} m_i^{-1/2} .$$

Thus the theory predicts that γ_e should be 1 for our experiments. Using least-squares line fitting, we found the line of best fit for the experimental data to be given by

$$v_{exp}^2 = (0.626T_e + 0.115) \times 10^{10} \text{ (cm/sec)}^2 .$$

Setting the T_e coefficients of the general and experimental expression for velocity equal to each other, and using the calculated standard deviation of the slope for the experimental curve, gives $\gamma_e = 0.86 \pm 0.03$. This is in fairly good agreement with the $\gamma_e = 1$ value predicted theoretically and is in good agreement with a previous independent experimental determination of γ_e.[37] Thus we have again verified that the ion acoustic wave propagation in our discharge tube plasmas involves collisionless isothermal compression of the electron gas.

5.8 SYMMETRIC DISCHARGE

O. C. Yonts E. D. Shipley

Study of electron transport in the PIG and the symmetric arc has been continued and will be reported in full in a separate paper. One of the more interesting portions will be reported here.

The change in cylinder current with cylinder voltage in the symmetric arc has been previously reported.[38] It has been found that if cylinder voltage is pushed beyond the point where cylinder current and large rf signals appear, there is a second, more gradual, very large break in current,

[36]I. Alexeff and W. D. Jones, *Thermonuclear Div. Semiann. Progr. Rept. Apr. 30, 1964*, ORNL-3652, sect. 4.6, p. 56.

[37]I. Alexeff and W. D. Jones, *Phys. Rev. Letters* 15, 286 (1965).

[38]*Thermonuclear Div. Semiann. Progr. Rept. Apr. 30, 1967*, ORNL-4150, sect. 5.6.

accompanied by a rise in rf continuum. In fact, approximately 80% of the anode current shifts to the cylinder or to the end walls. For example, 850 mA of anode current became 150 mA after V_c, the critical voltage, was reached. Of the 700 mA that left the anode, 480 mA appeared on the cylinder. The remainder appeared on the end walls of the system. The system appears much as a "mode II" discharge, except that electrons instead of ions are flowing outward from arc to cylinder across the magnetic field. A natural experiment was to try to superimpose this discharge on a mode II discharge and to study this interaction.

A schematic diagram of the equipment is shown in Fig. 5.34. The cylindrical electrode surrounding the discharge is split and fed from the tuned circuit as shown. The arc is established in the usual fashion, and then pressure is reduced until the mode II discharge is established. This is shown by the positive ion current trace of the Faraday cup. Figure 5.35*a* shows a typical trace using argon. Sweep time is 10 μsec/cm. The time variation of current is caused by the rotating "flute" of the mode II discharge. The following series of photographs, Figs. 5.35*b*–5.35*g*, show what happens as the cylinder voltage is raised. Figure 5.35*b* has cylinder voltage plus 68, the floating voltage during mode II operation. The parameter in each photograph is the 68 V plus an applied voltage to give the indicated cylinder voltage. The interesting point here is that both the frequency and the amplitude of oscillation decrease as the cylinder voltage increases. The 200 V required to stop the oscillation was approximately the V_c mentioned above. Electron

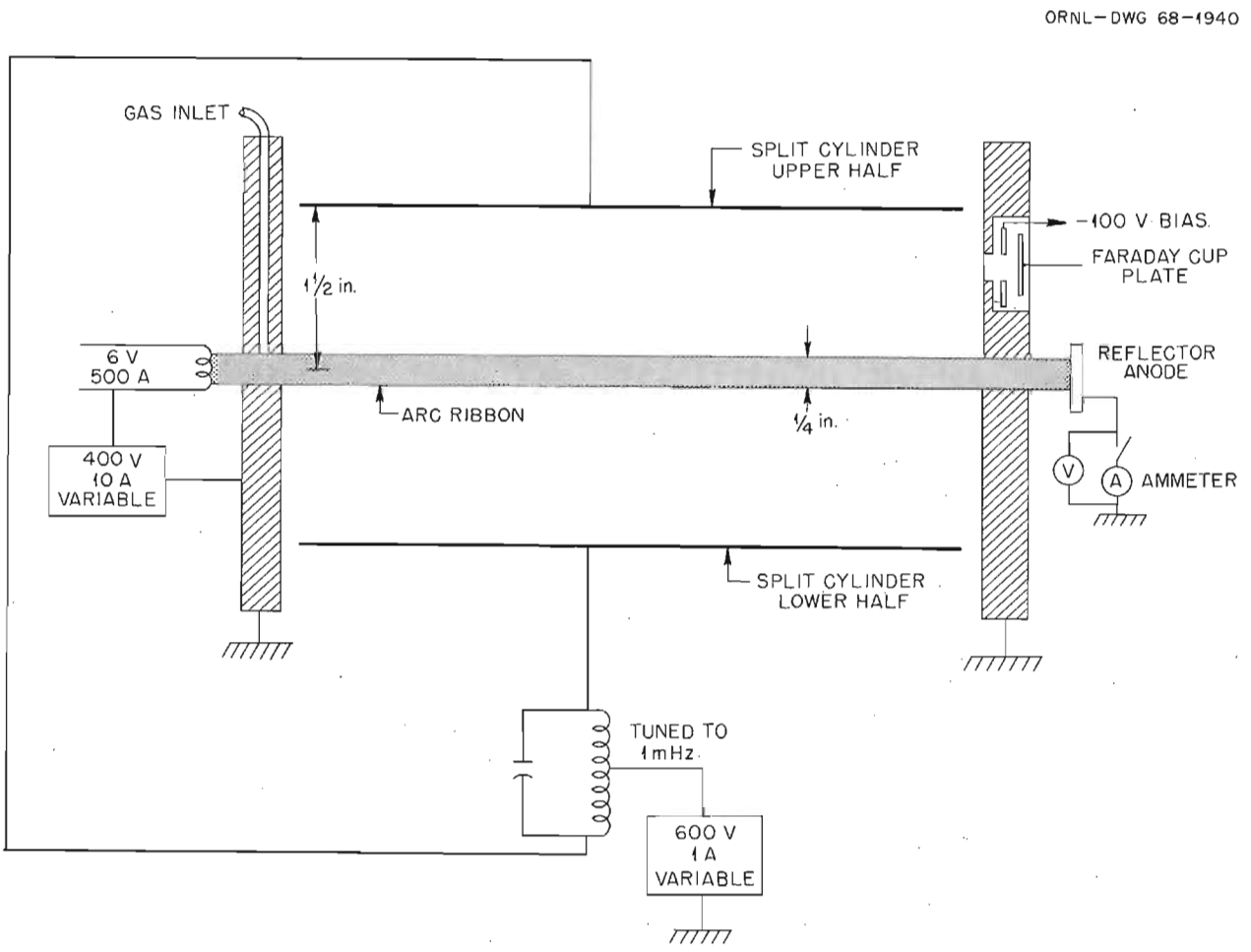

Fig. 5.34. Symmetric Discharge Schematic.

PHOTO —90781

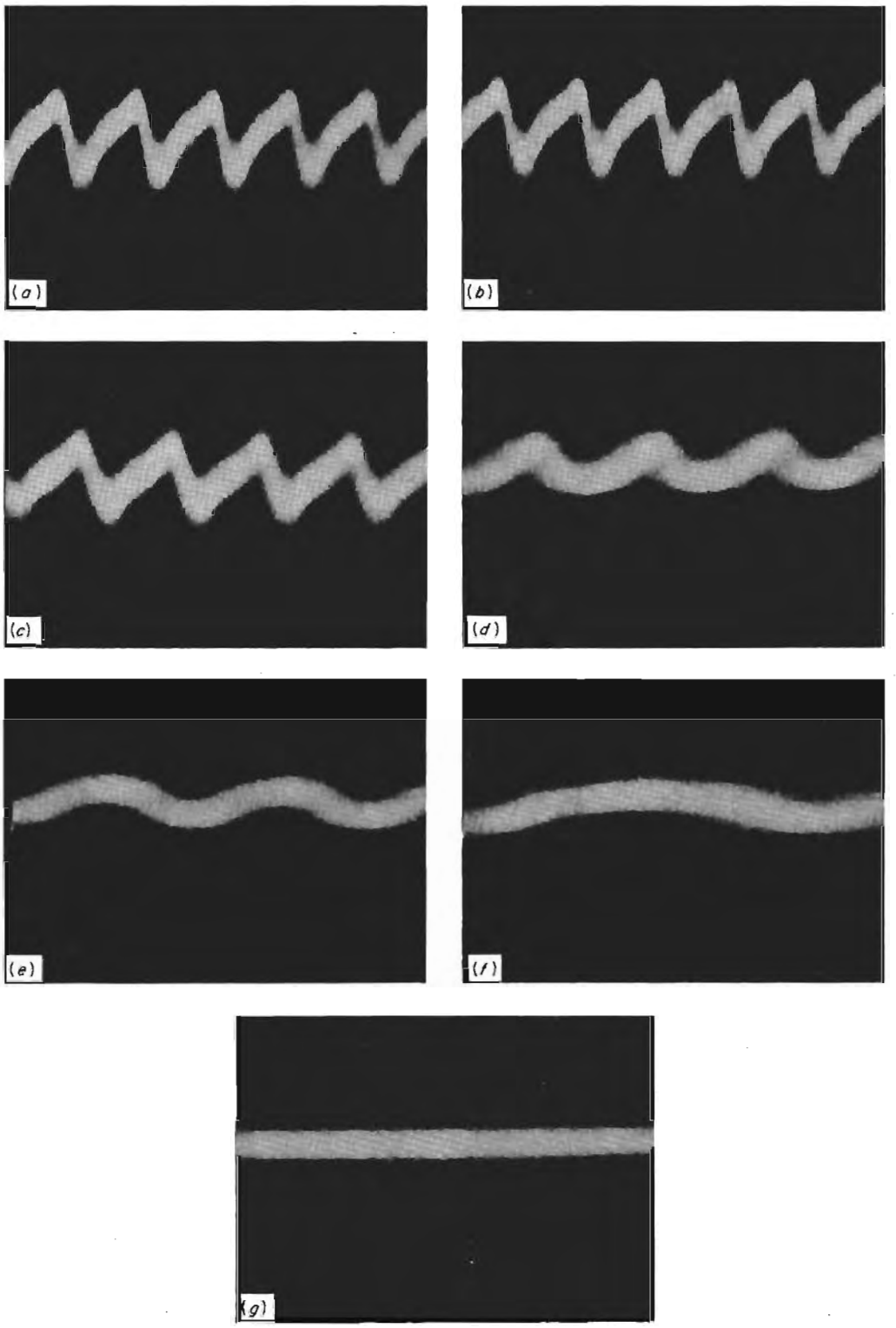

Fig. 5.35. (*a*) Faraday Cup Trace During Mode II Operation. (*b*) Cylinder Voltage + 68. (c) Cylinder Voltage + 90. (*d*) Cylinder Voltage + 120. (e) Cylinder Voltage + 140. (*f*) Cylinder Voltage + 175. (*g*) Cylinder Voltage + 200.

current required to stop the oscillation is only 150 mA.

The energy of the ions going into the Faraday cup is unchanged by application of the cylinder voltage. In addition, the characteristic pulsations due to mode II in the arc stream do not go away with application of voltage to the cylinder. Thus it seems that the external rotation has been stopped without affecting the mechanism which produces the mode II and the energetic ions. Argon and helium have both been used in the experiment with similar results. All the photographs shown are for argon.

5.9 ELECTRON-CYCLOTRON HEATING IN A MIRROR MACHINE USING A SIMPLE DIPOLE ANTENNA

I. Alexeff W. D. Jones

In our work on plasma electron heating, we had formerly thought that cavities were required to contain the microwave radiation. In this particular experiment, however, we find that placing a dipole antenna in the magnetic field near the resonance region is adequate to produce strong electron-cyclotron heating. The experiment was performed in the Magnion solenoid in the Plasma Physics Laboratory. The central coils in the Magnion solenoid were disconnected, creating a small mirror machine with a mirror ratio of approximately 2:1. Microwave power at 3 cm was produced from a 100-W power supply obtained commercially from Raytheon. When the magnetic field and the microwave power supply were turned on, heating zones were evident at the dipole antenna in three locations. One location was outside the mirror region where the antenna entered, and two locations were symmetrically located opposite the midplane of the machine, where the electron cyclotron frequency was in resonance with the power input. The gas pressure used was the residual gas pressure in the system, which past measurements had shown to be approximately 10^{-5} torr. Under this condition of operation, heating was not very intense. Plasma was just produced around the wire in a region several millimeters thick and streamed out the ends. The plasma did not fill the mirror machine. However, as the magnetic field was increased, the two heating zones in the midplane of the machine gradually moved together until they finally coalesced. This corresponds to the heating zone being directly on the midplane of the mirror machine. Under this condition of operation, strong electron heating was observed, and instead of just having heating around the wire, a large hollow shell of plasma was formed. Evidently the electron temperature was high enough so that the plasma electrons had enough time to precess around the machine in the mirror gradient before being lost by scattering out through the mirrors. Rough estimates from the existence of the precessing electron shells show that the electron temperature should have been in the kilovolt region, although measurements with x-ray detectors showed no strong x-ray emission. Therefore, we can say roughly that the electron temperature and the maximum electron energy had to be less than approximately 20 keV. Since this technique of heating without a cavity looked so successful in this mirror machine, we proceeded to place this simple antenna system into our multipole. This is a levitated quadrupole under the direction of Michael Roberts. Subsequent experiments have demonstrated that at 100 W we get appreciable plasma production in the system without using what is considered a closed cavity. In the mirror machine, of course, we had no cavity whatsoever. Further experiments using the simple antenna for heating plasma were also done by Denver Jones in the iron core magnetic well system located in the Beta tanks. Again, at resonance, heating was observed, but in this case extensive studies were not carried on.

In conclusion, for simple heating experiments of electrons by electron cyclotron resonance, it does not appear necessary to have a closed cavity. Our preliminary experiments suggest that when plasma is brought into cyclotron resonance with the input power, the impedance match is very good, and the radiated microwave radiation is relatively low. This considerably simplifies electron plasma heating experiments.

5.10 TOROIDAL MULTIPOLES

M. Roberts I. Alexeff W. Halchin

5.10.1 Introduction

The ORNL toroidal multipole program is involved with two major experiments: one associated with the levitated toroidal quadrupole and the

other with the helical hexapole. The measurement of plasma confinement in a magnetic field is basic to both, as is the use of electromagnetic levitation to assure as much azimuthal symmetry as possible. Both experiment and theory are involved in the program, although to different degrees in the quadrupole and hexapole. What is described below is the work done on the measurements of plasma behavior in the levitated toroidal quadrupole and the work that has begun on the characteristics of a levitated hexapole. The basic idea of the hexapole is described in some detail by Dory in the previous semiannual report.[39]

For the sake of completeness, it is noted here that this project began just before the beginning of the previous reporting period, September 1966. In the last period, we were able to demonstrate levitation[40] of two rings in a usable manner, constructed guns for plasma production in the quadrupole, and made the entire system – vacuum, magnetic field, and plasma gun – ready for the experiments reported on here.

5.10.2 Quadrupole Experiments

Apparatus. – The equipment used in the quadrupole experiments discussed below was described in the previous semiannual progress report.[41] A much improved quadrupole facility is nearly completed and is shown in Fig. 5.36. Access is

[39] *Thermonuclear Div. Semiann. Progr. Rept. Apr. 30, 1967*, ORNL-4150, p. 1.

[40] M. Roberts and I. Alexeff, *Bull. Am. Phys. Soc.* 12, 26 (1967).

[41] *Thermonuclear Div. Semiann. Progr. Rept. Apr. 30, 1967*, ORNL-4150, p. 90.

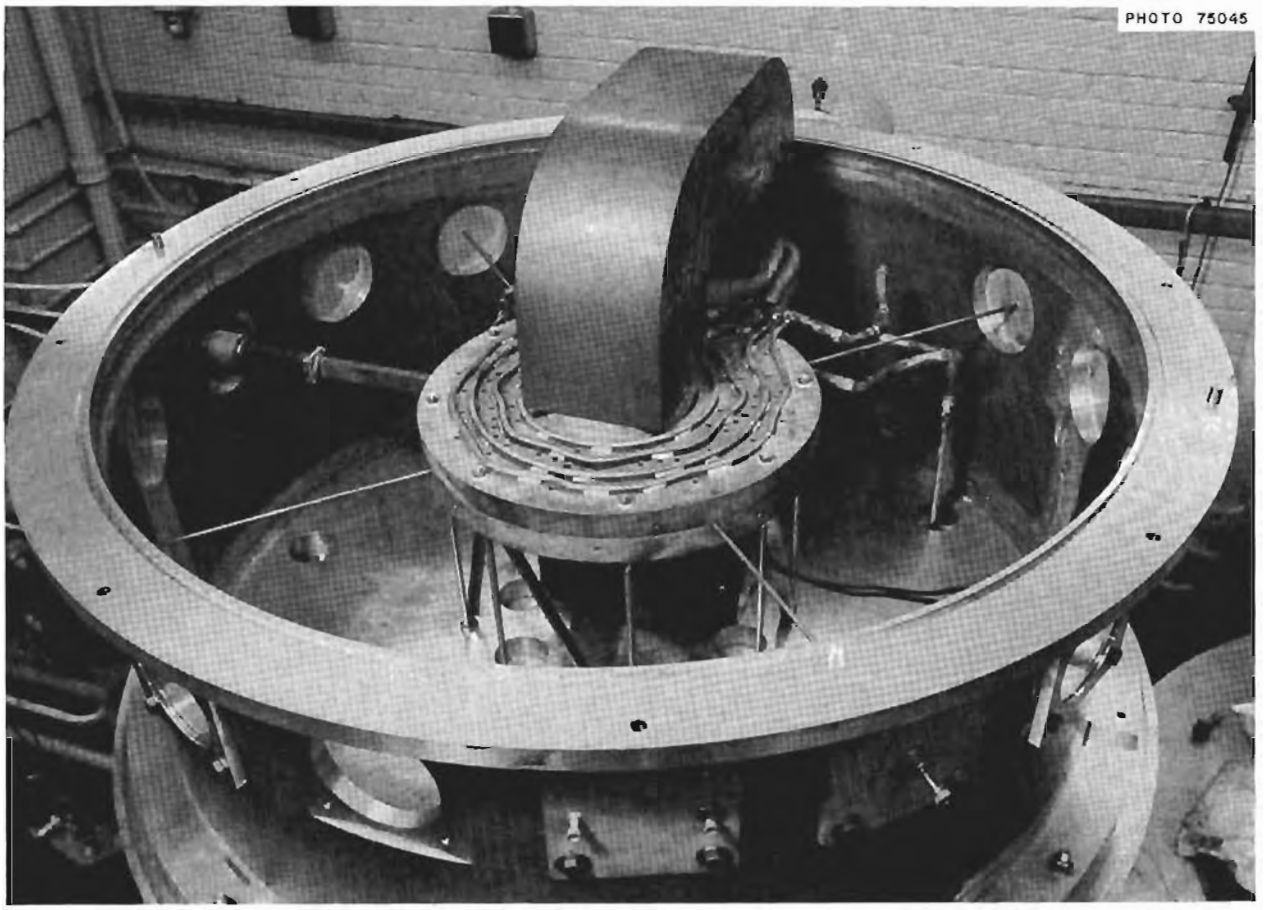

Fig. 5.36. Improved Facility for Quadrupole Experiments.

available to many locations on the torus, the maximum magnetic field has been doubled by filling all the available central space with a larger iron core than previously, and the torus itself is slightly different from the original one. In this second torus, the access holes have been reduced from $\frac{3}{4}$ to $\frac{1}{4}$ in. in diameter, and the wall cross section has been enlarged slightly in the region between the hoops. A view of the torus with the top half removed is shown in Fig. 5.37. The eddy current jumpers are located on the right side, encircling the iron core, and the 3-cm microwave input is shown on the left side of the torus. Steel pins can be lowered to press the hoops against the torus bottom, greatly enhancing the cooling rate of the hoops.

Operation of Experiment. – The experiments are conducted in the following manner: The basic restrictions on operation are that the current in the bars must be inductively driven, it must be on as short as possible a time to prevent heating, and it must be increased smoothly in order to center the levitated hoops. As a result, the magnetic field is increased from zero to its maximum amplitude in a time comparable to $\frac{1}{4}$ to $\frac{1}{2}$ sec and is then reduced quickly after the peak has been reached. Plasma production is accomplished by either of two means, gun injection or electron-cyclotron resonance heating. A titanium washer stack gun is usually used for the source, although a Bostick-type lithium gun was also used. The guns are located at different azimuths, but each

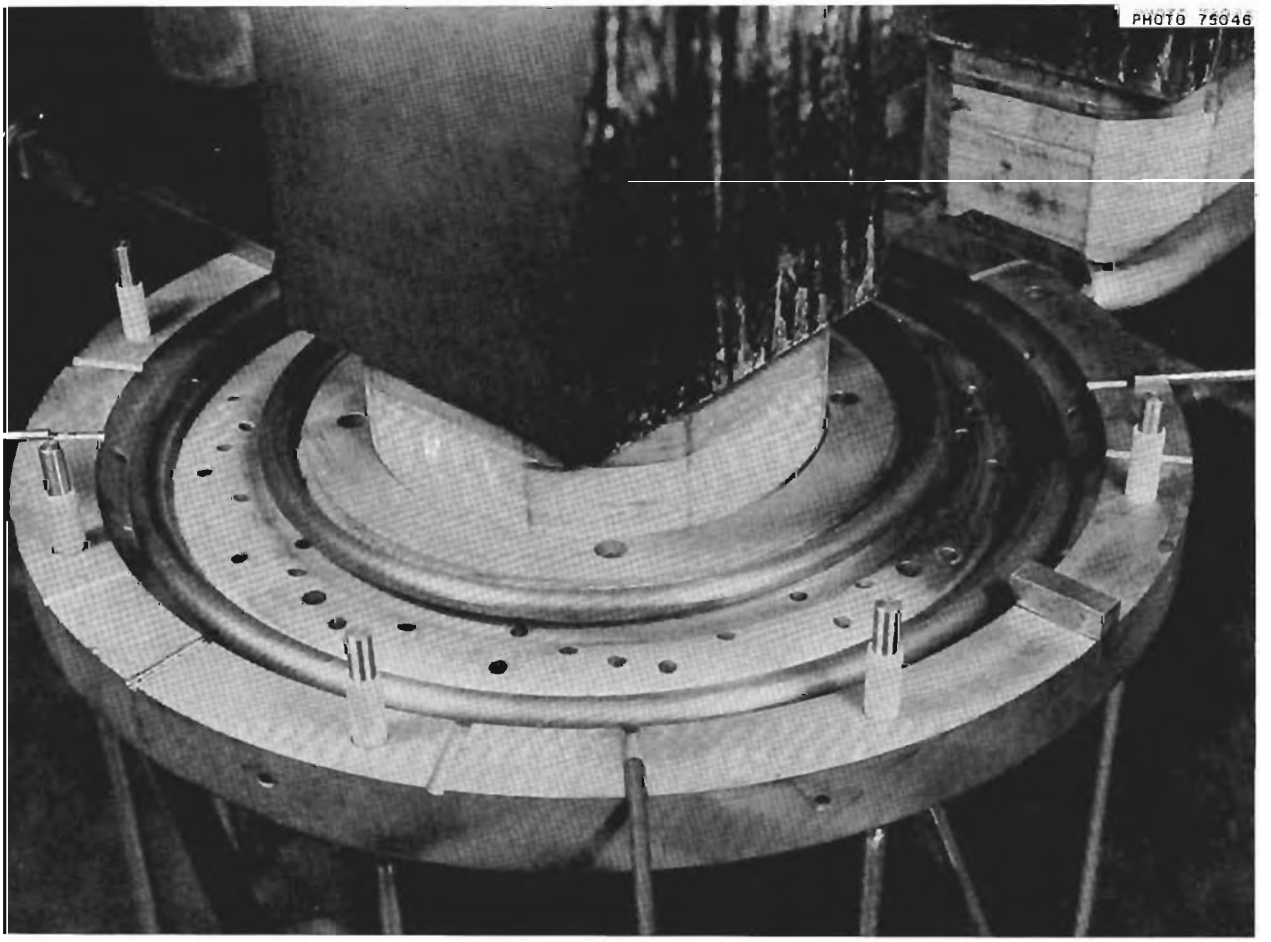

Fig. 5.37. Quadrupole Hoops Levitated on Bottom Half of Copper Torus.

is located so as to fire directly up toward the field zero. In the microwave heating, tens of watts at 12 cm wavelength are introduced through an access hole under the field zero and are used to break down the plasma. In the injection experiments the gun can be triggered to fire at any specified phase of the magnetic field. Similarly, the microwave power can be turned off and then on at specified times during the cycle of the magnetic field. As yet, the principal diagnostic tools have been a number of floating double probes placed around the azimuth in the field zero. Characteristic time constants can be measured directly, as well as times of flight. Densities are then inferred from the ion saturation current measurements. Electron temperatures are obtained roughly from the probe characteristics. Measurement of broad-band light from the central region is a corroborating check on the temporal behavior of the density in the microwave plasma.

Results. – The principal set of experiments conducted with the gun plasmas involve measuring the e-folding times as a function of total probe area in the device at peak magnetic field strength. The number and size of the probes were reduced so that the probe area varied over a factor of 10. Over a hundred oscillograms were reduced to the four points shown on Fig. 5.38. The filled-in circles represent the average values of the decay rates, and the spread of values is indicated by the vertical error bars. Uncertainty in the effective area of the probes is the reason for the horizontal spread. Extrapolation of the straight line to zero probe area yields a residual inverse loss rate of 1 over 1 msec. The pressure rise in the large vacuum tank, about 400 liters in volume, is up to 6×10^{-6} torr, so that the instantaneous neutral pressure in the torus, which has a volume of about 1 liter, could be as high as 10^{-3} torr, in which case the neutral gas scattering time would be on the order of 1 msec. In addition, the sinusoidal 60-Hz magnetic field has an approximate e-folding time of 3 msec. There is also a diffusion of the magnetic field into the wall, which, at a speed 1 mm/msec, would have an effective e-folding time of about 3 msec. It is then unnecessary at this stage to invoke any further mechanisms to explain the intercept until

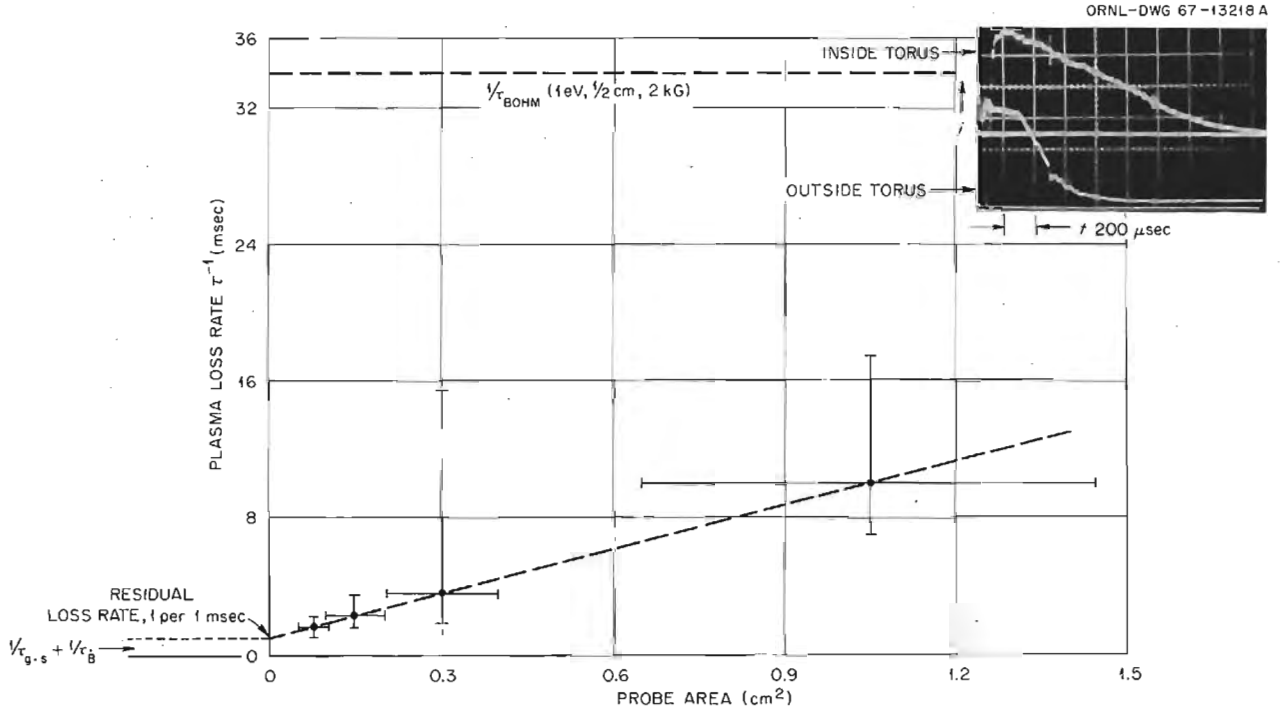

Fig. 5.38. Plasma Loss Rate vs Probe Area for Gun Plasma Confined in the Levitated Quadrupole.

the gas scattering and magnetic field decay times have been reduced as discussed below. When plotted on semilogarithmic graph paper, many of the decay curves were exponential, some were piecewise exponential, and some nearly linear, as might be expected if the probe were not completely in the ion saturation region and a reduction in current caused an increase in bias voltage. Using the parameters $T_e \approx 3$ eV, an average $B \approx 2$ kG, and a scale length of about $\frac{1}{2}$ cm, the Bohm diffusion time is calculated to be about 30 μsec or one-thirtieth the measured time; the best measured values for the decay time were on the order of 1 msec. The classical Coulomb scattering time, however, is much greater than 100 times the measured value.

During the course of the decay measurements, azimuthal density gradients and also localized fluctuations were measured. The current signals dropped by nearly two orders of magnitude progressing from the gun ($\theta = 0°$) to $\theta = 180°$, halfway around the torus, although the density appeared to have become azimuthally uniform after the initial disturbance had dissipated, that is, about 500 μsec to 1 msec. Fluctuations of the order of 300 kHz were measured only in the vicinity of $\theta = 180°$ from the gun for both the hydrogen and the lithium guns, which were themselves 90° apart in azimuth and fired at separate times. Fluctuations persisted for the duration of the experiment, about 2 msec for hydrogen and 200 μsec for lithium, and did not appear to propagate away from $\theta = 180°$ (see Fig. 5.39). A typical oscillograph trace is shown in Fig. 5.40. Transit time measurements on the hydrogen plasma around the torus indicate a minimum velocity of $\approx 10^6$ cm/sec (50 cm traversed in 50 μsec), corresponding to a minimum "T_i" $\approx$ 1 eV. The density at $\theta = 180°$ is on the order of 10^9 cm^{-3} (using the 10^6-cm/sec velocity). The maximum T_i of the particles near the exit of the gun is probably $\approx$100 eV, whereas the highest T_i that a contained particle would be expected to

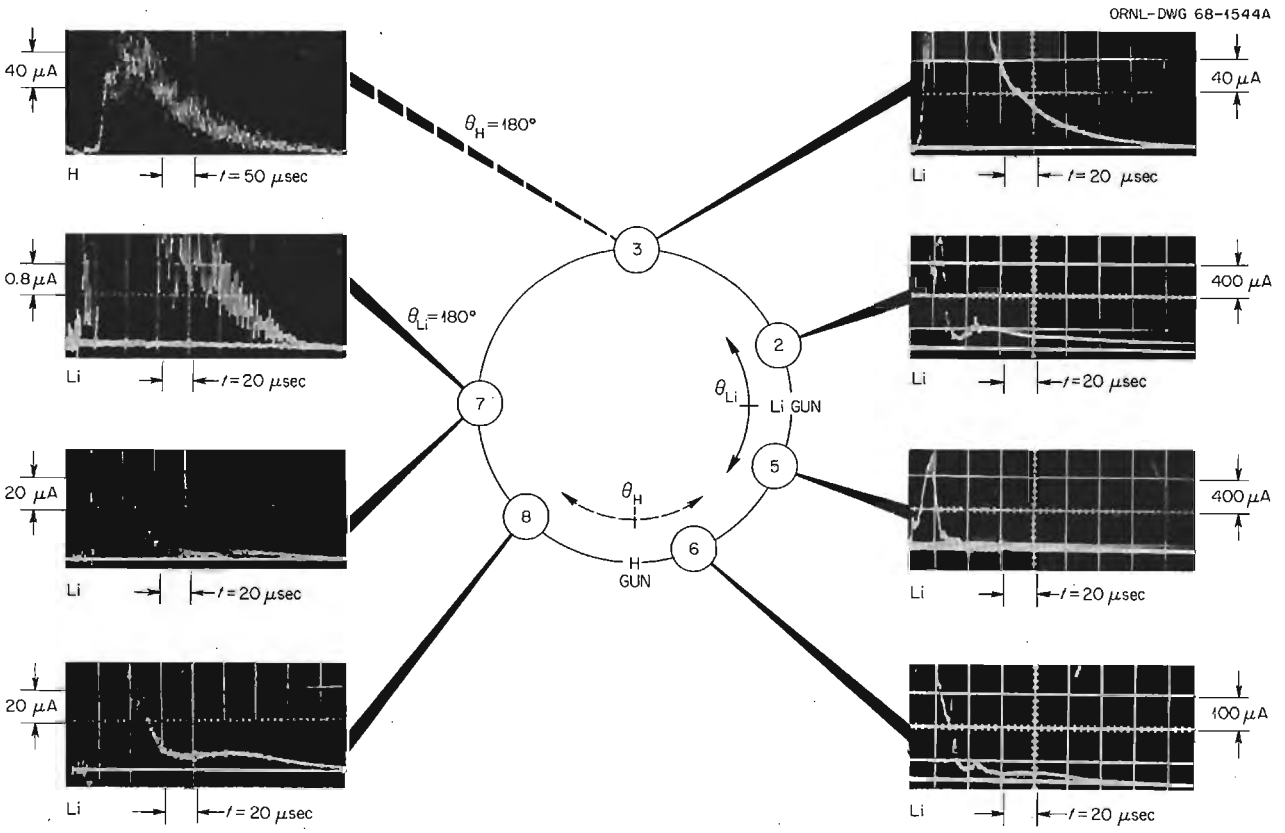

Fig. 5.39. Azimuthal and Temporal Variation of Lithium Plasma Injected into Levitated Quadrupole.

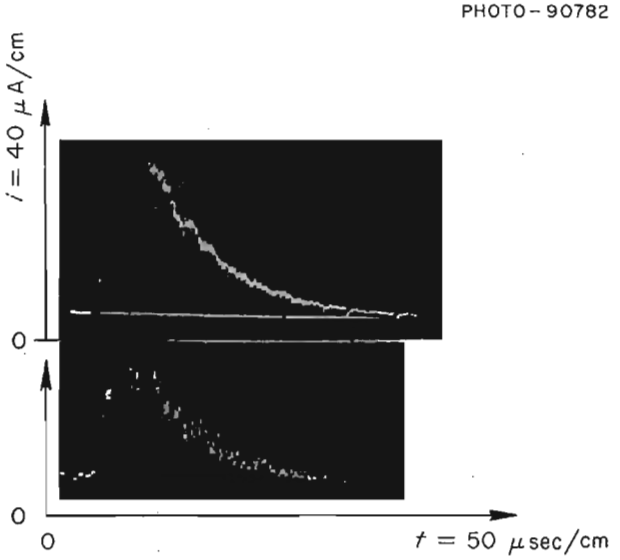

Fig. 5.40. Typical Ion Saturation Current Measurements of Hydrogen Plasma Confined in Levitated Quadrupole.

have in the 3-kG field would be about one-tenth or one-fifth that value.

In order to test a wider range of parameters than available with the washer gun, studies were started using electron-cyclotron resonance heating of hydrogen in the torus. Microwave power at 12 cm wavelength was introduced on a two-wire antenna at the end of a coaxial line with coupling to the magnetic field sufficiently localized that the maximum field was limited to about $1\frac{1}{2}$ kG near the bars, in order to maintain a resonance condition within the influence of the antenna. The magnetic field was sinusoidal, and the microwave power was on continuously except for a pulsed off-time whose length and duration was adjustable, permitting afterglow studies as well as transit time measurements. The gage pressure for these measurements has been about 8×10^{-5} torr, with discharges possible at somewhat lower pressures to about 4×10^{-5} torr. Densities on the order of 10^{10} cm^{-3} were measured with fluctuations ($\Delta n/n$) on the order of 0.05 in the range 300 kHz in the field zero region. Probe characteristics as shown in Fig. 5.41 indicate an "equilibrium" temperature (i.e., at times different from the sharpest resonance condition) of about 30 eV, with possibly locally and instantaneously higher values at the resonance point. The afterglow decay time was approximately 30 μsec, which was again about 30 times the Bohm time, since there had been a factor of 10 increase in the temperature and a factor of 3 reduction in the magnetic field.

Conclusions. – As a result of these early probe measurements on gun-injected and microwave-produced plasmas, it is possible to draw some conclusions about the plasmas under study and make some recommendations for continued improvement in the measurements. The filling process in the quadrupole is characterized by large density gradients and then localized long-lasting fluctuations near the collision point. These elements would indicate poor plasma communication along the azimuthal direction, in agreement with recent experiments of Yoshikawa.[42] This process differs from the octopole filling described by Kerst[43] and should be looked at in greater detail. Use of two or more guns will be an interesting technique for possibly filling the torus more quickly than with a single source. Experiments on the extended lifetime of the plasma as a function of inserted probe area seem to show that gas scattering and magnetic field decay can account for residual loss rates. The high instantaneous torus pressure comes about because the gun is not optimized for a low ratio of neutral to plasma particles. Improved design[44] and construction of new guns has been completed, and testing is now in progress. At this stage, it is possible to say that the gas pressure rise on firing the improved source is orders of magnitude lower than with the older guns, although the nature of the plasma is not yet known. The magnetic field decay can be reduced in two ways; the first is to try to keep the source constant, that is, crowbar the field at the maximum current. One is then limited by diffusion into the walls and hoops, which goes as L/R. Increasing L by making the volume greater and reducing R by increasing the skin depth by reducing the excitation frequency would tend to slow down the flux velocity into the copper. Scaling up by three times and reducing to 16 Hz would allow a 100-msec e-folding time based upon the 18-msec e-folding time in a small test quadrupole. The comparison of gun plasma lifetime with the Bohm time was

[42] S. Yoshikawa, invited paper 1D-8, Ninth Annual Meeting, Division of Plasma Physics, American Physical Society, November 1967, Austin, Tex.

[43] R. A. Dory *et al.*, *Phys. Fluids* 9, 997 (1966).

[44] The help of F. H. Coensgen and W. E. Nexsen, Jr., of Lawrence Radiation Laboratory, Livermore, Calif., is gratefully acknowledged.

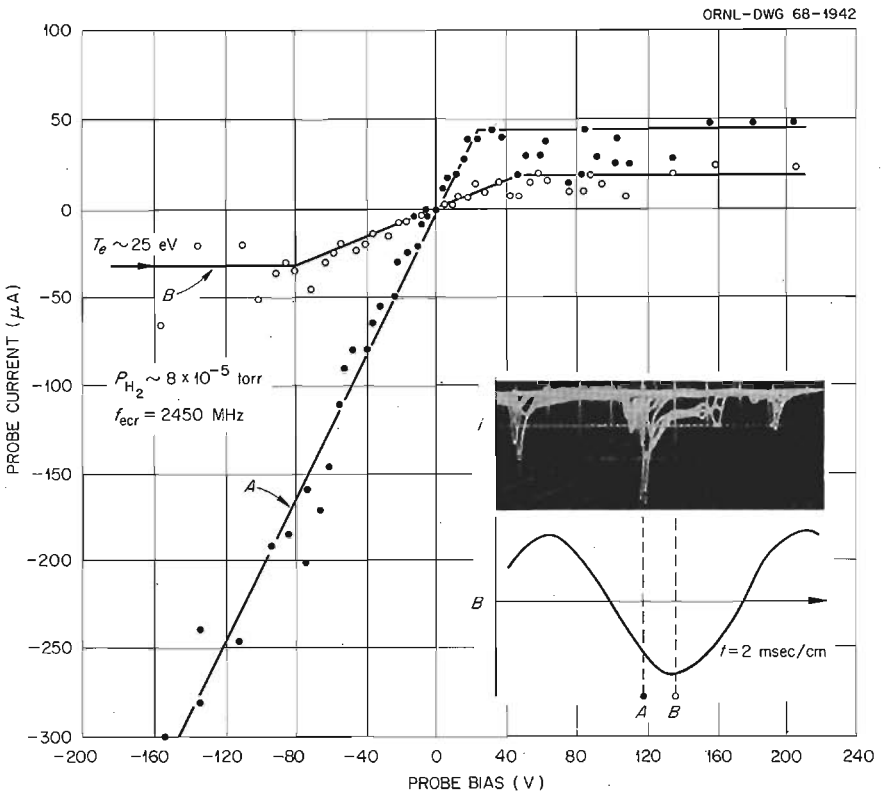

Fig. 5.41. Double Probe Characteristic for Hydrogen Plasma Produced by Electron Cyclotron Resonance at $f = 2450$ MHz.

made for a single set of values of temperature and field. The behavior of the confinement with changing magnetic field must be considered more carefully, and now with a large field available in the new quadrupole facility (up to 6 kG) it should be possible to explore the range of e-folding times as a function of B over at least a factor of 6 change in B, allowing sufficient information to find the B dependence. It is now clear that a measurement of ion energy is extremely important, and an ion energy analyzer modeled after those used by Kerst[45] and Eubank and Wilkerson[46] is now under construction. Finally, with the improvement in the control over the cooling of the bars by pressing them mechanically against the cold torus, it will be possible to make clearer studies of the effect of the resistive voltage drop in the bars. The electron-cyclotron resonance heating is being continued with higher power – up to 1000 W at 12 cm wavelength and also up to 1000 W at 3 cm wavelength.[47]

5.10.3 Hexapole Experiments

The twisted multipole described in the previous semiannual report by Dory[41] has undergone a number of tests of design for levitation feasibility. The initial idea was to twist the four bars of an octopole one-quarter turn (with respect to an adjacent set at a radial cut) to achieve rigidity and the benefits of some shear. A later factor was the realization of the nested flux tube region in the center of a sufficiently high-pitched multipole described by Grad.[48] In addition to these two

[45]C. W. Erickson, *Rev. Sci. Instr.* 37, 1308 (1966).

[46]H. P. Eubank and T. D. Wilkerson, *Rev. Sci. Instr.* 34, 12 (1963).

[47]The help of R. Dandl's group in providing the 3-cm supply is gratefully acknowledged.

[48]H. Grad, *Phys. Rev. Letters* 18, 585 (1967).

considerations, it was thought that a twisted multipole with proper pitch would have all forces directed along the metallic conductors, perhaps reducing the difficulty of the stress problem. For simplicity, hexapoles of $\frac{1}{2}$-in. copper bars were built with $4\frac{1}{3}$ and $6\frac{1}{3}$ turns around the loop. Both of these had high inductances because of large field volume, and each pinched itself together at one azimuth. The $\frac{1}{2}$-in. copper bars had been annealed and simply were not strong enough. Work then centered around the one-third turn hexapole, since it is the simplest twisted (or helical) multipole to build of stronger material. Helical hexapoles using $\frac{3}{4}$-, 1-, and $1\frac{1}{2}$-in.-diam copper bars have been built (Fig. 5.42 shows the 1-in. bar hexapole), and each fits in the structure shown in Fig. 5.43. The $\frac{3}{4}$-in.-diam device collapsed easily at low current and was still limited in current strength by the high inductance. Tests with the 1-in.-diam device after it had been work hardened so that it would collapse elastically indicated currents on the order of 10 kA; it collapsed near the peak currents. On the basis of this 1-in. bar model, the $1\frac{1}{2}$-in.-diam device was constructed having about four times the torsional strength and still smaller inductance. This last device is presently under test and is being made ready for plasma experiments. The liner for the hexapole (shown in Fig. 5.43) is designed to be a microwave cavity for 3-cm power, and in initial experiments we will be looking at the effect of the twist and the better connection length of the hexapole on the density, temperature, and fluctuation profiles for microwave-induced and gun-injected plasmas. This apparatus has been placed in the vacuum tank in which the first quadrupole experiments were conducted, since the quadrupole is now in the larger tank described above.

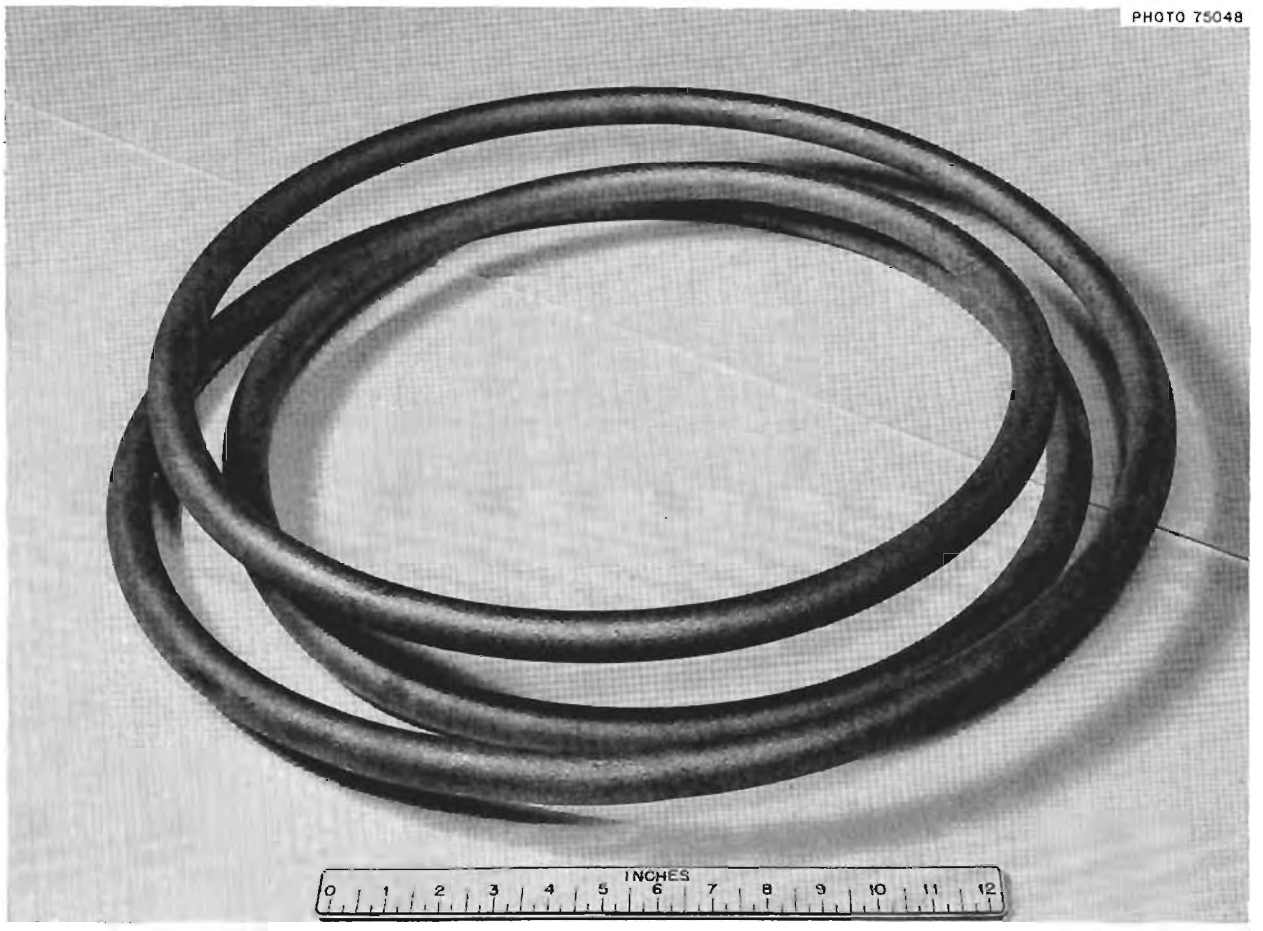

Fig. 5.42. Helical Hexapole Structure Made from a 1-in.-diam Copper Bar.

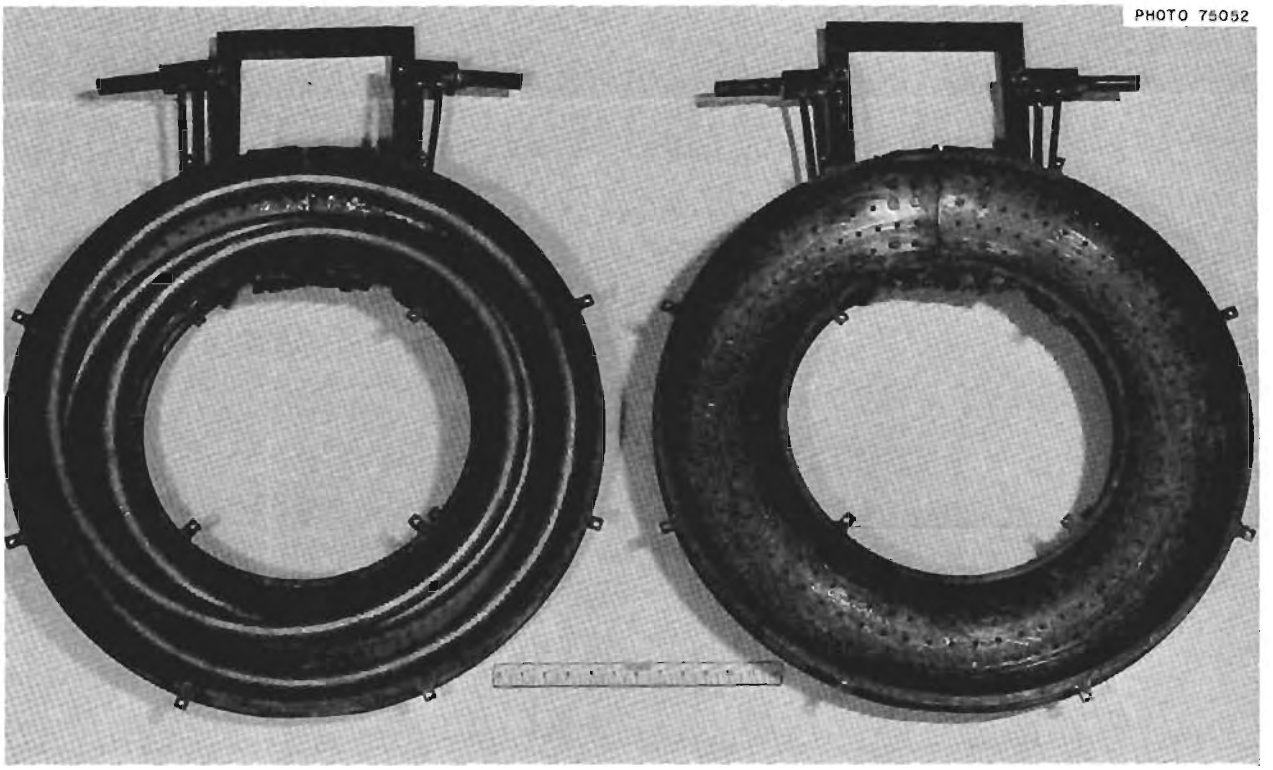

Fig. 5.43. $\frac{3}{8}$-in.-thick Copper Torus That Encloses the Helical Hexapole.

5.10.4 Guiding Experiments
(with W. L. Stirling)

A supporting experiment has been designed and constructed to test the feasibility of guiding plasmas from a plasma gun into the multipole in such a way as to reduce the ratio of neutrals to ions, thus reducing the neutral gas background during the gun injection phase of the experiments.

In the first set of experiments a washer gun is being fired into the throat of a $1\frac{1}{2}$-in.-diam tube that has been bent into an arc 90° in extent. The plasma escaping from the far end is then measured on a double probe. It is planned to change the type of material used for the tube, then perforate the tube and try to assess the change in the ratio of neutrals to ions arriving at the end.

6. Atomic and Molecular Cross Sections

C. F. Barnett
M. O. Krause
R. A. Langley
J. A. Ray
I. A. Sellin

6.1 RYDBERG STATE AUTOIONIZATION OF H_2, D_2, AND HD

Previously[1] we have reported the formation of high quantum states of hydrogen molecules produced in electron capture by hydrogen molecular ions. These quantum states have been characterized as Rydberg states with energy $E_n \approx -(\mathrm{Ry}/n^2)$ in which a single orbital electron revolves around the molecular ion core at a Bohr radius proportional to n^2. In this description of these highly excited levels the state population for excited molecules should be approximately the same as for atoms of equal velocity, whereas measurements indicated that the sum of the H_2 state population with principal quantum number greater than 11 was a factor of 3 or more less than that for corresponding levels of the hydrogen atom. Theoretical studies have shown that states of H_2, HD, or D_2 can be depleted by the process of autoionization, in which the ion core of the Rydberg state is excited in any one of the vibrational-rotational states characteristic of the molecular ion H_2^+, HD^+, or D_2^+. When energetically allowed, the ion core can give up some of its energy to the outer electron, thus reverting to a lower vibrational-rotational state. The outer electron would be ejected with a characteristic energy equal to the energy change in the core minus the binding energy of the electron in state n. The salient features of the theory predict that: (1) All molecular states with the angular momentum $l > 0$ would decay by autoionization in a time short compared with the transit time between point of formation and the electric field stripper used to observe them. Thus the population of excited states should be less for molecules than for atoms. (2) Excited state lifetimes governed by $\Delta v = 1$ transitions (transitions between adjacent vibrational levels) have lifetimes that may be observed experimentally. (3) HD with its added induced dipole moment has smaller lifetimes for a given n than H_2 or D_2. Extrapolated values of lifetimes taken from a paper by Russek *et al.*[2] are shown in Table 6.1.

The lifetimes of Table 6.1 are comparable with experimental transit times and suggest that by

[1] ORNL-4150, p. 103.

[2] A. Russek, M. L. Patterson, and R. L. Becker, to be published in the *Physical Review*.

Table 6.1. Lifetimes of Principal Quantum States ($l = 0$)

n	τ (sec)	
	HD	H_2
7	8.2×10^{-10}	2.3×10^{-8}
8	1.9×10^{-9}	7.0×10^{-8}
9	3.0×10^{-9}	1.6×10^{-7}
10	4.8×10^{-9}	3.4×10^{-7}
11	7.4×10^{-9}	6.5×10^{-7}
12	1.1×10^{-8}	1.1×10^{-6}
13	1.6×10^{-8}	1.9×10^{-6}

varying the transit time these transition rates or lifetimes may be observed. The obvious way to change the transit time was to increase or decrease the particle energy; however, since the electron capture in a particular excited state is energy dependent, it was mandatory that the particle velocity or energy remain fixed.

The apparatus described and used previously was modified to permit the charge-exchange gas cell to be moved in the direction of the electric field stripper. The cell was 2 in. long, and the entrance and exit apertures were 0.030 and 0.090 in. respectively. Movement of the gas cell from 18 to 7 in. from the electric field stripper resulted in transit times of 10.44×10^{-8} sec to 4.21×10^{-8} sec for 100 keV/amu H_2^+, HD^+, and D_2^+. All measurements of distances and thereby mean transit times were made from the center of the gas cell. States with $l > 0$ decayed in the gas cell or within the first inch after exit, since these states have lifetimes $<10^{-9}$ sec. Parallel electric condenser plates were attached to the movable gas cell to provide means to remove positive ions from the neutral beam. The single silicon barrier detector used previously was replaced with two high-resolution silicon barrier detectors so that both the neutral and the charged beam could be recorded simultaneously as the electric stripper field was increased. These two detectors eliminated the systematic error resulting from beam intensity fluctuations between neutral and ion counting rate determinations. Even with the elimination of this error the level populations determined as a function of transit time were so erratic that no definite value could be assigned immediately to lifetimes. An averaging process described by Il'in *et al.*[3] was used to obtain better statistics.

The relative yield of highly excited atoms or molecules that can be stripped by an electric field E can be expressed as the fraction

$$F(E) = \frac{I^+(E)}{I_0}, \tag{1}$$

where I_0 is the neutral counting rate and where $I^+(E)$ is the ion counting rate for field E. The total neutral beam can be expressed as

$$F_0 = \sum_{n=1}^{\infty} F_n , \tag{2}$$

where the summation is over all principal quantum states. According to the Born approximation the proton or H_2^+ charge-exchange cross section into the nth Rydberg state is proportional to n^{-3}, so that one can write

$$\frac{F_n}{F_0} = \frac{a}{n^3}, \tag{3}$$

where a is a parameter depending on the particle energy and the gas in the exchange cell. According to the intense Stark effect theory the states of given n are destroyed by an electric field if

$$E_n \geqq b/n^4 , \tag{4}$$

where b is a constant derived from theory and measurements and is equal to 6.2×10^5 kV/cm. From (1) and (2) we can write

$$F(E) = \sum_{n=n_E}^{\infty} \frac{F_n}{F_0}, \tag{5}$$

where n_E is the principal quantum number of the atom ionized by the field E. For intense fields we have strong Stark splitting, and n can be regarded as continuous. By susbtituting (3) into (5) and integrating from n_E to ∞, we get

$$F(E) = 6.4 \times 10^{-4}\, a\sqrt{E} , \tag{6}$$

where E is in kilovolts per centimeter. Thus by plotting the fraction of ions formed as a function of the square root of the electric stripping field, we determine a, which is a parameter proportional to the excited state population.

The results of applying this averaging process are shown in Fig. 6.1, which is a semilogarithmic plot of a as a function of the transit time. The constant a was determined from a plot of $F(E)$ vs $\sqrt{E}$, with the slope being obtained from a least-squares fit to the data. Likewise the lines drawn for both H_2 and HD are least-squares fitted to the data points. The lifetime for the H_2 component as measured by this method was 3.5×10^{-7} sec and for HD 3.3. It is evident that these lifetimes can be shifted by as much as 50% with small changes in the drawing of the straight line. A comparison of these lifetimes with theoretical lifetimes[2] indicates that the theory and experimental values

[3] R. N. Il'in *et al.*, *Soviet Phys. – Tech. Phys.* 11, 921 (1967).

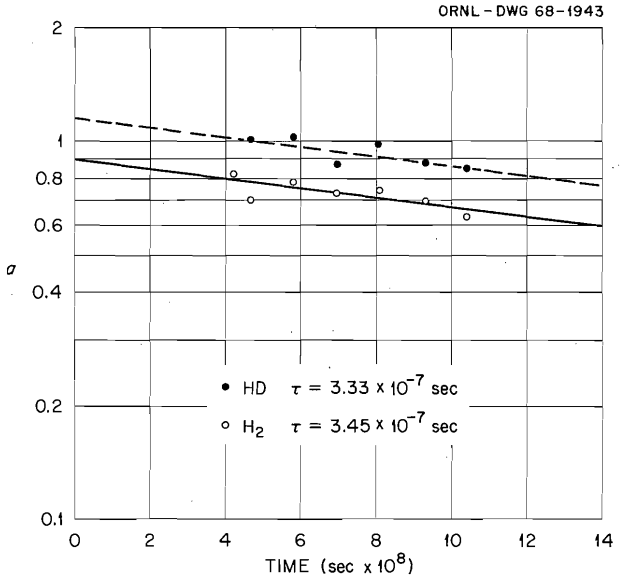

Fig. 6.1. The Constant *a*, Which Is Proportional to the Excited State Population, Plotted as a Function of H_2 and HD Transit Time.

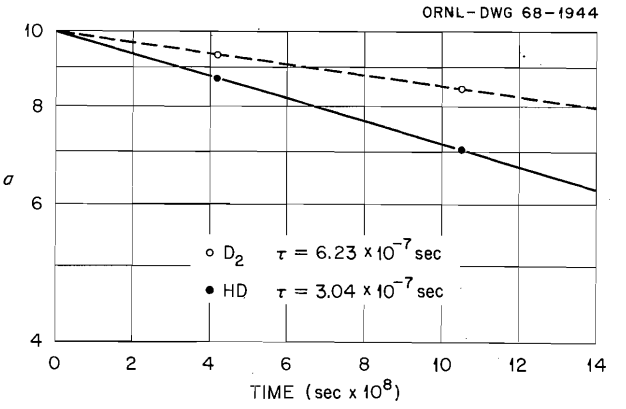

Fig. 6.2. The Constant *a* Plotted as a Function of D_2 and HD Transit Time for Fixed Ion Source Operating Parameters.

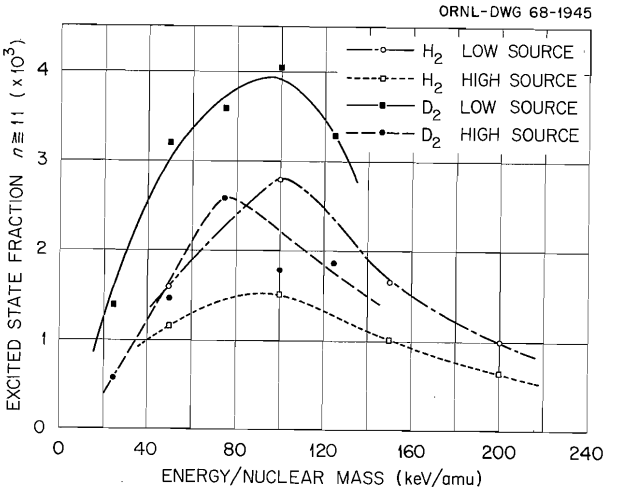

Fig. 6.3. The Fraction of H_2 and D_2 in Principal Quantum States $n \geq 11$ as a Function of Particle Energy. Shown are the state populations for "low" and "high" ion source conditions.

are compatible for H_2; however, for HD the experimental values are two orders of magnitude greater than theory. The approximately equal lifetimes for H_2 and HD suggest that the theoretical treatment grossly overestimates the contribution of the induced dipole in HD.

In all our previous measurements, we have been faced with an isotopic anomaly in that the state population of D_2 was greater than H_2. In the present series of measurements, it became apparent that the ion source conditions grossly affected the excited state yield. Results of these measurements will be presented in the next paragraph. To determine if source conditions were influencing lifetimes, a comparison was made between the lifetimes of HD and D_2. Measurements of HD and D_2 could be made with identical source conditions, since no gas flows need be interrupted. The results are shown in Fig. 6.2, where the normalized fraction *a* is plotted as a function of transit time. These plots yield an HD lifetime of 3×10^{-7} sec and a D_2 lifetime of 6.2×10^{-7} sec. Although the amount of data is meager, the difference between the lifetimes is outside the experimental error, and consequently the conclusion can be drawn that the lifetime of D_2 states is greater than that for HD states.

Mentioned in the previous paragraph was the fact that the ion source operating parameters affected the measured state population. The ion source used was an electron oscillating type, commonly called the "PIG source." In Fig. 6.3 the integral state population in states $n \geq 11$ is plotted as a function of particle energy for D_2 and H_2. The source operating parameter has been described as "low source" and "high

source." The "low source" operating mode can be described as minimum source gas flow, anode to cathode potential less than 500 V, discharge current less than 100 μA, and usually thought of as operating so that single collisions dominate in the source region. The "high source" mode results from increased source gas flow, 2 to 5 keV anode-cathode potential, and 2 to 10 mA discharge current, with multiple collisions likely in the source region. If these operating concepts are valid, then the low source mode should produce molecular ions in vibrational states by electron collisions according to the Franck-Condon principle. In the high source mode the same vibrational population would ensue; but, due to multiple collisions before the ions leave the source region, deactivation collisions would lower the average vibrational level. The molecular ions are then accelerated and passed through the gas cell. If during the electron capture event the vibrational level remains unchanged, which would be expected since no nuclear motion should be imparted in a capture collision into orbits of $r \propto n^2$, then the fraction of particles stripped by the field ionizer should be greater for the "low source" mode than for the "high source" mode. Indeed this is shown to be true in Fig. 6.3 for both H_2 and D_2.

In all measurements of the hydrogen isotopic molecular excited states, D_2 excited state population has been consistently greater than that of HD or H_2. This apparent anomaly is readily explained on the basis of autoionization. If the $n = 11$ state is taken as an example, it is known that the orbital electron is bound by 0.113 eV, so that when the ion core undergoes a spontaneous transition from one vibrational level to the next lower one, at least 0.113 eV energy must be available to autoionize the $n = 11$ state. Table 6.2 presents the energy levels and the relative populations of the first 15 molecular ion vibrational levels formed, using published Franck-Condon transition probabilities.[4]

[4]M. E. Wacks, *J. Res. Natl. Bur. Std. (U.S.), Ser.* A **68**, 631 (1964).

Table 6.2. Vibrational Levels in H_2 and D_2; Level Energies, Energy Differences, and Relative Populations

v'	H_2			D_2		
	E	ΔE	Population	E	ΔE	Population
0	0.1405	0.1405		0.0998	0.0998	
1	0.4099	0.2694	0.1751	0.2935	0.1937	0.0950
2	0.6639	0.2540	0.1959	0.4796	0.1861	0.1434
3	0.9026	0.2387	0.1700	0.6580	0.1784	0.1611
4	1.1258	0.2232	0.1275	0.8286	0.1706	0.1507
5	1.3370	0.2079	0.0874	0.9916	0.1630	0.1245
6	1.5263	0.1926	0.0566	1.1470	0.1554	0.0943
7	1.7034	0.1771	0.0355	1.2946	0.1476	0.0671
8	1.8652	0.1618	0.0219	1.4345	0.1399	0.0456
9	2.0116	0.1464	0.0134	1.5668	0.1323	0.0300
10	2.1427	0.1311	0.0082	1.6914	0.1246	0.0193
11	2.2584	0.1157	0.0051	1.8083	0.1169	0.0122
12	2.3586	0.1002	0.0032	1.9174	0.1091	0.0077
13	2.4436	0.0850	0.0020	2.0190	0.1016	0.0048
14	2.5131	0.0695	0.0013	2.1128	0.0938	0.0030
15	2.5673	0.0542	0.0008	2.1989	0.0861	0.0019

The table indicates that 0.113 eV of energy is available for any vibrational transition up to and including the 12 → 11 transition for H_2. Transitions between levels greater than $v = 12$ will not supply sufficient energy to autoionize the $n = 11$ electronic state. For D_2, again the 12 → 11 transition will supply sufficient energy; however, since the number of vibrational states of H_2 is 19 and D_2 is 27, then the populations of the various vibrational levels of H_2 and D_2 are different, as indicated by the fourth and seventh columns. Summing the relative populations of the states above $v = 12$, we find the total relative population of H_2 states that will not autoionize the $n = 11$ electronic state to be 0.008 and for the corresponding D_2 to be 0.0137. Dunn,[5] using more exact wave functions in calculating the Franck-Condon transition probabilities, finds the sum of the population of $v > 12$ states for H_2 to be 0.0193 and for D_2 0.05951, or a factor of 3.1. Thus it is expected on energy considerations alone that the measured population of D_2 should be a factor of 1.7 to 3.1 greater than H_2. The same arguments apply for the autoionization of all the high electronic quantum states. In Fig. 6.3 the D_2 population is approximately a factor of 2 greater than H_2 for the same source condition.

6.2 CHARGE EXCHANGE OF HYDROGEN PARTICLES IN MAGNESIUM

Charge-changing cross sections for hydrogen beams in materials of low ionization potential are of interest in connection with neutral injection experiments. Investigation of electron capture processes accompanied by high excitation of the emerging projectile is the principal goal.[6] The alkali metal vapors, as well as a few more tractable target materials like magnesium, have suitably low ionization potentials.

We have begun measurements of the relevant charge-changing cross sections in a few such materials. In so doing we are able to add to and compare with the results of similar recent experiments.[6] A considerable experimental advantage is our use of cooled surface-barrier detectors as opposed to Faraday cups for all the emerging particles. The errors in determining neutral detection efficiencies and in measuring very small currents are greatly reduced. We are able to make measurements of σ_{10}, σ_{01}, $\sigma_{1\bar{1}}$, and $\sigma_{0\bar{1}}$ simultaneously.

Figure 6.4 shows our results for hydrogen beams in magnesium vapor. Our measurements of $\sigma_{0\bar{1}}$ appear to give entirely new information. The other data can be compared with those of Futch

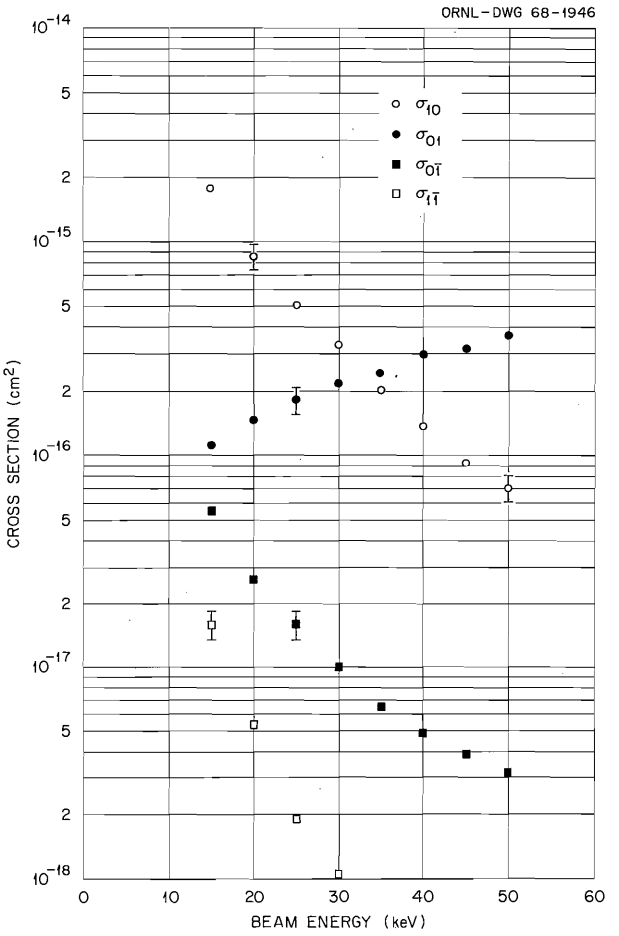

Fig. 6.4. The Charge-Changing Cross Sections σ_{10} (Single Capture), σ_{01} (Stripping), $\sigma_{0\bar{1}}$ (Single Capture), and $\sigma_{1\bar{1}}$ (Double Capture) vs Energy for Protons and Hydrogen Atoms in Magnesium Vapor.

[5] G. H. Dunn, *J. Chem. Phys.* 44, 2592 (1966).

[6] A general discussion of such possibilities is given by J. R. Hiskes, *Nucl. Fusion* 3, 124 (1963). Recent experimental results on capture processes in particular are found in the work of R. N. Il'in *et al.*, *JETP Letters* 2, 310 (1965). Recent work on charge exchange in magnesium is presented by A. H. Futch and K. G. Moses, abstract, *Fifth International Conference on the Physics of Electronic and Atomic Collisions*, p. 12 (1967).

and Moses.[6] Fairly good agreement of the energy dependence of σ_{10} and $\sigma_{1\bar{1}}$ is obtained. The magnitude would also agree fairly well if one ignores the fact that we have used more recent vapor pressure data.[7] Use of the new data makes our one- and two-electron capture cross sections roughly 25% lower than those of Futch and Moses. For σ_{01} there is definite disagreement in both energy dependence and magnitude. We have seen no sign of the dip they reported at a beam energy of 30 keV.

Our measurements were customarily reproducible to well within ±10% error. The error flags shown correspond to ±15%. More serious than this experimental uncertainty is the wide variation in published vapor pressures,[7] which comes to 30% in our case. At 300°C, for example, we have assumed a magnesium vapor pressure of 3.2×10^{-5} mm. Later corrections could be made by an appropriate multiplicative factor.

[7]We have used vapor pressure data from a recent private communication from R. Hultgren. The Futch and Moses work in ref. 6 was based on earlier data presented by R. Hultgren *et al.*, *Selected Values of Thermodynamic Properties of Metals and Alloys*, Wiley, New York, 1963.

6.3 ENERGY-DISPERSED BEAMS

Low-intensity neutral beams with energy dispersion between 0 and 40 keV have been previously described. These neutrals were created by the dissociation of H_2^+ in a gas cell which had a linear retarding potential applied along its length. No problems were encountered using geometries such as this for low-intensity beams; however, for currents of 10 to 50 mA the resulting ionization of the target gas produces electrical breakdown across the gas cell electrodes.

To avoid these breakdowns the geometry shown in Fig. 6.5 has been tested in conjunction with the DCX-1.5 group. The incident H_2^+ beams was collimated by an insluated plate with an aperture of 0.5 in. This plate could either be grounded or a potential could be placed on it. Inside of two liquid-nitrogen-cooled cylindrical copper cavities were mounted two fused arrays of glass capillaries. Each capillary was 100 μ long and 3 μ in diameter. Previous measurements have indicated that an H_2O vapor jet could thus be obtained with ~15° angular divergence. Retarding potentials were applied between the front plate and the cavities.

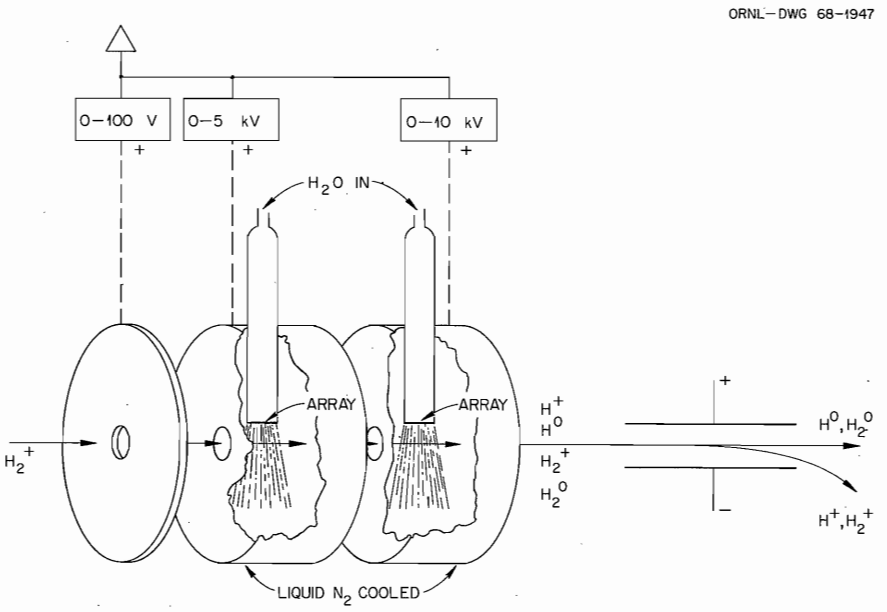

Fig. 6.5. Schematic Diagram of H_2O Vapor Jet Assembly Used to Produce Energy-Dispersed Beams of H^0.

A few volts positive potential applied to the front collimating plate extracted electrons from the beam region. Visible observations of the beam in the region between the ion source and collimating plate indicated that the H_2^+ beam was being "blown up" due to space charge. Thus, any applied retarding potential must not extract electrons from the space-charge-neutralized beam. The obvious thing to do is to immerse the electrodes in an axial magnetic field to prevent the radial loss of electrons.

Decelerating potentials of up to 5 kV could be applied to the electrodes in the presence of several milliamperes of beam and with the front electrode grounded. With a water vapor jet the degree of neutralization of the H_2^+ beam was less than 2%. Tests are now being performed with these and similar jets to determine the equilibrium fraction of H^0 expected from H_2O and other condensable vapors. No estimates or measurements have been obtained of vapor streaming from the jet assemblies.

6.4 CROSSED BEAM EXPERIMENT

Cross-section measurements have continued of the reactions

$$H_2^+ + e \longrightarrow H + H^+ + e ,$$

$$H_2^+ + e \longrightarrow 2H^+ + 2e .$$

At pressures of 10^{-9} torr the H or H^+ signal contribution from the electron beam is only one-tenth of that resulting from residual gas dissociation. To decrease the errors involved in comparing the H or H^+ signal with the H_2^+ signal, the electron beam is modulated by a gating circuit which also gates the silicon barrier detectors. In this manner the signal produced by the modulated electron beam is determined by subtracting the residual gas signal from the gas-plus-electrons signal. Since the difference of two large numbers is required, it is necessary that the pulse width of the timing pulse be reproducible to within 0.001%. The gating circuit used in the present measurements has been unreliable and has resulted in large uncertainties in the measured cross sections. New circuits with the desired accuracy have been designed and are undergoing tests.

6.5 MEASUREMENT OF SUBSHELL CONTRIBUTIONS TO THE TOTAL PHOTOABSORPTION CROSS SECTION OF Kr AND Xe IN THE RANGE 300 TO 2500 eV

Recent experiments[8-10] have shown that in the soft x-ray region photoabsorption cross sections do not exhibit the monotonic decrease above absorption edges that is typical of their behavior at higher energies. The departure from the familiar sawtooth shape of the photoabsorption curves at lower photon energies is mainly due to the breakdown of the hydrogen-like model of photoabsorption process which describes the electrons of the various subshells as moving in a screened Coulomb field. In addition, the spectral shape of the cross sections may be affected by electron-electron correlation effects, which become more pronounced for electrons in the less tightly bound shells.

Theory, regardless of the model used, always calculates partial (subshell) photoabsorption cross sections, whereas in the past, experiment has yielded only total cross sections. This has not impeded comparison between theory and experiment in regions where the hydrogen-like model[11] is valid, since partial cross sections there exhibit a similar behavior, and any error would appear in any partial as well as in the total cross section. In a more realistic theory[12] which uses a self-consistent field, partial cross sections vary in a somewhat irregular fashion, and discrepancies between total cross sections of theory and experiment may be due to errors in one or the other subshell cross section. Then it becomes desirable to *measure* partial photoabsorption cross sections to determine deficiencies of particular theoretical models. Rare-gas atoms are suitable for a detailed study because of the absence of solid-state effects, such as band structure, plasmon excitation, and scattering. In the present work, we measured relative subshell photoabsorption cross sections for krypton and xenon in

---

[8] A. P. Lukirskii, I. A. Brytov, and T. M. Zimkina, *Opt. Spectry.* **17**, 234 (1964); and *Opt. i Spektroskopiya* **20**, 368 (1966).

[9] D. L. Ederer, *Phys. Rev. Letters* **13**, 760 (1964).

[10] J. A. R. Samson, *J. Opt. Soc. Am.* **54**, 842 (1964).

[11] H. Hall, *Rev. Mod. Phys.* **8**, 358 (1936).

[12] J. W. Cooper, *Phys. Rev. Letters* **13**, 762 (1964); and *Phys. Rev.* **128**, 681 (1962).

the energy range from about 300 to 2500 eV. Photons of these energies are absorbed by L, M, and N electrons of krypton or by M, N, and O electrons of xenon. Theoretical subshell contributions and measured[8–10] total cross sections presented in Figs. 6.6 and 6.7 show the "unusual" behavior of the photoabsorption cross section in this energy range.

We used the photoelectron method to measure the subshell contribution. According to the relation

$$E_{ij} = h\nu_i - E_j ,$$

a photon of energy $h\nu_i$ ejects an electron of binding energy E_j (from subshell j) with the kinetic energy E_{ij}. The relative intensities P_{ij} of these photoelectrons E_{ij} are then a direct measure of the relative absorption probabilities or partial cross sections of the subshell electrons at a given photon energy. Characteristic x rays from a number of different targets were used, and the electrons produced were separated in an electrostatic analyzer described previously.[13] Figure 6.8 presents the photoelectron spectrum $f(E_{ij})$ for 3s, 3p, 3d, 4s, and 4p electrons of krypton that are ejected by Cu $L\alpha$ x rays and, to a lesser degree, by Cu $L\beta_{3,4}$, Cu $L\gamma$ and Cu Ll photons. We analyzed only those lines that are due to the strong Cu $L\alpha$ line. It can be seen immediately that the cross section is largest for 3d electrons and very small for 3s electrons as well as for 4s and 4p electrons. This result is in satisfactory agreement with the model calculation of Cooper,[14] who employed a central field in his calculation; but it is at variance with the Stobbe-Hall theory,[11] which is based on a screened Coulomb field of the atom (hydrogenic approximation). The latter theory predicts a cross section four times larger for 3s electrons than for 3d electrons.

A novel feature which has not been considered so far in calculations of photoabsorption cross section is the emission of the two electrons by a single photon, as evidenced by the skewed satellite peaks on the low-energy sides of the photolines[15] (cf. peaks near channels 22 and 55 of Fig.

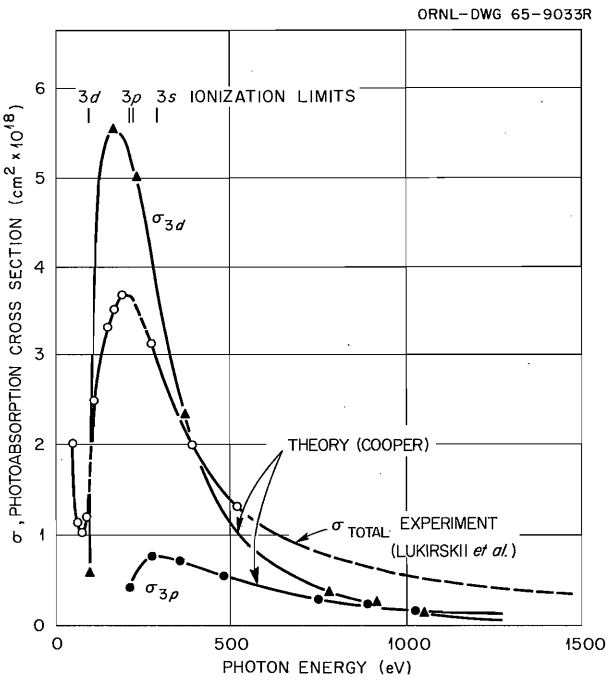

Fig. 6.6. Total Photoabsorption Cross Section of Krypton According to Lukirskii *et al.*[8] and Partial Cross Sections According to Cooper.[14]

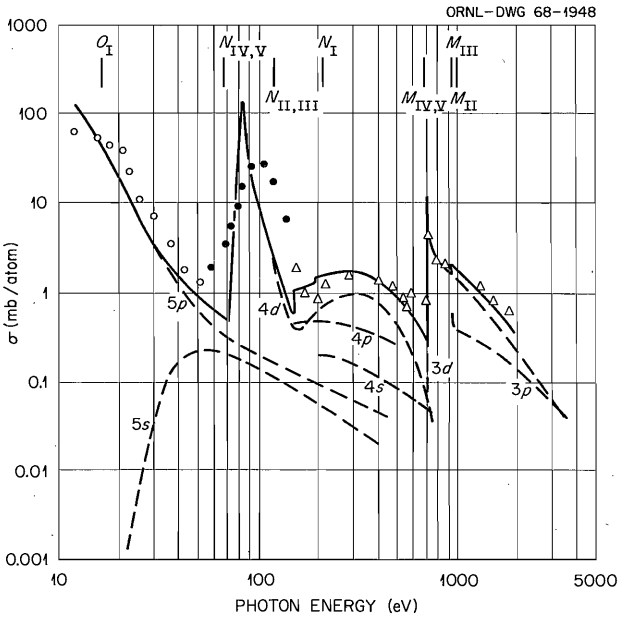

Fig. 6.7. Total Photoabsorption Cross Section of Xenon. Experimental points according to Samson,[10] Ederer,[9] and Lukirskii.[8]

A second feature which has not been considered so far in calculations of photoabsorption cross section is the emission of the two electrons by a single photon, as evidenced by the skewed satellite peaks on the low-energy sides of the photolines[15] (cf. peaks near channels 22 and 55 of Fig.

[13] M. O. Krause, *Phys. Rev.* **140**, A1845 (1965).

[14] J. W. Cooper (personal communication); see also ref. 5.

[15] Details of the effect are described elsewhere for absorption in the outer shells of He, Ne, and Ar [T. A. Carlson, *Phys. Rev.* **156**, 142 (1967)], in *KL* shells of Ne and Ar, and in *KM* shell of Ar (see sect. 6.6).

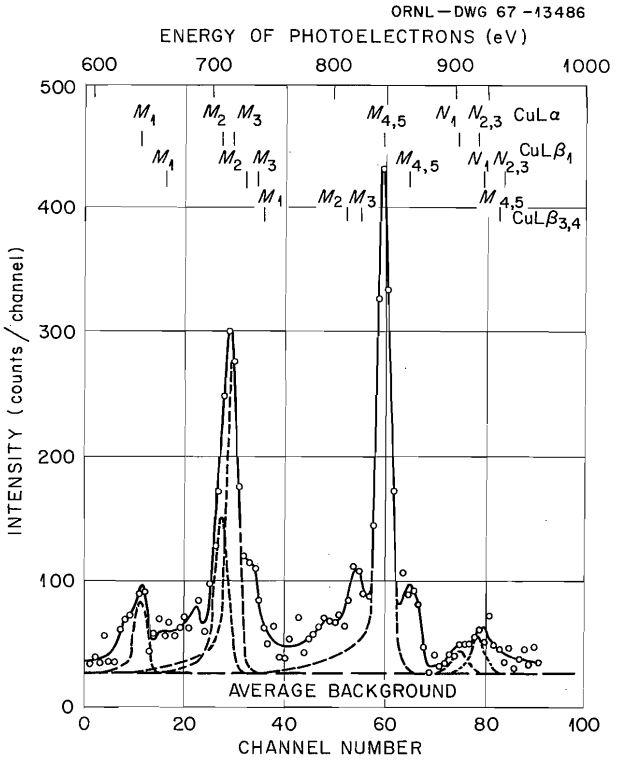

Fig. 6.8. Photoelectron Spectrum Produced by the Interaction of Cu *L* X Rays with Krypton. Intensities of the resolved (dashed) lines correspond to the photoabsorption cross sections of *M* and *N* electron subshells for Cu $L\alpha$ x rays.

6.8). They arise from the simultaneous emission of a 3*d* and 4*p* or 3*p* and 4*p* electron by a Cu $L\alpha$ photon. The emission of two electrons occurs in about 20% of the photoabsorption events and constitutes, therefore, a sizable contribution to the total photoabsorption cross section.

Photoelectron spectra of the same kind as shown in Fig. 6.8 were obtained for the interaction of about 12 different characteristic x-ray lines with *M* and *N* subshell electrons of krypton and *M*, *N*, and *O* subshell electrons of xenon. The final analysis of the data is under way, but a preliminary analysis shows that cross sections of *d* electrons are dominant over the entire range measured and that cross sections of *s* electrons remain small, even far above their respective thresholds. Although Cooper's theory reproduces the general features of the experimental data satisfactorily, a number of refinements, such as inclusion of exchange and correlation effects, seem to be indicated (i.e., the 3*d* cross section of xenon drops off more slowly than calculated). It can be anticipated that a "good" theory anchored to the data of the rare-gas atoms will also serve well for different elements and molecules.

6.6 ABSTRACT OF PAPER SUBMITTED TO *PHYSICAL REVIEW* FOR PUBLICATION: DOUBLE ELECTRON EJECTION FROM *KL* SHELL OF Ne AND Ar AND FROM *KM* SHELL OF Ar IN THE PHOTOABSORPTION PROCESS*

M. O. Krause, T. A. Carlson, and R. D. Dismukes**
Oak Ridge National Laboratory
Oak Ridge, Tennessee

Electrons emitted in the photoabsorption of Mg Kα and Al Kα x rays by neon and Ti Kα x rays by argon have been studied with an electrostatic energy analyzer. On the low-energy side of the photolines which are characteristic of single electron emission, discrete peaks and continua are observed which respectively indicate excitation and ionization of a second electron. From these electron spectra proabilities of a single photon to interact with two electrons are derived (per photon interaction): Ne KL: (18.5 $\pm$ 1.0)%; Ar KL: (2.5 $\pm$ 0.8)%; and Ar KM: (21.2 $\pm$ 1.4)%. In about 85% of the double events both electrons go into the continuum; in about 15% of the cases the less tightly bound electron is promoted to excited states by monopole transitions. Observed intensities compare favorably with values obtained from the theory of electron shakeoff, using single electron HF wavefunctions. The shape of the continuum electron spectra is in fair agreement with theoretical predictions; about 80% of the shakeoff electrons have energies of $0 \leqq E \geqq E_I$, where E_I is the binding energy of the L or M electron in the atom that lacks one K electron. Consequences of the present study in regard to x-ray and Auger-electron satellites are discussed, and it is found that specific satellites can be associated with specific double-hole configurations. The following relative intensities of Kα satellites were measured for Mg, Al, and Ti: 13%, 8.5%, and 4% respectively.

*Research sponsored in part by the U.S. Atomic Energy Commission under contract with the Union Carbide Corporation.
**U.S.A.E.C. Health Physics Fellow, Vanderbilt University, Nashville, Tennessee.

6.7 MULTIPLIER EVALUATION

As a continuing program in the evaluation of detectors for neutral and charged beams in atomic collisions and plasma physics, we have determined the response of a model M308 Bendix electron multiplier.

The Bendix multiplier is a continuous-strip-dynode $E \times H$ type multiplier. Previous evaluation[16] of a $\frac{3}{4}$- by $\frac{3}{4}$-in. tungsten cathode multiplier indicated a gain variation of 10^5 over the cathode face. The M308 multiplier has a 0.2- by 0.4-in. cathode aperture and should be somewhat less sensitive to gain changes across the multiplier face.

Using a 0.005-in.-diam proton beam as a probe, the relative response was measured as a function of the position of impact along the cathode surface. In Fig. 6.9 the multiplier response is plotted as a function of the position of proton impact from the dynode edge. Shown is the actual recorder tracing of the multiplier output current for 40-keV protons. For the smaller cathode the sensitivity to cathode position fluctuates only a factor of 2 to 3 across the cathode. Maximum gain was obtained when the beam was incident at the cathode center. The various minima resulted from the beam being intercepted by the grid wires im-

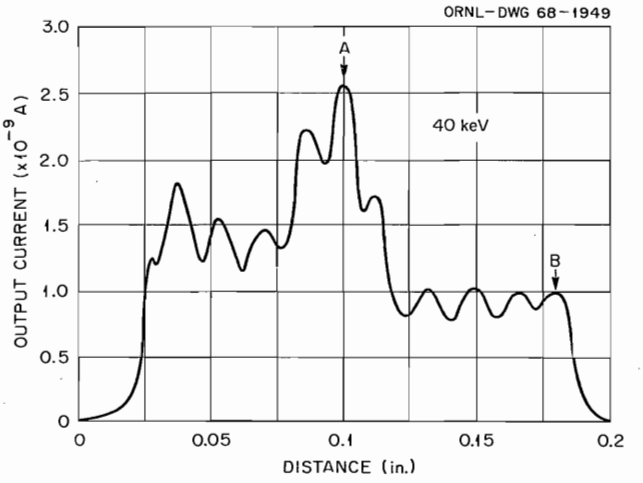

Fig. 6.9. Relative Response of a Bendix M308 Electron Multiplier as a Function of Beam Impact Position on the Cathode. Results are shown for a 40-keV H^+ beam 0.005 in. in diameter.

[16] *Thermonuclear Div. Semiann. Progr. Rept. Oct. 31, 1964*, ORNL-3760, p. 63 (1964).

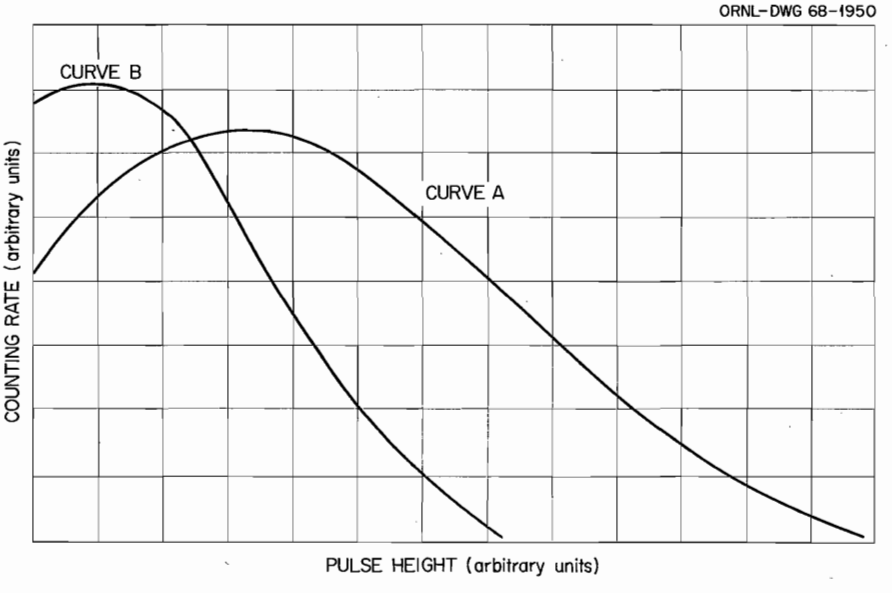

Fig. 6.10. Pulse-Height Spectrum Obtained from a Bendix M308 Electron Multiplier for 40-keV H^+ Impact. Curve *A* was obtained when beam was positioned in the center of the cathode; curve *B* resulted from beam striking cathode edge.

mediately in front of the cathode. This auxiliary grid is placed in front of the cathode by the manufacturer to provide field uniformity in the cathode region.

The pulse-height spectrum obtained under the same conditions as the current traces is plotted in Fig. 6.10. The beam was positioned on the cathode indicated by *A* and *B* in Fig. 6.9. The pulse-height spectrum is broad, which is expected from many stages of electron multiplication. Placing a solid-state silicon barrier detector in front of the multiplier permitted an absolute measurement of the proton counting rate. Comparing this counting rate with the multiplier counting rate revealed a multiplier efficiency of 56 and 37% at points *A* and *B* respectively. Similar results were obtained for proton impact energies of 20 keV.

6.8 ATOMIC AND MOLECULAR PROCESSES INFORMATION CENTER

C. F. Barnett R. A. Langley
D. A. Griffin J. A. Ray
M. O. Krause I. A. Sellin

With the publication of AMPIC-9, covering the first six months of 1967, the bibliographies of literature in the field of atomic and molecular processes are now up to date. Current literature is now being searched and evaluated on a monthly basis. This search is made available to the JILA information center in order to eliminate duplicate searching. The information in compiling the bibliography is machine stored, and computer printouts are used for reproduction. Additional bibliographies will be distributed in January and July of each year. Our computer technique can now partially retrieve references, processes, and reactants from machine storage.

The International Directory of Workers in the Field of Atomic and Molecular Collisions was reissued in May 1967 as AMPIC-5. Its 2300 entries are kept up to date by machine storage.

Our first comprehensive review, "Ion-Atom Interchange Reactions," to be published in the form of a monograph, is in final draft and will be sent to the publisher in December 1967. The rough draft of the second monograph, "Ionization, Excitation, and Dissociation by Heavy Particles," should be complete by January 1, 1968. Final plans have been completed and writing has begun on monograph 3, "Charge Exchange Cross Sections in Gases and Solids." Preliminary work has started on the two-volume third edition of "Cross Sections of Interest to Controlled Thermonuclear Research." Examination of the literature for monograph 2 necessitates the extraction of data from published graphs and replotting the data by computer in a more usable form. Our present method to process the graphical data is to trace the curve with a stylus which indicates an analog voltage signal corresponding to the *x-y* coordinates. The analog signal is digitalized and printed out on paper tape. This printout is then key-punched and placed on magnetic tape. The computer transforms the *x* and *y* units, and the CalComp plotter plots the data points in a usable graphical form. A program has been written to utilize the LINC-8 computer as a time-saving device in this process. The analog signals from the stylus are fed directly into the LINC-8 converter, which puts the data on punched paper tape. This is transferred to magnetic tape, which in turn drives the CalComp plotter.

The data center's activities have consisted primarily in reviewing and evaluating pertinent papers from the current and past literature, performing literature searches, and filling requests for various types of information. Progress is being made in searching and evaluating literature back to 1950 and storing it for retrieval.

7. High-Current Ion Beam Production and Injection

R. C. Davis G. G. Kelley
R. R. Hall O. B. Morgan[1]
R. F. Stratton

7.1 INTRODUCTION

The major effort during this report period has been on continuation of the ion-optical studies described in the last report. We have found that the limitation of beam quality is due entirely to the shape of the ion emission surface and the extraction field, at least in the situations examined. With large extracted currents the plasma surface has a complicated shape and strong curvature as a result of nonuniformity of plasma density in the ion source cup. Efforts to control this surface using conventional sources have not produced significantly better results. We are developing a new source which, it is hoped, will produce a more uniform plasma.

7.2 ION-OPTICAL STUDIES

This work has been pursued to get a better understanding of the factors which determine the optical properties of an accelerated beam. Figure 7.1 shows the system used in the studies. It consists of an ion source, usually of the Demirkhanov type,[2] with a plasma expansion region, an accelerating electrode, and a deaccelerating electrode, used to prevent electron drain from the drift region into the accelerating gap. The beam is space charge neutralized over almost its entire length by this means. There is a target 48 in. below the center of the lens coil which measures (calorimetrically) the ion current through a $\frac{1}{2}$-in. or a 2-in. aperture plate 46 in. below the coil. The arrangement described previously[2] for analyzing the angular distribution of the ion beam is located 16 in. below the center of the lens. In this more recent work, however, a Faraday cup replaces the copper-constantan thermocouple detector, giving a much faster response time. A beam can be scanned in 10 sec or less, limited by the response time of the X-Y recorder.

Figure 7.2 shows scans made of a 40-keV beam of $^4He^+$ ions at 100 and 200 mA. Figures 7.3 and 7.4 are the ion rays determined from these scans. The focal length of the lens was determined by measurement of the axial magnetic field and by an analog computer calculation of the ion trajectory through this field, assuming that the radial variation of the axial field can be neglected (which it can for rays sufficiently close to the axis). In the case shown in Figs. 7.3 and 7.4, the calculated focal length is 16 in., which is not significantly different from the value obtained for paraxial rays. When the lens is made stronger, however, the focal length determined by means of the analog computer may differ by as much as 20% from the paraxial approximation. The particle trajectories are as expected for the emission surface shapes shown in the figures. The downward dimple forms on the surface in the current range between 100 and 140 mA, depending on the extraction geometry. It can be seen that the current density is highest near the axis.

In most cases the response shape of a scanned line is determined by the slit size and detector aperture. The inferred radial temperature is less than

[1] Present address: University of Wisconsin, Madison, Wis.

[2] *Thermonuclear Div. Semiann. Progr. Rept. Apr. 30, 1967*, ORNL-4150.

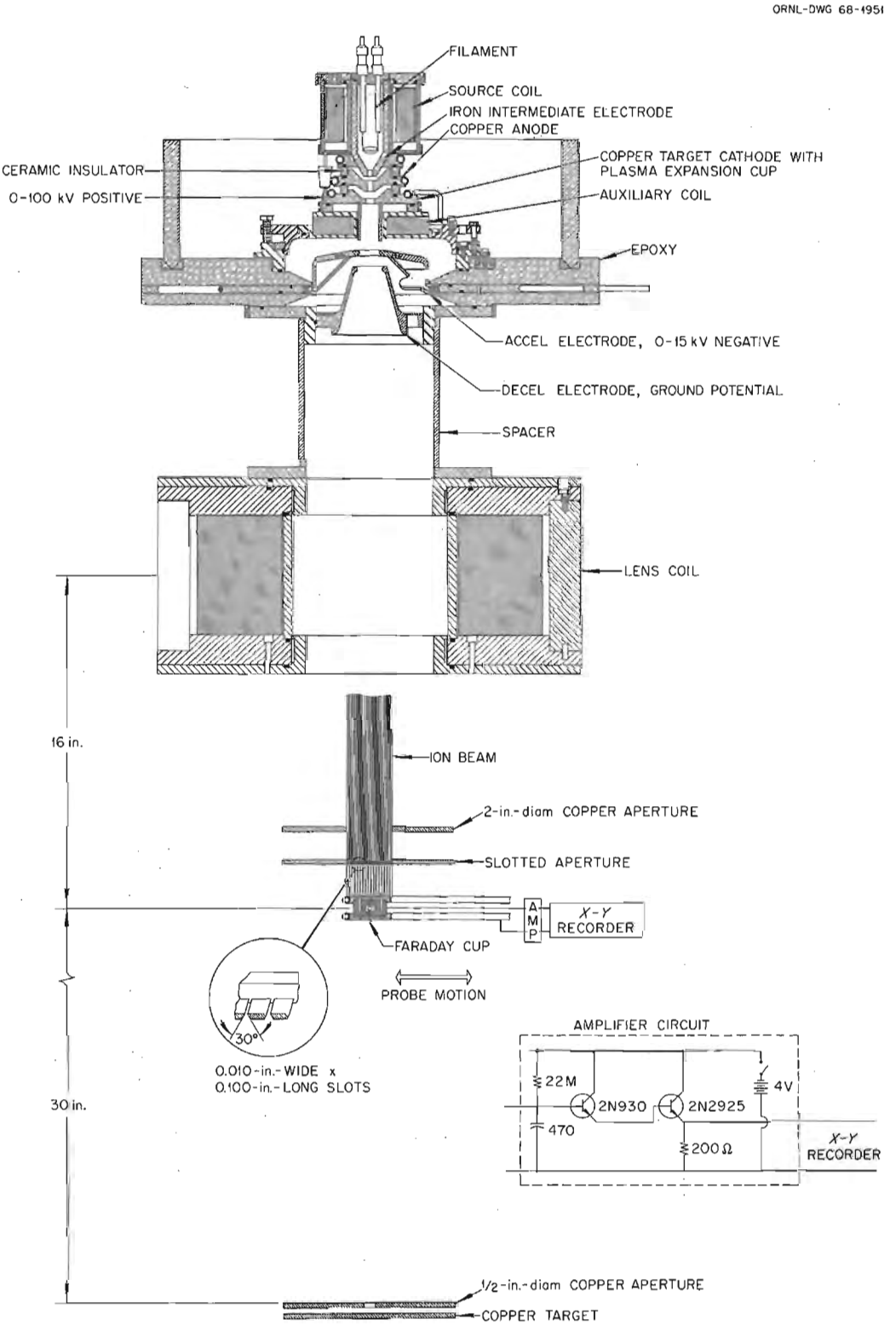

Fig. 7.1. System Used for Ion-Optical Studies.

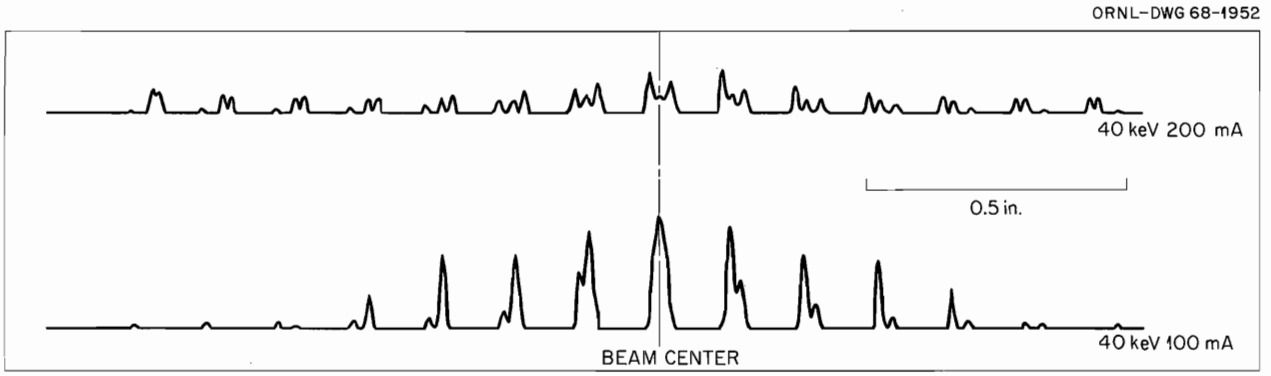

Fig. 7.2. Scans of $^4He^+$ Ion Beams 16 in. Below the Center of the Lens Coil Using the Faraday Cup Arrangement Shown in Fig. 7.1.

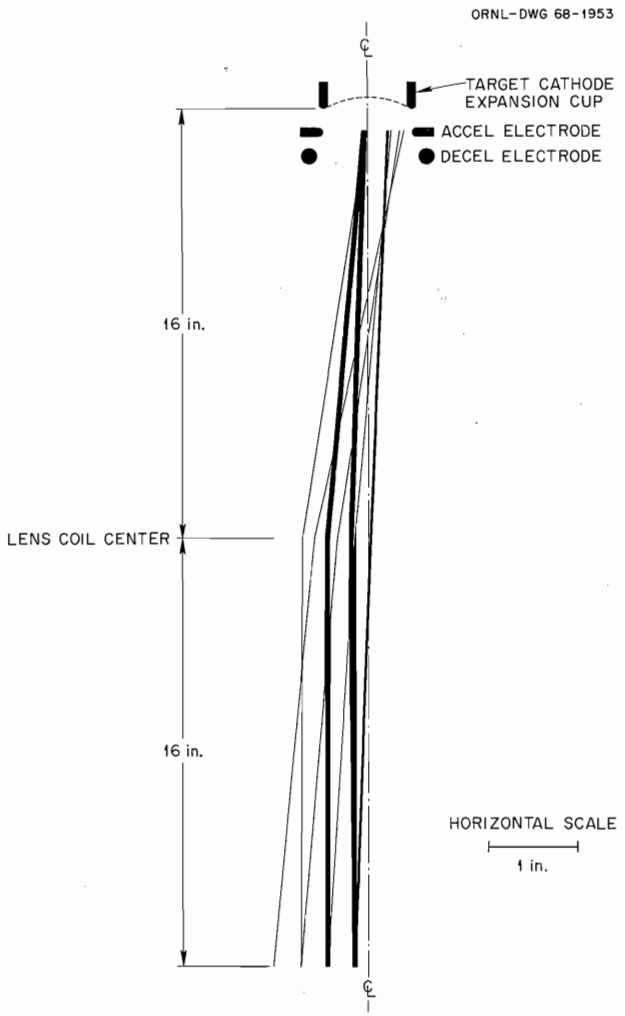

Fig. 7.3. Ion Trajectories for a 40-keV, 100-mA $^4He^+$ Beam as Determined from Data of Fig. 7.2.

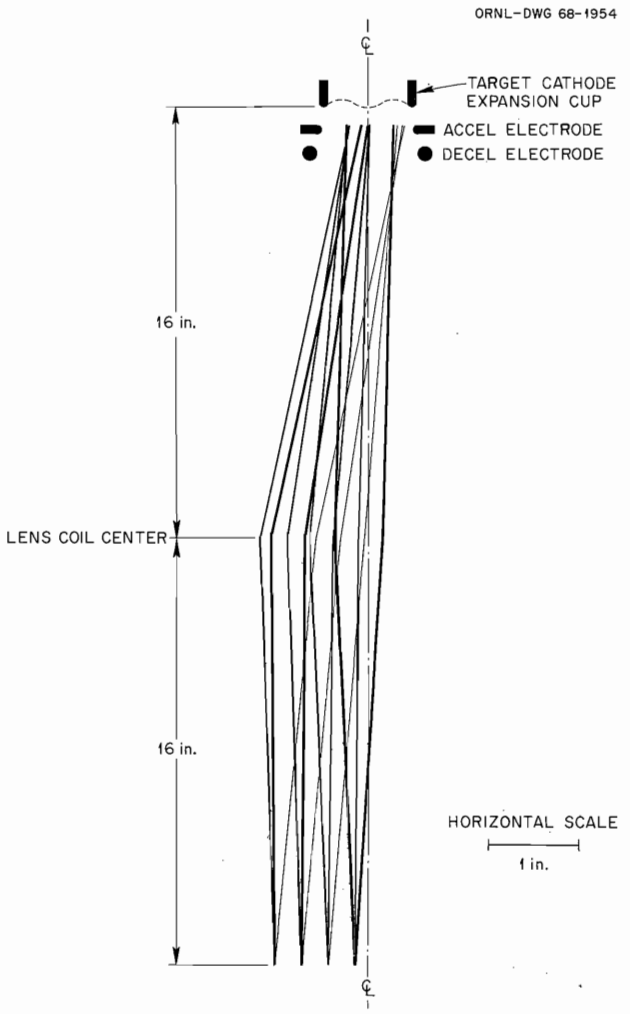

Fig. 7.4. Ion Trajectories for a 40-keV, 200-mA $^4He^+$ Beam as Determined from Data of Fig. 7.2, Showing the Effect of a Change in the Shape of the Plasma Surface with Increased Current.

1 eV. Apparently there are no effects which would imply fluctuating electric fields in the beam or at the surface of the plasma. The important conclusion is that all the properties of the extracted beam are determined by the ion-optical properties of the emission region and the expected focal length of the lens.

The effects of changes of source geometry were studied using both helium and hydrogen ions. It was hoped that results obtained with helium could be applied to hydrogen, helium being preferable for analysis since it has a single mass. It turned out, however, that a source geometry which gave a factor of 2 improvement in ion current over the previous best geometry with helium (copper target cathode with expansion cup) shows very little if any improvement with hydrogen (Table 7.1). To investigate the possibility that the difference was a mass effect, the experiment was run with deuterium. The results, given in Table 7.1, are ambiguous.

Table 7.1. Ion Current Focused Through ½- and 2-in. Apertures 46 in. Below the Lens Coil Center While Using Two Types of Target Cathodes

The copper target cathode is shown in Fig. 7.1, and the iron target cathode has the same geometry except that the expansion cup is omitted

Ion Species	Total Current (mA)	Current through ½-in. Aperture (mA)	Current through 2-in. Aperture (mA)	Type of Target Cathode
H_2^+	240	79	135	Iron
H^+	190	55	111	Iron
H_2^+	205	70	119	Copper
H^+	205	59	96	Copper
$^4He^+$	210	115	164	Iron
$^4He^+$	190	57	119	Copper
D^+	155	64	89	Copper
D_2^+	175	32	58	Copper
D^+	225	53	100	Iron
D_2^+	240	58	109	Iron

7.3 NEW SOURCE DEVELOPMENT

The iron intermediate electrode used in the conventional duoplasmatron causes the source arc to be very highly concentrated on axis and reduces plasma loss by radial diffusion in the region around the anode aperture. At the same time, however, it may make the radial density gradient larger than is desired from the standpoint of uniformity of the plasma in the expansion cup. It seems likely that a source in which magnetic lines of force extend through the region of constriction might yield an arc with a smaller radial density gradient. For this reason the source assembly shown in Fig. 7.5 is being made. The coils are of the ribbon type developed by Luton.[3] The coil around the intermediate electrode should produce 6.9 kG at a current of 500 A.

7.4 NEW 600-keV ACCELERATOR

The non-PIG 600-keV accelerator column[2] was assembled and tested. The main disk of epoxy was known to have voids and strains caused by improper pouring and curing procedures. The column broke down electrically at 370 keV, resulting in rupturing of the epoxy apparently at the location of a strain. The damage was repaired and voltage reapplied. This time breakdown occurred at 470 keV, damaging the main body of the epoxy to a point beyond repair. When the disk was cut into sections, it was found that the flaws were even more extensive than anticipated. We plan to pour another disk at lower ambient temperature and with extreme care to prevent air inclusion.

[3] *Thermonuclear Div. Semiann. Progr. Rept. Oct. 31, 1966*, ORNL-4063.

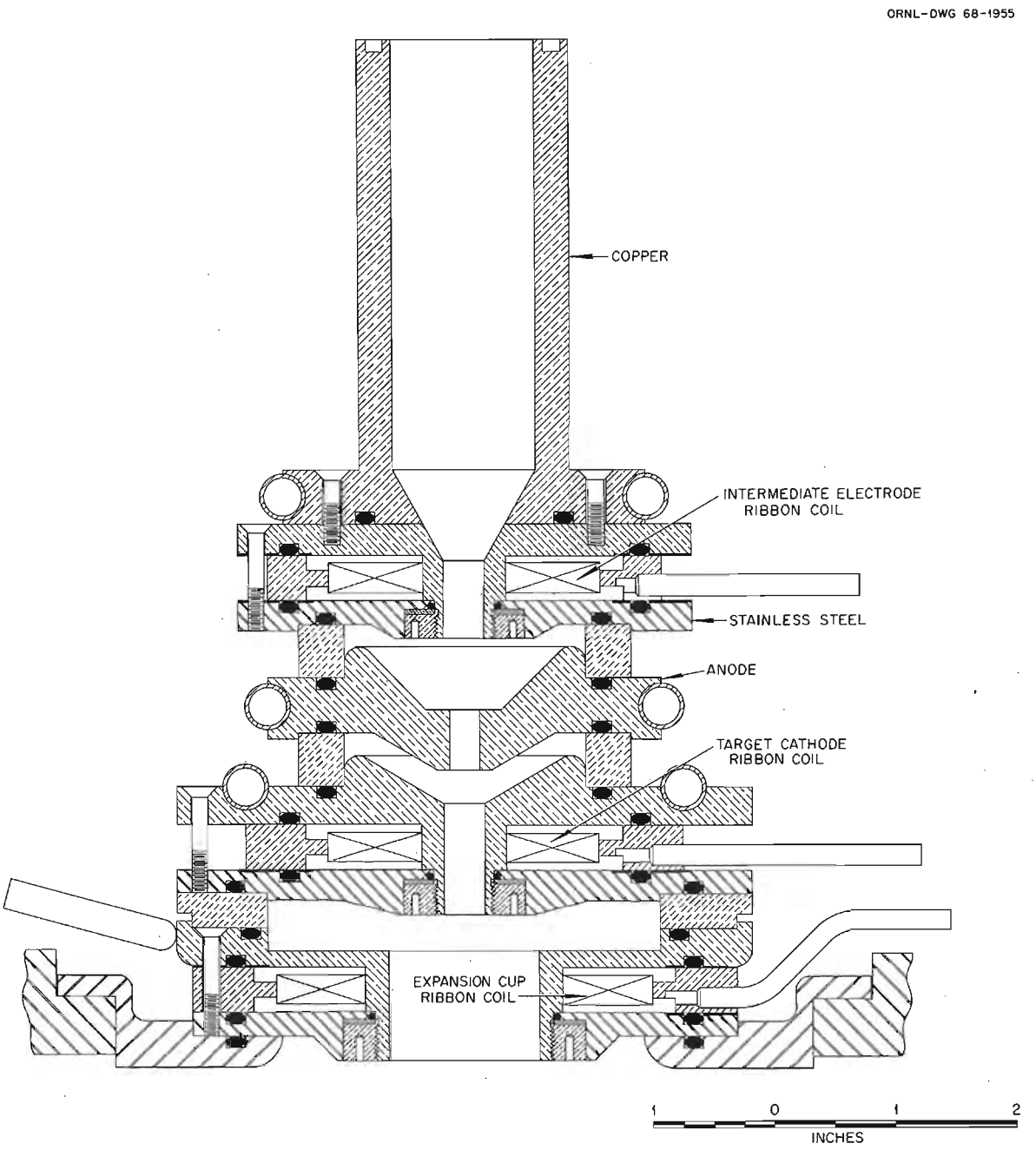

Fig. 7.5. Assembly of Ribbon Coils to Be Tried Singly or in Combination in an Attempt to Increase the Uniformity of the Plasma by Control of the Magnetic Field Shape.

8. Magnetics and Superconductivity

8.1 THE NEW ELMO MAGNETIC FIELD SYSTEM

J. N. Luton, Jr.

8.1.1 Introduction

The ELMO machine[1] is presently equipped with 8-mm microwaves for electron cyclotron resonance heating, but in the near future a 5-mm microwave source will be added. The resonant field strength for the shorter waves is 19.7 kG, which can be attained with the present coil system only near the centers of the two mirror coils. Since it is desirable to achieve the resonance field strength on a pair of surfaces which are located between the two mirror coils, the existing coil system is not suitable for use with the new 5-mm microwave source.

We earlier considered the possibility of increasing the field strength by connecting the existing mirrors to larger generators and simultaneously increasing the cooling capacity of the coils by the addition of drag-reducing agents to the cooling water. However, after rather detailed consideration, this approach was dropped.

Increasing the field strength by reducing the spacing of either the flat field coils or the mirror coils would require major modification of the structural parts of the machine. It is therefore necessary to replace one of these coil pairs. It was decided to replace the mirror coils because they are very much smaller than the flat field coils.

The mirror coils fit in small annular wells, and there would not be sufficient end room for the increased number of hydraulic terminations required by tubular-conductor coils of higher power. A ribbon coil[2] was therefore selected. The possibility exists of using a conductor with either transverse or longitudinal coolant grooves. In the first case, the cooling water flows parallel to the coil axis; in the second case, this flow is azimuthal. The first type was chosen because of the longer testing experience[3] and the expected ease of construction.

The annulus necessary to carry water to the midplane end of the mirror coil can be located either within a larger coil or surrounding a smaller coil. As can be seen in Fig. 8.1, the resulting heating contours are not much different, and the ELMO group was willing to accept the latter arrangement, which seemed somewhat simpler. Later, if a still stronger central field should become necessary, two longitudinal ribbon coils could replace the transverse ribbon coils. Since they do not require end headers, they could be placed $\frac{7}{8}$ in. nearer the midplane and thus would give a higher midplane field.

8.1.2 The Design of the New Ribbon Mirror Coils

Each coil is a spiral of a composite strip of three interleaved ribbons, each as wide (5 in.) as the length of the coil. The first ribbon is a copper ribbon, nominally 0.025 in. thick, with coolant grooves rolled across one face. The second ribbon is glass cloth impregnated with Teflon and has a thickness of 0.005 in. The third ribbon is made of 0.007-in. hard-drawn copper and is placed between the insu-

[1] For a description of ELMO, see *Thermonuclear Div. Semiann. Progr. Rept. Apr. 30, 1965*, ORNL-3836, p. 35; and *Thermonuclear Div. Semiann. Progr. Rept. Oct. 31, 1965*, ORNL-3908, p. 41.

[2] This type of coil has been described in earlier reports, the latest being *Thermonuclear Div. Semiann. Progr. Rept. Oct. 31, 1966*, ORNL-4063, pp. 111–17.

[3] One transverse ribbon coil has been run spasmodically over a period of many months without damage. It was energized for a total of 100 hr, cycled about 50 times, exposed to flowing water 200 additional hours, and except for one removal for inspection and cleaning, was in stagnant water the remainder of time.

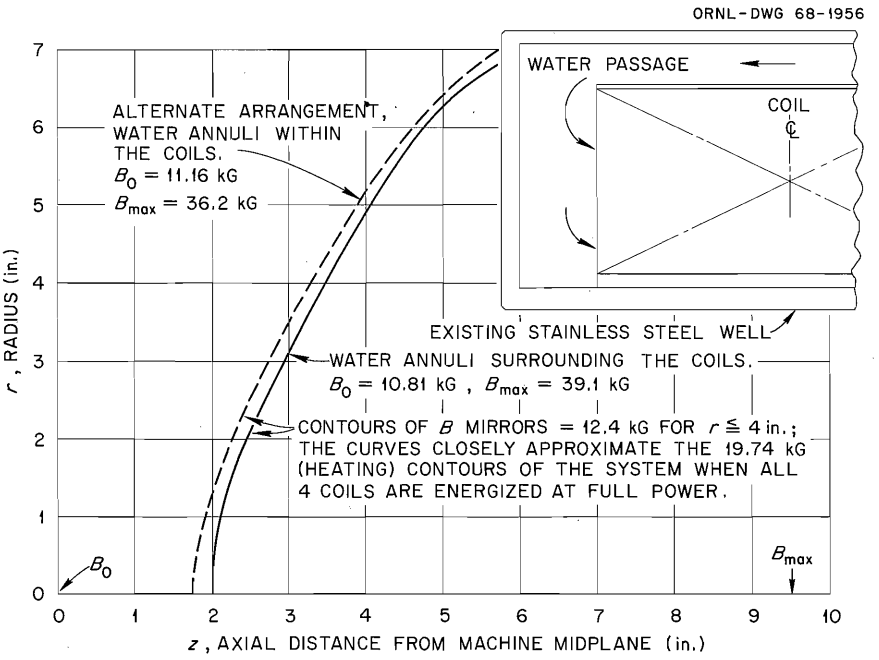

Fig. 8.1. Most Inward Locations of Heating Contours, for Coils Encompassed by the Water Annuli and Those Encompassing the Water Annuli.

lation ribbon and the grooved conductor in order (1) to increase the conductor surface area exposed to the cooling water and (2) to protect the insulation from the edges of the grooves.[4] The conductor ribbons were soft soldered to a winding mandrel, part *A* of Fig. 8.2, and fed through brakes as the mandrel was rotated to wind up the coil. When the allowable winding depth of 2.4 in. was reached, the three ribbons were cut off, and the ends of the two copper ribbons were butt welded to a single copper ribbon 7.9 in. wide. Four turns of the wider ribbon were then rolled and soldered together, forming cylinder *C* of Fig. 8.2. This cylinder will restrain the radially outward magnetic forces, conduct electricity to the outer ends of the conductor ribbons, and separate the entrance water chamber from the exit chamber. The cooling water will flow down the outside of cylinder *C* to the midplane end of the coil, radially across the face of the coil, and back through the cooling grooves to the annular exit header within *C*.

A suitable water filter is on hand and will be installed in the supply line as close to the coils as practical. In addition, the coils are designed so that they should not fail due to the blocking of one or more isolated cooling grooves. However, the grooves are so small (0.011 in. deep × 0.043 in. wide) and so numerous (12,300 grooves/coil) that it will be necessary to exercise extreme care in the installation and maintenance of the piping system downstream of the filter. Unfortunately, it will be necessary to open this line whenever ELMO is disassembled.

8.1.3 Preliminary Tests

Previously, some preliminary work had been done to test the feasibility of ribbon coils. Operational tests of small coils carrying current densities in the neighborhood of 200 kA/in.^{2} were previously reported.[5] These coils used an external support

[4] A close-up photograph of a coil winding of this type is shown in *Thermonuclear Div. Semiann. Progr. Rept. Oct. 31, 1966*, ORNL-4063, p. 113.

[5] *Thermonuclear Div. Semiann. Progr. Rept. Apr. 30, 1966*, ORNL-3989, pp. 110–13.

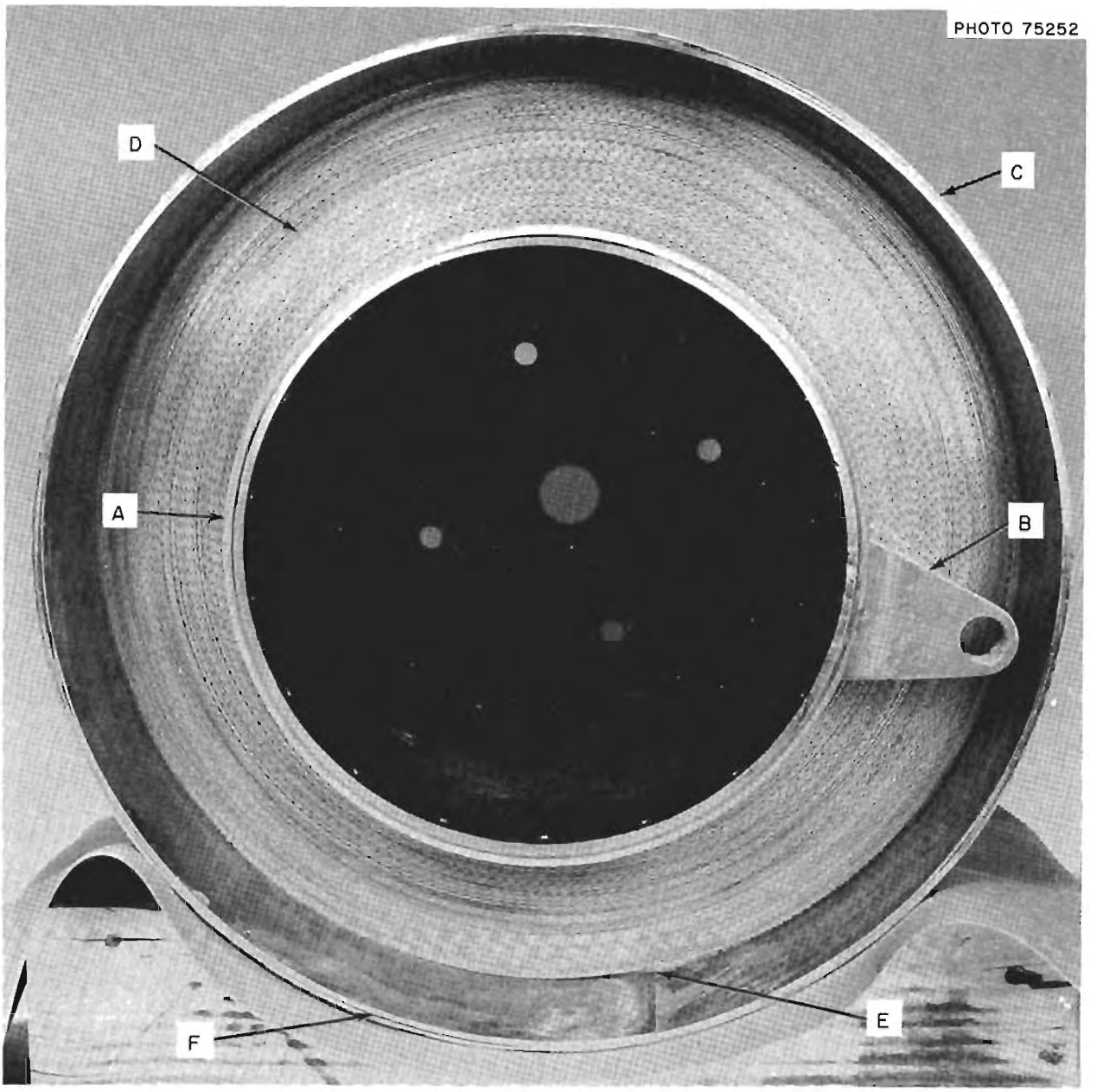

Fig. 8.2. Downstream Face of Partially Completed Coil. (*A*) Winding mandrel, which also serves as the inner current lead and a coolant pressure vessel. (*B*) Inner current lug with tapped hole for conductor rod. (*C*) Outer cylinder, which serves as the outer current lead and a pressure vessel. (*D*) Conductor-insulator spiral. (*E*) Transition from 5-in. ribbons to 8-in. ribbon. (*F*) Imperfections (gaps) in the outer cylinder.

ring rather than a cylinder formed of several turns of ribbon soldered together as is used by the ELMO design. Therefore, four turns of $\frac{1}{2}$-in.-wide copper ribbon were wound up, soft-soldered together to form a cylinder, and mounted around a hydraulic coil expander[6] previously constructed for the mechanical testing of superconducting windings. The test cylinder failed by stretching of the copper at one azimuth rather than by a shearing of the solder joint, although the joint was not so perfect that all layers of the cylinder ruptured simultaneously.

The combination of restricted winding depth, high power (2.5 MW/coil), and the difficulties of grooving very thin ribbon led to the choice of a very large coil current. The coils will be powered by two dc generators on a single shaft, each rated at 2.5 MW and 7150 A, and the coil current was chosen to be twice the generator rating. Although the original design of the regulators was intended only for independent or series operation of the generators, we have apparently succeeded in adapting them for use either singly, in series, or in parallel. The generators have been run stably in parallel up to the rating of the dummy load, 5000 A.

Because of the unusually high coil current, it seemed advisable to make current tests of the coil leads and their associated parts. Figure 8.3 shows the apparatus constructed to test the water cables *A*, cable connections *B*, feedthroughs *C*, copper

[6]See sect. 8.5.

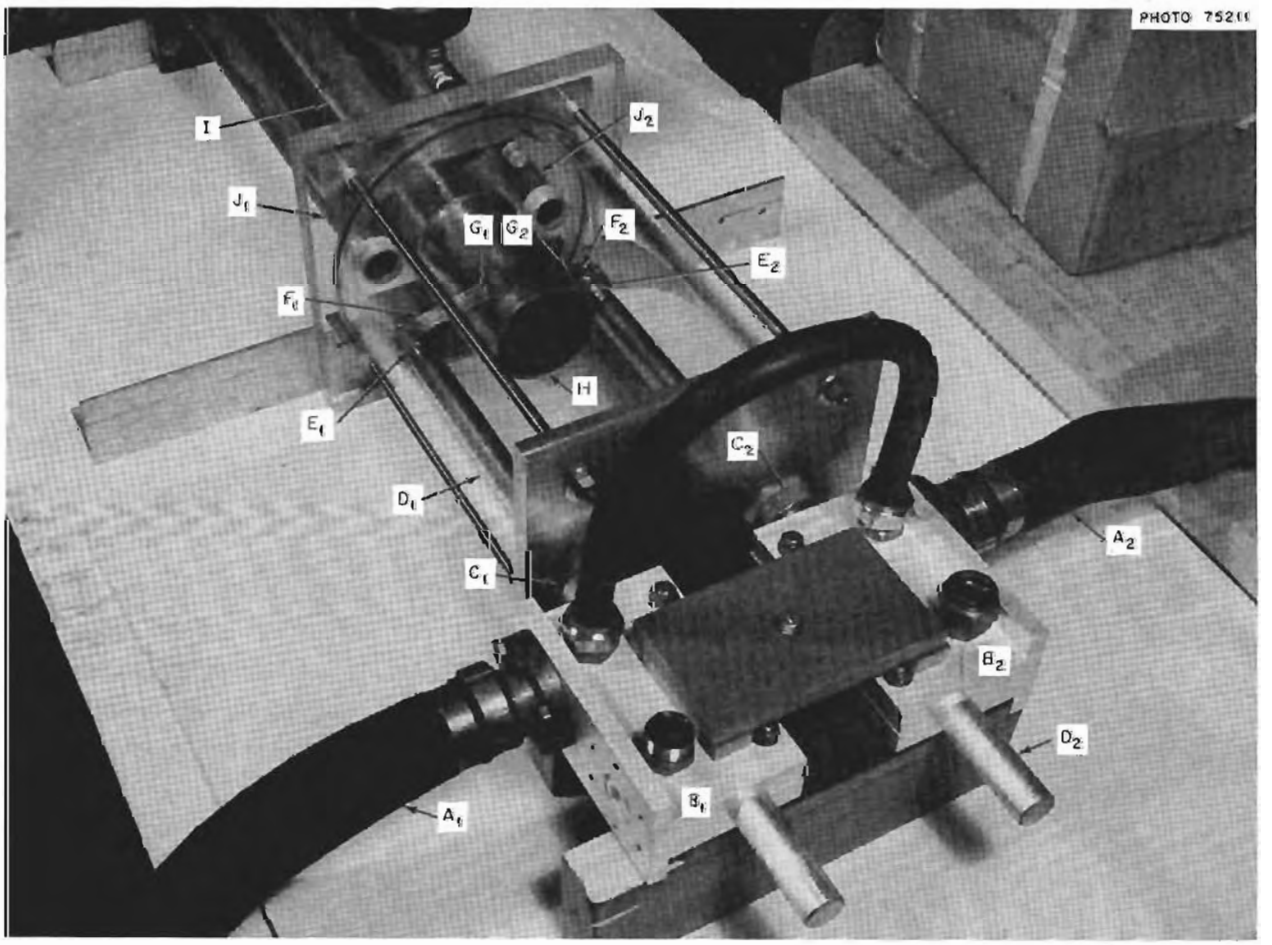

Fig. 8.3. Test Apparatus for Leads and Connectors. (*A*) Watercooled electrical cables. (*B*) Cable connectors. (*C*) Air-to-water feedthroughs. (*D*) Copper feed rods. (*E*) Pipe threads, $\frac{3}{8}$ in. nominal, male threads chrome plated for easier removal. (*F*) Copper lugs. (*G*) Lug-to-coil joints, screwed and soft soldered. (*H*) 3-in.-ID cylinder, formed of four turns of 5-in.-wide copper ribbon soldered together. (*I*) Inlet water pipe. (*J*) Outlet water pipes.

feed rods *D*, pipe threads *E*, lugs *F*, lug-to-coil joints *G*, and a cylinder *H* composed of four turns of copper ribbon soldered together. Items *A* through *E* are those intended for use on the actual coil, and the last three items are close imitations. For the permanent system, two cables will fasten to each connector *B*, and the connectors will not be so close to the feedthroughs. The apparatus does not duplicate the water flow pattern of the actual coil, nor does it test the ability of the various parts to withstand forces. With water flowing through the apparatus, leakage resistance across the feedthrough was 130 kΩ. The current was variable from 7 to 15.3 kA, over which range the total resistance from B_1 to B_2 rose from 49.4 to 51.6 μΩ. This corresponds to an average temperature rise of the copper of 21°F. The inlet water temperature remained constant at 74°F. Temperature-sensitive stickers which permanently change color at definite temperatures had been placed on parts *D*, *F*, and *H*, and no disturbing temperatures were discovered. Repeated abrupt switching of the current from 0 to 15 kA did not change the characteristics of the system.

Due to the stringent space restrictions, the mechanical design had to be based on relatively high stress values. Therefore, it seemed desirable to pressure test the more critical parts of the coil cans. This was done and revealed a defect in the Lucite end flanges. They are now in the shop being modified to eliminate tapped holes in their edges.

8.1.4 Construction Difficulties and Further Working Program

Bringing the coil of Fig. 8.2 to its present state of completion actually presented more difficulties than one would have imagined. First, during unpackaging, the edge of the thin ribbon suffered two gouges radially across the full winding depth of the spool. When the ribbon was unwound, the bent spots on the edge were repaired, one at a time, by light hammering. Second, surface dirt on the thicker conductor had to be cleaned off before it was usable. More importantly, this conductor was 0.001 in. thicker on one edge than on the other, and we were unable to correct this defect during the groove-rolling operation. As a result, the problems of alignment and of obtaining a uniform winding were greatly increased. Third, the original design called for the grooved side of the ribbon to be soft soldered to the inner cylinder. It proved very difficult to do this without blocking the grooves with solder, and we changed the design to allow the smooth side of the ribbon to join the cylinder. Finally, an axle support slipped slightly during the fabrication of the outer cylinder, giving a misalignment during the soldering process. In turn, this resulted in voids in the outer cylinder (Fig. 8.2, item *F*) and solder spillage on one face of the coil (not shown in Fig. 8.2).

We plan to clean the solder from the face of the first coil, check the coil for shorted turns and obstructed grooves, and attach the outer current lug. The coil will then be inserted in its can and installed on a special stand for pressure, water flow, and full-current electrical tests. Next, the second coil will be tested in a similar fashion, and the magnetic forces then will be increased by operating them simultaneously. During these latter tests, the generators will be fully loaded, and the opportunity will be taken to further adjust the regulator for parallel generator operation. When these tests are successfully carried out, the coils will be permanently installed in ELMO.

8.2 MAGNETIC PROBE POSITIONER

J. N. Luton, Jr. J. E. Roberts

The positioner to be described herein is a device for placing a magnetic probe at precisely determined locations in a magnetic field. To conform to the design of the field-producing apparatus (magnet coils, Ioffe bars, etc.), the positioner can be inserted with its axis oriented either vertically, horizontally, or obliquely.

Since most of our experimental facilities have either axisymmetric magnet systems or at least rotationally symmetric liners, the new positioner was designed to move the probe along cylindrical coordinates r, θ, z rather than along Cartesian coordinates. Except for electrical leads to the control and readout equipment, it is completely self-contained, and so it can be easily removed from one coil system and set up at another. Finally, it is cantilevered from a single mounting plate and thus requires access to only one end or one port of an experimental facility.

Figure 8.4 is a photograph of the positioner, mounted with its axis coincident with that of the *C* coil. The support tube *G* with all its appendages moves in the z direction with a stroke of 49

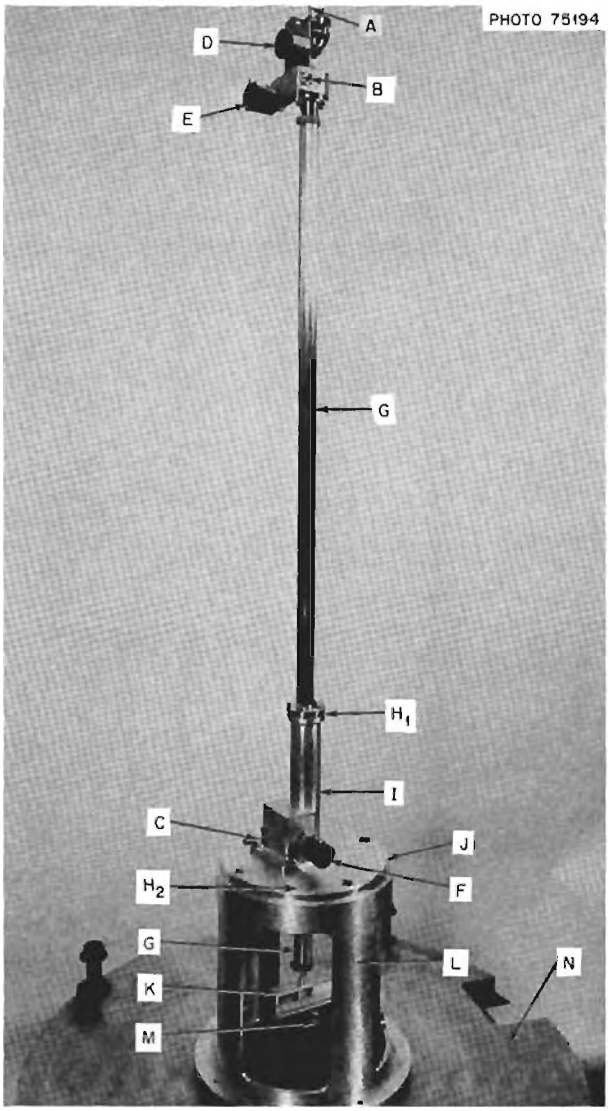

Fig. 8.4. Positioner Without Drive Motors and Electrical Leads. (*A*, *B*, *C*) r, θ, z drive shafts. (*D*, *E*, *F*) 10-turn potentiometers for readout of r, θ, z positions. (*G*) Hollow support tube with rack for z movement. (H_1, H_2) Locations of Teflon sleeve bearings. (*I*) Housing for z drive and support tube bearings. (*J*) Mounting plate. (*K*) Rotating head assembly. (*L*) Mounting sleeve with access holes. (*M*) Probe holder. (*N*) Top plate of magnet coil.

in. The support tube is guided by two Teflon sleeve bearings. One of them, H_1, is visible in the figure; the other, H_2, is on the underside of the mounting plate *J*. These bearings are approximately 12 in. apart and are firmly supported to allow horizontal operation, in which case the support tube is a cantilevered beam of variable length. The mounting plate *J* can be removed from the housing *I* and replaced with whatever plate is required to fit another facility. The support tube *G* is a hollow stainless steel tube, 1.25 in. OD with 0.125 in. wall thickness. It is supported and driven by a rack attached to its full length, the rack being driven by a worm and wheel inside the housing *I*. Tube *G* encloses two concentric tubes which drive the r and z motions. The inner tube, whose top end is labeled *A* in Fig. 8.4, drives the probe holder *M* in and out along the track in the head assembly *K*, from $r = -1.25$ in. to $r = +6.25$ in. The longer end of *K* is partially obscured from view by the mounting sleeve *L*. The middle tube is rotated by a worm and wheel at *B*, thus imparting angular motion to part *K*, which is fastened directly to the lower end of the middle tube. The allowable angular stroke is 370°. Not shown in the photograph are six microswitches which stop the motion in any direction if the positioner reaches the end of its design travel. The probe holder *M* is so mounted that it can be manually repositioned to allow a single probe to measure any one of the three field components during a scan. Alternatively, it can hold a commercial Hall probe assembly that simultaneously measures three mutually perpendicular components. The lead wires will be brought from the probe up between the middle tube and the support tube *G* and emerge near point *B*.

As far as practical, the entire positioner was made of standard parts in order to reduce the cost. All gears and worms, limit switches, and Helipots are stock items. All bearings except the Teflon sleeves H_1 and H_2 are standard-sized oil-impregnated bronze bearings. Recirculating-ball linear bearings could have been used at points H_1 and H_2 if the presence of magnetic materials could have been tolerated, but it was felt that ferromagnetic materials could disturb the field to be measured and that their immersion in kilogauss fields could interfere with the smooth movement of the positioner. The only ferromagnetic parts now in the positioner are the z-drive worm and the springs of the microswitches.

Satisfactory drive motors for the positioner have not yet been found. The original design called for small air motors,[7] one being fixed at point *C* of

[7]Standard Pneumatic model 2303.

Fig. 8.4 and the other two riding on the support tube at points *A* and *B*. Early tests revealed that the unloaded motors stalled at a field strength *B* of only 1.1 kG and did not restart until *B* was reduced to 0.17 kG. In addition, the starting torque varied incrementally with position. There is some hope that the manufacturer can correct the first defect by replacing magnetic parts by nonmagnetic ones. The second defect is not too objectionable since we expect to continuously scan the field and record the *B* vs position curve, in which case the starting smoothness of the motor is not important. In a magnetic field, a 10-rpm Bodine electric motor operated somewhat better than the air motors. It was just able to start in a 3-kG field parallel to its shaft or in a 0.29-kG perpendicular field. Electric motors using permanent magnet fields are also being considered. However, it now appears necessary to hold the drive motors stationary about 4 ft distant from the mounting plate (i.e., 4 to 8 ft from the probe itself) and, perhaps, to provide some magnetic shielding.

The positioner has been run outside a magnetic field to check it for smoothness and accuracy, using a 100-rpm 4.0-oz-in. Bodine[8] motor. In the vertical position it was necessary to partly counterbalance the weight of the support tube *G* with a constant force of 5 lb.[9] Then jerking was eliminated, and the support tube could be raised easily by the small (0.024-hp output) motor. In the horizontal position the *z* drive operates smoothly except when the support tube is nearly fully extended. The other two drives work well in all positions. With a 100-rpm motor, the *r*, θ, and *z* velocities are 5.05 in./min, 368°/min, and 11.78 in./min. After removing a minor play between the holder *M* and the head assembly *K* (Fig. 8.4), we expect a positional readout accuracy of $\pm\frac{1}{32}$ in. or less for all three coordinates.

8.3 CAST CROSSOVERS FOR WATER-COOLED MAGNET COILS

J. N. Luton, Jr.

8.3.1 Introduction

The "pancake" design[10] is commonly used for magnet coils with hollow water-cooled conductors. The electrical and hydraulic transition pieces from one plane to the other of one of these pancakes are called "crossovers." Prefabricated machined crossovers have been used in the *C* and *D* coils.[11,12] This type of crossover is expensive, there is danger of clogging of the drilled water holes by foreign objects, and water leaks sometimes develop because it is difficult to hold the wall thickness tolerances. In view of these difficulties with machined crossovers, the development of cast crossovers has been undertaken.

A preliminary cast crossover design has been described earlier.[13] It consists of a copper piece cast around a bent metal tube. Attempts by an outside vendor to produce such pieces were not successful. The Y-12 Plant of Union Carbide Corporation, Nuclear Division, eventually succeeded in vacuum casting void-free copper around a K-500 Monel tube. The decisive point was the cleaning of the Monel tube with nitric acid prior to the pour. Several other tube materials had previously been eliminated for one reason or another. Extended tests of this new crossover design and of an improved version of it are described below. From these tests, the usefulness of the cast crossover design for various applications can be determined.

8.3.2 Thermal and Metallurgical Tests of Cast Crossovers

Five cast crossovers, Fig. 8.5, of size identical to a certain group of crossovers of the *C* coil, were produced for testing. The Monel tube had a $\frac{3}{8}$-in. outer diameter and a $\frac{1}{32}$-in. wall thickness and was about $5\frac{1}{4}$ in. long. Using a resistivity of 61.5 $\mu\Omega$-cm, the calculated resistance of the tube was 3770 $\mu\Omega$. The resistances of the crossovers were first checked on a Kelvin bridge. The resistance from one end of the copper to the other was about 5.6 $\mu\Omega$, and the resistances between ends of the Monel tubes ranged between 195 and 350 $\mu\Omega$. Thus

[8] Bodine type KYC-23RB.

[9] Obtained by means of Negator constant-force spring motor, model A-2025-5.

[10] *Thermonuclear Div. Semiann. Progr. Rept. Oct. 31, 1963*, ORNL-3564, pp. 121–25.

[11] *Thermonuclear Div. Semiann. Progr. Rept. Oct. 31, 1964*, ORNL-3760, pp. 80–87.

[12] *Thermonuclear Div. Semiann. Progr. Rept. Oct. 31, 1965*, ORNL-3908, pp. 118–24.

[13] *Thermonuclear Div. Semiann. Progr. Rept. Apr. 30, 1966*, ORNL-3989, pp. 139–40.

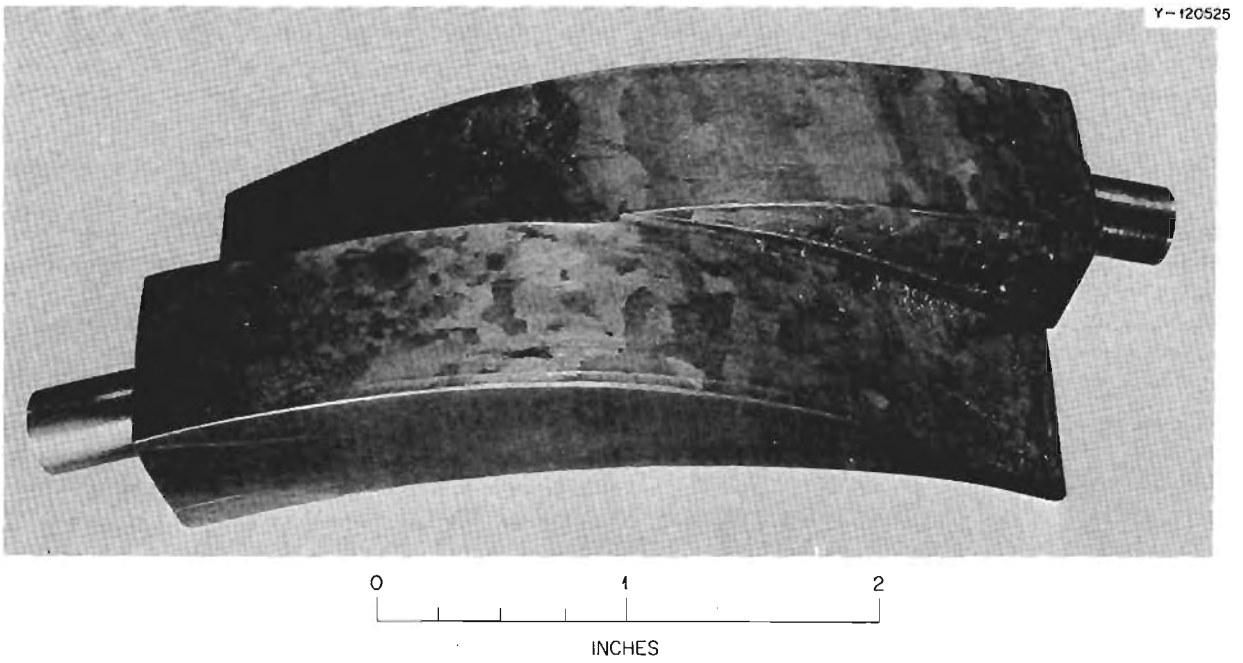

Fig. 8.5. Cast Crossover for Middle-Sized Conductor of the *C* Coil.

it appeared that electrically the bonds between Monel and copper were poor and rather erratic, or that a good bond was not developed closer than $\frac{1}{8}$ to $\frac{1}{2}$ in. from the ends of the crossovers. The measured resistances between Monel and copper also varied considerably and were as much as twice as large when the current was from copper to Monel as when it was reversed. It is of interest that the resistance measured between points inside the tube of a cast "*D*-size" crossover 1 in. from each tube end was only 8 or 9 $\mu\Omega$, whereas the resistance measured between the ends was much higher. This shows that, at least in the case of the cast *D*-coil crossover, the bond resistance near the ends is very high.

Both ends of the cast *C*-size crossovers were then joined with Sil-Fos[14] (without using flux) to short lengths of hollow conductors. The cooling water flow was set at 6 gpm, and the currents were raised to 14 kA. Voltages scaled linearly with current, temperatures scaled as current squared, and the voltage did not show much variation between samples. The resistances of the crossovers at 14 kA were between 5.6 and 6.2 $\mu\Omega$, agreeing sufficiently well with the bridge measurements. By means of a movable thermocouple, the conductor surface temperatures were investigated. Four of the crossovers had a hot-spot temperature 34 to 39°C hotter than the cooling water, and the fifth had a rise of 56°C. Neither remaking the joints with Easy-Flo 45[15] and flux, mechanical cleaning of the tube bore, or further acid cleaning of the tube bore had any appreciable effect on the high temperature of this crossover. As a standard, a machined *C*-coil crossover was then tested. Although the resistances of the cast crossovers were only about 12% above the standard, their hot-spot temperature rises were greatly above the 9.5°C rise occurring in the machined crossover at 14 kA.

Later work concerns only cast crossovers of the *D*-coil size. They are longer and have somewhat less copper area than the *C*-coil crossovers. The *D*-size crossovers were tested at their rated current of 10 kA. A machined crossover of the same dimensions was again used as a standard, and its resistance, hot-spot temperature, and temperature rise are shown in the first column of Table 8.1.

[14] Sil-Fos is Handy & Harman's trade name for a silver-copper solder with 5% phosphorus added to give a self-fluxing action on copper.

[15] 45% Ag, 15% Cu, 16% Zn, 24% Cd.

Table 8.1. Current Tests on *D*-Size Crossovers

	Machined (Standard) Crossover	Cast over Bare Tube				Cast over Plated Tube	
		Crossover No. 1		Crossover No. 2			
		1st Joints	3rd Joints	New	After Endurance Runs	Absolute	Normalized to Column 1
Resistance at 10,000 A, R	9.76 $\mu\Omega$	10.72 $\mu\Omega$	10.92 $\mu\Omega$	10.12 $\mu\Omega$	10.4 $\mu\Omega$	11.66 $\mu\Omega$	1.192
Inlet water temperature, T_1	24.4°C	25.4°C	21.5°C	21.4°C	16.7°C	23.1°C	0.95
Hot-spot temperature, T_{HS}	38.1°C	65.0°C	72.1°C	52.2°C	50.2°C	55.4°C	1.45
T_{HS} minus T_1, ΔT	13.7°C	39.6°C	50.6°C	30.8°C	33.5°C	32.0°C	2.34

The results for the first cast crossover, joined to the conductor tubes with Easy-Flo 45, are in the second column. The joints were then remelted twice, and tests showed that the operating temperature rise ΔT was considerably increased each time (column 3). The second cast crossover was then tested, with results as given in the fourth column of Table 8.1. To see if hard usage might damage the Monel-copper bond as did heating it to soldering temperatures, the second crossover was cycled 20 times to 10 kA and 20 times to 12.8 kA and was run 33 hr at 12 kA (the maximum available for extended times). Its characteristics were gradually and mildly degraded to the values of column 5.

Figure 8.6 shows two photomicrographs (100× and 500×) of a polished but unetched cross section of the bond region between the Monel and the copper of one of the cast *D*-size crossovers. Although the Monel-copper interface appears flawless, a dark line of impurities exists in the copper, about 0.0015 in. from the interface. In other sections the flaw line is wavy, or in some cases even broken into many pockets surrounded by copper. These latter cases, which indicate good bonds, were always away from the tube ends. It was felt that the impurity, perhaps Al_2O_3, might have been on the surface of the Monel at the moment of casting and was displaced by the diffusion of the copper into the Monel.

8.3.3 Tests of an Improved Type of Cast Crossover

In an attempt to improve the bond between the copper and the Monel tube, a tube was routinely plated with copper to a depth of 0.001 in. before the casting was poured. Figure 8.7 shows the resulting bond areas to the same magnifications as Fig. 8.6. No flaws were seen in any of the sections examined. The bond defect in Fig. 8.6 represents a mechanical weakness and at least a slight thermal barrier, and other photomicrographs show that the defect forms a continuous sheath around the Monel tube. We therefore infer from Figs. 8.6 and 8.7 that the mechanical and thermal properties of the improved crossover are superior to those of the original design.

The improved crossover was soldered to the conductors with Easy-Flo 45 and run for 14 hr at 12 kA. Because ΔT was not dramatically reduced from that of the earlier cast crossovers, the tube bore was then cleaned with acid and further cleaned by forcing an abrasive slurry through it.[16] Current tests were made periodically, but the crossover was not significantly improved by the changes, nor was its performance degraded by subsequent abuse. The sixth column of Table 8.1 shows the last measurements taken.

Every crossover tested had its hot spot located at the outer tip of the ramp. In a cast crossover the total temperature drop from the hot spot to the cooling water is the sum of the temperature drops occurring at the wetted tube surface, across the Monel tube wall, at the bond area (interface and alloyed zones), and in the copper. Using a thermal conductivity of 0.443 W $(°C)^{-1}$ $in.^{-1}$ for the K-500 Monel,[17] the temperature drop across the

[16] Borescopic examination then verified that the tube was free of scale and bright at least as far as the tube bend would permit observation.

[17] *Engineering Properties of Monel Alloy K-500*, Tech. Bull. T-9, Huntington Alloy Products Div., The International Nickel Co., Inc., p. 2.

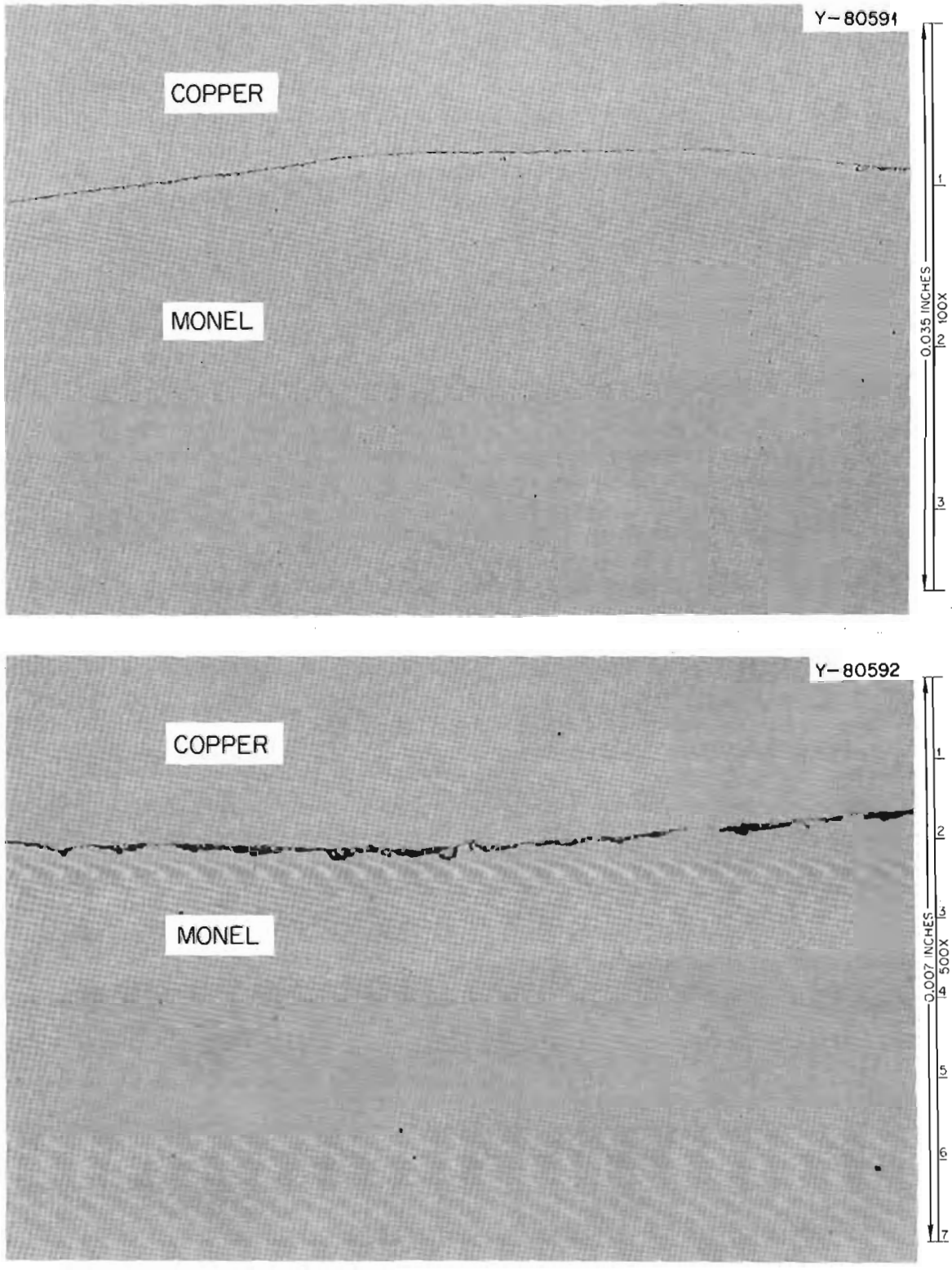

Fig. 8.6. Photomicrograph of Bond Between Cast Copper and Acid-Cleaned Monel K-500.

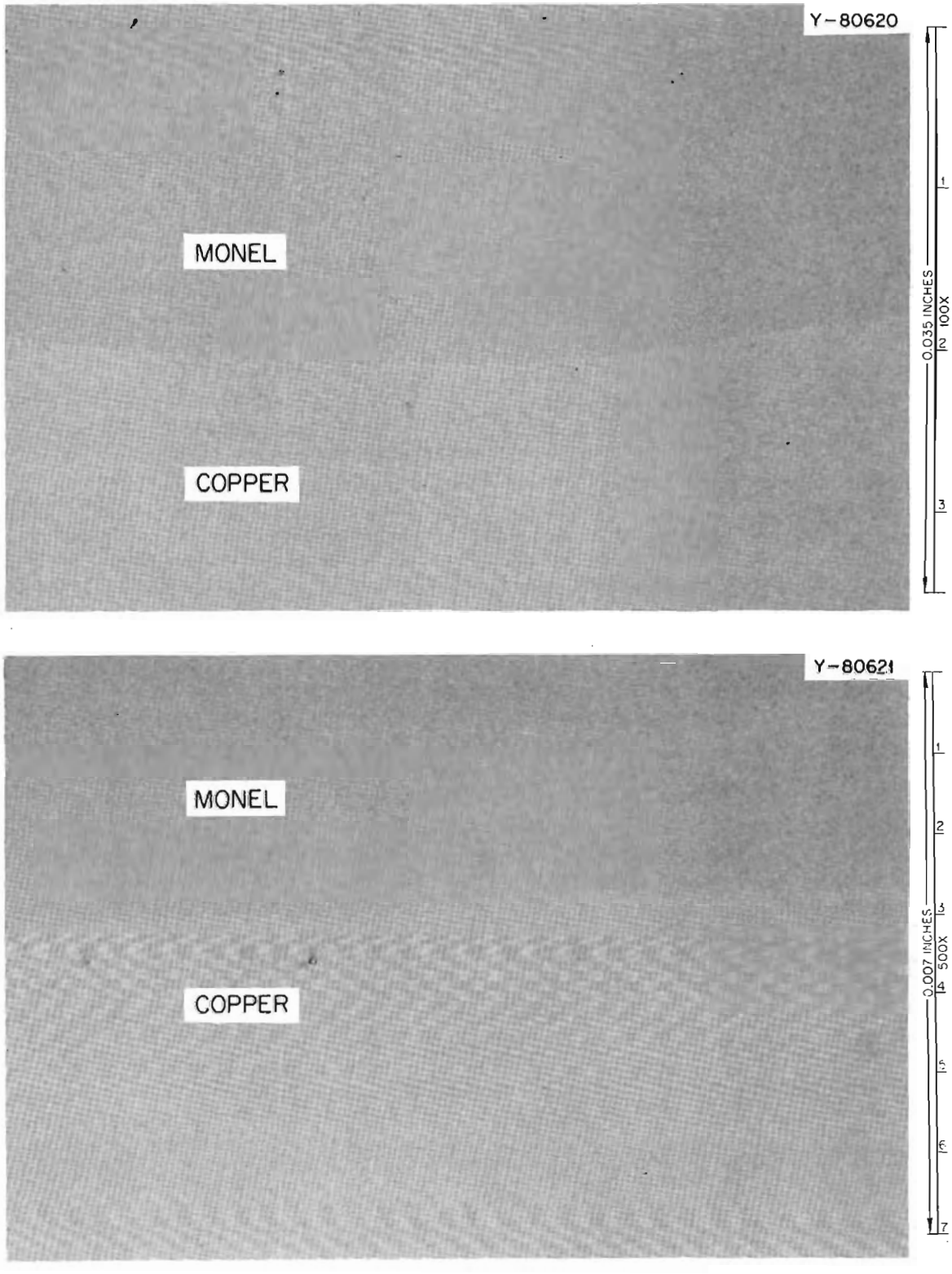

Fig. 8.7. Photomicrograph of Bond Between Cast Copper and Copper-Plated Monel K-500.

tube wall is calculated to be 11.9°C. The path length for heat flow in the copper is slightly less for the cast crossover than for the machined crossover, so the temperature drop in the cast metal would be slightly less. However, the machined hole should be somewhat rougher than the honed Monel surface, and with constant flow velocity the smoother bore gives a somewhat higher temperature drop across the water film on its surface. If these two small and opposite effects are assumed to cancel, then for the cast crossover the sum of the temperature drops in the water film and in the copper corresponds to that measured for the machined crossover. Corrected by the ratio of power losses, it becomes 15.9°C. The higher average temperature of the cast crossover decreases its thermal conductivity by 6% and so raises the 15.9°C to approximately 16.8°C. Figure 8.7 shows no flaw line, so the temperature drop at the interface is taken as zero. The alloyed zone should have a thickness of about 0.0015 in. (Fig. 8.6), and if its thermal conductivity is at worst that of Monel, its drop is below 0.56°C. The total calculated ΔT is thus 29.2°C, or 2.8°C below the measured value. This 2.8°C discrepancy is rather large when compared with the 11.9°C drop through the Monel tube wall.

There is also a discrepancy in that the measured resistance of the plated-tube crossover is 19% above that of the machined crossover (Table 8.1, last column). Substitution of Monel for copper cross section accounts for a change of 7.5%, and the increase of electrical resistivity with temperature gives another increase of 6.2%, but the remaining 5% is unexplained. Since the crossovers were cast at various times and since the resistance of the plated-tube crossover is even higher than that of the other cast crossovers, it might be that the copper of this casting is slightly impure and that its conductivity is below that of the other crossovers.

It is discouraging that the temperature rise of the improved cast crossover is still more than twice that of the machined one (Table 8.1, column 7). However, the absolute difference in hot-spot temperature is only 17°C, and in most large coils the coolant temperature rise is about twice this value. In such cases the extra 17°C at the midpoint of the water circuit would only raise the insulation temperature at that point to a value approximately equal to that at the exit end of the tube.

8.3.4 Mechanical Properties of Cast Crossovers and of Joints

As a necessary supplement to the current tests, various mechanical tests were made on the crossovers and on the crossover-to-conductor joints. The joints were all made by silver soldering the Monel tube ends into conductors which were counterbored $\frac{3}{8}$ in. deep, with the solder also forming a butt joint between the copper pieces. Twelve joints were tested in all. Ten were sawed through the butt joint until a ring of Monel was exposed, and then were hydrostatically tested at 1000 to 1500 psi. None ruptured, and only one leaked, in spite of the fact that several of the bonds were very poor. A bond was considered "bad" if during a tensile test the Monel tube slipped from its counterbore (Fig. 8.8, sample *C*) and "good" if the Monel tube broke (Fig. 8.8, sample *A*). This tensile test was normally made with the copper-to-copper part of the joint sawed away; otherwise the failure always occurs in the virgin copper at the root of the counterbore, where the metal cross section is smallest (pair *B* of Fig. 8.7). Bad bonds were observed in joints when Sil-Fos was used with or without flux, and in crossovers when the tube was not plated before casting. When the Monel was tinned with Easy-Flo 45 with flux and then soldered with Sil-Fos without flux, the results were erratic. Easy-Flo 45 with flux gave good bonds consistently.

8.3.5 Conclusions

Copper crossovers vacuum cast over a copper-plated K-500 Monel tube proved to be mechanically excellent and did not deteriorate with use. Compared with machined crossovers there is less danger that the water passage will be obstructed by foreign matter in the cooling water. The cast crossovers are more rugged and are cheaper than the machined ones. The disadvantages are that the cast crossovers are electrically and thermally inferior to the machined crossovers. However, the use of these cast crossovers is appropriate if the temperature of the hot spots can be kept below the water exit temperature. When they are used, the joints between them and the conductors should be made with Easy-Flo 45, and great care should be taken to remove all flux before leak checks are made.

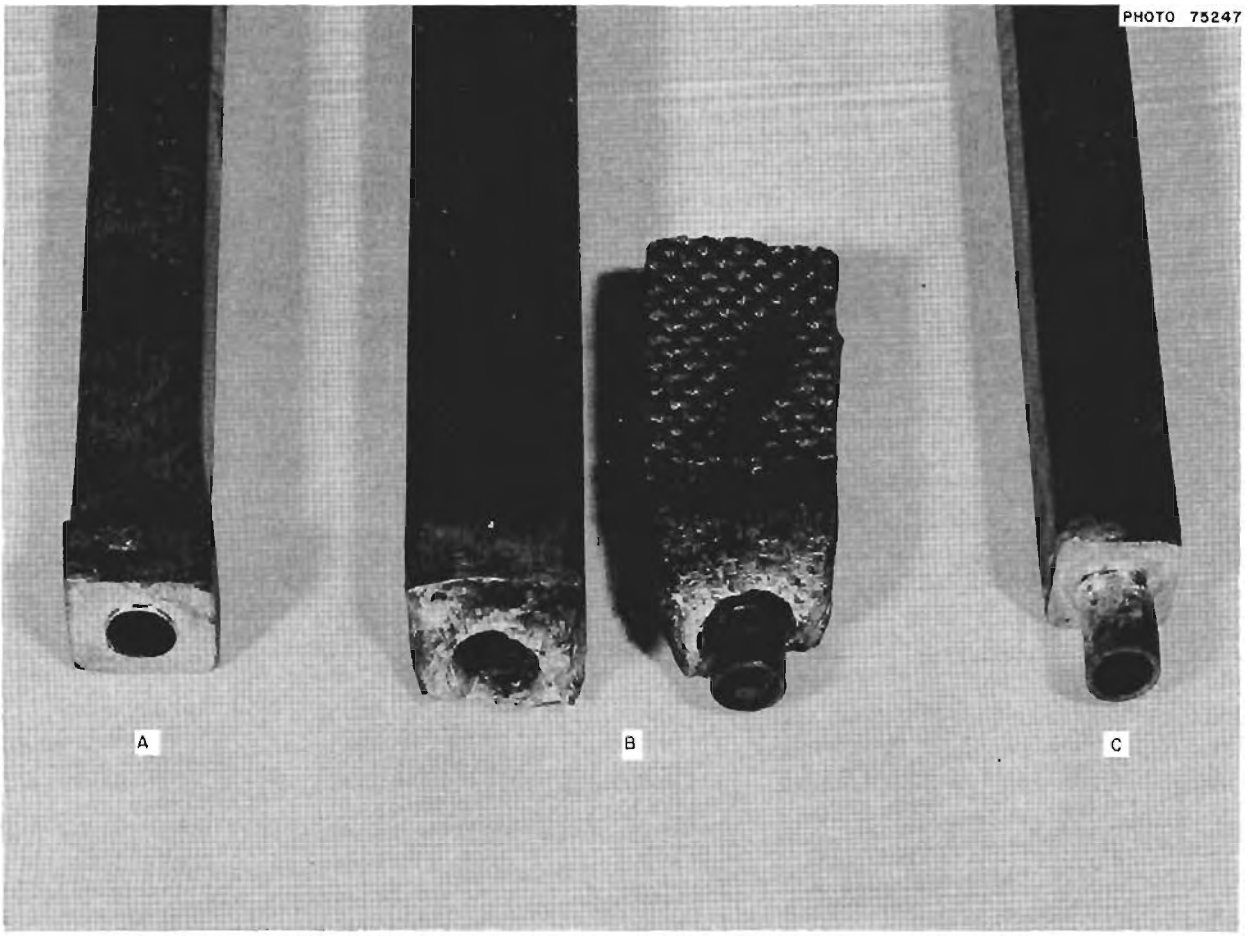

Fig. 8.8. Types of Tensile Failure of Solder Joints and Casting Bonds. Monel tubes in copper.

If it is necessary to improve the heat-transfer capabilities of the cast crossovers to that of the machined ones, two alternatives are suggested. First, it might be possible to cast the copper around a thick-walled copper tube cooled so that its inner surface remains solid during the casting process, whereas its outer surface fuses with the poured material. Second, although a tube was originally felt necessary to prevent leaks through the casting, radiographs of the castings look so void-free that the tube may not be necessary, in which case an investment casting might be feasible.

8.4 REVIEW OF OUR BASIC WORK ON SUPERCONDUCTIVITY

K. R. Efferson W. F. Gauster
J. B. Hendricks D. M. Kroeger
M. S. Lubell

Our basic work on superconductivity is under joint sponsorship of the Thermonuclear Branch of the U.S. Atomic Energy Commission and of the George C. Marshall Space Flight Center, National Aeronautics and Space Administration. The title

of the NASA Government Order No. H-29278A is "Magnetic Flux Flow and Superconductor Stabilization." The quarterly reports of this government order include essential parts of our entire basic research on superconductivity sponsored by both NASA and AEC. The abstract of the first quarterly NASA report, covering the period from April 1 to June 30, 1967 (ORNL-TM-1943), reads:

"Flux flow experiments were made with a bare strip of superconducting Nb–25 A% Ti. Due to low pinning forces it was possible to observe the flux flow voltage in the full range of external fields from zero to 75 kG. Near H_{c2} pronounced peak effects could be observed. It does not seem to be possible to explain the takeoff points simply on the basis of the heat transfer to the helium bath. Current-voltage characteristics of a short sample of a stabilized Nb-Ti conductor were taken with currents up to 1340 amp and with external fields up to 75 kG. Also, in this case, the takeoff points were not simply related to the transition from nucleate to film boiling of the surrounding liquid helium. Since the resistance of the copper stabilizer at varying magnetic fields could be sufficiently well determined by means of recovery point measurements, it was possible to calculate the values of the current flowing through the superconductor at varying temperature and external fields. The temperature dependence proved to be linear in accordance with other published work. However, the field dependence measured here deviates from previous data. Some preliminary measurements of heat transfer from metal surfaces to liquid helium are discussed. Finally, for comparison, a review of a previous compound conductor stability criterion is presented."

The abstract of the second quarterly report, covering the period from July 1 to September 30, 1967 (ORNL-TM-2075), is as follows:

"Our previously reported work on flux flow of a bare strip of superconducting Nb–25% Ti, on the current-voltage characteristics of short samples of commercially available stabilized Nb-Ti conductors, and on heat transfer from a cylindrical metal surface to liquid helium have been continued during this second report period. An analysis of the test data obtained with the bare Nb–25% Ti strip suggested that the flux flow stability can be better understood by considering the takeoff current instead of the takeoff power. The current-voltage characteristics of the stabilized wires were indicative of a heat transfer law in the form $\dot{Q} = h^* \tau^n$ with $n \simeq 2.5$. Test results obtained with poorly stabilized samples could be explained by considering the simultaneous occurrence of sections in the superconducting and in the normal state, or in the superconducting and in the flux flow state. The measurements of heat transfer from metal surfaces to liquid helium have been appreciably improved."

8.5 THE CUSP COIL TEST FOR SUPERCONDUCTING WINDING MATERIAL

D. L. Coffey
M. W. Garrett[18]
W. F. Gauster
C. E. Parker

8.5.1 Introduction

The cusp coil test is a new method for testing the winding material of superconducting magnet coils. The self-field of two coils which are energized in opposite directions (cusp coils), combined with a superimposed homogeneous field perpendicular to the cusp coil axis, results in a nonaxisymmetrical field with high field gradients. In this way the winding material of the cusp coils is exposed to fields similar to those which occur in full-sized nonaxisymmetrical magnet coil systems. With stabilized conductors (superconducting wires in good electrical and thermal contact with nonsuperconducting metallic stabilizers), high current densities can be achieved, and large electromagnetic forces are generated in the cusp coil windings. Thus the cusp coil tests make it possible to study simultaneously the influence of nonaxisymmetrical fields on the quenching currents and the action of high magnetic forces on the winding material.

8.5.2 Description of the Test Arrangement

We built two types of cusp coils. The larger one (Fig. 8.9) has a winding inside diameter of 3.5 in. and an outside diameter of 5.5 in. Each half of the winding is 3 in. long. The gap between the windings is $\frac{3}{8}$ in. The corresponding dimensions of the smaller cusp coil are: inside diameter, 1 in.; outside diameter, 3.2 in.; length of half the winding, 1 in.; gap width, $\frac{1}{4}$ in. The cusp coil spools are made of 310 stainless steel, since the electromagnetic forces can be extremely high.

[18] Consultant.

The larger cusp coil serves for tests of stabilized superconducting wires with critical currents in the order of 1000 A (at 20 kG). The external field for the larger cusp coil is produced by either the "*C*" or "*D*"[19] coil of our Magnet Laboratory. These coils generate fields up to 60 kG and have bores of about 12 in., in which a Dewar vessel with 9.5 in. working diameter can be inserted. The smaller cusp coil is tested in the 80-kG "*B*"[19] coil of our Magnet Laboratory, which has a bore of 6.5 in. (Dewar working diameter 5 in.). The current supply[20] for the windings of the cusp coils has a special voltage-current characteristic which limits the short-circuit currents.

[19]Proceedings Les Champs Magnétiques Intenses leur production et leurs applications, Grenoble, Sept. 12–14, 1966.

[20]W. F. Gauster and J. B. Hendricks, "Flux Flow and Thermal Stability of Stabilized Superconductors," presented at 1967 Applied Superconductivity Conference, Austin, Tex. (proceedings to be published).

8.5.3 Field Analysis

The shape of the magnetic field produced by a pair of cusp coils is well known. The center field is zero, and maximum field strengths occur in the midplane and in the coil bores. *B*-constant lines of a cusp coil field (without superimposed homogeneous field) are shown in Fig. 8.10. Only one quadrant of the coil is represented. This figure is for a coil geometry similar to that of the smaller cusp coil pair described in the previous section; that is, the same dimensional proportions (outside radius, inside radius, coil length, and gap width between the coils) were used. The maximum field strength B_{max} for zero external field occurs in the coil bore (point S_1 in Fig. 8.10). A relative maximum of the field strength with the value $B'_{max} = 0.876B_{max}$ can be found at the side plane of the coil (point S_3). S_1 and S_3 are singular points located on the winding boundary. Other singular points occur inside the winding volume. S_5 is a

ORNL-DWG 67-13141A

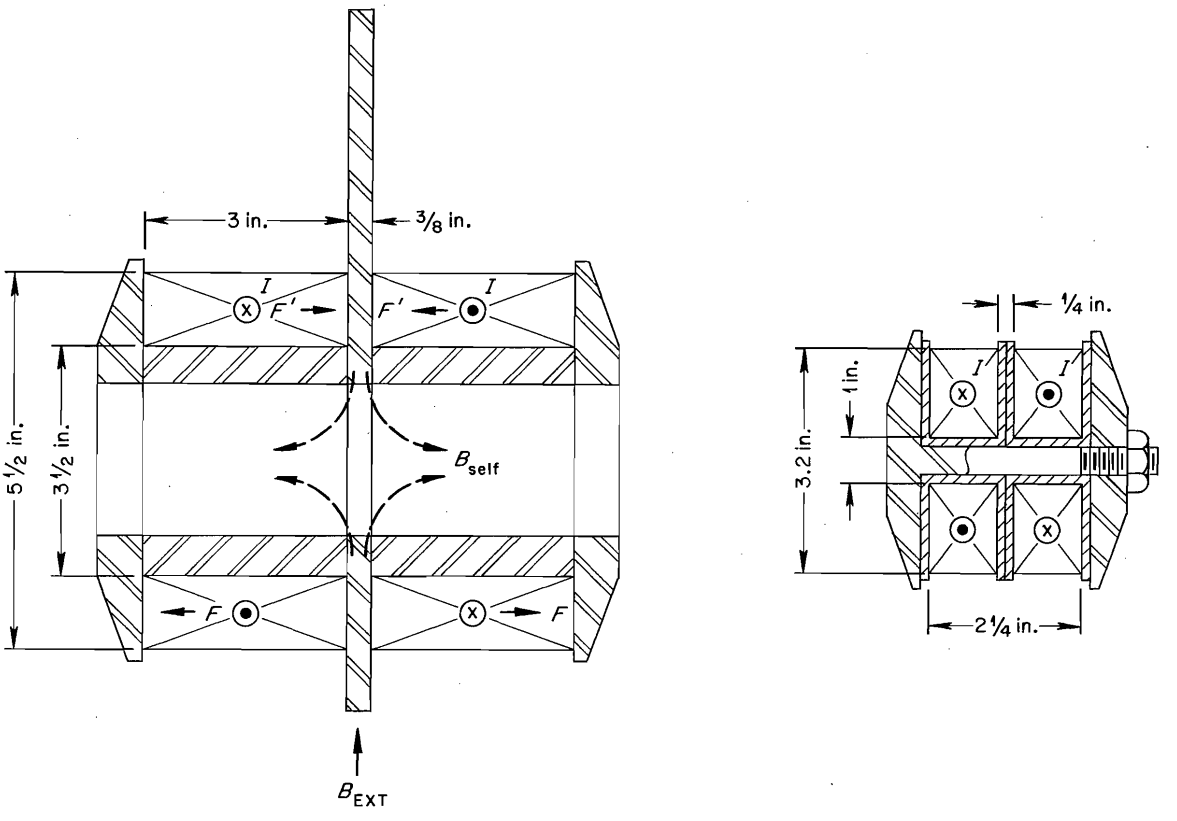

LARGE CUSP TEST COIL

SMALL CUSP TEST COIL

Fig. 8.9. Cross-Sectional Views of Large and Small Cusp Coils.

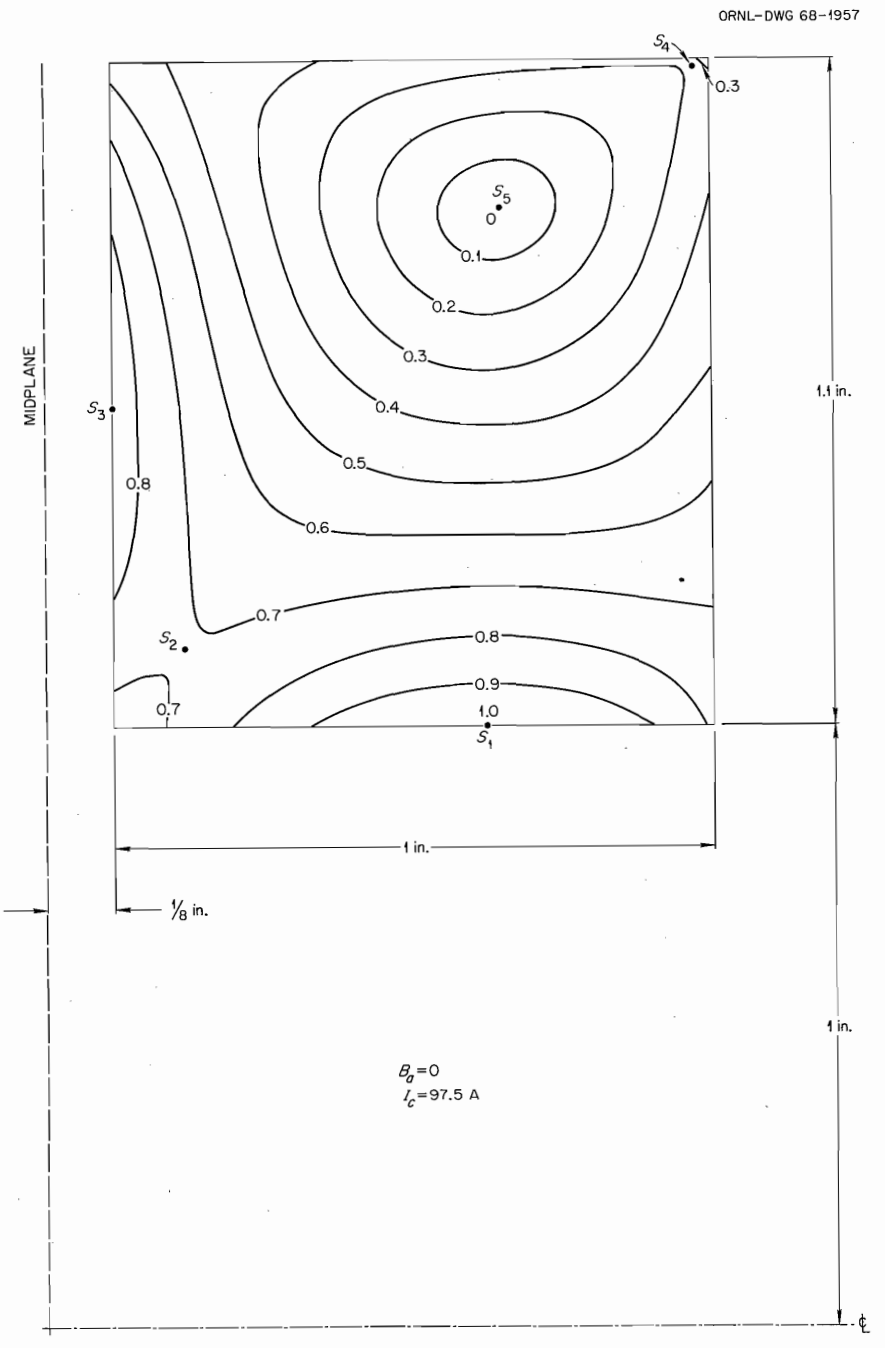

Fig. 8.10. Field Contours in the Small Cusp Coil with I = 97.5 A, H_a = 0.

point with zero field strength, S_2 a point with $B''_{max} = 0.705B_{max}$, and S_4 another with $B'''_{max} = 0.300B_{max}$.

The field configuration with a superimposed homogeneous field which is directed perpendicular to the coil axis depends on the ratio of current density, J (number of turns times current, divided by coil cross section area), to the magnitude of the superimposed field B_a.

Figure 8.11 applies to an actual small test coil with 1927 turns. An observed critical current was 61.0 A, with a superimposed field of B_a = 45 kG.

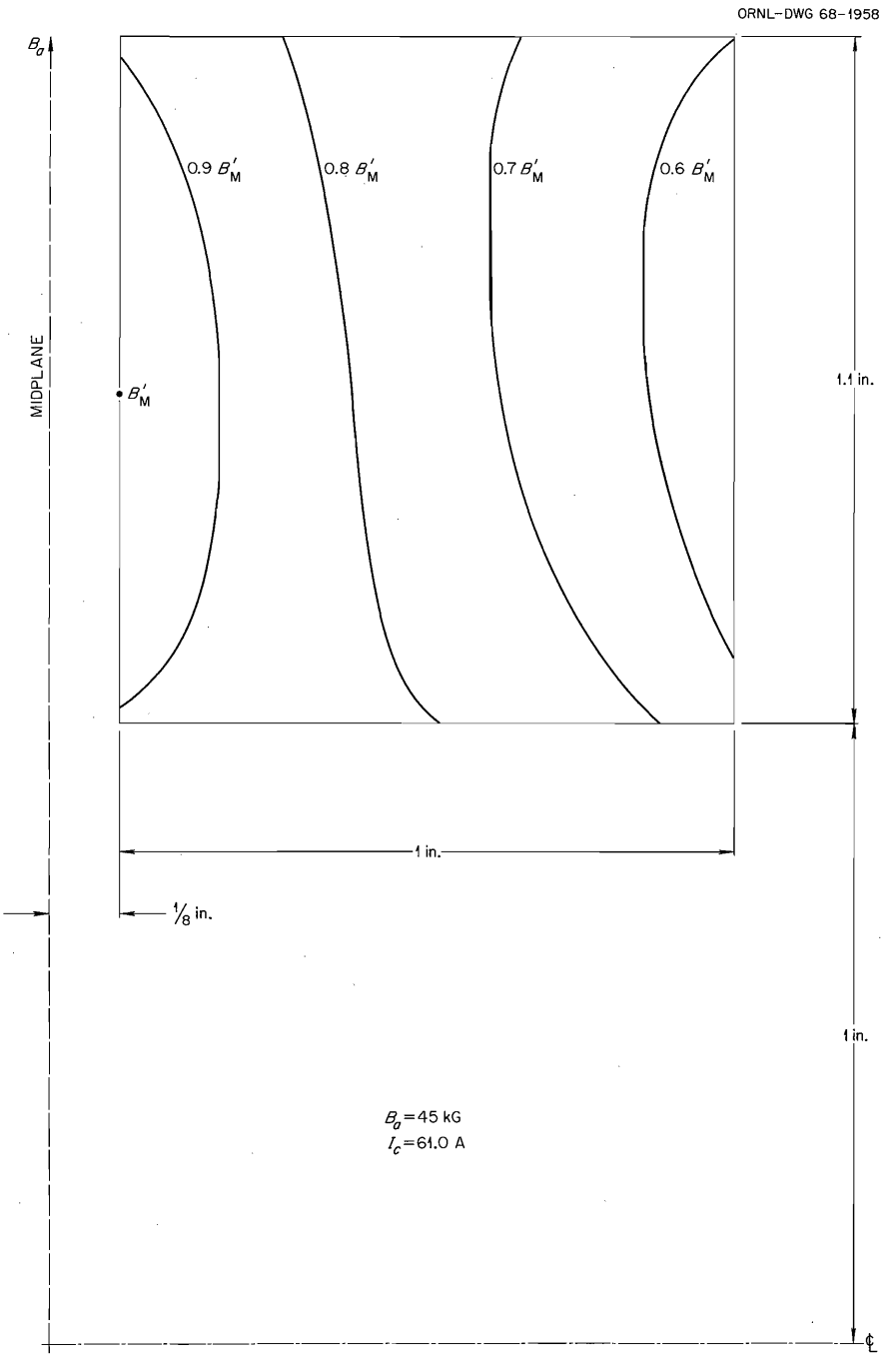

Fig. 8.11. Field Contours in the Small Cusp Coil with $I = 61.0$ A, $H_a = 45$ kG.

With this high superimposed field, a singular point located on the side plane of the coil occurs (with $B'_{max} = 65.9$ kG); the singular point at the coil bore has disappeared. With the still stronger external field $B_a = 75$ kG and a critical current of 32.6 A, the field inside the cusp coil winding changes only between 100 and 80.4% (Fig. 8.12).

The field calculation for Figs. 8.11 and 8.12 were made for nonsuperconducting windings. Scanning in the narrow midplane of a superconducting

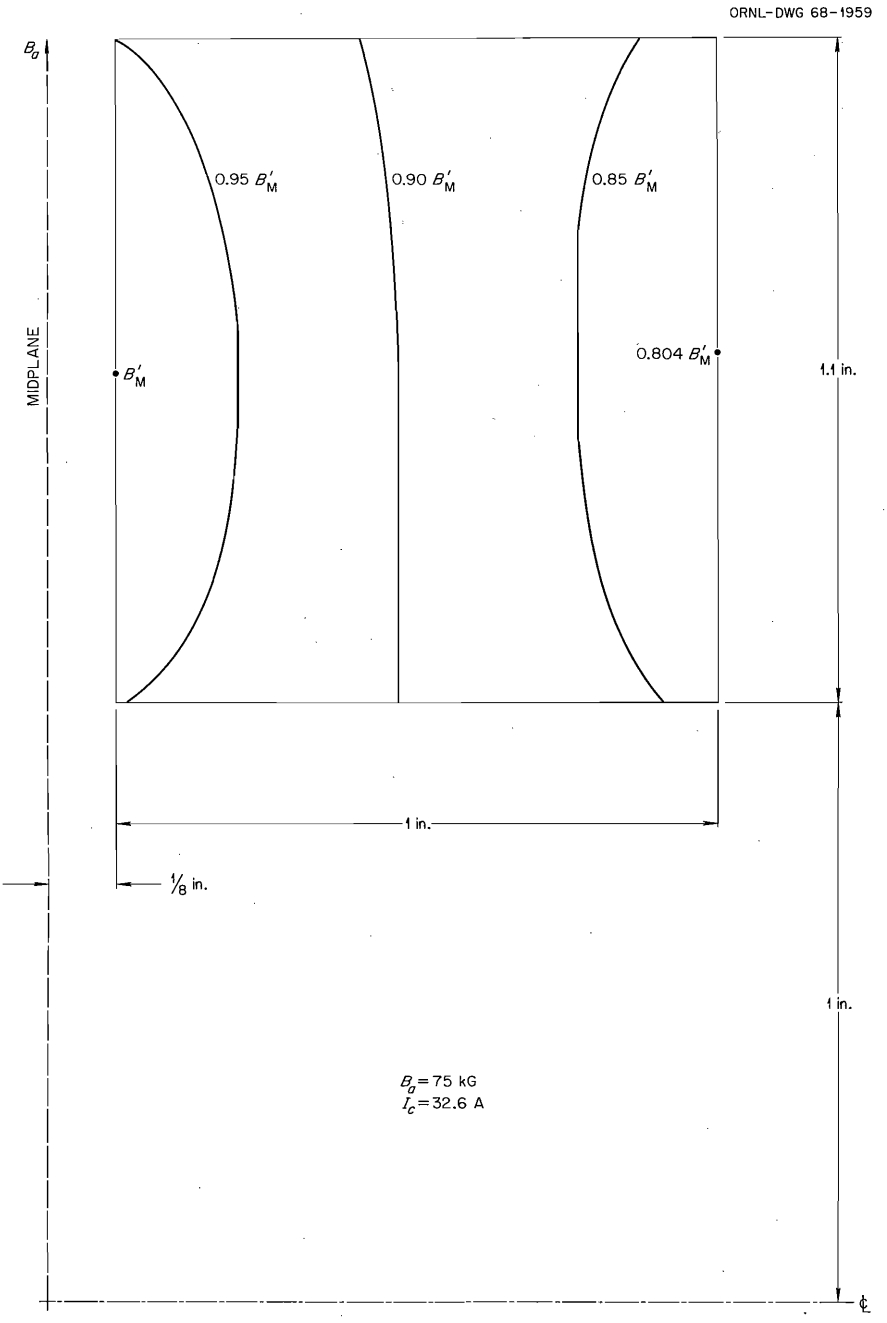

Fig. 8.12. Field Contours in the Small Cusp Coil with $I = 32.6$ A, $H_a = 75$ kG.

winding[21] shows field distortion due to the imperfect field penetration into the superconducting winding material. However, with field larger than the lower critical field H_{c1} of the superconductor (which is in our case a few hundred gauss) the deviation becomes insignificant.

Cusp coil tests yield critical current density values J_c dependent upon the applied field B_a. In order to compare these results with those of short-

[21] *Thermonuclear Div. Semiann. Progr. Rept. Oct. 31, 1965,* ORNL-3908, pp. 137–41.

sample tests it is necessary to find in each case the value B_{max}, that is, the maximum field strength which occurs anywhere in the cusp coil winding. It would be tedious to calculate for each observed pair of values B_a and J_c the value of B_{max}. This can be avoided by using the following plotting technique: By means of a computer code a sufficient number of B_{max} values were calculated with arbitrarily assumed B_a and J_c values. In a coordinate system the calculated B_{max} values were plotted as abscissas and the J_c values as ordinates. In this way B_a-constant lines were drawn. A point plotted with the ordinate J_c on the B_a-constant line concerned has the abscissa B_{max}; therefore, no further computation is necessary. For comparison the short-sample test values can be plotted in the same graph. It must be kept in mind that the external fields of the short-sample tests correspond to the maximum field values B_{max} of the cusp coil tests and not to the applied field values B_a. Actual test values are shown in Fig. 8.13.

8.5.4 Test Results

In the cusp coil test the superconducting winding material is exposed to very high electromagnetic forces. Sometimes, in our experiments, the yield point of the copper cladding (15,000 psi) has been exceeded. This test is also, of course, a very strict one for the electrical insulation. We made, involuntarily, even a mechanical test for the spool material. In the first design the cusp coil spool was made of the aluminum alloy 7039, and no sufficient provision had been made to relieve corner stresses. The fractured coil spool is shown in Fig. 8.14.

With the Supercon wire T-48B (Nb-Ti core with 0.01 in. diameter, copper cladding OD = 0.02 in.) tests were made with the small cusp coils (Fig. 8.9). The wire was insulated with 0.0005-in. Formvar, and a spiral wrapping (Nomex, 0.001 in. thick, 50% surface covering) around the wire was used. Critical current densities at several applied fields B_a are shown in Fig. 8.13. With applied fields down to 15 kG the cusp coil characteristic follows exactly the short-sample curve. With lower applied fields the critical cusp coil current density is smaller than that of the short sample. It seems that the special field configuration of the cusp coil produces "degradation."

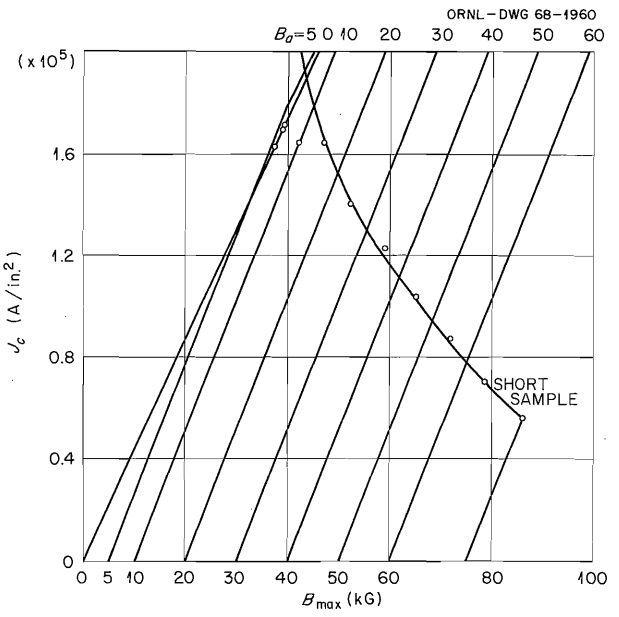

Fig. 8.13. J_c-B_{max} Diagram, Showing B_a-Constant Lines. Actual coil test data are represented by circled points.

8.5.5 Conclusion

In the cusp coil test the superconducting winding material and its insulation are subjected to very high electromagnetic forces. Similar high forces can be produced in axisymmetrical test coils which are exposed to coaxial applied fields. However, in the latter case, because of symmetry the forces can be more easily withstood by tension in the windings. For cusp coil tests it is necessary to secure the winding strongly in order to avoid deformation. Similar conditions exist for actual, "full size" nonaxisymmetrical magnet systems (e.g., mirror-quadrupole systems). Therefore, the cusp coil tests are most appropriate for evaluating the mechanical properties of the winding material and for determining the suitability of the winding technique.

Careful measurements of the current-voltage characteristics of short samples in the flux flow state are very revealing with respect to the electrical stability of superconducting winding material. However, since it is known that for imperfectly stabilized material the stability is not determined solely by heat-transfer conditions, the flux flow measurements are not decisive for predicting the

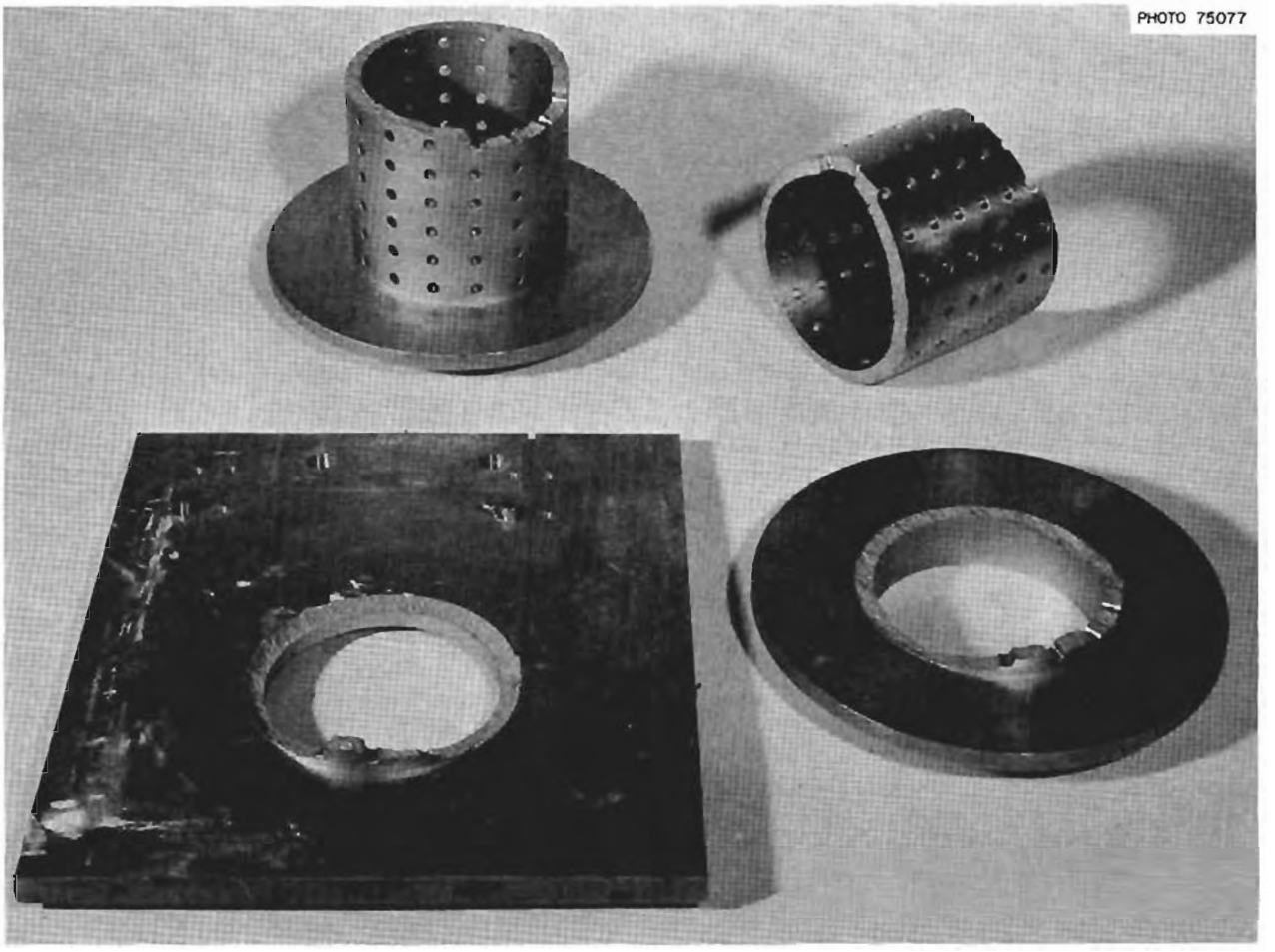

Fig. 8.14. Fractured Mechanical Part of a Large Cusp Coil.

quenching current in actual magnet systems. It would be desirable to reproduce, in small-scale tests, degradation phenomena which might occur in large nonaxisymmetrical superconducting magnet systems. It seems that the cusp coil test reproduces to some extent these degradation effects; however, more complete data are required. At any rate, the cusp coil test and careful analysis of short-sample flux flow characteristics are at this time the most realistic methods for evaluating the performance of superconducting winding material.

8.6 RADIO-FREQUENCY SPUTTERING TECHNIQUE FOR PRODUCING THIN FILMS

J. E. Simpkins

8.6.1 Introduction

For several of our experiments, uniform layers of copper upon Nb-Ti ribbons are required. The copper should be of high purity; the thickness of these films should vary from a few thousand angstroms to

a few microns. Perhaps the most difficult requirement is to achieve good bonding of the copper to the superconductor, since oxide layers can form on the surface of the superconductor. For other experiments, dielectric coatings are needed.

8.6.2 Remarks on the Physics of RF Sputtering

After considering the above requirements and the existing techniques for achieving them, it was decided to employ rf sputtering. Although sputtering of a cathode in a glow discharge was observed in 1852,[22] this phenomenon was not used extensively for the deposition of thin films until recently. Previously, the limited application of sputtering was probably due to the difficulties of producing films of high purity and to the low sputtering rates achieved by early workers. The present dc and rf sputtering technique allows the production of metal films of high purity with excellent adherence to their substrates. Under proper conditions, it is possible to obtain films with a crystalline structure which is similar to that of the target material.[23] If the sputtering is performed in an atmosphere containing a reactive gas, various metal compounds (such as insulating films of metal oxides) may be deposited. The rf sputtering technique makes it possible to sputter semiconductors and dielectrics in addition to metals.

Presently, three different phenomena are considered in the analysis of the sputtering process. They are momentum transfer, high-temperature spots, and volatile chemical transfer; of these, the first appears to be the most important. The momentum transfer mechanism was described by Kingdom and Langmuir.[24] Ions striking the surface of the target (cathode) undergo a series of collisions, after which neutral atoms and ions of the target material leave the surface. These particles may be deflected through the crystal lattice, producing a focusing effect.[25] This would account for the occurrence of films having a crystalline structure similar to that of the target material. If the substrate has a structure similar to that of the target, an epitaxial film may be achieved.

The positive gas ions which initiate sputtering are easily obtained from a glow discharge. The breakdown voltage in a glow discharge is determined by the pressure and spacing of the electrodes. This breakdown voltage region is followed by a region of constant voltage and increasing current. In the next region, called the "abnormal glow," both voltage and current increase. This is the region of interest for sputtering.

If rf power is applied, the electron path will be longer, and the pressure may be lowered. An rf glow discharge may be sustained at a pressure of only 2 μ. At this low pressure, the sputtered ions will have somewhat higher energy and fewer collisions with the gas. Higher sputtering rates result, together with an increase in film purity. An additional advantage is that these films are extremely uniform in thickness. By employing a magnetic field in the glow discharge region, an even lower operating pressure can be achieved, but film uniformity may suffer unless the magnetic field is very homogeneous in this region.

An important application of rf sputtering is the deposition of semiconductor and dielectric films.[26] This is not possible with dc because of positive surface charges which accumulate on the dielectric. Since the electrons in the plasma have a much higher mobility than the ions, this positive surface charge is not only neutralized but becomes even negative. If a blocking capacitor is placed between the rf supply and electrode, metals may be sputtered also.

8.6.3 An RF Sputtering Apparatus

We built an rf sputtering apparatus which is shown schematically in Fig. 8.15. The water-cooled target support and shield to prevent back sputtering are similar to the arrangement used by Davidse and Maissel.[27] A spacing of 0.5 cm is maintained between the target holder and shield. The target consists of a 4-in.-diam 0.99999 copper plate, which is bonded to the holder by conductive epoxy. The substrate table contains provisions for both heating and cooling the substrate and a thermocouple for monitoring its temperature. After

[22] W. R. Grove, *Phil. Trans.* 1 (1852).

[23] G. K. Wehner, *Phys. Rev.* **102**, 690 (1956).

[24] K. H. Kingdom and I. Langmuir, *Phys. Rev.* **22**, 210 (1923).

[25] R. H. Silsbee, *J. Appl. Phys.* **28**, 1246 (1957).

[26] G. S. Anderson, W. N. Mayer, and G. K. Wehner, *J. Appl. Phys.* **33**, 2991 (1962).

[27] P. D. Davidse and L. I. Maissel, *J. Appl. Phys.* **37**, 574 (1966).

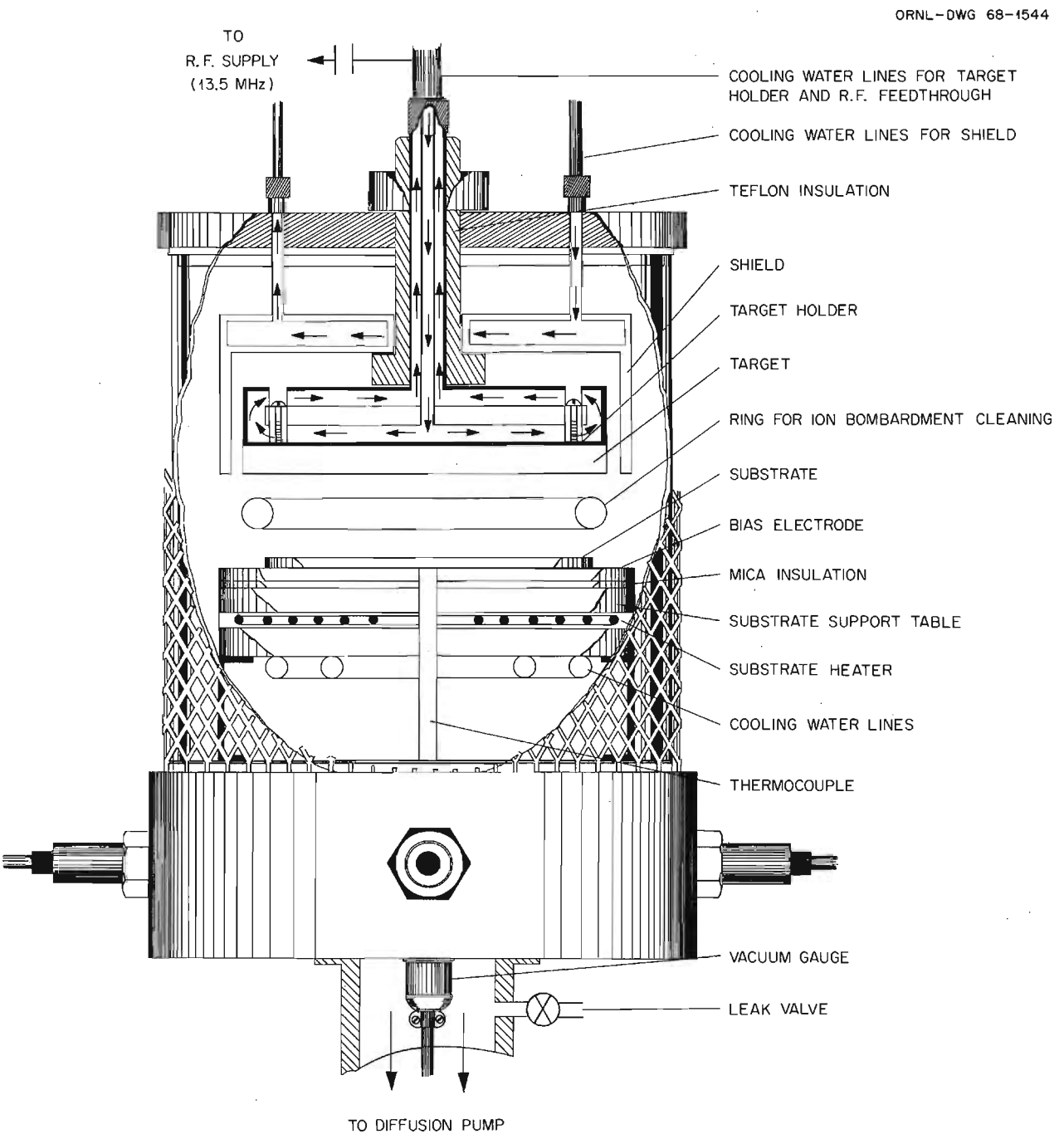

Fig. 8.15. Schematic of RF Sputtering Module.

pumping the system to 2×10^{-6} torr, 0.9999 argon is bled to a pressure of 100 μ. A metal ring, placed between substrate and target, is used to clean the substrate by ion bombardment at this pressure. The pressure is then lowered to about 3 μ, and rf power is turned on. A negative bias of about 200 V is applied to the substrate. This produces a continuous ion bombardment of the film during its deposition, effecting the preferential removal of adsorbed gas from the film.[28]

At the present time, the available power at the target is about 150 W. At this power limit, we are able to deposit copper at a rate of 40 Å/min. Improvements in the transmitter are being made, and the power is expected to be increased to about 1 kW.

Preliminary results are encouraging. Films deposited at room temperature on glass substrates are smooth, and adherence to the glass is excellent. Likewise, the films deposited on Nb-Ti ribbons are very adherent and assume the structure of the underlying substrate. For some applications it is desirable to deposit the film on a heated surface. Films sputtered on heated glass substrates (400°C) exhibited oxidation. Presently we are working on a procedure which should eliminate this difficulty.

8.7 DESIGN OF THE IMP MAGNET SYSTEM

R. L. Brown
D. L. Coffey
R. J. Colchin
J. L. Dunlap
R. S. Edwards
K. R. Efferson
W. F. Gauster
J. L. Horton
C. E. Parker
H. Postma
E. R. Wells
W. L. Wright

8.7.1 Introduction

The several methods developed here to optimize the design of nonaxisymmetrical magnet systems and to evaluate the anticipated electrical and mechanical performance of such a magnet system recently have been reviewed elsewhere.[29,30] The choice of a proper superconductor is critical.

As noted in the last semiannual report,[31] superconductor for IMP had been ordered on the basis of short-sample critical current specifications, and delivery was expected in July and August 1967. The first samples of this conductor were available in August. Tests, as detailed in Sect. 8.7.2, showed that the order specifications were met but that the conductor was not sufficiently stable. A new order has been placed with revised specifications. The procurement schedule, also detailed in Sect. 8.7.2, makes it unlikely that IMP mirror coil operation (phase I) can be obtained before May 1968.

The present design efforts are concentrated on phase I. Progress is reviewed in Sect. 8.7.3.

8.7.2 Conductor Procurement and Tests

It has been shown[32] that improved and carefully analyzed short-sample tests can yield useful information about the stabilized performance of composite superconducting wire. It was by these tests that the initial indication was found that the first IMP wire was not adequate for the magnet system. In the improved ORNL short-sample tests, the wire is mounted in a self-supporting manner totally surrounded by unobstructed liquid helium. A complete test cycle is run at each 5-kG interval up to 75 kG. The data show the regions of (1) resistanceless superconducting performance; (2) superconductor in flux flow state, with current sharing between superconductor and stabilizer; (3) takeoff to a fully resistive state; and (4) recovery to the flux flow or to the resistanceless superconducting state. Analysis of these data yields the extent of current sharing, the maximum surface heat flux at the point of takeoff, and the magnetoresistance of the copper stabilizer. For the first IMP wire the test showed unusually low values of surface heat flux at takeoff (i.e., $\dot{Q} \leq 0.1$ W/cm^2). Such low values suggest a poor thermal bond between the superconductor and the stabilizer or an inherently unstable superconductor.

A more critical evaluation of the expected coil performance of the superconductor is found in the

[28] L. I. Maissel and P. M. Schaible, *J. Appl. Phys.* **36**, 237 (1965).

[29] W. F. Gauster and D. L. Coffey, "Problems in Designing Non-Axisymmetrical Superconducting Magnet Systems," presented at the 1967 Applied Superconductivity Conference, Austin, Tex. (proceedings to be published).

[30] *Thermonuclear Div. Semiann. Progr. Rept. Apr. 30, 1967*, ORNL-4150, pp. 119–24.

[31] *Ibid.*, pp. 142–47.

[32] W. F. Gauster and J. B. Hendricks, "Flux Flow and Thermal Stability of Stabilized Superconductors," presented at the 1967 Applied Superconductivity Conference, Austin, Tex. (proceedings to be published).

ORNL cusp coil tests.[31,33] Approximately 1000 ft of superconductor is wound to form a two-coil set connected in series opposition (cusp mode). The cusp set is mounted with a horizontal axis in a Dewar in the vertical bore of a 65 kG copper magnet. Operation of the cusp set in the intense applied field produces conditions of high fields, large field gradients, high current densities, extreme forces, and restricted helium flow, simulating conditions in a full-size coil. A cusp coil set of the first IMP wire was tested in a background field of 50 kG. The coils were successfully operated through nine normal-state transitions, ranging from 390 to 450 A. On the tenth excitation the coil frame ruptured at 455 A. The full design current density of 8500 A/cm^2 was reached. However, the superconducting material achieved only about 75% of the short-sample conductor current. This degradation correlates with the very low $\dot{Q}$ at takeoff in the short-sample tests and suggests that the IMP coil systems would experience an unpredictable degradation with this particular superconducting material.

As a result of the cusp coil tests and the new short-sample tests, we concluded that superconducting wire specifications should include a range of stable operation in the current-sharing (flux flow) region.

Since it was not possible to amend the initial IMP superconductor wire order to the new specification requirements, the order was canceled. A new order has been placed with another manufacturer for the wire for the IMP mirror coils, subject to acceptance of a preproduction lot in short-sample tests.

A second order, for the quadrupole coil wire, will be placed in April 1968 after further tests. Sample lengths of appropriate rectangular superconducting wire are being obtained from several manufacturers, including the supplier of the first IMP wire. The wire will be studied in cusp coil tests and in short-sample tests prior to requesting bids on the quadrupole winding material, which constitutes about 90% of that required for the full coil system. It appears that the quadrupole coil winding will not begin before May 1968.

The use of a square (0.080 × 0.080 in.) conductor in the first cusp coil set caused some difficulty in that the wire had a natural tendency to twist up on one corner rather than to lie flat on the coil spool. This slight twist presents an opportunity for internal shearing of insulation in the coil when conductor movement occurs. To reduce or eliminate the effect, the new wire order is for 0.057 × 0.114 in. rectangular wire with approximately the same cross-section area as before.

[33] See sect. 8.5, this report.

8.7.3 Design Status

Initial operation of the IMP facility will be with mirror coils only, expected to start in May 1968. Design efforts have recently concentrated on this phase. Finish detailing is now well advanced on the mirror coil cans and the external vacuum tank, and these items are scheduled for shop work soon. The mirror coil spools are to be machined from solid forgings of 310 stainless steel (13 in. diameter × 9.5 in. thick). This approach, though expensive, avoids a possible problem with low-temperature weld strength in the highly stressed areas of the coil system. Additional design work is still in progress on the electrical connections between coils, the input current leads, and the cryogenic system.

Considerable attention has been given to the electromagnetic forces in the IMP facility. Dr. Heinz Parkus, professor at the University of Technology, Vienna, Austria, and the Mechanical and Nuclear Engineering Department of the Franklin Institute, Philadelphia, under the directorship of Dr. Zenon Zudans, did extensive work on the stress analysis of the mechanical structure. The design work is essentially complete on the mirror coil cans, but much still needs to be examined in the quadrupole coil system.

The current densities and fields of the IMP magnet system generate very substantial electromagnetic forces. Figure 8.16 shows the forces in the mirror coils of the system. The two mirror coils, when energized alone, generate a net force of 12,300 lb directed toward the center of the system. When the quadrupole coils around these mirror coils are energized, an additional net force of 5100 lb is generated on each mirror coil. The forces are due to the end turnarounds of the quadrupole coils, and both forces are directed to the right in the figure.

An analysis of the forces in the winding material of each mirror coil shows that maximum forces occur at 90° angles around the coil. The forces are alternately directed inward and outward (Fig.

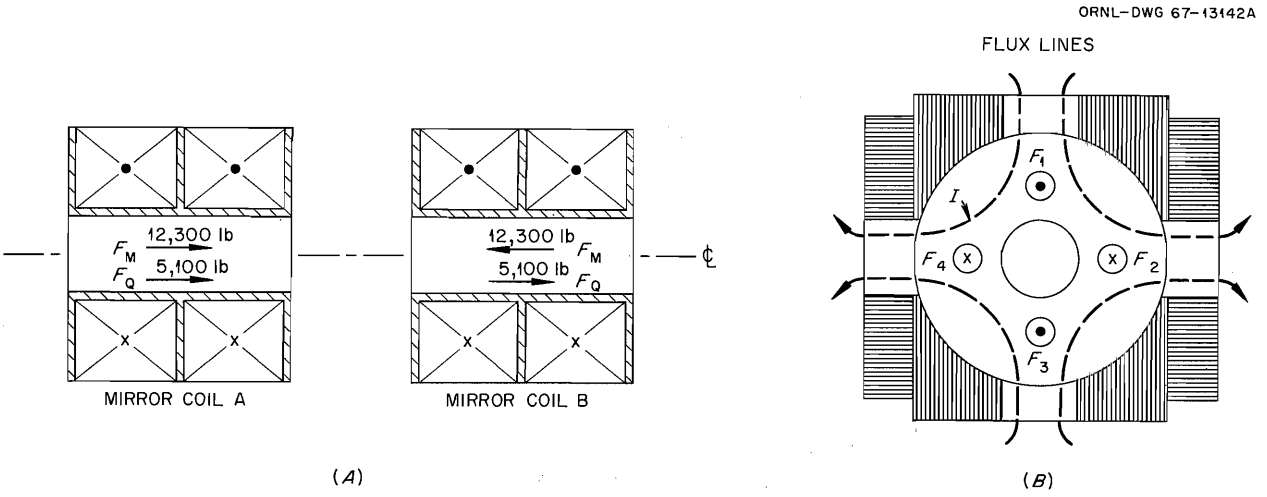

Fig. 8.16. IMP Mirror Coil Forces.

8.16*B*). The integral forces on each quadrant of mirror coil *A* are indicated by F_1 to F_4. Their values are (in pounds) +91,800, −83,000, +91,900, and −83,000 respectively. These forces are much greater than the uniform 3075-lb quadrant force which occurs when the mirror coils are energized alone.

The very high forces, fields, and current densities to be employed in the superconducting IMP magnet system have led us to a number of new and somewhat unique tests to evaluate conductor material in the magnet. It is not adequate to use only wire tensile test data to predict performance of the wire in the coil can. We have devised a "coil expander test" machine, shown in Fig. 8.17, to evaluate the performance of the conductor under conditions of high radial stress. By means of this device the expansion of the conductor winding under radial stress can be monitored.

Figure 8.18 shows the essential part of a "compression test device" for evaluating the insulation used on our wire. In this case the wire under test was 0.080 × 0.080 in. copper with 15 niobium-titanium filaments embedded within the copper. A spiral wrap of 0.005 in. thick × 0.080 in. wide Mylar tape has been applied to the conductor for insulation. Approximately 50% of the conductor surface was exposed. We used this test to evaluate both Nomex paper and Mylar insulations. The Nomex paper was found to be subject to tears due to its low shear strength, but it has the advantage that it allows only about one-half as much coil "breathing" and therefore may prove the superior material. These tests were made at room and at liquid-nitrogen temperatures.

The information obtained from the electrical and mechanical tests described has been essential in the design of the IMP magnet system.

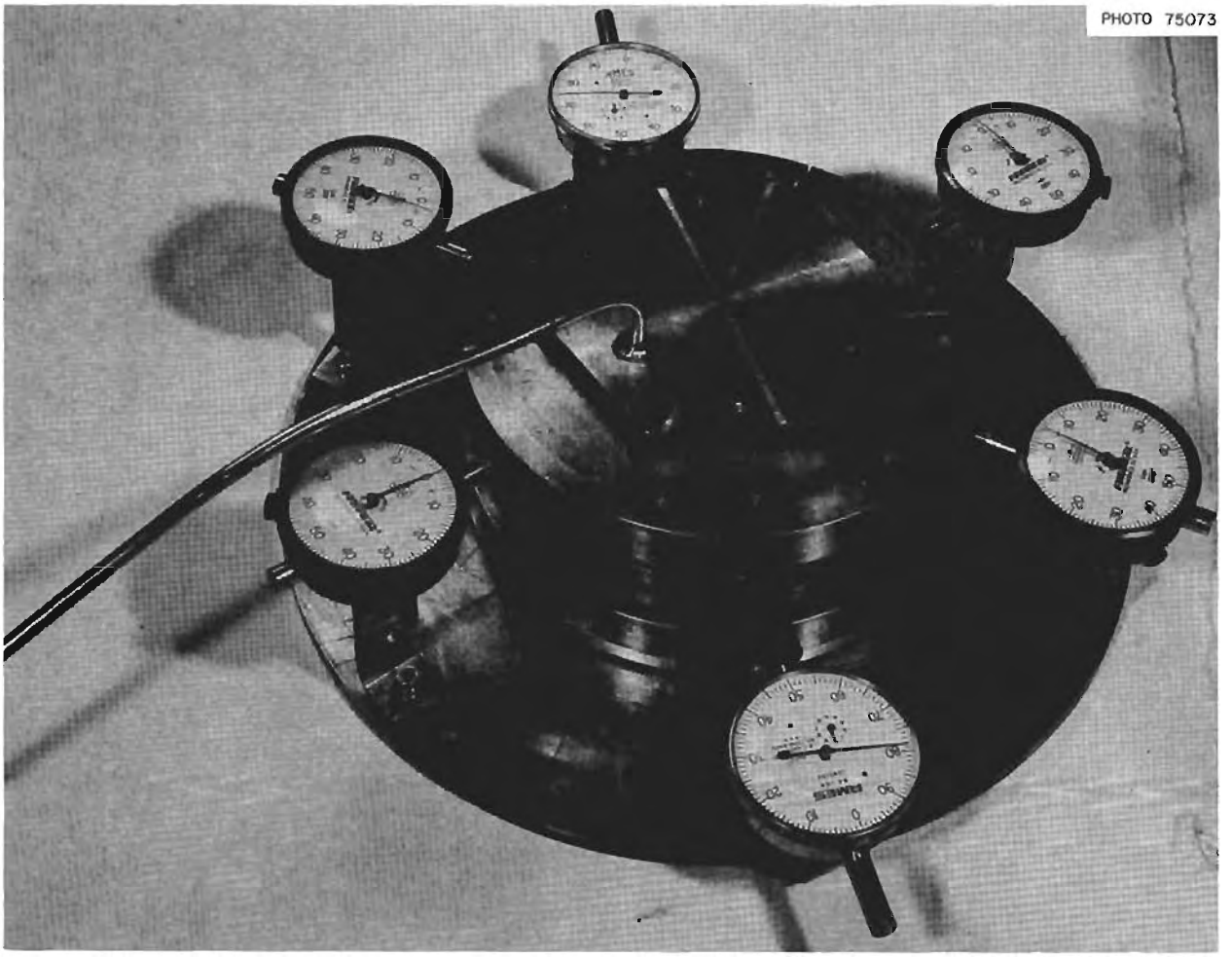

Fig. 8.17. Coil Expander Machine. Hydraulic pressure on the central section simulates radial electromagnetic forces. Six displacement meters monitor the reaction of the winding material.

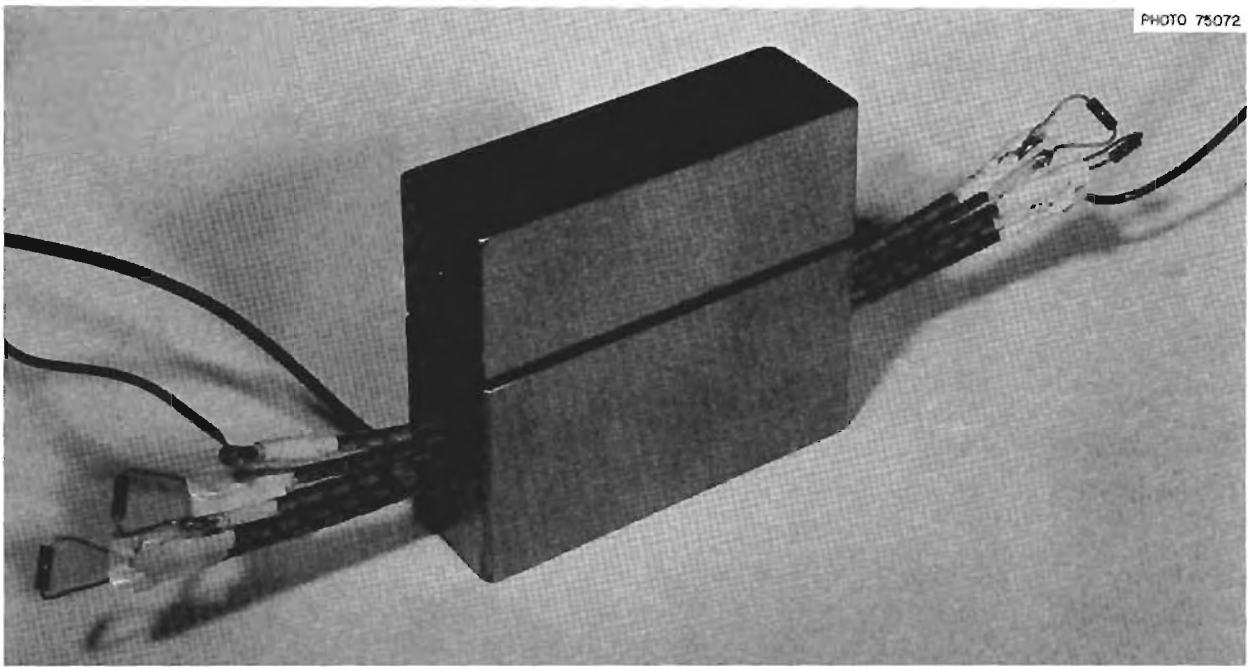

Fig. 8.18. Wire Compression Test Device Used to Evaluate Wire Insulation.

9. Design and Engineering: Service Report

Design and engineering services are generally reported incidentally with those of the research groups of the Division. This work includes executing or coordinating engineering design, shop fabrication, building operations, and maintenance for the Division.

Design activities for this reporting period are summarized as follows:

Jobs on hand 4-31-67 on which work had not started	3
New jobs received	100
Total jobs	103
Jobs completed	96
Jobs in progress	4
Backlog of jobs 10-31-67	3
Total drawings completed for period (does not include drawings for slides, reports, etc.)	192

Shop fabrication for this reporting period is summarized as follows:

Machine shops	
Completed jobs requiring 16 man-hours or less	75
Completed jobs requiring 17 to 1200 man-hours	135
Completed jobs of miscellaneous character (in plating, carpenter, electrical, glass, lead, etc., shops)	68
Average manpower per week	12.5
Number of jobs in progress	20
Electromagnet fabrication	
Completed jobs	4
Number of jobs in progress	1
Average manpower per week	1.5

Publications, ORNL Reports, Papers, and Traveling Lectures

OPEN LITERATURE

Author(s)	Title of Article	Journal (or Book)
Igor Alexeff, W. D. Jones, Karl Lonngren,[1] and David Montgomery[2]	Dispersion of Ion-Acoustic Waves	*Phys. Letters* **25A**, 629 (1967)
I. Alexeff and W. D. Jones	Landau Damping of Ion-Acoustic Waves Produced by a Light Contaminant	P. 357 in *Proc. Eighth Intern. Conf. Phenomena Ionized Gases, Vienna, Austria, Aug. 27–Sept. 2, 1967*, IAEA, Austria
I. Alexeff, W. D. Jones, and D. Montgomery[2]	Controlled Landau Damping of Ion-Acoustic Waves	*Phys. Rev. Letters* **19**, 422 (1967)
K. C. Hines and D. J. Sigmar	Energy Loss of Charged Particles in a Plasma	P. 295 in *Proc. Eighth Intern. Conf. Phenomena Ionized Gases, Vienna, Austria, Aug. 27–Sept. 2, 1967*, IAEA, Austria
G. G. Kelley	High Current DC Ion Beams	P. 29 in *Proc. U.S. Natl. Particle Accelerator Conf. Washington, D.C., Mar. 1–3, 1967* [*IEE Trans. Nucl. Sci.* **NS-14**(3), 29 (June 1967)]
	Elimination of Ambipolar Potential-Enhanced Loss in a Magnetic Trap	*Plasma Phys.* **9**, 503 (1967) (Research Note)
M. O. Krause and T. A. Carlson	Vacancy Cascade in the Reorganization of Krypton Ionized in an Inner Shell	*Phys. Rev.* **158**, 18 (1967)
J. R. McNally, Jr.	Atomic Spectra, Including Zeeman and Stark Effects	Part 7, chap. 2 of *Handbook of Physics*, E. U. Condon and Hugh Odishaw, Eds., McGraw-Hill, New York, 1967
R. V. Neidigh, Igor Alexeff, and W. D. Jones	Production of D-D Reactions by Beam-Plasma Interaction in the Steady-State	*Phys. Rev. Letters* **18**, 1109 (1967)

[1]Summer participant, University of Iowa.

[2]Consultant, University of Iowa.

ORNL REPORTS

Author(s)	Title	Number
Compiled by Atomic and Molecular Processes Information Center	Bibliography of Atomic and Molecular Processes for January–June 1965	ORNL-AMPIC-4
	International Directory of Workers in the Field of Atomic and Molecular Collisions	ORNL-AMPIC-5
	Bibliography of Atomic and Molecular Processes for July–December 1965	ORNL-AMPIC-6
	Bibliography of Atomic and Molecular Processes for January–June 1966	ORNL-AMPIC-7
	Bibliography of Atomic and Molecular Processes for July–December 1966	ORNL-AMPIC-8
	Bibliography of Atomic and Molecular Processes for January–June 1967	ORNL-AMPIC-9
R. A. Dandl, G. E. Guest, and N. H. Lazar	ORNL Target Plasma Program	ORNL-4080
W. D. Jones	Sound Waves in Plasmas – A Basic Phenomenon and a Simple Diagnostic Tool	ORNL-4089
A. H. Snell *et al.*	Thermonuclear Div. Semiann. Progr. Rept. Oct. 31, 1966	ORNL-4063
	Thermonuclear Div. Semiann. Progr. Rept. Apr. 30, 1967	ORNL-4150

PAPERS PRESENTED AT SCIENTIFIC AND TECHNICAL MEETINGS

ASTM Conference, Symposium on Photoelectron Spectroscopy, Denver, Colo., May 14–19, 1967

M. O. Krause, "Electron Spectrometry of Double-Electron Ejection from Rare Gas Atoms in the Photoabsorption Process" (invited paper).

American Physical Society, Division of Plasma Physics, Toronto, Canada, June 21–23, 1967

Igor Alexeff and W. D. Jones, "Controlled Landau Damping of Ion-Acoustic Waves."

R. E. Budwine, E. G. Harris,[1] and R. Sugihara,[1] "Non-Linear Coupling of Plasma Oscillations and Ion Sound Waves to Transverse Electromagnetic Waves."

J. F. Clarke, J. F. Lyon, and R. F. Stratton, "Micro-Instability in the DCX-2 Ion Beam."

W. M. Farr and R. E. Budwine, "Flute-Like 'Loss-Cone' Instabilities in Multi-Component Plasmas."

R. V. Neidigh, Igor Alexeff, and W. D. Jones, "Production of D-D Reactions by Beam-Plasma Interaction in the Steady State."

C. E. Nielsen,[2] "Role of the Partially Ionized Transition Layer in Gas-Bounded Plasmas."

M. Roberts, I. Alexeff, W. Halchin, and D. F. Howell, "Plasma Injected into a Levitated Toroidal Quadrupole."

W. L. Stirling and C. E. Nielsen,[2] "Characteristics of a Magnetically Collimated High-Pressure Helium Arc."

---

[1]Consultant, University of Tennessee.

[2]Consultant, Ohio State University.

International Symposium on Fluctuations and Diffusion in Plasmas, Princeton University, Princeton, N.J., June 26–30, 1967

E. G. Harris,[1] "Kinetic Theory of Unstable Plasmas."

Fifth International Conference on the Physics of Electronic and Atomic Collisions, Leningrad, USSR, July 17–23, 1967

M. O. Krause and W. E. Hunt,[3] "Multiple Charge Transfer of Multiply-Charged Xenon Ions in Neon, Argon, Krypton and Xenon."

C. F. Barnett, J. A. Ray, R. A. Langley, and A. Russek,[4] "Rydberg States of Hydrogen Molecules."

Special Topics in Nuclear Education and Research, Gatlinburg, Tennessee, Aug. 28, 1967

J. L. Dunlap, "Fusion and Plasmas."

VIIIth International Conference on Phenomena in Ionized Gases, Vienna, Austria, Aug. 27–Sept. 2, 1967

K. C. Hines and D. J. Sigmar, "Energy Loss of Charged Particles in a Plasma."

I. Alexeff, W. D. Jones, and D. Montgomery,[5] "Landau Damping of Ion-Acoustic Waves Produced by a Light Contaminant."

International Conference on Spectroscopy, Bombay, India, Jan. 9–18, 1967

J. R. McNally, Jr., "Excitation Heating of Ions to Moderate Temperatures" (presented by M. L. N. Shastri, Kanpur, India).

TRAVELING LECTURE PROGRAM

The Traveling Lecture Program is conducted in cooperation with Oak Ridge Associated Universities, Inc., as a part of the AEC's program of disseminating scientific and technical information to universities, particularly those in the South. Lectures delivered by ORNL personnel present unclassified atomic energy information to university undergraduate and graduate students and members of the faculty. The principal objectives of the program are to stimulate interest in atomic energy and related research in the university departments and to assist the teaching staff in expanding the scope of instruction offered under their regular curricula. One member of the Thermonuclear Division staff participated in the Traveling Lecture Program during this report period:

J. F. Clarke	"An Introduction to the Properties of the Plasma State," Villa Madonna College, Covington, Ky., Oct. 11, 1967.
	"Current Thermonuclear Research," Texas Technological College, Lubbock, Tex., Nov. 15, 1967.
	"An Introduction to the Properties of the Plasma State," Texas College of Arts and Industries, Kingsville, Tex., Nov. 14, 1967.
	"Current Thermonuclear Research," Georgia Institute of Technology, Atlanta, Ga., Oct. 26, 1967.

[3]Consultant, David Lipscomb College.

[4]Consultant, University of Connecticut.

[5]Consultant, University of Iowa.